# Atmosphere
# Entry

# AIAA SELECTED REPRINT SERIES

### Editors-in-Chief

ROBERT A. GROSS, Columbia University
New York, N.Y.

HOWARD S. SEIFERT, Stanford University
Stanford, California

## VOLUME I

## ATMOSPHERE ENTRY

### Editor

ALFRED J. EGGERS, JR., NASA, Washington, D.C.

# AIAA SELECTED REPRINT SERIES

### Editors-in-Chief

ROBERT A. GROSS, Columbia University
New York, N. Y.

HOWARD S. SEIFERT, Stanford University
Stanford, California

## VOLUME I

## ATMOSPHERE ENTRY

### Editor

ALFRED J. EGGERS, JR., NASA, Washington, D. C.

## CONTENTS

## CONTENTS

# INTRODUCTION

Serious attention to the problems of atmosphere entry developed during the early 1950's with the advent of large-scale effort to develop long range ballistic missiles. Among the results of this early activity was the discovery that motion and convective heating are intrinsically coupled and that for the range of weights and speeds of interest, blunting the body would reduce the heating problem. It was soon discovered too how lift might best be used to maneuver in the atmosphere; however, it became clear in the course of events that the price of lift was added weight to heat shield the entry vehicle. These results were shown to be valid at both subsatellite and supersatellite speeds and, within the framework of approximate inviscid flow and boundary layer theory plus available experimental data, they provided an orderly methodology for understanding the atmosphere entry problem for velocities approaching Earth escape speed. This methodology was also suitable for including consideration of heat sink, ablation, film, or radiation cooling.

Much remained to be done, however, in improving flow field calculations and in accounting for radiative heat transfer, alone and in combination with convective heat transfer at speeds the order of and greater than Earth escape speed, where ionization becomes thermally significant. More recent research has been concentrated on these and other aspects of hyperbolic entry.

The first seven papers reprinted in this volume span the spectrum of fundamental contributions to the understanding of atmosphere entry made during the earlier period. The more recent advances rest, in many cases, on these and similar works. A number of these advances along with some remaining problems are reviewed in the eighth and last paper reprinted herein.

In order to assist the reader who wishes to go beyond the papers compiled herein, there is also included a bibliography of publications on atmosphere entry. Both the papers and bibliography have, however, been limited by considerations of length to only a fraction of the many worthy contributions made throughout the dozen or more years that atmosphere entry has been a problem of high importance. If this book represents a proper fraction of contributions, the credit must go in large measure to my colleague, Nathaniel B. Cohen, whose efforts have been invaluable in compiling the contents.

Alfred J. Eggers, Jr.

# BIBLIOGRAPHY

Books

1. Liepmann, H. W. and Roshko, A., Elements of Gas Dynamics, John Wiley & Sons, Inc., New York, 1957.

2. Hayes, W. D., and Probstein, R. F., Hypersonic Flow Theory, Academic Press, New York, 1959.

3. Chernyi, G. G. (translated and edited by Ronald F. Probstein) Introduction to Hypersonic Flow, Academic Press, New York, 1961.

4. Dorrance, William H., Viscous Hypersonic Flow-Theory of Reacting and Hypersonic Boundary Layers, McGraw-Hill Book Company, Inc., New York, 1962.

5. Loh, W. H. T., Dynamics and Thermodynamics of Planetary Entry, Prentice-Hall, Inc., Englewood Cliffs, N. J., 1963.

6. Penner, S. S., Chemistry Problems in Jet Propulsion, Pergamon Press, London, England, 1957.

7. Penner, S. S., Quantitative Molecular Spectroscopy and Gas Emissivities, Addison-Wesley, Reading, Mass., 1959.

Reviews and Surveys

1. Allen, H. Julian, "Hypersonic Flight and the Re-Entry Problem, The Twenty-First Wright Brothers Lecture," J. Aero Sci., vol. 25, no. 4, 1958, pp. 217-227.

2. Eggers, A. J., Jr., and Wong, T. J., "Motion and Heating of Lifting Vehicles During Atmosphere Entry," ARS Jour., vol. 31, no. 10, 1961, pp. 1364-1375.

3. Allen, H. Julian, "Gas Dynamics Problems of Space Vehicles," Proc. NASA - University Conference on the Science and Technology of Space Exploration, vol. 2, NASA SP-11, no. 54, 1962, pp. 251-267.

4. Trimpi, Robert L., Grant, Frederick C., and Cohen, Nathaniel B., "Aerodynamics and Heating Problems of Advanced Reentry Vehicles," Proc. NASA - University Conference on the Science and Technology of Space Exploration, vol. 2, NASA SP-11, no. 53, 1962, pp. 235-248.

5. Cheng, Hsien K., "Recent Advances in Hypersonic Flow Research," AIAA Jour., vol. 1, no. 2, 1963, pp. 295-310.

6.  Allen, H. Julian, "The Aerodynamic Heating of Atmosphere Entry Vehicles –
    A Review," presented at the Symposium on Fundamental Phenomana in Hyper-
    sonic Flow, June 25-26, 1964, Buffalo, New York.

7.  Love, Eugene S., "Factors Influencing Configuration and Performance of
    Multipurpose Manned Entry Vehicles," Jour. Spacecraft and Rockets, vol. 1,
    no. 1, 1964, pp. 3-12.

8.  Nerem, Robert M., "Radiating Flows Around Re-entry Bodies," presented at
    the XVIth IAF International Congress, September 13-18, 1965, Athens, Greece.

Flight Mechanics, Motion, and Heating

1.  Eggers, Alfred J., Jr., Allen, H. Julian, and Neice, Stanford E., "A Com-
    parative Analysis of the Performance of Long-Range Hypervelocity Vehicles,"
    NACA Report 1382, 1958.

2.  Eggers, Alfred J., Jr., "The Possibility of a Safe Landing," Space Technology,
    Edited by Howard S. Seifert, John Wiley and Sons, Inc., New York, 1959,
    pp. 13-01 to 13-53.

3.  Chapman, Dean R., "An Approximate Analytical Method for Studying Entry
    into Planetary Atmospheres", NASA TR R-11, 1959.

4.  Chapman, Dean R., "An Analysis of the Corridor and Guidance Requirements
    for Supercircular Entry into Planetary Atmospheres," NASA TR R-55, 1960.

5.  Lees, L., Hartwig, F. W., and Cohen, C. B., "Use of Aerodynamic Lift
    During Entry into the Earth's Atmosphere," ARS Jour. vol. 29, no. 9, 1959,
    pp. 633-641.

6.  Loh, W. H. T., "Dynamics and Thermodynamics of Re-Entry," J. Aero/Space
    Sci., vol. 27, no. 10, 1960, pp. 748-762.

7.  Wong, T. J., and Slye, R. E., "The Effect of Lift on Entry Corridor Depth
    and Guidance Requirements for the Return Lunar Flight," NASA TR R-80, 1960.

8.  Loh, W. H. T., "Some Exact Analytical Solutions of Planetary Entry,"
    AIAA Jour., vol. 1, no. 4, 1963, pp. 836-842.

9.  Carlson, Robert W., and Swenson, Byron L., "Maneuvering Flight within
    Earth-Entry Corridors at Hyperbolic Speeds," Jour. Spacecraft and Rockets,
    vol. 3, no. 3, 1966, pp. 353-358.

## Aerothermochemistry and Transport Properties

1. von Karman, Th., "Fundamental Equations in Aerothermochemistry," Selected Combustion Problems II, AGARD Liege, Butterworths Scientific Publications, London, 1956, pp. 167-184.

2. Lighthill, M. J., "Dynamics of a Dissociating Gas. Part I, Equilibrium Flow," Jour. Fluid Mechs., vol. 2, part 1, 1957, pp. 1-32.

3. Lighthill, M. J., "Dynamics of a Dissociating Gas. Part 2, Quasi-Equilibrium Transfer Theory," Jour. Fluid Mechs., vol. 8, part 2, 1960, pp. 161-182.

4. Freeman, N. C., "Dynamics of a Dissociating Gas: Non-Equilibrium Theory," High Altitude and Satellite Rockets, The Royal Aeronautical Society and the British Interplanetary Society, London, 1958, pp. 72-81.

5. Hansen, C. Frederick, "Approximations for the Thermodynamic and Transport Properties of High-Temperature Air," NASA TR R-50, 1959.

6. Yos, Jerrold M., "Transport Properties of Nitrogen, Hydrogen, Oxygen, and Air to 30,000° K," Avco Report RAD TM-63-7, 1963

7. Ahtye, Warren F., "A Critical Evaluation of Methods for Calculating Transport Coefficients of Partially and Fully Ionized Gases," NASA TN D-2611, 1965.

## Inviscid Flow Fields

1. Belotserkovsky, O. M., "Flow Past a Circular Cylinder with a Detached Shock Wave," Doklady, Akad. Nauk SSSR, vol. 113, no. 3, 1957, pp. 509-512.

2. Garabedian, P. R., and Lieberstein, H. M., "On the Numerical Calculation of Detached Bow Shock Waves in Hypersonic Flow," J. Aero. Sci., vol. 25, no. 2, 1958, pp. 109-118.

3. Lomax, Harvard, and Inouye, Mamoru, "Numerical Analysis of Flow Properties about Blunt Bodies Moving at Supersonic Speeds in an Equilibrium Gas," NASA TR R-204, 1964.

4. Bohachevsky, Ihor O., Rubin, Ephraim L., and Mates, Robert E., "A Direct Method for Computation of Nonequilibrium Flows with Detached Shock Waves," presented at the AIAA Second Aerospace Sciences Meeting, Jan. 25-27, 1965, (AIAA Paper No. 65-24)

5. Kaattari, George E., "Shock Envelopes of Blunt Bodies at Large Angles of Attack," NASA TN D-1980, 1963.

## Convective Heat Transfer

1.  Lees, Lester, "Laminar Heat Transfer Over Blunt-Nose Bodies at Hypersonic Flight Speeds," Jet Propulsion, vol. 26, no. 4, 1956, pp. 259-269, 274.

2.  Lees, Lester, "Recovery Dynamics - Heat Transfer at Hypersonic Speeds in a Planetary Atmosphere," Space Technology, Edited by Howard S. Seifert, John Wiley and Sons, Inc., New York, 1959, pp 12-01 to 12-20.

3.  Kemp, N. H., Rose, P. H., and Detra, R. W., "Laminar Heat Transfer around Blunt Bodies in Dissociated Air," J. Aero/Space Sci., vol. 26, no. 27, 1959, pp. 421-430.

4.  Cohen, Nathaniel B., "Boundary-Layer Similar Solutions and Correlation Equations for Laminar Heat Transfer Distribution in Equilibrium Air at Velocities up to 41,000 Feet per Second," NASA TR R-118, 1961.

5.  Fay, James A., and Kemp, Nelson H., "Theory of Stagnation-Point Heat Transfer in a Partially Ionized Diatomic Gas," AIAA Jour., vol. 1, no. 12, 1963, 2741-2751.

6.  Hoshizaki, H., "Heat Transfer in Planetary Atmospheres at Super-Satellite Speeds," ARS Jour., vol. 32, no. 10, 1962, pp. 1544-1552.

7.  Howe, John T., and Sheaffer, Yvonne S., "Effects of Uncertainties in the Thermal Conductivity of Air on Convective Heat Transfer for Stagnation Temperature up to 30,000° K," NASA TN D-2678, 1965

8.  Rose, Peter H., Probstein, Ronald F., and Adams, Mac C., "Turbulent Heat Transfer Through a Highly Cooled, Partially Dissociated Boundary Layer," J. Aero/Space Sci., vol. 25, no. 12, 1958, pp. 751-760.

9.  Dorrance, W. H., "Dissociation Effects upon Compressible Turbulent Boundary Layer Skin Friction and Heat Transfer," ARS Jour., vol. 31, no. 1, 1961, pp 61-70.

## Radiative Heat Transfer

1.  Kivel, B., and Bailey, K., "Tables of Radiation from High Temperature Air," Avco-Everett Res. Lab. Res. Rep't. 21, 1957.

2.  Kivel, Bennett, "Radiation from Hot Air and its Effect on Stagnation Point Heating," J. Aero/Space Sci., vol. 28, no. 2, 1961, pp. 96-102.

3.  Nardone, M. C., Breene, R. G., Zeldin, S. S., and Riethof, T. R., "Radiance of Species in High Temperature Air," General Electric Co., Space Sciences Lab. Rep't. R63SD3, 1963.

4. Biberman, L. M., Iakubov, I. T., Norman, G. E., and Borobyov, V. S., "Radiation Heating Under Hypersonic Flow," Astronautica Acta, vol. X/fasc. 3-4, 1964, pp. 238-252.

5. Goulard, R., "Fundamental Equations of Radiation Gas Dynamics," The High Temperature Aspects of Hypersonic Flow, ed., W. C. Nelson, The Macmillan Co., New York, N.Y., 1964, pp. 529-554.

6. Scala, S. M., and Sampson, D. H., "Heat Transfer in Hypersonic Flow with Radiation and Chemical Reaction," Supersonic Flow, Chemical Processes, and Radiative Transfer, Edited by D. B. Olfe and V. Zakkay, The Macmillan Co., New York, N.Y. 1964, pp 319-354.

7. Yoshikawa, K. K., and Chapman, D. R., "Radiative Transfer and Absorption Behind a Hypersonic Normal Shock Wave," NASA TN D-1424, 1962.

8. Wick, Bradford H., "Radiative Heating of Vehicles Entering the Earth's Atmosphere," The High Temperature Aspects of Hypersonic Flow, ed., W. C. Nelson, The Macmillan Co., New York, N.Y., 1964, pp. 607-627.

9. Hoshizaki, H., and Wilson, K. H., "Viscous, Radiating Shock Layer about a Blunt Body," AIAA Jour., vol. 3, no. 9, 1965, pp. 1614-1622.

## Mass Transfer Cooling and Ablation

1. Lees, Lester, "Convective Heat Transfer with Mass Addition and Chemical Reactions," Third Combustion and Propulsion Colloquium, Pergamon Press, London, England, 1958, pp. 451-498.

2. Bethe, Hans A., and Adams, Mac C., "A Theory for the Ablation of Glassy Materials," J. Aero/Space Sci., vol. 26, no. 6, 1959, pp. 321-328, 350.

3. Roberts, Leonard, "Mass Transfer Cooling Near the Stagnation Point," NASA TR R-8, 1959.

4. Roberts, Leonard, "A Theoretical Study of Stagnation - Point Ablation," NASA TR R-9, 1959

5. Scala, S. M., and Gilbert, L. M., "Thermal Degradation of Char-Forming Plastics During Hypersonic Flight," ARS Jour., vol. 32, no. 6, 1962, pp. 917-924.

6.  Munson, T. R., and Spindler, R. J., "Transient Thermal Behavior of Decomposing Materials, Part I: General Theory and Application to Convective Heating," presented at the IAS 30th Annual Meeting, Jan. 22-24, 1962, New York, N. Y. (IAS Paper No. 62-30)

7.  Steg, L., and Lew, H., "Hypersonic Ablation," The High Temperature Aspects of Hypersonic Flow, ed. W. C. Nelson, The Macmillan Co., New York, N.Y., 1964, pp. 629-680.

8.  Howe, John T., and Sheaffer, Yvonne S., "Mass Addition in the Stagnation Region for Velocity up to 50,000 feet per second," NASA TR R-207, 1964.

9.  Vojvodich, Nick S., and Pope, Ronald B., "The Influence of Ablation on Stagnation Region Convective Heating for Dissociated and Partially Ionized Boundary-Layer Flows," Proceedings of the 1965 Heat Transfer and Fluid Mechanics Institute, ed., Andrew F. Charwat, Stanford University Press, Stanford, Calif., 1965, pp. 114-137.

# REPORT 1381

# A STUDY OF THE MOTION AND AERODYNAMIC HEATING OF BALLISTIC MISSILES ENTERING THE EARTH'S ATMOSPHERE AT HIGH SUPERSONIC SPEEDS [1]

By H. Julian Allen and A. J. Eggers, Jr.

## SUMMARY

A simplified analysis is made of the velocity and deceleration history of ballistic missiles entering the earth's atmosphere at high supersonic speeds. It is found that, in general, the gravity force is negligible compared to the aerodynamic drag force and, hence, that the trajectory is essentially a straight line. A constant drag coefficient and an exponential variation of density with altitude are assumed and generalized curves for the variation of missile speed and deceleration with altitude are obtained. A curious finding is that the maximum deceleration is independent of physical characteristics of a missile (e. g., mass, size, and drag coefficient) and is determined only by entry speed and flight-path angle, provided this deceleration occurs before impact.

The results of the motion analysis are employed to determine means available to the designer for minimizing aerodynamic heating. Emphasis is placed upon the convective-heating problem including not only the total heat transfer but also the maximum average and local rates of heat transfer per unit area. It is found that if a missile is so heavy as to be retarded only slightly by aerodynamic drag, irrespective of the magnitude of the drag force, then convective heating is minimized by minimizing the total shear force acting on the body. This condition is achieved by employing shapes with a low pressure drag. On the other hand, if a missile is so light as to be decelerated to relatively low speeds, even if acted upon by low drag forces, then convective heating is minimized by employing shapes with a high pressure drag, thereby maximizing the amount of heat delivered to the atmosphere and minimizing the amount delivered to the body in the deceleration process. Blunt shapes appear superior to slender shapes from the standpoint of having lower maximum convective heat-transfer rates in the region of the nose. The maximum average heat-transfer rate per unit area can be reduced by employing either slender or blunt shapes rather than shapes of intermediate slenderness. Generally, the blunt shape with high pressure drag would appear to offer considerable promise of minimizing the heat transfer to missiles of the sizes, weights, and speeds of usual interest.

## INTRODUCTION

For long-range ballistic trajectories one of the most difficult phases of flight the designer must cope with is the reentry into the earth's atmosphere, wherein the aerodynamic heating associated with the high flight speeds is intense. The air temperature in the boundary layer may reach values in the tens of thousands of degrees Fahrenheit which, combined with the high surface shear, promotes very great convective heat transfer to the surface. Heat-absorbent material must therefore be provided to prevent destruction of the essential elements of the missile. It is characteristic of long-range rockets that for every pound of material which is carried to "burn-out," many pounds of fuel are required in the booster to obtain the flight range. It is clear, therefore, that the amount of material added for protection from excessive aerodynamic heating must be minimized in order to keep the take-off weight to a practicable value. The importance of reducing the heat transferred to the missile to the least amount is thus evident.

For missiles designed to absorb the heat within the solid surface of the missile shell, a factor which may be important, in addition to the total amount of heat transferred, is the rate at which it is transferred since there is a maximum rate at which the surface material can safely conduct the heat within itself. An excessively high time rate of heat input may promote such large temperature differences as to cause spalling of the surface, and thus result in loss of valuable heat-absorbent material, or even structural failure as a result of stresses induced by the temperature gradients.

For missiles designed to absorb the heat with liquid coolants (e. g., by transpiration cooling where the surface heat-transfer rate is high, or by circulating liquid coolants within the shell where the surface heat-transfer rate is lower), the time rate of heat transfer is similarly of interest since it determines the required liquid pumping rate.

These heating problems, of course, have been given considerable study in connection with the design of particular missiles, but these studies are very detailed in scope. There has been need for a generalized heating analysis intended to show in the broad sense the means available for minimizing the heating problems. Wagner, reference 1, made a step toward satisfying this need by developing a laudably simple motion analysis. This analysis was not generalized, however, since it was his purpose to study the motion and heating of a particular missile.

It is the purpose of this report to simplify and generalize the analysis of the heating problem in order that the salient features of this problem will be made clear so that successful solutions of the problem will suggest themselves.

A motion analysis, having the basic character of Wagner's approach, precedes the heating analysis. The generalized results of this analysis are of considerable interest in themselves and, accordingly, are treated in detail.

## ANALYSIS

### MOTION OF THE BODY

Consider a body of mass m entering the atmosphere from great height. If, at any altitude $y$, the speed is $V$ and the angle of approach is $\theta$ to the horizontal (see sketch), the



Impact point (0,0)
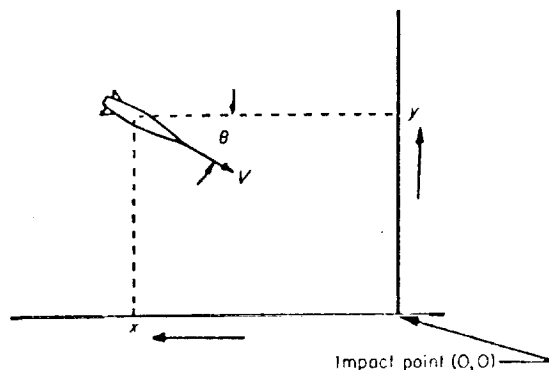
parametric equations of motion can be written [2]

$$\left.\begin{array}{l} \dfrac{d^2y}{dt^2}=-g+\dfrac{C_D\rho V^2 A}{2m}\sin\theta \\[2mm] \dfrac{d^2x}{dt^2}=-\dfrac{C_D\rho V^2 A}{2m}\cos\theta \end{array}\right\} \qquad (1)$$

where

$C_D$    drag coefficient, dimensionless
$V$    speed, ft/sec
$A$    reference area for drag evaluation, sq ft
$m$    mass of the body, slugs
$\rho$    mass density of the air, slugs/ft^{3}
$g$    acceleration of gravity, ft/sec[2]
$x,y$    horizontal and vertical distance from the point of impact with the earth, ft
$\theta$    angle between the flight path and the horizontal, deg

(See Appendix A for complete list of symbols.)

In general, the drag coefficient varies with Mach number and Reynolds number, while the density and, to a very minor extent, the acceleration of gravity vary with altitude. Hence it is clear that exact solution of these equations is formidable. Let us first, then, consider the following simplified case:

1. The body descends vertically.
2. The drag coefficient is constant.[3]
3. The acceleration of gravity is constant.[4]
4. The density as a function of altitude is given by the relation

$$\rho=\rho_0 e^{-\beta y} \qquad (2)$$

where $\rho_0$ and $\beta$ are constants. This relation is consistent with the assumption of an isothermal atmosphere.

---

[2] Properly, the analysis should consider those effects resulting from the fact that the earth is a rotating sphere, but since the altitude range for which drag effects are important is less than 1 percent of the radius of the earth, the rectilinear treatment given in this analysis is permissible.

[3] As is well known, this assumption is generally of good accuracy at the high Mach numbers under consideration, at least as long as the total drag is largely pressure drag.

[4] The acceleration of gravity decreases by only 1 percent for every 100,000-foot increase in altitude.

Equations (1) then reduce to the single equation

$$\frac{d^2y}{dt^2}=-\frac{dV}{dt}=-g+\frac{C_D\rho_0 A}{2m}e^{-\beta y}V^2 \qquad (3)$$

Noting that

$$\frac{dV}{dt}=-V\frac{dV}{dy}$$

we let

$$Z=V^2$$

and equation (3) becomes the linear differential equation

$$\frac{dZ}{dy}-\frac{C_D\rho_0 A}{m}e^{-\beta y}Z+2g=0 \qquad (4)$$

which has the well-known solution

$$Z=e^{\int\frac{C_D\rho_0 A}{m}e^{-\beta y}dy}\left(-2g\int e^{-\int\frac{C_D\rho_0 A}{m}e^{-\beta y}dy}dy+const.\right)$$

Performing the integrations, we obtain as the solution of this relation

$$Z=V^2=e^{-\frac{C_D\rho_0 A}{\beta m}e^{-\beta y}}\left[\frac{2g}{\beta}\sum_{n=1}^{\infty}\frac{\left(\frac{C_D\rho_0 A}{\beta m}e^{-\beta y}\right)^n}{n\lfloor n}-2gy+const.\right] \qquad (5)$$

so that the deceleration becomes, in terms of gravity acceleration,

$$-\frac{dV}{dt}{g}=\frac{C_D\rho_0 A}{2mg}e^{-\beta y}e^{-\frac{C_D\rho_0 A}{\beta m}e^{-\beta y}}\left[\frac{2g}{\beta}\sum_{n=1}^{\infty}\frac{\left(\frac{C_D\rho_0 A}{\beta m}e^{-\beta y}\right)^n}{n\lfloor n}-2gy+const.\right]-1 \qquad (6)$$

As an example, consider the vertical descent of a solid iron sphere having a diameter of 1 foot. For a sphere the drag coefficient may be taken as unity, based on the frontal area for all Mach numbers greater than about 1.4. In equation (2), which describes the variation of density with altitude, the constants should clearly be so chosen as to give accurate values of the density over the range of altitudes for which the deceleration is large. It is seen in figure 1 that for

$$\rho_0=0.0034 \text{ slugs/ft}^3$$

and

$$\beta=\frac{1}{22,000}\text{ ft}^{-1}$$

which yields

$$\rho=0.0034\,e^{-\frac{y}{22,000}} \qquad (7)$$

the calculated density is in good agreement with the NACA standard atmosphere values obtained from references 2 and 3 for the altitude range from 20,000 to 180,000 feet. These relations have been used in calculating the velocity and deceleration of the sphere for various altitudes, assuming
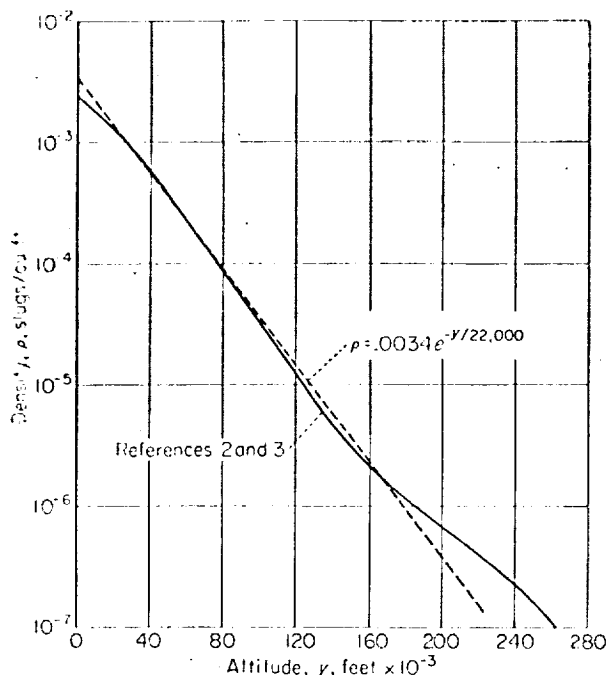
**FIGURE 1.**—Variation of density with altitude.
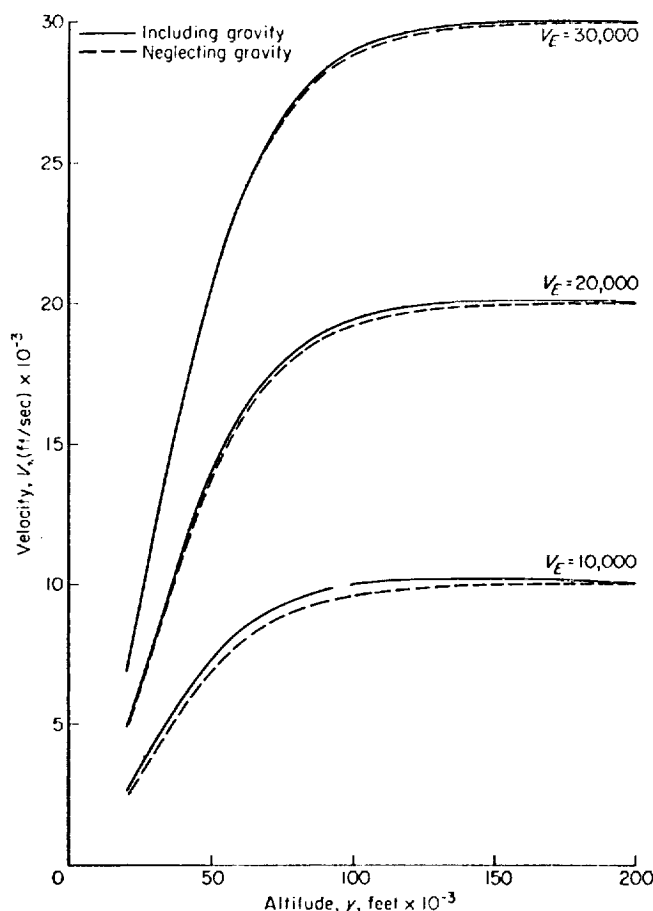


**FIGURE 2.**—Variations of velocity with altitude for a 1-foot diameter, solid iron sphere entering the earth's atmosphere vertically at velocities of 10,000, 20,000, and 30,000 ft/sec.

vertical entrance velocities of 10,000, 20,000, and 30,000 feet per second at 40 miles altitude which, for these cases, may be considered the "outer reach" of the atmosphere. The results of these calculations are presented as the solid curves in figures 2 and 3.

It is seen in figure 3 that for the high entrance speeds considered, the decelerations reach large values compared to the acceleration of gravity. This suggests that the gravity term in equation (3) may be neglected without seriously affecting the results.[5] When this term is neglected the equation of motion becomes

$$-\frac{dV}{dt} = V\frac{dV}{dy} = \frac{C_D \rho_o A}{2m} e^{-\beta y} V^2 \tag{8}$$
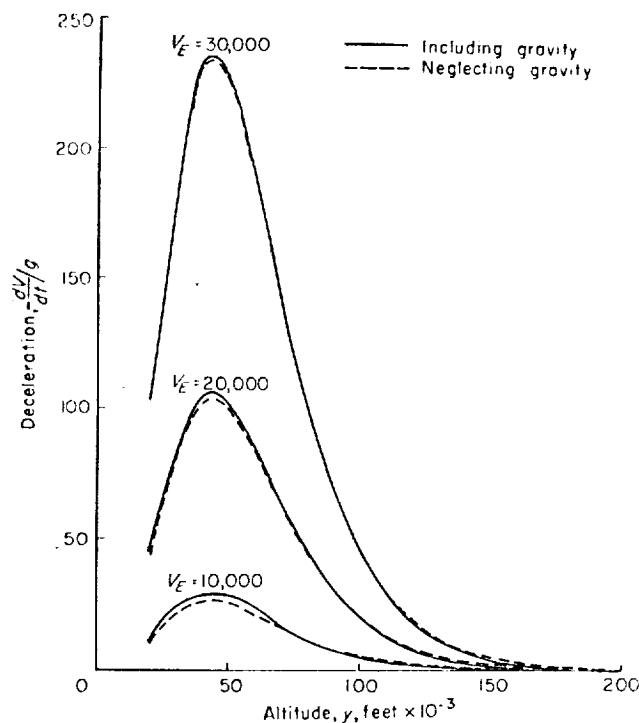


**FIGURE 3.**—Variations of deceleration with altitude for a 1-foot diameter, solid iron sphere entering the earth's atmosphere vertically at velocities of 10,000, 20,000, and 30,000 ft/sec.

Integration gives

$$\ln V = -\frac{C_D \rho_o A}{2\beta m} e^{-\beta y} + const.$$

or

$$V = const. \times e^{-\frac{C_D \rho_o A}{2\beta m} e^{-\beta y}}$$

At the altitude of 40 miles it can readily be shown that the term

$$e^{-\frac{C_D \rho_o A}{2\beta m} e^{-\beta y}}$$

is very nearly unity so that the velocity may be written

$$V = V_E e^{-\frac{C_D \rho_o A}{2\beta m} e^{-\beta y}} \tag{9}$$

---

[5] It is usual to neglect the gravity acceleration a priori (see e. g., refs. 1 and 4.)

and

$$-\frac{\frac{dV}{dt}}{g} = \frac{C_D \rho_o A V_E^2}{2mg} e^{-\beta y} e^{-\frac{C_D \rho_o A}{\beta m} e^{-\beta y}} \tag{10}$$

where $V_E$ is the entrance speed.

By use of equations (9) and (10) the vertical-descent speeds and decelerations for the 1-foot-diameter sphere previously considered have been calculated for the same entrance speeds. The results are shown as the dashed curves in figures 2 and 3. It is seen that these approximate calculations agree very well with those based on the more complete equation of motion (eq. (3)).

The above finding is important, for it indicates that in the general case, wherein the body enters the atmosphere at high speed at angle $\theta_E$ to the horizontal, the gravity term, provided $\theta_E$ is not too small, may be neglected in equation (1) to yield

$$\left.\begin{array}{l} \dfrac{d^2y}{dt^2} = \dfrac{C_D \rho V^2 A \sin \theta_E}{2m} \\[2mm] \dfrac{d^2x}{dt^2} = \dfrac{C_D \rho V^2 A \cos \theta_E}{2m} \end{array}\right\} \tag{11}$$

so that the flight path is essentially a straight line (i. e., $\theta = \theta_E$), and the resultant deceleration equation becomes

$$-\frac{dV}{dt} = \frac{C_D \rho A V^2}{2m} \tag{12}$$

Now, again, if the density relation given by equation (2) is used and it is noted that

$$V = \frac{-\frac{dy}{dt}}{\sin \theta_E} \quad \text{or} \quad -\frac{dV}{dt} = V \sin \theta_E \frac{dV}{dy}$$

equation (12) becomes

$$\frac{dV}{V} = \frac{C_D \rho_o A}{2m \sin \theta_E} e^{-\beta y} dy$$

which can be integrated to yield

$$V = V_E e^{-\frac{C_D \rho_o A}{2\beta m \sin \theta_E} e^{-\beta y}} \tag{13}$$

and the deceleration is then

$$-\frac{\frac{dV}{dt}}{g} = \frac{C_D \rho_o A V_E^2}{2mg} e^{-\beta y} e^{-\frac{C_D \rho_o A}{\beta m \sin \theta_E} e^{-\beta y}} \tag{14}$$

The altitude $y_1$ at which the maximum deceleration occurs is found from this relation to be

$$y_1 = \frac{1}{\beta} \ln \frac{C_D \rho_o A}{\beta m \sin \theta_E} \tag{15}$$

If $y_1$ is positive the velocity $V_1$ (from eqs. (13) and (15)) at which the maximum deceleration occurs becomes

$$V_1 = V_E e^{-\frac{1}{2}} \cong 0.61 V_E \tag{16}$$

and the value of the maximum deceleration is

$$-\left(\frac{\frac{dV}{dt}}{g}\right)_{max} = -\left(\frac{\frac{dV}{dt}}{g}\right)_1 = \frac{\beta V_E^2 \sin \theta_E}{2ge} \tag{17}$$

If equations (13) and (14) are rewritten to make the altitude reference point $y_1$ rather than zero, then

$$V = V_E e^{-\frac{C_D \rho_o A}{2\beta m \sin \theta_E} e^{-\beta(y_1 + \Delta y)}}$$

and

$$-\frac{\frac{dV}{dt}}{g} = \frac{C_D \rho_o A V_E^2}{2mg} e^{-\beta(y_1 + \Delta y)} e^{-\frac{C_D \rho_o A}{\beta m \sin \theta_E} e^{-\beta(y_1 + \Delta y)}}$$

respectively, where $\Delta y$ is the change in altitude from $y_1$. Substitution of equation (15) into these expressions can readily be shown to give

$$\frac{V_{\Delta y}}{V_E} = e^{-\frac{1}{2} e^{-\beta \Delta y}} = F'(\beta \Delta y) \tag{18}$$

and

$$\frac{\left(\frac{dV/dt}{g}\right)_{\Delta y}}{\left(\frac{dV/dt}{g}\right)_1} = e^{-\beta \Delta y} e^{(1 - e^{-\beta \Delta y})} = F''(\beta \Delta y) \tag{19}$$

Equations (18) and (19) are generalized expressions for velocity and deceleration for bodies of constant drag coefficient and, together with equations (15) and (17), can be used to determine the variation of these quantities with altitude for specific cases. The dependence of $F'(\beta \Delta y)$ and $F''(\beta \Delta y)$ on $\beta \Delta y$ is shown in figure 4.
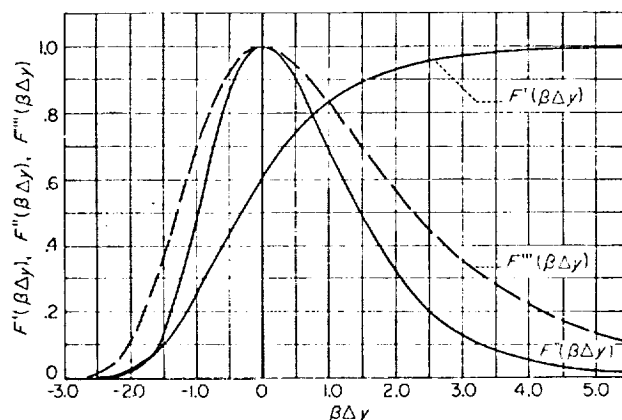


FIGURE 4.—Variations of $F'(\beta \Delta y)$, $F''(\beta \Delta y)$, and $F'''(\beta \Delta y)$ with $\beta \Delta y$.

The maximum deceleration and the velocity for maximum deceleration as given by equations (17) and (16) apply only if the altitude $y_1$, given by equation (15), is positive. Otherwise the maximum deceleration in flight occurs at sea level with the velocity (see eq. (13))

$$V = V_o = V_E e^{-\frac{C_D \rho_o A}{2\beta m \sin \theta_E}} \tag{20}$$

and has the value

$$-\left(\frac{dV}{dt}\,\frac{1}{g}\right)_{max}=-\left(\frac{dV}{dt}\,\frac{1}{g}\right)_0=\frac{C_D\rho_o A V_E^2}{2mg}\,e^{-\frac{C_D\rho_o A}{\beta m \sin \theta_E}} \qquad (21)$$

## HEATING OF THE BODY

It was noted previously that for practicable rocket missiles, it is vital that the weight of the missile be kept to a minimum. The total heat transferred to a missile from the air must be absorbed by some "coolant" material. Since this material has a maximum allowable temperature, it follows that it can accept only a given amount of heat per unit weight. Hence, the total heat input to the missile must be kept at a minimum for minimum missile weight.

Often the coolant material is simply the shell of the missile and as such must provide the structural strength and rigidity for the missile as well. The strength of the structure is dictated, in part, by the stresses induced by temperature gradients within the shell. Since these temperature gradients are proportional to the time rate of heat input, the maximum time rate of heat input is important in missile design. The heating, of course, varies along the surface but, since the shell transmits heat along as well as through itself, the strength of the structure as a whole may be determined by the maximum value of the average heat-transfer rate over the surface. This is simply the maximum value of the time rate of heat input per unit area. On the other hand, the structural strength at local points on the surface may be determined primarily by the local rate of heat input. Hence, the maximum time rate of heat input per unit area at the surface element where the heat transfer is greatest may also be of importance in design.

If liquid cooling is employed, the maximum surface heat-transfer rates retain their significance but, now, in the sense that they dictate such requirements as maximum coolant pumping rate, or perhaps shell porosity as well in the case of transpiration cooling. Whichever the case, in the analysis to follow, these elements of the heating problem will be treated:

1. The total heat input.
2. The maximum time rate of average heat input per unit area.
3. The maximum time rate of local heat input per unit area.

Since it is the primary function of this report to study means available to the missile designer to minimize the heating problem, the analysis is simplified to facilitate comparison of the relative heating of one missile with respect to another —accurate determination of the absolute heating of individual missiles is not attempted. With this point in mind, the following assumptions, discussed in Appendix B, are made:

1. Convective heat transfer predominates (i. e., radiation effects are negligible).
2. Effects of gaseous imperfections may be neglected.
3. Shock-wave boundary-layer interaction may be neglected.
4. Reynolds' analogy is applicable.
5. The Prandtl number is unity.

Total heat input.—The time rate of convective heat transfer from the air to any element of surface of the body may be expressed by the well-known relation

$$\frac{dH}{dt}=h_l(T_r-T_w)_l \qquad (22)$$

where

$H$    heat transferred per unit area, ft-lb/ft$^2$

$h$    convective heat-transfer coefficient, $\dfrac{\text{ft-lb}}{\text{ft}^2\ \text{sec}^\circ\text{R}}$

$T_r$    recovery temperature, °R

$T_w$    temperature of the wall, °R

$t$    time, sec

and the subscript $l$ denotes local conditions at any element of the surface $dS$.

It is convenient in part of this analysis to determine the heating as a function of altitude. To this end, noting that

$$dt=\frac{-dy}{V\sin\theta_E}$$

we see that equation (22) may be written

$$\frac{dH}{dy}=-\frac{h_l(T_r-T_w)_l}{V\sin\theta_E} \qquad (23)$$

With the assumption that the Prandtl number is unity, the recovery temperature is

$$T_r=T_l\left(1+\frac{\gamma-1}{2}M_l^2\right)=T\left(1+\frac{\gamma-1}{2}M^2\right)$$

where

$M$    Mach number at the altitude $y$, dimensionless

$\gamma$    the ratio of specific heat at constant pressure to that at constant volume, $C_p/C_v$, dimensionless

$T$    static temperature at the altitude $y$, °R

so that

$$(T_r-T_w)_l=T-T_{w_l}+\frac{\gamma-1}{2}M^2T$$

It is seen that for large values of the Mach number, which is the case of principal interest, the third term is large compared to reasonably allowable values of $T-T_w$. It will therefore be assumed that $T-T_w$ is negligible [6] so that

$$(T_r-T_w)_l=\frac{\gamma-1}{2}M^2T \qquad (24)$$

Moreover, since

$$M^2T=\frac{V^2}{(\gamma-1)C_p}$$

equation (24) may be written

$$(T_r-T_w)_l=\frac{V^2}{2C_p} \qquad (25)$$

[6] It should be noted that without this assumption, the heat input determination would be greatly complicated since the changing wall temperature with altitude would have to be considered to obtain the heat input (see e. g., ref. 1). For high-speed missiles which maintain high speed during descent, the assumption is obviously permissible. Even for high-speed missiles which finally decelerate to low speeds, the assumption is generally still adequate since the total heat input is largely determined by the heat transfer during the high-speed portion of flight.

Now the local heat-transfer coefficient $h_l$ is, by Reynolds' analogy, for the assumed Prandtl number of unity

$$h_l = \frac{1}{2} C_{f_l} C_{p_l} \rho_l V_l \tag{26}$$

where $C_{f_l}$ is the local skin-friction coefficient based on conditions $\rho_l$, $V_l$, etc., just outside the boundary layer. Thus, since $(T_r - T_w)$ is essentially constant over the entire surface $S$, the rate of total heat transfer with altitude becomes from equations (23) through (26)

$$\frac{dQ}{dy} = \int_S \frac{dH}{dy}\, dS = -\frac{V}{4 C_p \sin \theta_E} \int_S C_{f_l} C_{p_l} \rho_l V_l\, dS$$

where $Q$ is the heat transferred to the whole surface $S$. This equation may be written

$$\frac{dQ}{dy} = -\frac{C_f' \rho V^2 S}{4 \sin \theta_E} \tag{27}$$

wherein $C_{p_l}$ is set equal to $C_p$ and

$$C_f' = \frac{1}{S} \int_S C_{f_l} \left(\frac{\rho_l}{\rho}\right)\left(\frac{V_l}{V}\right) dS \tag{28}$$

The parameter $C_f'$ is termed "the equivalent friction coefficient," and will be assumed constant,[7] independent of altitude, again on the premise that relative rather than absolute heating is of interest. With equations (2) and (13), then, equation (27) is written

$$\frac{dQ}{dy} = -\frac{C_f' S \rho_o V_E^2}{4 \sin \theta_E} e^{-\beta y} e^{-\frac{C_D \rho_o A}{\beta m \sin \theta_E} e^{-\beta y}} \tag{29}$$

Comparison of equation (29) with equation (14) shows that the altitude rate of heat transfer is directly proportional to the deceleration, so that

$$\frac{dQ/dy}{\left(\frac{dV/dt}{g}\right)} = \frac{mg}{2 \sin \theta_E} \left(\frac{C_f' S}{C_D A}\right) \tag{30}$$

and therefore the maximum altitude rate of heat transfer occurs at the altitude $y_1$ (see eq. (15)) and is given by

$$\left(\frac{dQ}{dy}\right)_{max} = \left(\frac{dQ}{dy}\right)_1 = -\frac{\beta m V_E^2}{4e}\left(\frac{C_f' S}{C_D A}\right) \tag{31}$$

It follows, of course, that the altitude rate of heat transfer varies with incremental change in altitude from $y_1$ in the same manner as deceleration, and thus (see eq. (19))

$$\frac{(dQ/dy)_{\Delta y}}{(dQ/dy)_1} = F''(\beta \Delta y) \tag{32}$$

[7] This assumption would appear poor at first glance since the Mach number and Reynolds number variations are so large. Analysis has indicated, however, that the effects of Mach number and Reynolds number variation are nearly compensating. The variation in $C_f'$ for typical conical missiles was found to be, at most, about 50 percent from the maximum $C_f'$ in the altitude range in which 80 percent of the heat is transferred.

The total heat input to the body at impact follows from equation (29) (integrating over the limits $0 \le y \le \infty$) and is

$$Q = \frac{1}{4}\left(\frac{C_f' S}{C_D A}\right) m V_E^2 \left(1 - e^{-\frac{C_D \rho_o A}{\beta m \sin \theta_E}}\right) \tag{33}$$

The impact velocity, $V_o$ (the velocity of body at $y=0$), is

$$V_o = V_E\, e^{-\frac{C_D \rho_o A}{2\beta m \sin \theta_E}}$$

so that equation (33) may be written in the alternative form

$$Q = \frac{m}{4}\left(\frac{C_f' S}{C_D A}\right)(V_E^2 - V_o^2) \tag{34}$$

**Maximum time rate of average heat input per unit area.—** To determine the time rate of average heat transfer per unit area, equations (25), (26), and (28) with equation (22) may be shown to give

$$\frac{dH_{av}}{dt} = \frac{1}{4} C_f' \rho V^3 \tag{35}$$

which, together with equations (2) and (13), becomes at altitude $y$

$$\frac{dH_{av}}{dt} = \frac{C_f' \rho_o V_E^3}{4} e^{-\beta y} e^{-\frac{3 C_D \rho_o A}{2\beta m \sin \theta_E} e^{-\beta y}} \tag{36}$$

The maximum time rate of average heat transfer per unit area is found from this expression to be

$$\left(\frac{dH_{av}}{dt}\right)_{max} = \left(\frac{dH_{av}}{dt}\right)_2 = \frac{\beta}{6e}\left(\frac{C_f'}{C_D A}\right) m V_E^3 \sin \theta_E \tag{37}$$

and it occurs at the altitude

$$y_2 = \frac{1}{\beta} \ln\left(\frac{3 C_D \rho_o A}{2\beta m \sin \theta_E}\right) \tag{38}$$

where the velocity is

$$V_2 = V_E\, e^{-1/3} \cong 0.72\, V_E \tag{39}$$

As with altitude rate of heat transfer, it can be shown that

$$\frac{(dH_{av}/dt)_{\Delta y}}{(dH_{av}/dt)_2} = F''(\beta \Delta y) \tag{40}$$

Equations (37), (38), and (39) apply if the altitude for maximum time rate of average heat transfer per unit area occurs above sea level. If $y_2$, by equation (38), is negative, then this rate occurs at sea level and is, from equation (36),

$$\left(\frac{dH_{av}}{dt}\right)_{max} = \left(\frac{dH_{av}}{dt}\right)_o = \frac{C_f' \rho_o V_E^3}{4} e^{-\frac{3 C_D \rho_o A}{2\beta m \sin \theta_E}} \tag{41}$$

**Maximum time rate of local heat input per unit area.—** The elemental surface which is subject to the greatest heat transfer per unit area is, except in unusual cases, the tip of the missile nose which first meets the air. It seems unlikely that a pointed nose will be of practical interest for high-speed missiles since not only is the local heat-transfer rate exceedingly large in this case, but the capacity for heat retention is small. Thus a truly pointed nose would burn away.

Body shapes of interest for high-speed missiles would more probably, then, be those with nose shapes having nearly hemispherical tips. The following analysis applies at such tips.

It is well known that for any truly blunt body, the bow shock wave is detached and there exists a stagnation point at the nose. Consider conditions at this point and assume that the local radius of curvature of the body is $\sigma$ (see sketch).
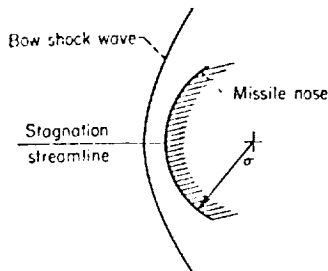


The bow shock wave is normal to the stagnation streamline and converts the supersonic flow ahead of the shock to a low subsonic speed flow at high static temperature downstream of the shock. Thus, it is suggested that conditions near the stagnation point may be investigated by treating the nose section as if it were a segment of a sphere in a subsonic flow field.

The heat-transfer rate per unit area at the stagnation point is given by the relation

$$\frac{dH_s}{dt} = -\frac{Nu_r k_r (T_w - T_r)}{\sigma}$$

where $k_r$ is the thermal conductivity of the gas at the recovery temperature (i. e., total temperature) $T_r$, and $Nu_r$ is the Nusselt number of the flow. If the flow is assumed to be laminar and incompressible,[8] $Nu_r$ is given, according to reference 5, by the relationship

$$Nu_r = 0.934 Re_\sigma^{\frac{1}{2}} Pr^{\frac{2}{5}}$$

We retain the assumption that the Prandtl number is unity, note that $Re_\sigma = \rho V \sigma / \mu_r$, and substitute equation (25) into equation (42) to obtain

$$\frac{dH_s}{dt} = 0.47 \sqrt{\frac{\rho V \mu_r}{\sigma}} V^2 \qquad (43)$$

Now it is well known that at the high temperatures of interest here, the coefficient of viscosity $\mu_r$ varies nearly as the square root of the absolute temperature and is given by the relation

$$\mu_r = 2.31 \times 10^{-8} T_r^{\frac{1}{2}}$$

If this expression is combined with equation (25) (neglecting $T_w$), equation (43) may then be written [9]

$$\frac{dH_s}{dt} = 6.8 \times 10^{-6} \sqrt{\frac{\rho}{\sigma}} V^3 \qquad (44)$$

---

[8] The assumption of constant density certainly may invalidate this analysis for any quantitative study of the relatively "cold-wall" flows of interest here. For the purpose of studying relative heat transfer it should, however, prove adequate.

[9] The constant in equation (44) is obtained with the assumption of incompressible flow in the stagnation region. The effects of compressibility and dissociation of the molecules of air in the region tend to increase the value of the constant by as much as a factor 2 in the speed range of interest in this report. For the comparative purpose of this report it is unnecessary to take these effects into account.

which, when combined with equations (2) and (13), becomes

$$\frac{dH_s}{dt} = 6.8 \times 10^{-6} \sqrt{\frac{\rho_o}{\sigma}} V_E^3 e^{-\frac{\beta y}{2}} e^{-\frac{3C_D \rho_o A}{2\beta m \sin \theta_E} e^{-\beta y}} \qquad (45)$$

The maximum value of $dH_s/dt$ can readily be shown to be

$$\left(\frac{dH_s}{dt}\right)_{max} = \left(\frac{dH_s}{dt}\right)_3 = 6.8 \times 10^{-6} \sqrt{\frac{\beta m \sin \theta_E}{3 e C_D \sigma A}} V_E^3 \qquad (46)$$

which occurs at the altitude

$$y_3 = \frac{1}{\beta} \ln \left(\frac{3 C_D \rho_o A}{\beta m \sin \theta_E}\right) \qquad (47)$$

corresponding to the velocity

$$V_3 = V_E e^{-\frac{1}{6}} \cong 0.85 V_E \qquad (48)$$

The manner in which the heat-transfer rate per unit area at the stagnation point varies with incremental change in altitude from $y_3$ can be shown to be

$$\frac{(dH_s/dt)_{\Delta y}}{(dH_s/dt)_3} = e^{-\frac{\beta \Delta y}{2}} e^{\frac{1}{6}(1 - e^{-\beta \Delta y})} = F'''(\beta \Delta y) \qquad (49)$$

The dependence of $F'''(\beta \Delta y)$ on $\beta \Delta y$ is shown in figure 4.

Equation (46) applies only if $y_3$ is above sea level. If $y_3$, from equation (47), is negative, then the maximum heat-transfer rate per unit area at the stagnation point occurs at sea level and is

$$\left(\frac{dH_s}{dt}\right)_{max} = \left(\frac{dH_s}{dt}\right)_0 = 6.8 \times 10^{-6} \sqrt{\frac{\rho_o}{\sigma}} V_E^3 e^{-\frac{3C_D \rho_o A}{2\beta m \sin \theta_E}} \qquad (50)$$

## DISCUSSION

### MOTION

The motion study shows some important features about the high-speed descent of missiles through the atmosphere. The major assumptions of this analysis were that the drag coefficient was constant and the density varied exponentially with altitude. It was found that the deceleration due to drag was generally large compared to the acceleration of gravity and, consequently, that the acceleration of gravity could be neglected in the differential equations of motion. The flight path was then seen to be a straight line, the missile maintaining the flight-path angle it had at entry to the atmosphere.

For most missiles, the maximum deceleration will occur at altitude. One of the most interesting features of the flight of such a missile is that the maximum deceleration is independent of physical characteristics (such as mass, size, and drag coefficient of the missile), being dependent only on the entry speed and flight-path angle (see eq. (17)). The missile speed at maximum deceleration (eq. (16)) bears a fixed relation to the entrance speed (61 percent of entrance speed), while the corresponding altitude (eq. (15)) depends on the physical characteristics and the flight-path angle but not on the entrance speed. It is also notable that for a given incremental change in altitude from the altitude for

maximum deceleration, the deceleration and speed bear fixed ratios to the maximum deceleration and the entry speed, respectively (see fig. 4 and eqs. (19) and (18)), hence, the deceleration and speed variation with altitude can readily be determined.

If the missile is very heavy, the calculated altitude for maximum deceleration (eq. (15)) may be fictitious (i. e., this altitude is negative) so the maximum deceleration in flight, which occurs just before impact at sea level, is less than that calculated by equation (17) and is dependent on the body characteristics as well as the entry speed and flight-path angle (see eq. (21)). However, the variation of speed and deceleration with altitude from the fictitious altitude given by equation (15) can still be obtained from figure 4.

### HEATING

**Total heat input.**—In the heating analysis, a number of simplifying assumptions were made which should limit its applicability to the determination of relative values of heating at hypersonic speeds. It is in this relative sense that the following discussion pertains.

In considering the total heat transferred by convection to a missile, it is evident from equation (33) that the course the designer should take to obtain the least heating is affected by the value of the factor

$$\frac{C_D \rho_o A}{\beta m \sin \theta_E} = B \qquad (51)$$

To illustrate, first consider the case of a "relatively heavy" missile for which this factor is small compared to unity (the term "relatively heavy" is used to denote that the denominator involving the mass is very large as compared to the numerator involving the drag per unit dynamic pressure, $C_D A$). Then

$$1 - e^{-\frac{C_D \rho_o A}{\beta m \sin \theta_E}}$$

is small compared to 1. If this function is expanded in series and only the leading term retained, equation (33) becomes

$$Q \approx \frac{C_f' S \rho_o V_E^2}{4 \beta \sin \theta_E} \qquad (52)$$

For the relatively heavy missile, then, the least heat will be transferred when $C_f' S$ is a minimum—that is to say, when the total shear force acting on the body is a minimum. This result is as would be expected, if one notes that requiring $B \ll 1$ is tantamount to requiring the missile to be so heavy that it is retarded only slightly by aerodynamic drag in its motion through the atmosphere. Hence, the heat input to the missile is simply proportional to the shear force.

Now let us consider the case when $B \gg 1$, or, in other words, when this missile is "relatively light." In this event,

$$1 - e^{-\frac{C_D \rho_o A}{\beta m \sin \theta_E}} \approx 1$$

and equation (31) can be approximated

$$Q \approx \frac{1}{4} m V_E^2 \left( \frac{C_f' S}{C_D A} \right)$$

For the relatively light missile, then, the least convective heating is obtained when $C_f' S / C_D A$ is a minimum. This is at first glance a rather surprising result, for it indicates that the heating is reduced by increasing the total drag, provided the equivalent frictional drag is not increased proportionately as fast. Physically, this anomaly is resolved if the problem is viewed in the following way: The missile entering the atmosphere has the kinetic energy $\frac{1}{2} m V_E^2$ but, if

$$e^{-\frac{C_D \rho_o A}{\beta m \sin \theta_E}} = \left( \frac{V_o}{V_E} \right)^2$$

is small, then nearly all its entrance kinetic energy is lost, due to the action of aerodynamic forces, and must appear as heating of both the atmosphere and the missile. The fraction of the total heat which is given to the missile is,[10] from equation (33),

$$\frac{1}{2} \left( \frac{C_f' S}{C_D A} \right)$$

Thus, by keeping this ratio a minimum, as much as possible of the energy is given to the atmosphere and the missile heating is therefore least.

In order to illustrate these considerations in greater detail, calculations have been made using the previously developed equations to determine the heat transferred by convection to a series of conical missiles. Two classes of missiles have been considered. Missiles in the first class were required to have a base area of 10 square feet. Missiles in the second class were required to have a volume of 16 cubic feet. Gross weights of 0, 1,000, 5,000, 10,000, and ∞ pounds have been assumed, and the entrance angle, $\theta_E$, has been taken as 30° of arc in all cases. Missile heating, up to the time of impact, has been calculated as a function of cone angle for entrance speeds of 10,000, 20,000, and 30,000 feet per second. In these calculations the pressure drag coefficient was taken as constant for a particular cone at the value corresponding to the entrance Mach number (a value of $T_E = 500°$ R was assumed throughout). These coefficients were determined from reference 6 for cone angles of 10° and greater. For cone angles less than 10°, reference 7 was employed to determine these coefficients (base drag was neglected in all cases). The total drag coefficient was taken as the sum of the pressure drag coefficient plus the skin-friction coefficient, the latter coefficient being taken at its value for maximum total heat-input rate with altitude. The boundary layer was assumed to be wholly turbulent since the Reynolds number, based on length of run along the surface of a cone and local conditions just outside the boundary layer, was always greater than about $6 \times 10^6$ and, in fact, was of the order of billions for the more slender cones. Turbulent-boundary-layer data were obtained from references 8 and 9, and Sutherland's law for the variation of viscosity with temperature was used in obtaining "equivalent flat-plate" heat-transfer coefficients.

---

[10] Note that even that if all drag is frictional drag, only half the heat is transferred to the body. The other half is contained in the boundary layer and is left in the air in the body wake.

(a) $V_E = 10,000$ ft/sec
(b) $V_E = 20,000$ ft/sec
(c) $V_E = 30,000$ ft/sec

FIGURE 5.—Convective heat transferred at impact to conical missiles of same area entering the earth's atmosphere at an angle of 30° to the horizontal and velocities of 10,000, 20,000, and 30,000 ft/sec (base area = 10 sq ft).



(a) $V_E = 10,000$ ft/sec
(b) $V_E = 20,000$ ft/sec
(c) $V_E = 30,000$ ft/sec
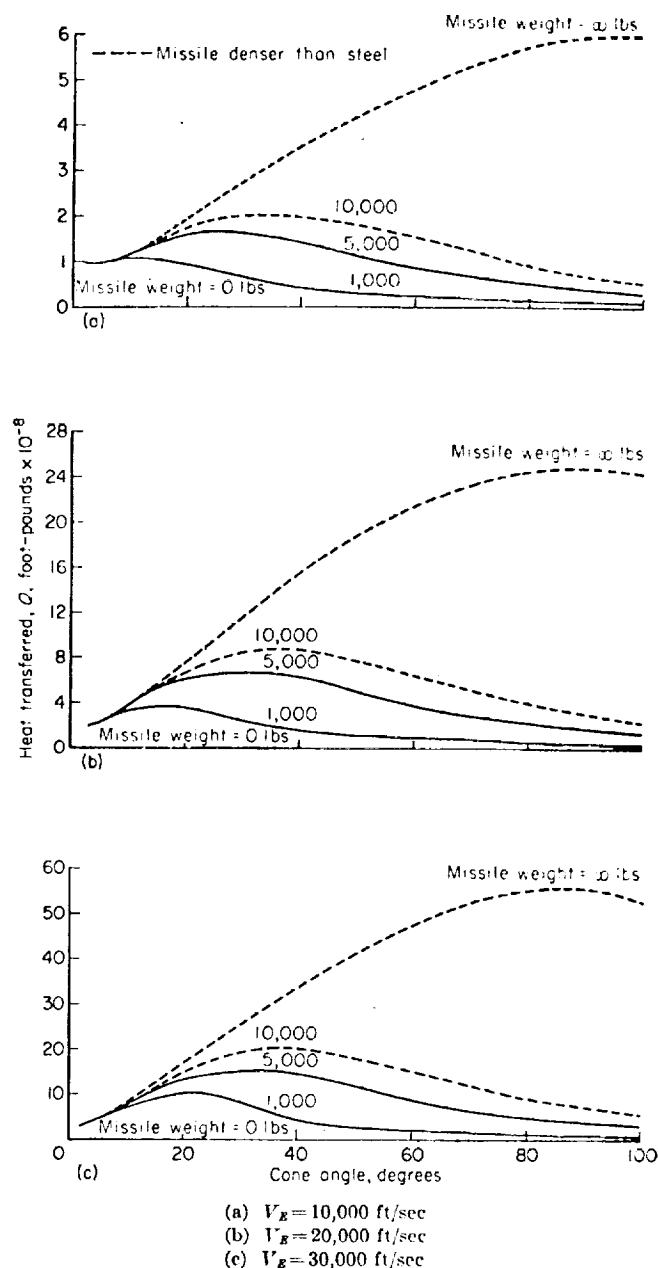
FIGURE 6.—Convective heat transferred at impact to conical missiles of same volume entering the earth's atmosphere at an angle of 30° to the horizontal and velocities of 10,000, 20,000, and 30,000 ft/sec (volume = 16.34 cu ft).

Missile heating calculated in this manner for the fixed-base-area and fixed-volume cones is presented in figures 5 and 6, respectively. Curves for missiles having densities greater than steel are considered improbable and are shown as dashed lines. It is clear that for both classes of bodies, when the missile is relatively heavy, the optimum solution is obtained by making $C_f S$ as small as possible (small cone angle case) and this optimum is accentuated with increase in speed. On the other hand, when the missile is relatively light, reduced heating is obtained by making $C_f S/C_D A$ as small as possible (the large cone angle case). It is noted

also that, in general, the advantage of reduced heating of the relatively light, blunt cones is more pronounced in the fixed-base-area case than in the fixed-volume case.

**Maximum time rate of average heat input per unit area.—** It was previously noted that the maximum time rate of average heat input per unit area may be of serious importance in determining the structural integrity of missiles entering the atmosphere at high speeds.[11] In order to illustrate this fact, consider the case of a missile having a shell made of solid material and assume that the rate of heat transfer per unit area does not vary rapidly from one surface element to the next. Then the rate of transfer of heat along the shell will be small compared with the rate of transfer through the shell. The shell stress due to heat transfer is that resulting from the tendency toward differential expansion through the shell and it is proportional to $dT_\eta/d\eta$ where $T_\eta$ is the temperature at any point $\eta$ within the shell and $\eta$ is measured perpendicular from the shell surface. We define $k_\eta$ as the thermal conductivity of the shell material; then the rate at which heat transfers through the shell per unit area is $k_\eta(dT_\eta/d\eta)$ and this must, at $\eta=0$, equal the rate of heat input per unit surface area. For the missile considered as a whole, the maximum value of the average thermal stress in the shell is a measure of the over-all structural integrity and the maximum value of this stress will occur at the surface when

$$\frac{dH_{ar}}{dt}=\frac{1}{S}\left(\frac{dQ}{dt}\right)$$

is a maximum.

The course the designer should take to minimize the thermal stress for the missile as a whole is dependent, as for the case of total heat input, upon whether the missile is relatively heavy or light. For the relatively heavy missile the value of $B$, given by equation (51), is small compared to unity. The maximum value of the average thermal stress in this case is proportional to (see eq. (41))

$$\left(\frac{dH_{ar}}{dt}\right)_o=\frac{C_f'\rho_o V_E^3}{4} \tag{54}$$

and, hence, the least average thermal stress is obtained by making $C_f'$ a minimum. On the other hand, for the relatively light missile the maximum value of the average thermal stress is proportional to (see eq. (37))

$$\left(\frac{dH_{ar}}{dt}\right)_2=\left(\frac{C_f'}{C_D A}\right)\frac{\beta m V_E^3 \sin\theta_E}{6e} \tag{55}$$

and, hence, the least average thermal stress occurs when $C_f'/C_D A$ is a minimum.

In order to illustrate these considerations in greater detail, the maximum values of the time rate of average heat input per unit area have been calculated for the constant-base-area and the constant-volume cones previously discussed in the section on total heat input. These values were determined in much the same manner as those of total heat input, with the exception that $C_f'$ was evaluated at $y_2$ (rather than $y_1$), given by equation (38) when it applies, and otherwise at $y_0=0$. The results are shown in figures 7 and 8. It is seen that the

(a) $V_E=10,000$ ft/sec
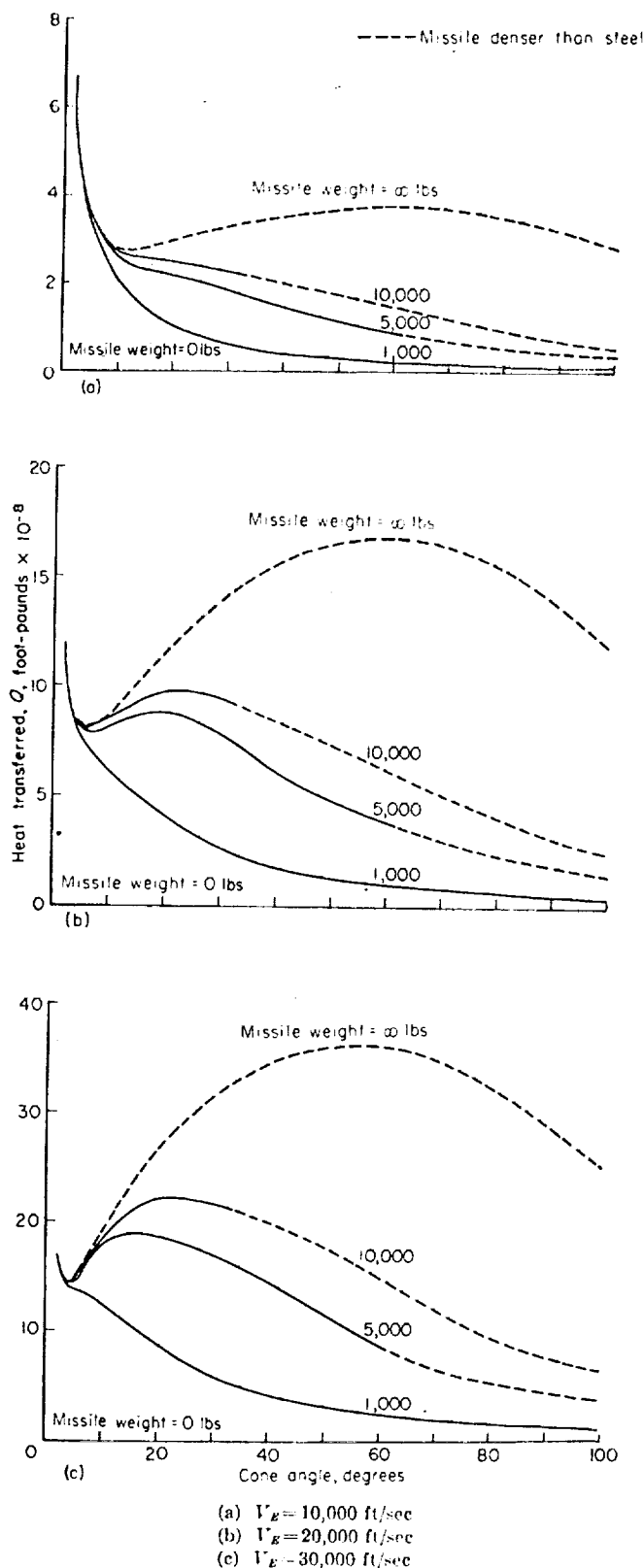(b) $V_E=20,000$ ft/sec
(c) $V_E=30,000$ ft/sec

FIGURE 7.—Maximum average rate of convective heat transfer to conical missiles of the same base area entering the earth's atmosphere at an angle of 30° to the horizontal and velocities of 10,000, 20,000, and 30,000 ft/sec (base area=10 sq ft).

maximum values of average thermal stress are reduced for both the slender cones and blunt cones as compared to the relatively large values of this stress experienced by cones of intermediate slenderness.

**Maximum time rate of local heat input per unit area.—** Perhaps even more important than the maximum value of the average shell stress is the maximum stress that occurs in the shell at the surface element of the missile nose,[12] where the local heat-transfer rate is probably the greatest, for, in general, this latter stress is many times larger. In fact, this rate of local heat input can be so large as to promote

(a) $V_E = 10,000$ ft/sec
(b) $V_E = 20,000$ ft/sec
(c) $V_E = 30,000$ ft/sec
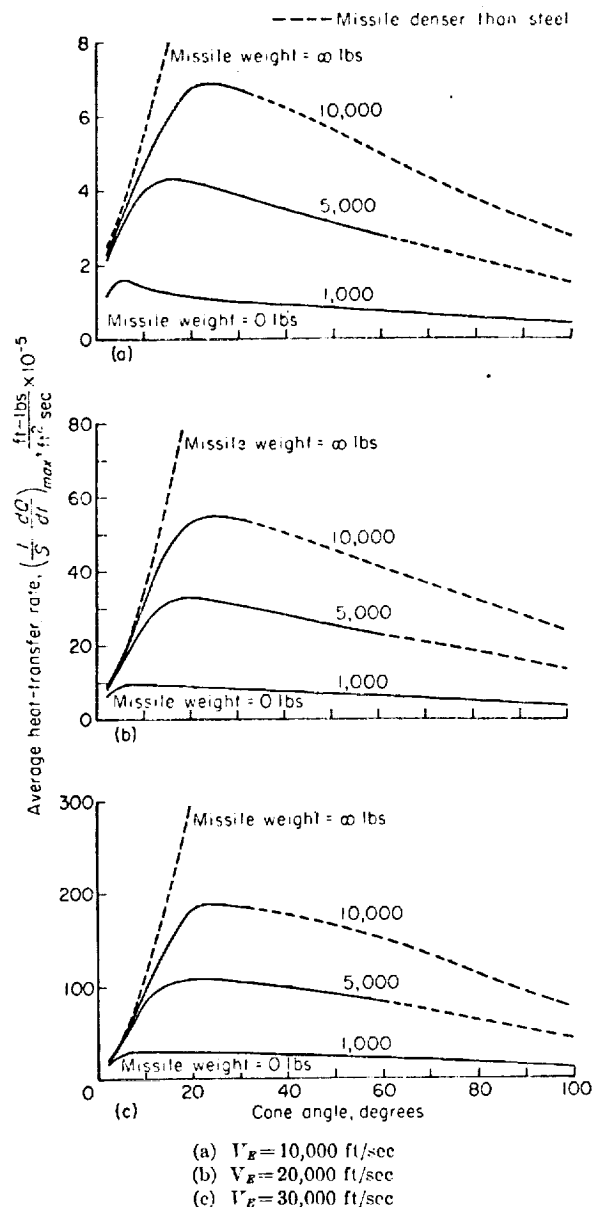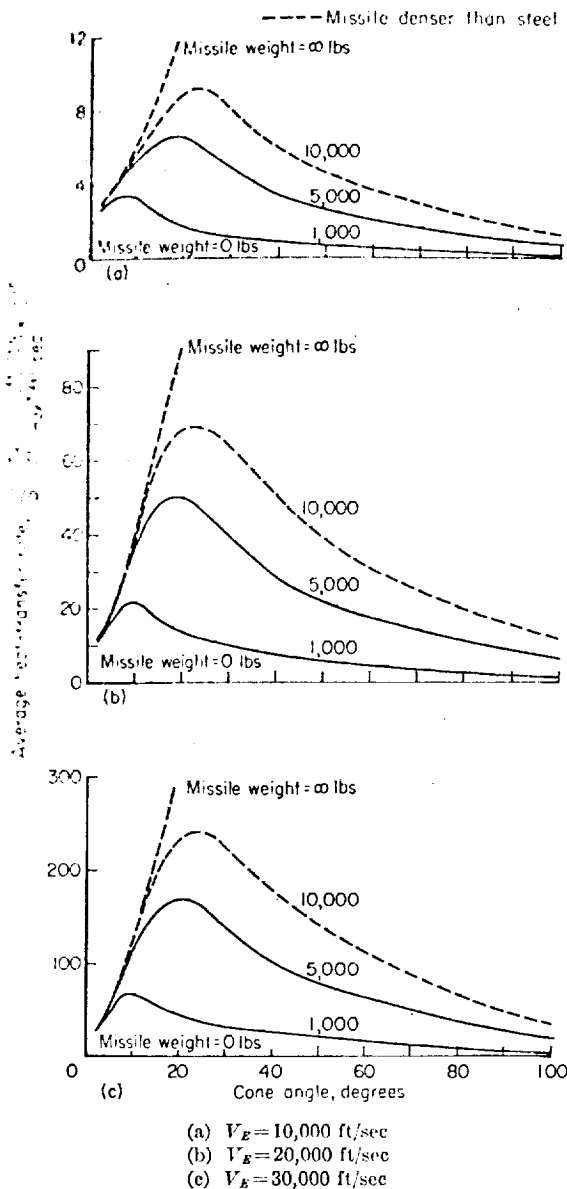
FIGURE 8.—Maximum average rate of convective heat transfer to conical missiles of the same volume entering the earth's atmosphere at an angle of 30° to the horizontal and velocities of 10,000, 20,000, and 30,000 ft/sec (volume = 16.34 cu ft).

temperature gradients through the shell that are intolerable even with the most highly conductive materials (copper, silver, etc.).[13] Thus some additional means of cooling, such as transpiration cooling, may, in any case, be required in this region.

It was stated previously that pointed-nose bodies are undesirable due, in part, to the fact that the local heat-transfer rate per unit area at the tip is excessive. The validity of this statement is demonstrated by the results of the analysis. It is clear (see eq. (44)) that since the local transfer rate varies inversely with the square root of the tip radius, not only should pointed bodies be avoided, but the rounded nose

[13] See reference 1 for further discussion.

should have as large a radius as possible. The question then arises; if the nose radius is arbitrarily fixed, what course is available to the missile designer to minimize the problem of local heating at the stagnation point? From both equations (46) and (50), it is seen that for an arbitrary nose radius, if the mass, entry speed, and flight-path angle are fixed, then the only way to reduce the stagnation rate of heat input per unit area is to increase the product $C_D A$. In fact, a relative stagnation-point heat-transfer rate per unit area, $\psi$ may be expressed in terms of $B$ (see eq. (51)), if it is defined as the ratio of the maximum stagnation-point heat-transfer rate per unit area for a given missile to the maximum rate the same missile would experience if it were infinitely heavy. For the infinitely heavy missile, the maximum rate occurs at sea level and is (see eq. (50))

$$6.8 \times 10^{-6} \sqrt{\frac{\rho_0}{\sigma}} V_E^3$$

so that from equation (50)

$$\psi = e^{-\frac{3C_D \rho_0 A}{2\beta m \sin \theta_E}} = e^{-\frac{1}{3}B} \tag{56}$$

if the given missile also attains its maximum rate at sea level (i. e., $y_3 = 0$; eq. (47)); whereas

$$\psi = \sqrt{\frac{\beta m \sin \theta_E}{3e C_D \rho_0 A}} = \frac{1}{\sqrt{3eB}} \tag{57}$$

if the given missile attains its maximum rate above sea level (eq. (46), $y_3$ positive). The variation of $\psi$ with $1/B$ is shown in figure 9. Clearly, the high pressure drag shape has the advantage over the slender shape in this respect.

In order to illustrate these considerations in greater detail, again consider the constant-base-area and constant-volume cones discussed earlier. Assume the pointed tips of all the
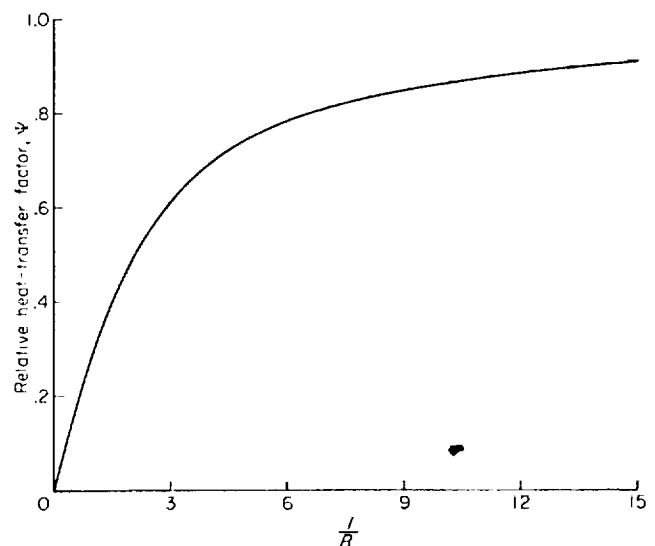


FIGURE 9.—Variation of relative heat-transfer factor $\psi$ with $\frac{1}{B}$.

cones are replaced by spherical tips of the same radius $\sigma$. The relative effect of varying the cone angle on the stagnation-point heating can then be assessed by determining the variation of the product

$$\sqrt{\sigma}\left(\frac{dH_s}{dt}\right)_{max}$$

This product has been calculated for the various cones, assuming $C_D$ to be unaffected by the addition of the hemispherical tip (the tip radius may be arbitrarily small), and the results are shown in figures 10 and 11. It is seen again that the missiles having large cone angle (high drag coefficient) are considerably superior.



(a) $V_E = 10,000$ ft/sec
(b) $V_E = 20,000$ ft/sec
(c) $V_E = 30,000$ ft/sec
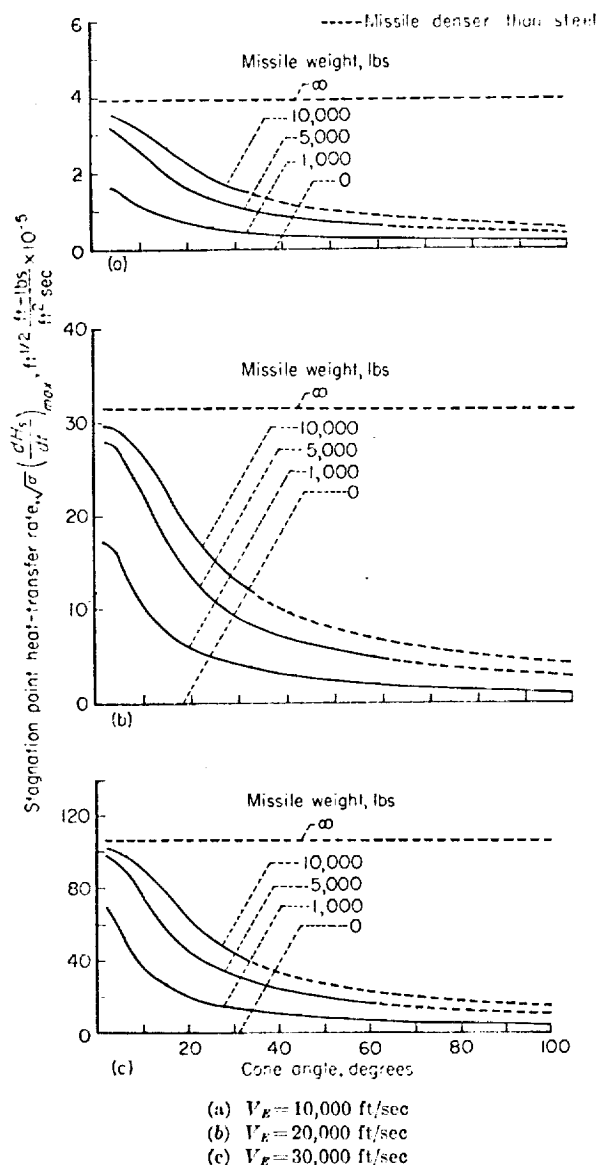
FIGURE 10.—Maximum rate of convective heat transfer to the stagnation point of spherically tipped cones of the same base area entering the earth's atmosphere at an angle of 30° to the horizontal and velocities of 10,000, 20,000, and 30,000 ft/sec (base area=10 sq ft).



(a) $V_E = 10,000$ ft/sec
(b) $V_E = 20,000$ ft/sec
(c) $V_E = 30,000$ ft/sec
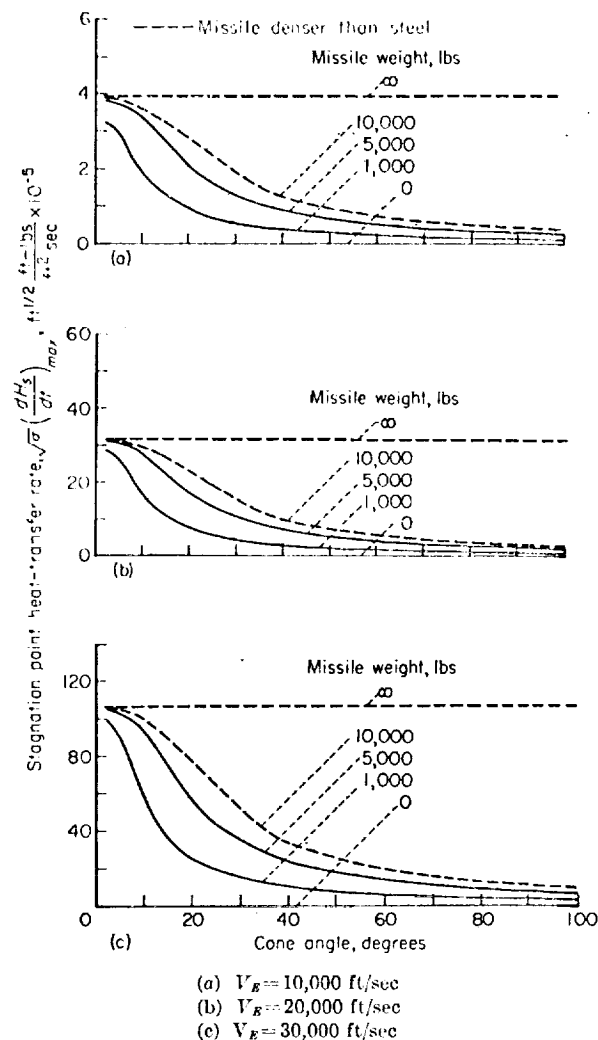
FIGURE 11.—Maximum rate of convective heat transfer to the stagnation point of spherically tipped cones of the same volume entering the earth's atmosphere at an angle of 30° to the horizontal and velocities of 10,000, 20,000, and 30,000 ft/sec (volume=16.34 cu ft).

## DESIGN CONSIDERATIONS AND CONCLUDING REMARKS

In the foregoing analysis and discussion, two aspects of the heating problem for missiles entering the atmosphere were treated. The first concerned the total heat absorbed by the missile and was related to the coolant required to prevent its disintegration. It was found that if a missile were relatively light, the least required weight of coolant (and hence of missile) is obtained with a shape having a high pressure drag coefficient, that is to say, a blunt shape. On the other hand, it was found that if the missile were relatively heavy the least required weight of coolant, and hence of missile, is obtained with a shape having a low skin-friction drag coefficient, that is to say, a long slender shape.

The second aspect of the heating problem treated was concerned with the rate of heat input, particularly with regard to thermal shell stresses resulting therefrom. It was seen that the maximum average heat-input rate and, hence, maximum average thermal stress could be decreased by

using either a blunt or a slender missile, while missiles of intermediate slenderness were definitely to be avoided in this connection. The region of highest local heat-transfer rate and, hence, probably greatest thermal stress was reasoned to be located at the forward tip of the missile in most cases. This was assumed to be the case and it was found that the magnitude of this stress was reduced by employing a shape having the largest permissible tip radius and over-all drag coefficient; that is to say, the blunt, high drag shape always appears to have the advantage in this respect.

These results provide us with rather crude, but useful, bases for determining shapes of missiles entering the atmosphere which have minimized heat-transfer problems. If the over-all design considerations of payload, booster, et al, dictate that the re-entry missile be relatively heavy in the sense of this report, then it may be most desirable to make this missile long and slender, especially if the entry speed is very high (say 20,000 ft/sec or greater). Perhaps the slender conical shape is appropriate for such a missile. It seems clear, too, that the tip of this missile should be given the largest practicable nose radius in order to minimize the maximum local heat-transfer rate and hence maximum local shell stress problem. Even then it may be necessary to employ additional means to minimize the heat-transfer rate and, hence, thermal stress encountered in this region (e. g., by transpiration cooling).

Let us now consider the case where the over-all design conditions dictate that the re-entry missile be relatively light in the sense of this report. This case will be the more usual one and, therefore, will be treated at greater length.

A shape which should warrant attention for such missile application is the sphere, for it has the following advantages:

1. It is a high drag shape and the frictional drag is only a few percent of the total drag.
2. It has the maximum volume for a given surface area.
3. The continuously curved surface is inherently stiff and strong.
4. The large stagnation-point radius significantly assists in reducing the maximum thermal stress in the shell.
5. Aerodynamic forces are not sensitive to attitude and, hence, a sphere may need no stabilizing surfaces.
6. Because of this insensitivity to attitude, a sphere may purposely be rotated slowly, and perhaps even randomly [14] during flight, in order to subject all surface elements to about the same amount of heating and thereby approach uniform shell heating.

[14] Note that if rotation is permitted, slow, random motion may be required in order to prevent Magnus forces from causing deviation of the flight path from the target. It should also be noted that at subsonic and low supersonic speeds gun-fired spheres, presumably not rotating, have shown rather large lateral motions in flight (see ref. 10). It is not known whether such behavior occurs at high supersonic speeds.

On the other hand, the sphere, in common with other very high drag shapes may be unacceptable if:
1. The low terminal speed cannot be permitted (e. g., because of excessive wind drift).
2. The magnitude of the maximum deceleration is greater than can be allowed.

The first of these disadvantages of the sphere might be minimized by protruding a flow-separation-inducing spike from the front of the sphere to reduce the drag coefficient to roughly half (see ref. 11). Stabilization would now be required but only to the extent required to counterbalance the moment produced by the spike. Special provision would have to be made for cooling the spike.

Both of the disadvantages of very high drag shapes may however be alleviated by using variable geometry arrangements. For example, an arrangement which suggests itself is a round-nosed shape with conical afterbody of low apex angle employing an extensible skirt at the base. With the skirt flared, the advantages of high drag are obtained during the entry phase of flight where the aerodynamic heating is intense. Later, the skirt flare may be decreased to vary the drag so as to produce the desired deceleration and speed history. If the deceleration is specified in the equation of motion (see motion analysis), the required variation of drag coefficient with altitude can be calculated.

The examples considered, of course, are included only to demonstrate some of the means the designer has at hand to control and diminish the aerodynamic heating problem. For simplicity, this problem has been treated, for the most part, in a relative rather than absolute fashion. In any final design, there is, clearly, no substitute for step-by-step or other more accurate calculation of both the motion and aerodynamic heating of a missile.

Even from a qualitative point of view, a further word of caution must be given concerning the analysis of this paper. In particular, throughout, we have neglected effects of gaseous imperfections (such as dissociation) and shock-wave boundary-layer interaction on convective heat transfer to a missile, and of radiative heat transfer to or from the missile. One would not anticipate that these phenomena would significantly alter the conclusions reached on the relative merits of slender and blunt shapes from the standpoint of heat transfer at entrance speeds at least up to about 10,000 feet per second. It cannot tacitly be assumed, however, that this will be the case at higher entrance speeds (see Appendix B). Accurate conclusions regarding the dependence of heat transfer on shape for missiles entering the atmosphere at extremely high supersonic speeds must await the availability of more reliable data on the static and dynamic properties of air at the high temperatures and pressures that will be encountered.

AMES AERONAUTICAL LABORATORY
NATIONAL ADVISORY COMMITTEE FOR AERONAUTICS
MOFFETT FIELD, CALIF., *Apr. 28, 1953*

# APPENDIX B

## SIMPLIFYING ASSUMPTIONS IN THE CALCULATION OF AERODYNAMIC HEATING

As noted in the main body of the report, the heating analysis is simplified by making the following assumptions:

1. Convective heat transfer is of foremost importance; that is, radiative effects may be neglected.
2. Effects of gaseous imperfections, in particular dissociation, may be neglected.
3. Effects of shock-wave boundary-layer interaction may be neglected.
4. Reynolds' analogy is applicable.
5. Prandtl number is unity.

The restrictions imposed by these assumptions will now be considered in some detail.

In assumption 1, two simplifications are involved; namely, (1) radiation from the surface of the body is neglected, and (2) radiation to the body from the high-temperature disturbed air between the shock wave and the surface is neglected. The first simplification may be justified on the premise that the maximum allowable surface temperature will be about the same for one body as compared with another, irrespective of shape, and, consequently, radiation away from the surface will be approximately the same. Hence, neglecting this form of heat transfer should not appreciably change the relative heating which is of principal interest in this paper.

The second simplification of ignoring radiative heat transfer from the disturbed air to the body is not so easily treated. At ordinary flight speeds this form of heat transfer is negligible since it is well established that at temperatures not too different from ambient temperature, air is both a poor radiator and a poor absorber. At the flight speeds of interest, temperatures in the tens of thousands of degrees Fahrenheit may be easily obtained in the disturbed air flow, especially about the heavier blunt bodies. At these temperatures it does not follow, a priori, that air is a poor radiator. Data on the properties of air at these temperatures are indeed meager. Hence, it is clear that calculations of radiative heat transfer from air under these conditions must, at best, be qualitative. Nevertheless, several such calculations have been made, assuming for lack of better information that air behaves as a grey body radiator and that Wein's law may be used to relate the wave length at which the maximum amount of radiation is emitted to the temperature of the air (this assumption, in effect, enables low-temperature data on the emissivity of air to be used in calculating radiation at high temperatures). In these calculations effects of dissociation in reducing the temperature of the disturbed air have also been neglected and hence from this standpoint, at least, conservative (i. e., too high) estimates of radiative heat transfer should evolve. The results of these calculations indicate the following: (1)

Radiative heat transfer from the disturbed air to the body is of negligible importance compared to convective heat transfer at entrance speeds in the neighborhood of, or less than, 10,000 feet per second; (2) Radiative heat transfer, in the case of relatively massive blunt bodies, may have to be considered in heat-transfer calculations at entrance speeds in the neighborhood of 20,000 feet per second; (3) Radiative heat transfer, in the case of relatively massive blunt bodies, may be of comparable importance to convective heat transfer at entrance speeds in the neighborhood of 30,000 feet per second. From these results, we conclude, then, that the neglect of radiative heat transfer from the disturbed air to the body is probably permissible for all except, perhaps, very blunt and heavy shapes at entrance speeds up to 20,000 feet per second. However, this simplification may not be permissible, especially in the case of heavy blunt bodies entering the atmosphere at speeds in the neighborhood of, or greater than, 30,000 feet per second.

In assumption 2, the neglect of effects of gaseous imperfections, particularly dissociation, on convective heat transfer would appear to be permissible at entrance speeds up to and in the neighborhood of 10,000 feet per second, since at such speeds the temperatures of the disturbed air are not high enough for these imperfections to become significantly manifest. On the other hand, as the entrance speeds approach 20,000 feet per second, temperatures of the disturbed air may easily exceed 10,000° Rankine, in which case appreciable dissociation may be anticipated, inside the boundary layer for all bodies, and inside and outside the boundary layer in the case of blunt bodies. The magnitude of these effects is at present in some doubt (see, e. g., the results of refs. 12 and 13.) Hence, for the present, the neglect of effects of gaseous imperfections on convective heat transfer is not demonstrably permissible at entrance speeds in the neighborhood of 20,000 feet per second or greater.

In assumption 3, it has been shown by Lees and Probstein (ref. 14), and more recently by Li and Nagamatsu (ref. 15), that shock-wave boundary-layer interaction may significantly increase laminar skin-friction coefficients on a flat plate at zero incidence and Mach numbers in excess of about 10. Lees and Probstein found somewhat the opposite effect on heat-transfer rate in the case of weak interaction. It is not now known how this phenomenon depends upon body shape or type of boundary layer. However, it is reasonable to anticipate that there will be some effect, and certainly if the skin-friction coefficient is increased in order of magnitude at Mach numbers approaching 20, as indicated by the results of Li and Nagamatsu for strong interaction, then the phenomenon cannot be presumed negligible. Hence, we conclude that from this standpoint, also, the convective

# APPENDIX A

## SYMBOLS

$A$    reference area for drag evaluation, ft²

$B$    body factor, dimensionless (See eq. (51).)

$C_D$    drag coefficient, dimensionless

$C_f$    skin-friction coefficient based on conditions just outside the boundary layer, dimensionless

$C_f'$    equivalent skin-friction coefficient, dimensionless (See eq. (28).)

$C_p$    specific heat at constant pressure, $\frac{\text{ft-lb}}{\text{slug }^\circ\text{R}}$

$C_v$    specific heat at constant volume, $\frac{\text{ft-lb}}{\text{slug }^\circ\text{R}}$

$F', F'', F'''$    functions of $\beta\Delta y$, dimensionless (See eqs. (18), (19), and (49).)

$g$    acceleration due to force of gravity $\left(\text{taken as } 32.2 \ \frac{\text{ft}}{\text{sec}^2}\right)$

$h$    convective heat-transfer coefficient, $\frac{\text{ft-lb}}{\text{ft}^2 \text{ sec }^\circ\text{R}}$

$H$    heat transferred per unit area, $\frac{\text{ft-lb}}{\text{ft}^2}$

$k$    thermal conductivity, $\frac{\text{ft-lb}}{\text{sec ft}^2 \ (^\circ\text{R/ft})}$

$m$    mass, slugs

$M$    Mach number, dimensionless

$Nu$    Nusselt number, dimensionless

$Pr$    Prandtl number, dimensionless

$Q$    total heat transferred, ft-lb

$Re$    Reynolds number, dimensionless

$S$    surface area, ft²

$T$    temperature (ambient temperature of air at altitude $y$ unless otherwise specified), °R

$t$    time, sec

$V$    velocity, $\frac{\text{ft}}{\text{sec}}$

$x,y$    horizontal and vertical distance from impact point, ft

$Z$    variable of integration, $\frac{\text{ft}^2}{\text{sec}^2}$

$\beta$    constant in density—altitude relation, ft⁻¹ (See eq. (2).)

$\gamma$    ratio of specific heat at constant pressure to specific heat at constant volume, $C_p/C_v$ dimensionless

$\Delta$    increment

$\eta$    distance within the shell measured normal to shell surface, ft

$\theta$    angle of flight path with respect to horizontal, deg

$\mu$    coefficient of absolute viscosity, $\frac{\text{slugs}}{\text{ft sec}}$

$\rho$    air density, $\frac{\text{slug}}{\text{ft}^3}$

$\sigma$    radius, ft

$\psi$    relative heat-transfer factor, dimensionless (See eqs. (56) and (57).)

### SUBSCRIPTS

$0$    conditions at sea level ($y=0$)

$1$    conditions at altitude $y_1$ (eq. (15))

$2$    conditions at altitude $y_2$ (eq. (38))

$3$    conditions at altitude $y_3$ (eq. (47))

$E$    conditions at entrance to earth's atmosphere

$l$    local conditions

$r$    recovery conditions

$s$    stagnation conditions

$w$    wall conditions

$\eta$    conditions within the shell of the missile

heat-transfer calculations of this report may be in error at entrance speeds of the order of 20,000 feet per second or greater.

The assumption that Reynolds' analogy may be used to relate skin-friction and heat-transfer coefficient does not, especially in the light of recent work by Rubesin (ref. 16), seem out of line with the purposes of this paper, at least at entrance speeds up to and in the neighborhood of 10,000 feet per second. However, it does not follow, a priori, that this assumption remains valid at substantially higher entrance speeds, especially in view of the imperfect gas and shock-wave boundary-layer-interaction effects already discussed.

The assumption of Prandtl number equal to unity would also appear permissible for the analysis of relative heating of missiles at the lower entrance speeds considered here. However, in view of the questionable effect (see again refs. 12 and 13) of dissociation on Prandtl number, it is not clear that this assumption is strictly valid at the intermediate and higher entrance speeds treated in this report.

From these considerations it is concluded that the simplifying assumptions made in the main heat-transfer analysis of this paper will not significantly influence the results at entrance speeds in the neighborhood of or less than 10,000 feet per second. However, at entrance speeds in the neighborhood of and greater than 20,000 feet per second, these results must be viewed with skepticism. More accurate calculations of heat transfer at these speeds must, among other things, await more accurate determinations of both the static and dynamic properties of air under these circumstances.

## REFERENCES

1. Wagner, Carl: Skin Temperature of Missiles Entering The Atmosphere at Hypersonic Speed. Tech. Rep. No. 60, Ord Res. & Dev. Division, Dept. of Army, Oct. 1949.

2. Diehl, Walter S.: Standard Atmosphere—Tables and Data. NACA Rep. No. 218, 1925.

3. Warfield, Calvin N.: Tentative Tables for the Properties of the Upper Atmosphere. NACA TN 1200, 1947.

4. Grimminger, G.: Probability that a Meteorite Will Hit or Penetrate a Body Situated in the Vicinity of the Earth. Jour. Appl. Phys., vol. 19, no. 10, Oct. 1948, pp. 947–956.

5. Sibulkin, M.: Heat Transfer Near the Forward Stagnation Point of a Body of Revolution. Jour. Aero. Sci., vol. 19, no. 8, Aug. 1952, pp. 570–571.

6. Mass. Inst. of Tech. Dept. of Elec. Engr., Center of Analysis: Tables of Supersonic Flow Around Cones, by the Staff of the Computing Section, Center of Analysis, under direction of Zdenek Kopal: Tech. Rep. No. 1, Cambridge, 1947.

7. Eggers, A. J. Jr., and Savin, Raymond C.: Approximate Methods for Calculating the Flow About Nonlifting Bodies of Revolution at High Supersonic Airspeeds. NACA TN 2579, 1951.

8. Van Driest, E. R.: Turbulent Boundary Layer in Compressible Fluids. Jour. Aero. Sci., vol. 18, no. 3, Mar. 1951, pp. 145–146.

9. Van Driest, E. R.: Turbulent Boundary Layer on a Cone in a Supersonic Flow at Zero Angle of Attack. Jour. Aero. Sci., vol. 19, no. 1, Jan. 1952, pp. 55–57.

10. Richards, Elizabeth: Comparative Dispersion and Drag of Spheres and Right Cylinders. Aberdeen Proving Ground, Md., Ballistic Research Laboratories, Rep. 717, 1950.

11. Moeckel, W. E.: Flow Separation Ahead of a Blunt Axially Symmetric Body at Mach Numbers 1.76 to 2.10. NACA RM E51I25, 1951.

12. Moore, L. L.: A solution of the Laminar Boundary-Layer Equations for a Compressible Fluid with Variable Properties, Including Dissociation. Jour. Aero. Sci., vol. 19, no. 8, Aug. 1952, pp. 505–518.

13. Crown, J. Conrad: The Laminar Boundary Layer at Hypersonic Speeds. NAVORD Rep. 2299, Apr. 15, 1952.

14. Lees, Lester, and Probstein, Ronald F.: Hypersonic Viscous Flow Over a Flat Plate. Princeton University Aeronautical Engineering Laboratory Rep. 195, Apr. 20, 1952.

15. Li, Ting-Yi, and Nagamatsu, Henry T.: Shock Wave Effects on the Laminar Skin Friction of an Insulated Flat Plate at Hypersonic Speeds. GALCIT Memorandum No. 9, July 1, 1952.

16. Rubesin, Morris W.: A Modified Reynolds Analogy for the Compressible Turbulent Boundary Layer on a Flat Plate. NACA TN 2917, 1953.

# On the Corridor and Associated Trajectory Accuracy for Entry of Manned Spacecraft into Planetary Atmospheres

By

## Dean R. Chapman[1]

(With 10 Figures)

*(Received June 18, 1959)*

### Abstract — Zusammenfassung — Résumé

*On the Corridor and Associated Trajectory Accuracy for Entry of Manned Spacecraft into Planetary Atmospheres.* An analysis has been developed which determines the corridor through which manned spacecraft must be guided in order to avoid excessive deceleration for human occupants and yet to encounter sufficient deceleration for completing entry. The analysis introduces a dimensionless parameter coupling the aerodynamic characteristics of the vehicle with certain planetary characteristics evaluated at the perigee altitude corresponding to the approach conic trajectory. This perigee parameter conveniently bridges the two-body orbit equations to the re-entry motion equations, and provides a general basis for specifying the corridor width for entries from either elliptic, parabolic, or hyperbolic approach trajectories. The results apply to vehicles of arbitrary weight, shape, and size entering a planetary atmosphere. Illustrative calculations are presented for Earth, Venus, Mars, Jupiter, and Titan.

It is shown that the altitude of an entry corridor depends strongly on the vehicle weight, size, and drag coefficient, but that the corridor width between its overshoot and undershoot boundaries is independent of these characteristics. For certain planets (Earth, Venus, Jupiter) the corridor width is much greater for vehicles with aerodynamic lift than for nonlifting vehicles, but for other planets (e.g., Mars, Titan) aerodynamic lift cannot effectively broaden the entry corridor. For example, the 10-Earth-$G$ corridor width for single-pass parabolic entry of a non-lifting vehicle can be increased from 0 kilometers for Jupiter, 11 for Earth, and 13 for Venus, to 83, 82, and 83 kilometers, respectively, by employing a vehicle with a lift-drag ratio of 1; the corresponding corridor widths for Mars and Titan cannot be similarly increased very much beyond the values of 650 and 2,200 kilometers, respectively, corresponding to vehicles without lift. For any lift-drag ratio the corridor width decreases rapidly as the entry velocity is increased (e.g., for nonlifting vehicles entering the earth's atmosphere, the corridor decreases from about 290 kilometers wide at circular velocity, to 11 at parabolic velocity, to 0 at hyperbolic velocities greater than $1.8 \times$ circular).

The guidance requirements on accuracy of velocity and flight-path angle as determined by the corridor width are compared with the corresponding guidance requirements for other technological missions such as those for putting a vehicle into orbit, for hitting the moon from the earth, and for achieving intercontinental ballistic missile accuracy.

---

[1] Aeronautical Research Scientist, National Aeronautics and Space Administration, Ames Research Center, Moffett Field, California, U.S.A.

**Über die Genauigkeit von „Korridor"- und verwandten Bahnen beim Eintritt bemannter Raumfahrzeuge in Planetenatmosphären.** In der vorliegenden Arbeit wird eine Analyse zur Bestimmung des Korridors ausgeführt, durch den ein bemanntes Raumfahrzeug geführt werden muß, um übermäßige Verzögerung für die menschliche Bemannung zu vermeiden und trotzdem ausreichende Verzögerung für das Gelingen des Eintritts in die Atmosphäre zu erreichen. Die Analyse führt einen dimensionslosen Parameter ein, der die aerodynamischen Kennzeichen des Raumfahrzeuges mit bestimmten planetaren Charakteristiken verbindet, die bei der Höhe des Perigäums ausgewertet werden, das der konischen Annäherungsbahn entspricht. Dieser Perigäumparameter verbindet in geeigneter Weise die Zwei-Körper-Bahngleichungen mit den Bewegungsgleichungen für den Wiedereintritt und schafft eine allgemeine Grundlage für die Feststellung der Korridorweite für die Rückkehr entweder aus elliptischer bzw. parabolischer oder hyperbolischer Annäherungsbahn. Die Ergebnisse beziehen sich auf Raumfahrzeuge von willkürlich anzunehmendem Gewicht, Gestalt und Größe, die in eine Planetenatmosphäre eindringen. Illustrative Rechnungen werden für die Erde, Venus, Mars, Jupiter und Titan angeführt.

Es wird gezeigt, daß die Höhe des Eintrittskorridors sehr von Gewicht, Größe und Widerstandskoeffizient des Fahrzeuges abhängen, daß aber die Korridorbreite zwischen seinen obersten und untersten Grenzen unabhängig von diesen Kennzeichen ist. Im Falle bestimmter Planeten (Erde, Venus, Jupiter) ist die Korridorbreite viel größer für Fahrzeuge mit aerodynamischem Auftrieb als für Fahrzeuge ohne Auftrieb, aber bei anderen Planeten (z. B. Mars, Titan) kann der aerodynamische Auftrieb den Eintrittskorridor nicht wirksam verbreitern. Beispielsweise kann die Korridorbreite von 10 irdischen $g$ für einen parabolischen Einpaßeintritt eines auftriebslosen Fahrzeuges von 0 km für Jupiter, 11 für die Erde und 13 für die Venus auf 83, bzw. 82 und 83 km erhöht werden, wenn ein Fahrzeug mit einem Auftrieb-Widerstand-Verhältnis von 1 verwendet wird. Die entsprechenden Korridorbreiten für Mars und Titan können nicht in ähnlicher Weise sehr stark über die Werte von 650 bzw. 2200 km erhöht werden, welche auftriebslosen Fahrzeugen entsprechen. Für irgendein Auftrieb-Widerstand-Verhältnis nimmt die Korridorbreite schnell ab, wenn die Eintrittsgeschwindigkeit vergrößert wird (z. B. nimmt für auftriebslose Fahrzeuge, welche in die Erdatmosphäre eintreten, der Korridor von ungefähr 290 km Breite bei Kreisgeschwindigkeit auf 11 bei parabolischer Geschwindigkeit und auf 0 bei hyperbolischen Geschwindigkeiten ab, die größer als das 1,8fache der Kreisbahngeschwindigkeit sind).

Die Lenkungserfordernisse hinsichtlich der Genauigkeit von Geschwindigkeit und Flugwegwinkel, wie sie durch die Korridorbreite bestimmt werden, werden mit den entsprechenden Lenkungserfordernissen für andere technologische Aufträge verglichen, wie z. B. dem, ein Fahrzeug in die Umlaufbahn zu bringen, von der Erde aus den Mond zu treffen, und für die Verwirklichung genauer interkontinentaler ballistischer Geschosse.

**Précision de la trajectoire et corridor de rentrée d'un astronef piloté dans une atmosphère de planète.** Analyse du corridor dans lequel un astronef doit être guidé pour obtenir une décélération suffisante et cependant tolérable par les occupants. Un paramètre sans dimension couple les caractéristiques aérodynamiques du véhicule avec certaines caractéristiques planétaires évaluées au périgée de la conique d'approche. Il assure la transition entre les équations du problème des deux corps avec celles de la trajectoire de rentrée et forme la base générale permettant de spécifier la largeur du corridor dans une approche du type elliptique, parabolique ou hyperbolique. Les résultats sont applicables aux véhicules de forme, poids et dimensions arbitraires pénétrant une atmosphère planétaire. Application numérique est faite pour la Terre, Venus, Mars, Jupiter et Titan.

L'altitude d'un corridor de rentrée dépend fortement du poids, des dimensions et du coefficient de trainée du véhicule. Mais la largeur du corridor est indépendante de ces caractéristiques. Pour certaines planètes (Terre, Venus, Jupiter) cette largeur est plus grande en présence de portance; pour d'autres (Mars, Titan) la portance ne peut élargir appréciablement le corridor. Par exemple la largeur d'un corridor de

10 $g$ (terrestres) pour une passe d'approche simple parabolique peut passer de 0 kilomètres pour Jupiter, 11 pour la Terre et 13 pour Vénus à respectivement 83, 82 et 83 par l'emploi d'un rapport portance/trainée de 1. Les largeurs correspondantes pour Mars et Titan ne peuvent être accrues sensiblement au delà des valeurs de 650 et 2200 kilomètres obtenues sans portance. Quel que soit le rapport portance/ /trainée la largeur décroit rapidement avec la vitesse d'approche. Par exemple pour une approche sans portance dans l'atmosphère terrestre, elle décroit de 290 kilomètres, à la vitesse orbitale, à 11, à la vitesse de libération, et 0 pour des vitesses hyperboliques, supérieures à 1,8 fois la vitesse orbitale.

La précision du guidage en vitesse et angles, déterminée par la largeur du corridor, est comparée à celle requise par d'autres performances telles que la mise en orbite, la capture lunaire et la précision balistique intercontinentale.

## Introduction

It is generally anticipated that the first entry of a manned space vehicle into the earth's atmosphere will be from a near-circular orbit. Because of this the entry problems of deceleration and heating have been studied for near-circular velocities much more than for supercircular velocities. In the hopefully near future, entry at essentially parabolic velocity will be of practical concern (e.g., upon return from a manned moon mission), as will be entry at hyperbolic velocities in the more distant future.



Fig. 1. Entry corridor for manned spacecraft

One problem which is important for supercircular entries, yet is relatively unimportant for near-circular entries, is that associated with the guidance requirements for avoiding excessive deceleration or heating during entry. In terrestrial flight of aircraft, an undershoot approach in landing is easily corrected by a brief application of a small amount of power, and an overshoot approach is easily corrected by making a return pass. In space flight, undershoot or overshoot approaches can also be corrected by analogous procedures, but the consequences are much more severe. If a guidance error causes the spacecraft to undershoot the intended trajectory too much, as illustrated by the inner two dashed trajectories in Fig. 1, the vehicle will enter the atmosphere at an excessively steep angle and experience excessive deceleration for human occupants. It would take a relatively large amount of fuel to correct the trajectory once the vehicle is within or near the planet's atmosphere. If, at the other extreme, a guidance error results in overshooting the intended trajectory too much, as illustrated by the outer dashed trajectories in Fig. 1, then the vehicle will not encounter enough atmosphere for slowing sufficiently to complete entry, and will have to make a return pass. Return passes not only would require additional traverses of any radiation belt around the planet, but also would require in most cases an additional retrorocket thrust to complete entry in other than a large number of such passes. After excluding approach trajectories representing overshoot and excessive undershoot (shaded portions in Fig. 1), all that is left for some planets is a meagerly narrow corridor through which a spacecraft must be guided. The outer and inner boundaries of this single-pass entry corridor are referred to herein as the overshoot and undershoot boundaries, respectively.

This paper summarizes some results of a general study of the entry corridor and its boundaries. Entry guidance and aerodynamic heating problems are considered for spacecraft having various lift-drag ratios entering various planets at velocities between circular and twice circular velocity. A more detailed account of the research summarized herein, including development of the mathematical aspects of the analysis, may be found in [1]. The present paper attempts only to describe certain results; essential equations are stated and explained, but not derived. The results described are based on several hundred solutions to a transformed, nonlinear, differential equation representing entry motion in a planetary atmosphere.

## Results and Discussion

### Dimensionless Parameters Characterizing Entry

Many of the symbols employed in characterizing supercircular entries and in presenting results which follow are illustrated in Fig. 2. A spacecraft of mass $m$ enters a planet's atmosphere along the trajectory represented by the solid curve.

This curve intercepts the "sensible atmosphere" at $(i)$, at which point the flight-path angle is equal to the "initial angle" $\gamma_i$. This angle conventionally is employed to characterize an entry motion but is not employed herein. For shallow supercircular entries which just graze an outer edge of atmosphere, appropriate initial conditions are cumbersome to specify because, at all points along that portion of approach trajectory for which aerodynamic forces are negligible (that is, at points for which $y > y_i$), the flight-path angle $\gamma$, velocity $V$, and altitude $y$ change continuously as the initial altitude $y_i$ is approached. Moreover, the appropriate initial $\gamma_i$ and



Fig. 2. Sketch illustrating notation

$y_i$ are different for each vehicle and each approach angle. If the atmosphere were not present and the spacecraft encountered no drag, the vehicle would continue along a conic trajectory and pass through a perigee point designated in Fig. 2 as the conic perigee. The actual entry trajectory does not pass through this conic perigee point because it is diverted by aerodynamic forces. The velocity $V_p$, altitude $y_p$, and flight-path angle $(\gamma_p = 0)$ at the conic perigee, however, are unique and unchanging for all points along the approach trajectory; thus the conic perigee does not depend on where the sensible atmosphere begins. Primarily for this reason, a parameter based on conditions at the conic perigee, and not on $\gamma_i$, is employed for convenience in characterizing supercircular entries.

The mathematical basis for the significance of the particular perigee parameter $F_p$ used throughout this report is not established herein (see [1]); it will suffice to note that this parameter can be applied to any exponential planetary atmosphere and to vehicles of arbitrary weight, size and shape. The perigee parameter couples characteristics of the vehicle with characteristics of the atmosphere at the conic perigee. It is defined as

$$F_p = \frac{\rho_p}{2\,(m/C_D A)}\sqrt{\frac{r_p}{\beta}} \tag{1}$$

where $r_p$ is the radius to the conic perigee altitude, $\rho_p$ is the density at this altitude, $C_D$ is the vehicle drag coefficient based upon a fixed reference area $A$, and $\beta$ is the exponential decay parameter for the atmosphere defined by
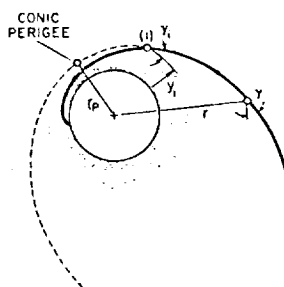
$$-\frac{d}{dy}(\ln \varrho) = \beta . \tag{2}$$

The parameter $\beta$ is the reciprocal of the scale height of the atmosphere, and is related to the characteristics of the atmosphere through the well-known equation

$$\beta = \frac{Mg}{RT} . \tag{3}$$

Here $M$ is the molecular weight of the atmosphere, $T$ the temperature, $R$ the universal gas constant, and $g$ the gravitational constant. The dimensionless initial velocity used in presenting subsequent results is defined as

$$\overline{V}_i = \frac{V_i}{\sqrt{gr}} . \tag{4}$$

This has the physical significance that $\overline{V}_i = 1$ represents circular entry, $1 < \overline{V}_i < \sqrt{2}$ elliptic entry, $\overline{V}_i = \sqrt{2}$ parabolic entry, and $\overline{V}_i > \sqrt{2}$ hyperbolic entry. For shallow entries $\overline{V}_i$ is equal to $\overline{V}_p$, the dimensionless velocity at conic perigee.

Three dimensionless parameters completely characterize any shallow supercircular entry into a spherically symmetric, nonrotating, exponential atmosphere, provided the aerodynamic coefficients are sensibly constant. One parameter is the dimensionless initial velocity $\overline{V}_i$; another is the perigee parameter $F_p$. The third dimensionless parameter combines certain characteristics of the planetary atmosphere with the lift-drag ratio of the vehicle, and is equal to $\sqrt{\beta r}\,(L/D)$. It will be employed here in the normalized form $\sqrt{(\beta r)}_\oplus\,(L/D)$, where the subscript $\oplus$ designates a value relative to that for the earth, for example,

$$\sqrt{(\beta r)}_\oplus \equiv \frac{\sqrt{\beta r}}{\sqrt{(\beta r)_{Earth}}} . \tag{5}$$

These three dimensionless quantities determine the overshoot boundary of the entry corridor, and also the undershoot boundary for any given value of the dimensionless maximum deceleration:

$$\overline{G}_{max} \equiv \frac{G_{max}}{g_\oplus \sqrt{(\beta r)_\oplus}} \cdot \frac{\sqrt{1 + [\sqrt{(\beta r)}_\oplus L/D]^2}}{\sqrt{1 + (L/D)^2}} . \tag{6}$$

The dimensionless deceleration $\overline{G}$ is equal to $G$, the deceleration in earth sea level $G$'s, only for entry into the earth's atmosphere. Inasmuch as the entry corridor width depends upon the maximum deceleration arbitrarily selected, it follows from eq. (6) that the calculation of corridor widths for various planets requires a knowledge of $g_\oplus$ and $\sqrt{(\beta r)}_\oplus$. Approximate values of these parameters for different celestial objects of the solar system are listed in the following table (also listed for later use are values of the altitude increment $\mathit{\Delta}_{10}y$ over which the density changes by a factor of 10):

| | $g_\oplus$ | $\sqrt{(\beta r)}_\oplus$ | $\mathit{\Delta}_{10}y$ for 10:1 change in $\varrho$, km |
|---|---|---|---|
| Venus .......... | 0.87 | 1.0 | 14 |
| Earth .......... | 1.00 | 1.00 | 16 |
| Mars ........... | .38 | .47 | 42 |
| Jupiter ........ | 2.6 | 2.0 | 42 |
| Titan .......... | .22 | .27 | 70 |

In the calculations of aerodynamic heating, additional equations and planetary constants would be needed. These are given in [1]. The main qualitative aspects of the aerodynamic heating problem are discussed with the aid of two simple equations presented later.

## Corridor Width

The entry corridor width can be calculated readily from the distance between the overshoot and undershoot boundaries on a plot wherein $\log_{10} F_p$ is used as one of the coordinates. From the defining eq. (1), the corridor with $y_{P_{ov}} - y_{P_{un}}$ between conic perigee altitudes at overshoot and undershoot is simply

$$\frac{y_{P_{ov}} - y_{P_{un}}}{J_{10}\,y} = \frac{y_{P_{ov}} - y_{P_{un}}}{(2.303\,\beta)} = \log_{10}\frac{(F_p\,m/C_D A)_{un}}{(F_p\,m/C_D A)_{ov}}. \tag{7}$$

It follows that, if $m/C_D A$ is the same at overshoot and undershoot, then the corridor width represented by an increment of one unit in $\log_{10} F_p$ is simply equal to $J_{10}\,y$, the quantity tabulated above.

The importance of guidance problems for supercircular entries, and the relative unimportance for near circular entry, may be seen from the curves in Fig. 3 which show overshoot and undershoot boundaries of the entry corridor as a function of the initial velocity. In the dimensionless coordinates employed, these curves can be applied to any planet. The spacing between values of $\log_{10} F_p$ which represents a 100 km corridor width in the earth's atmosphere (for constant $m/C_D A$) has been indicated for reference in Fig. 3. The curves apply for the case $\sqrt{(\beta r)_\oplus}\, L/D = 1$, which represents $L/D = 1$ for the earth's atmosphere $(L/D = -1$ along the overshoot boundary, and $L/D = +1$ along undershoot boundary). Curves for other lift-drag ratios show exactly



Fig. 3. Effect of initial velocity on overshoot and undershoot boundaries of entry corridor

the same trends, namely, a pronounced decrease in the corridor width (proportional to the spacing between the overshoot boundary and the undershoot boundary in Fig. 3) as the entry velocity is increased. In the case of $G = 5$, for example, the corridor width for parabolic entry ($V_i = \sqrt{2}$) is only about 1/13th as wide as for circular entry, and for hyperbolic entry at $V_i = 2.0$, is only a few percent of the corresponding width for circular entry.

Although the curves in Fig. 3 are designated as applying to a fixed value of $\sqrt{(\beta r)_\oplus}\, L/D$, the $L/D$ need not be held constant during an entire entry. At overshoot $L/D$ would have to be constant only until the point of local circular velocity is reached, and at undershoot, only until the point of maximum deceleration is reached. Beyond these points $L/D$ could be varied and the curves would still apply.

One qualitative result evident from a study of the three different undershoot boundaries shown in Fig. 3, concerns the influence of the arbitrarily selected maximum deceleration on the corridor width. The corridor width for $\bar{G}_{max} = 10$
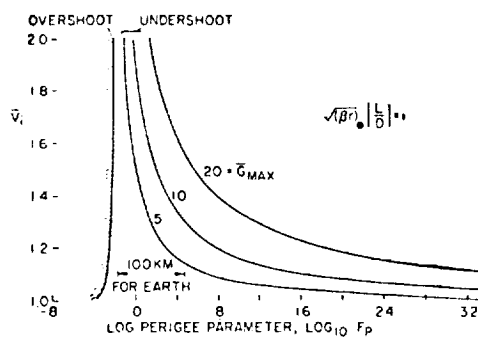
17*

is approximately twice that for $\overline{G}_{max} = 5$, and likewise the corridor width for $\overline{G}_{max} = 20$ is about twice that for $G_{max} = 10$. This rough proportionality of corridor width to $G_{max}$ applies throughout the range of entry velocities considered in Fig. 3, but it applies only to vehicles with substantial lift-drag ratios, that is, with lift-drag ratios such that $\sqrt{(\beta r)_\oplus} \cdot L/D > 0.5$ approximately (see [1]). For vehicles without lift the corridor widths are not even approximately proportional to the value of $G_{max}$; for example, the values of $(y_{p_{ov}} - y_{p_{un}})/\mathsf{l}_{10} y$ for $G_{max}$ of 5, 10, and 20 are 0, 0.7, and 2.0, respectively. Nonlifting vehicles do exhibit, however, the same trend of decreasing corridor width with increasing entry velocity as exhibited by lifting vehicles; for example, the values of $(y_{p_{ov}} - y_{p_{un}})/\mathsf{l}_{10} y$ with $G_{max} = 10$ are 18, 0.7, and 0, for $V_i$ of 1.0, 1.4, and 1.8, respectively. The corresponding corridor widths for entry into Earth ($\mathsf{l}_{10} y 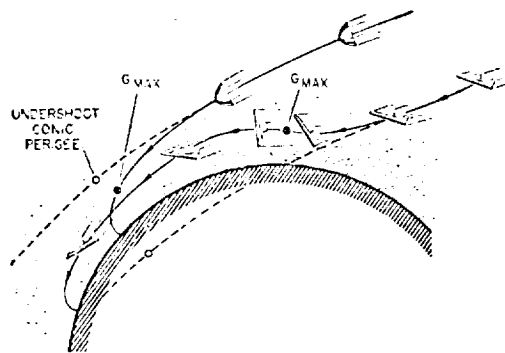= 16$ km), for example, would decrease from 290 km at $V_i = 1$, to 11 at $V_i = 1.4$, to 0 at $V_i = 1.8$. These values apply to the case where $m/C_D A$ is the same at overshoot as at undershoot.

The results just discussed, illustrating how the corridor shrinks as the entry velocity increases and broadens as the permissible deceleration increases, are understandable from simple physical considerations. The results to be presented shortly concerning the influence of positive and negative $L/D$ on the corridor boundaries, however, are less easily understood without some simple



Fig. 4. Lowering the undershoot boundary by means of positive aerodynamic lift

physical explanation. Consequently, before presenting additional mathematical results in terms of dimensionless parameters, a simple physical explanation will be outlined. In Fig. 4, two entries are depicted, one without lift and one with positive lift. In both cases the entry corresponds to that along the undershoot boundary and results in the same maximum deceleration. The dotted lines represent what the trajectories would have been had there been no aerodynamic force; they pass through their respective conic perigee points corresponding to the undershoot boundary. The nonlifting vehicle descends in a smooth monotonic fashion, experiencing its maximum deceleration at the point indicated. The lifting vehicle has the same value of $m/C_D A$, but, as it enters the atmosphere, the transverse lifting force deflects the trajectory away from the planet's center. Maximum deceleration is experienced at roughly the same altitude as for the nonlifting vehicle, even though the lifting vehicle enters at a much steeper angle and would pass through a conic perigee much closer to the planet's center. Once the vehicle passes the point of maximum deceleration it would skip out of the atmosphere if the $L/D$ were held constant. Consequently, in order to avoid this skip and complete entry on the first pass, $L/D$ must be reduced essentially to 0, and in some cases to small negative values, shortly after experiencing maximum deceleration (a mathematical demonstration of this has been given by LEES, HARTWIG, and COHEN in [2]). A reduction in $L/D$ can be accomplished either by reducing the angle of attack $\alpha$ of a lifting surface if the vehicle is operating in the low-drag portion of its drag polar, or by increasing $\alpha$ if operating in the high-drag portion. The latter, or high-drag mode of reducing $L/D$ is preferable because it results in much less aerodynamic heating. Hence the reduction in $L/D$ in Fig. 4 is represented by an increase

in angle of attack of the lifting surface just following the point of maximum deceleration. After the vehicle has slowed substantially in this high-drag attitude of small lift-drag ratio, it can then begin to reduce its angle of attack, thereby increasing the lift-drag ratio and entering into an extended terminal glide phase, as represented by the last attitude sketched for the lifting vehicle. By the use of lift in this manner the undershoot boundary for entry into certain planets can be lowered considerably from that for nonlifting vehicles, as will be evident subsequently.

In addition to the capability of lowering the undershoot boundary of the corridor, the judicious use of aerodynamic lift can also raise the overshoot boundary. In this case, however, the direction of application of the lift force with respect to the planet's center must be inverted. This is illustrated by the sketches in Fig. 5. The three trajectories shown are intended to represent those of the overshoot boundary in each case. At overshoot aerodynamic forces are relatively small and the actual



Fig. 5. Raising the overshoot boundary by means of negative aerodynamic lift or drag device

trajectory will pass only a small distance below the conic perigee point, as illustrated by each of the three trajectories in Fig. 5. The nonlifting, projectilelike configuration has the lowest perigee altitude of the three. If this nonlifting vehicle aimed at a conic perigee altitude which was slightly higher than that of the overshoot boundary, the vehicle would pass through an outer edge of atmosphere, exit from the atmosphere, orbit, and then have to make a return pass in order to complete entry. If the vehicle aimed at any perigee altitude lower than that for overshoot, entry would be completed on the first pass. A vehicle with aerodynamic lift can aim at a higher conic perigee altitude, as illustrated by the middle trajectory in Fig. 5 and still complete entry in a single pass, provided the aerodynamic lift is directed toward the planet's center (negative lift). This upward extension of the overshoot boundary through the application of negative lift is not really large, however, because there is not much atmosphere at the higher altitudes to work with in deflecting the vehicle's path. As we will see later, the overshoot boundary can be extended upward to a considerably greater degree by the use of a light, high-drag device, than by the use of negative aerodynamic lift. This is indicated schematically by the outer trajectory in Fig. 5. The drag device may be thought of as consisting of metallic cloth fabricated from very thin threads of a high-temperature alloy, and as being deployed over as large an area normal to the direction of flight as is practical. In this way the drag



Fig. 6. Effect of lift-drag ratio on parabolic entry corridor

chute encounters a sufficient mass of air to complete entry in a single pass even though it aims at a much higher conic perigee altitude than the other vehicles.

The trends anticipated from the foregoing physical considerations are illustrated by the curves representing overshoot and undershoot on a plot of the dimensionless lift-drag parameter $\sqrt{(\beta r)_\oplus}\, L/D$ versus the perigee parameter $\log_{10} F_p$. as presented in Fig. 6. The solid undershoot boundary corresponds to constant $L/D$ only up to maximum deceleration, and the dotted boundary (discussed later) corresponds to a variable $L/D$ with the initial $L/D$ at entry equal to that plotted as the ordinate. Since the drag coefficient usually is referred to a fixed reference area of a fixed mass, it follows from eq. (7) that the corridor width in such cases is

$$ y_{p_{or}} - y_{p_{un}} = A_{10}\, y \left[ \log_{10} \left( \frac{F_p}{C_D} \right)_{un} - \log_C \left( \frac{F_p}{C_D} \right)_{or} \right]. \tag{8} $$

This equation shows that, for any given value of $\sqrt{(\beta r)_\oplus}\, L/D$, the corridor width is proportional to the spacing between the overshoot and undershoot boundaries in Fig. 6, provided $C_D$ is the same at these two boundaries. The reference arrows indicate what would be a 90 km corridor for the earth's atmosphere. The undershoot boundary in this particular plot represents $G_{max} - 10$ and the initial velocity represents parabolic entry. As is evident from this figure, the corridor width for lifting vehicles is considerably broader than for nonlifting ones having the same $C_D$. For the earth's atmosphere the corridor width would be 10 km for all nonlifting vehicles, irrespective of the value of $m/C_D A$ (as long as it is the same at undershoot and overshoot). The use of negative lift to extend the overshoot boundary toward smaller values of $F_p$ (corresponding to smaller densities and higher altitudes) broadens the earth's corridor by only about 20 km. The use of positive lift to extend the undershoot boundary to higher values of $F_p$ is seen to be about three times as effective, resulting in an extension of about 60 km for the undershoot limit. The total corridor width, with positive lift used to extend downward the undershoot boundary, and negative lift to extend upward the overshoot boundary, is seen to be a maximum of about 90 km at $\sqrt{(\beta r)_\oplus}\, L/D$ of about 2. The corridor for $\sqrt{(\beta r)_\oplus}\, L/D - 1$ is almost as wide as the maximum width, and for $\sqrt{(\beta r)_\oplus}\, L/D - 0.5$ is about 2/3 as wide as the maximum width.

It is emphasized that the variation in spacing between the corridor boundaries with varying $L/D$ in Fig. 6 is representative of the actual variation in corridor width only if $C_D$ is the same for all $L/D$'s. The corridor width, according to eq. (8), really depends on the difference in $\log F_p/C_D$ for vehicles of fixed $m$ and $A$. With any aerodynamic device $C_D$ is always coupled to $L/D$; large $L/D$'s in hypersonic Newtonian flow, for example, are obtained only with slender configurations having small $C_D$, whereas large $C_D$'s are obtained with blunt configurations having small $L/D$. If the aerodynamic coupling between $L/D$ and $C_D$ is taken as that corresponding to lifting surfaces wherein both $L/D$ and $C_D$ are changed by varying the angle of attack, then the actual overshoot extension attains a maximum at $L/D$'s of about $-0.5$, and amounts to about 10 km for Earth. This is one half of the extension possible if $C_D$ could be maintained the same for $L/D - 2$ as for $L/D$ 0.

Extending overshoot by applying negative lift is less effective than increasing drag. By keeping $L/D$ 0, for example, and deploying a light high-drag device, $m/C_D A$ can be changed by a factor of about 1000, which corresponds to an extension upward of the overshoot boundary by $3 A_{10} y$, which is about 50 km for the earth's atmosphere. This is five times the extension possible if negative lift

were employed, and is comparable to the 60 km extension in undershoot boundary provided by positive lift with constant $L/D$ and $C_D$.

When the aerodynamic coupling between $L/D$ and $C_D$ for lifting surfaces is considered, the actual lowering of the undershoot boundary by use of positive $L/D$ is somewhat greater than the apparent trend of the solid boundary in Fig. 6 would suggest. At $L/D = 2$ the 60 km apparent extension would really be about 80 km.

The dotted undershoot boundary in Fig. 6 labeled "variable $L/D$ with constant $C_D$" represents entry with an initial $L/D$ corresponding to the value plotted, and with lift modulated in a particular fashion which keeps both $G$ and $C_D$ constant during the modulation period, in which the lift force is reduced to alleviate the resultant deceleration. This dotted curve showing the greatest apparent extension in the undershoot boundary with increasing $L/D$, is based on the original analysis of modulated lift given by LEES, HARTWIG, and COHEN in [2]. It is applicable only to the earth's atmosphere. In order to realize this desirable extension in undershoot, $C_D$ would have to be maintained substantially constant (or decreased) during the lift modulation period when $L/D$ is reduced from its initial value at entry to essentially zero. If $L/D$ is reduced by increasing the angle of attack of a lifting surface operating in the high-drag range of the drag polar, then $C_D$ increases markedly in the process and thereby increases the horizontal component of deceleration more than the decrease in $L/D$ alleviates the transverse component, so that no net gain is achieved. If, on the other hand, $L/D$ is reduced by decreasing $a$ of a lifting surface operating in the low-drag portion of the drag polar, then $C_D$ is reduced moderately, and the apparent extension represented by the dotted undershoot boundary can be fully realized. A complication arises, however. Sizable extensions in corridor width over that for constant $L/D$ are possible only with relatively large $L/D$ which have small $C_D$, and, for the low-drag portion of a polar, result in a large heating penalty. The aerodynamic heating can be one to two orders of magnitude greater under these conditions than for operation in the high-drag portion with a small, constant $L/D$.

## Aerodynamic Heating

It is unfortunate that vehicles cannot be designed with large lift-drag ratios (the order of 4, say) and simultaneously large drag coefficients. Large $L/D$ is desirable in order to maximize the entry corridor width and large $C_D$ is desirable in order to minimize the aerodynamic heating. As a lifting vehicle changes its attitude within the high-drag regime from essentially normal entry with $L/D = 0$ and maximum $C_D$ (as indicated by the configuration sketched in the lower left portion of Fig. 7), through progressively smaller angles of attack producing higher lift-drag ratios, the effective slenderness of the configuration necessarily changes, and $C_D$ decreases. Since laminar convective heating varies as $C_D^{-0.5}$, and turbulent convective heating as $C_D^{-0.8}$ (see [3] and [1], for example), a reduction in $C_D$ brought about by the use of larger $L/D$ ratios would result in an increase in aerodynamic heating for both types of convection. This is illustrated by the two curves in Fig. 7 which represent heating for lifting surfaces. These curves are normalized with respect to the amount of heating for the maximum drag attitude at $L/D = 0$. Depending on the relative amount of laminar and turbulent flow, a slender vehicle designed to produce $L/D = 3$, for example, would have between about 6 and 16 times as severe a heating problem as a blunt vehicle designed to produce no lift. In any practical case the beneficial effect of employing lifting

vehicles to broaden the entry corridor would have to be tempered by its adverse effect on aerodynamic heating. For $L/D$'s of 0.5 to 1, this penalty does not appear to be too severe, and within this range the trade-off between a broadened corridor and a more severe heating problem would favor the lifting vehicle over the non-lifting one. For larger $L/D$'s the trade-off is much more difficult to assess.
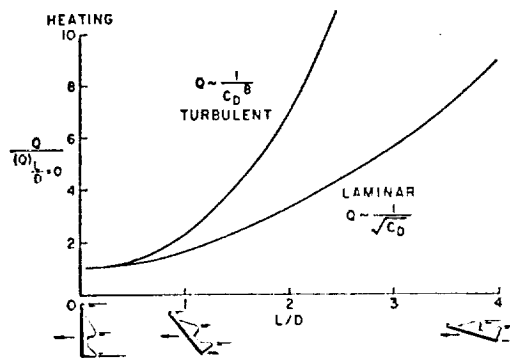


Fig. 7. Increase in convective heating with increasing $L/D$

In discussing the aerodynamic heating problem associated with the entry corridor, a distinction must be made between the total heat absorbed during entry and the rate at which it is absorbed. For an ablation-type heat shield, the total heat absorbed is of principal importance, but for a radiation-cooled vehicle, the maximum rate of heating is important. The type of heating problem which exists at the overshoot boundary is different from that at the undershoot boundary, as may be deduced from a general relationship between aerodynamic heating and deceleration discussed in [1]. This qualitative relationship for the maximum rate of laminar heating states that

$$\left(\frac{dQ}{dt}\right)_{max} \sim \sqrt{G_{max}}$$

and, for the total laminar heat absorbed, that

$$Q = \frac{1}{\sqrt{G_{mean}}}.$$

In view of this relationship we see that the total heat absorbed will be much less at the undershoot boundary where the deceleration is large than at the overshoot boundary where it is small. A typical variation within the earth-atmosphere corridor is that the decelerations are about nine times as large at the 10-$G$ undershoot boundary as at overshoot, so that the total laminar heat absorbed at this undershoot boundary is about one third of that at overshoot. The maximum heating rates, however, follow an opposite relationship. They are largest at undershoot where decelerations are maximum, and smallest at overshoot where decelerations are minimum. A study of the approximate numerical values involved [1] indicates the situation to be about as follows: At undershoot where the heating rate is relatively large, pure radiation cooling for parabolic entry into the earth's atmosphere is currently impractical, but the total heat absorbed is within practical bounds of present heat absorption techniques. At overshoot, on the other hand, where the heating rate is relatively small, pure radiation cooling is practical, but the total heat absorbed is about three times that at undershoot. For efficient heat protection of spacecraft, therefore, it is desirable to develop versatile shields which can radiate efficiently if the vehicle happens to enter near overshoot, ablate efficiently if it enters near undershoot, and blend these functions efficiently if it enters anywhere in between.

## Guidance Requirements

In order to provide a visual picture of the wide variation in entry corridors of different planets in the solar system, and of the corresponding wide variation in guidance requirements, the sketches in Figs. 8 and 9 have been prepared. These sketches are approximately to scale showing each entry corridor in proper proportion to the diameter of its parent planet (or parent celestial satellite in the case of Titan). The corridors for Earth and Venus are sufficiently similar that they have been represented by a single sketch in Fig. 8. The actual width of the corridor for the particular conditions considered ($\overline{V}_i = 1.4$, $G_{max} = 20$, and $|L/D| = 1$) varies from about 170 km at $r/r_0 \cong 1$ to about 400 km at $r/r_0 = 4$. This corridor
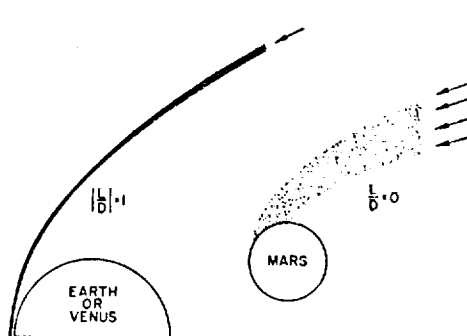


Fig. 8. Parabolic entry corridors for Earth, Venus, and Mars; $G_{max} = 20$
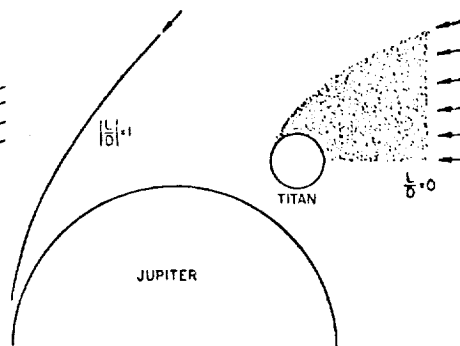
Fig. 9. Parabolic entry corridors for Jupiter and Titan; $G_{max} = 20$

appears to be neither impractically narrow nor pleasingly broad. It is much narrower, though, than the corresponding corridor for Mars, also shown in Fig. 8. The Mars corridor would not be expected to impose a really severe guidance problem. For such broad corridors, the entry angle at undershoot is sufficiently steep (47° for Mars) that aerodynamic lift is not effective in broadening the corridor; hence $L/D$ is taken as zero for such corridors. Corridor widths calculated for nonlifting entry into Mars are 340 km for $G_{max} = 5$, 650 km for $G_{max} = 10$, and 2,000 km for $G_{max} = 20$. These values include an allowance of 130 km for the overshoot altitude.

The corresponding parabolic entry corridors for Jupiter and Titan, as sketched in Fig. 9, illustrate the very wide variations encompassed by different objects in the solar system. The corridor for Jupiter is so narrow that it is difficult to illustrate by other than a relatively narrow line. At the opposite extreme, the corridor for Titan is so broad that it includes all possible trajectories which would "hit" this satellite. Even direct vertical entry into Titan's atmosphere at $\overline{V}_i = \sqrt{2}$ would result only in $G_{max} \cong 5$.

In order to determine the trajectory which passes along the center of an entry corridor it would be necessary to make precise three-dimensional orbit calculations giving full consideration to a number of perturbations, such as those due to planetary oblateness, the sun, moon, and perhaps other planets. In calculating the small deviations permissible from this desired centerline trajectory, however, the effects of the perturbations on these deviations will be disregarded, and the entry guidance tolerances calculated as those of a two-body problem. This procedure appears reasonable inasmuch as the terminal correction to an entry approach would presumably be made relatively near the target planet where the trajectory is mainly in one plane and is essentially a conic trajectory.

Guidance tolerances imposed by different parabolic entry corridors can vary widely, as illustrated in Fig. 10. Here the ordinate represents the permissible deviation in flight-path angle $\pm\Delta\gamma$ from that of the centerline trajectory which bisects the overshoot and undershoot boundaries at any given distance $r/r_0$. These calculations are based on the assumption that there are no errors in velocity or position. The maximum deceleration is taken as $10\,G$ for these curves. As would be expected, the more distant a spacecraft is from the planet, the more severe the requirement is for aligning a trajectory to pass through the entry corridor. At distances close to the planet the required accuracy on $\pm\Delta\gamma$ is least, but the fuel which would have to be expended in making corrections close to the planet
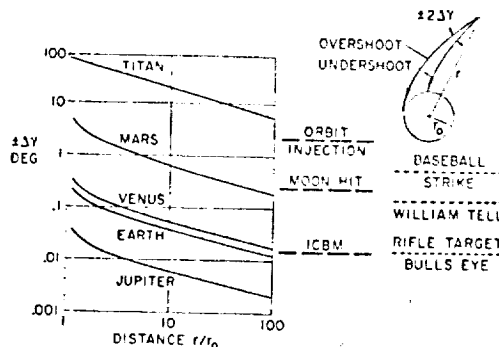


Fig. 10. Guidance requirements on flight path angle for various parabolic entry corridors ($G_{max} = 10$)

is much larger than at distances far removed from the planet. Hence, the best place to make such corrections would be at some intermediate distance. The range $1 < r/r_0 < 100$ covered in Fig. 10 would seem to encompass the range of practical interest.

For purposes of comparison, three technological guidance requirements on $\pm\Delta\gamma$ (which also are calculated under the assumption that there are no errors in velocity) are shown in Fig. 10 just to the right of the $r/r_0$ 100 line. These correspond to typical requirements for orbiting an earth satellite, for hitting the moon from the earth, and for aligning the azimuthal angle of an ICBM to achieve a miss distance of 1/5000 of the range. As would be expected, the requirements on $\pm\Delta\gamma$ to enter the corridor of Titan are not very severe, and are even much less severe than the comparison guidance requirement on $\pm\Delta\gamma$ of approximately 2° to eject a satellite into orbit around the earth. The corresponding requirements for Mars are seen to be considerably less severe than the comparison requirement of about $\pm0.25°$ for hitting the moon from the earth (see [4]). The corresponding requirements for Venus and Earth are seen to be somewhat less severe than the comparison ICBM requirement.

It is to be noted that the approximate requirements on $\pm\Delta\gamma$ discussed above are based on the unrealistic assumption that no errors in velocity exist. When simultaneous velocity and position errors are considered, the practical requirements on $\pm\Delta\gamma$ for guiding a vehicle through an entry corridor would be several times as severe as those illustrated in Fig. 10. Since the corridor widths are specified in terms of the difference in conic perigee altitudes, it is an easy matter to compute the approximate permissible errors in velocity and position, as well as in flight path angle, from the well-known Newtonian equations for two-body orbits. It may suffice here, perhaps, to observe that the study of velocity tolerances in reference 1 for parabolic entry into the corridor of Earth or Venus indicates $\pm\Delta V/V$ (for no error in $\gamma$) to be about 0.003, which is a less severe requirement than the corresponding velocity tolerance of 0.001 for hitting the moon from the earth [4].

For further comparison purposes, three nontechnological, but equally illuminating guidance requirements on $\pm\Delta\gamma$ are included in the right-hand portion of Fig. 10. These may serve to place the corresponding technological requirements in more balanced perspective. Thus, entry into the corridor of Mars requires

about the same guidance accuracy as that with which a skilled man can throw a ball, as exemplified by the accuracy required of a baseball pitcher to pitch a strike; entry into the corridors of Venus and Earth require about the same accuracy as required of William Tell to hit an apple at 20 paces. To enter the corridor of Jupiter requires an accuracy almost an order of magnitude greater than required to hit the bull's eye of a rifle target ( ± 1 minute of arc), which is achieved essentially 100 percent of the time by skilled individuals although under relatively comfortable and favorable conditions.

The most important difference between these various technological, non-technological, and entry-corridor requirements probably lies not so much in the numerical difference between requirements, but in the difference in reliability with which the individual guidance requirements must be obtained. The consequences of failing to achieve the guidance requirements associated with injecting a satellite into orbit, hitting the moon, scoring a rifle target bull's-eye, or pitching a baseball strike, may be no more severe than that of bad publicity, but the consequences of failing to achieve the guidance requirements associated with the entry corridor for manned spacecraft could result in a catastrophe, as could have resulted if William Tell had failed to achieve his guidance requirements. In such light the reliability with which the guidance requirements on flight-path angle must be obtained may impose perhaps the most challenging technological problem.

## References

1. D. R. Chapman, An Analysis of the Corridor and Guidance Requirements for Supercircular Entry into Planetary Atmospheres. NASA Report, 1959.
2. L. Lees, F. W. Hartwig, and C. B. Cohen, The Use of Aerodynamic Lift During Entry Into the Earth's Atmosphere. Space Technology Labs. Inc., GM-TR-0165--00519, Nov. 1958.
3. H. J. Allen and A. J. Eggers, Jr., A Study of the Motion and Aerodynamic Heating of Ballistic Missiles Entering the Earth's Atmosphere at High Supersonic Speeds. NACA Rep. 1381, 1958. (Supersedes NACA TN 4047.)
4. H. A. Lieske, Accuracy Requirements for Trajectories in the Earth-Moon System. RAND Rep. P-1022, Feb. 1957.

# The Supersonic Blunt-Body Problem—Review and Extension

## MILTON D. VAN DYKE*

*Ames Aeronautical Laboratory, NACA*

### SUMMARY

A survey of existing analytical treatments of the supersonic or hypersonic blunt-body problem indicates that none is adequate for predicting the details of the flow field. Reasons are given for the failure of various plausible approximations. A numerical method, which is simpler than others proposed, is set forth for solving the full inviscid equations using a medium-sized electronic computer. Results are shown from a number of solutions for bodies that support detached shock waves described by conic sections.

### SYMBOLS

| | | |
|---|---|---|
| $B$ | = | bluntness of conic section [see Eq. (1)] |
| $C$ | = | $1 - B$, |
| $C_p$ | = | pressure coefficient referred to free-stream conditions |
| $f$ | = | $p/\rho^\gamma$ |
| $M$ | = | free-stream Mach Number |
| $p$ | = | pressure referred to $\rho_\infty V_\infty^2$ |
| $R$ | = | nose radius |
| $r$ | = | coordinate normal to free stream |
| $u, v$ | = | components of velocity in $\xi, \eta$ directions |
| $\vec{V}$ | = | velocity vector referred to free-stream speed |
| $x$ | = | coordinate in free-stream direction |
| $\gamma$ | = | adiabatic exponent |
| $\delta$ | = | $(\gamma - 1)/(\gamma + 1)$ |
| $\Delta$ | = | standoff distance of shock from body nose |
| $\xi, \eta$ | = | orthogonal curvilinear coordinates [see Eq. (2)] |
| $\Delta\xi, \Delta\eta$ | = | mesh widths in numerical computation |
| $\nu$ | = | 0 for plane flow, 1 for axisymmetric flow |
| $\rho$ | = | density referred to free-stream value |
| $\Psi$ | = | stream function |
| $\omega$ | = | modified stream function [see Eq. (11)] |
| $\theta$ | = | polar angle |
| $( )_s$ | = | value on shock wave |
| $( )_b$ | = | value on body |
| $( )_\infty$ | = | free-stream value |
| $( )_{st}$ | = | value at stagnation point |

### INTRODUCTION

**P**HOTOGRAPHS of the detached shock wave that forms ahead of a blunt body in supersonic flight show a beautiful simplicity that has in the last decade lured a number of aerodynamicists into trying to predict its shape. Recently there have arisen more urgent reasons for finding the complete flow field (particularly in hypersonic flow), and a considerable fraction of the theoretical aerodynamicists in the United States, England, and (apparently) Russia have become involved with the problem. The attacks have been mainly analytical, though within the last year electronic computers have been brought to bear.

The present paper aims, first, to evaluate the mass of existing analytical treatments and, second, to put forth a new and relatively simple numerical procedure.† The survey will show that existing analytical methods are generally inadequate for predicting the details of flow near a blunt nose. With the numerical method, accurate solutions have been carried out for members of a one-parameter family of plane and axisymmetric bodies.

### (1) REVIEW OF EXISTING ANALYTICAL SOLUTIONS

Existing analytical attacks on the supersonic blunt-body problem fall mainly into four categories: (1) Potential flow approximations.[1-4] (2) Taylor series expansions from shock.[5-11] (3) Incompressible approximations.[12-15] (4) Newtonian approximation and improvements thereon.[16-25]

The only other noteworthy approach is that of explosion and similarity solutions[26, 27] which gives the asymptotic flow field downstream on a slender blunt-nosed body. This elegant and useful theory is not intended to treat the vicinity of the nose and will, accordingly, not be considered here. The four methods listed above will now be discussed in succession, drawing where necessary on the accurate numerical solutions described in section (2) as a standard of comparison. Other numerical methods[28-32] will be discussed in section (3).

#### (1.1) Potential Flow Approximations

The oldest attack on the blunt-body problem consists in attempting somehow to relate the actual flow behind the detached shock wave to the subsonic (often incompressible) potential flow past the same body. The standoff distance for spheres in air ($\gamma = 7/5$) predicted by several such theories is compared in Fig. 1 with the results of the numerical solutions described later. The standoff distance is a convenient test because it is easily measured from schlieren photographs and should be given accurately by any theory that is to predict other more important properties of the flow field. Moreover, its prediction is actually the main objective of most of these approximations.

† Another survey of the blunt-body problem in the special case of hypersonic flow will appear in the monograph *Hypersonic Flow Theory* by Wallace D. Hayes and Ronald F. Probstein, to be published soon.
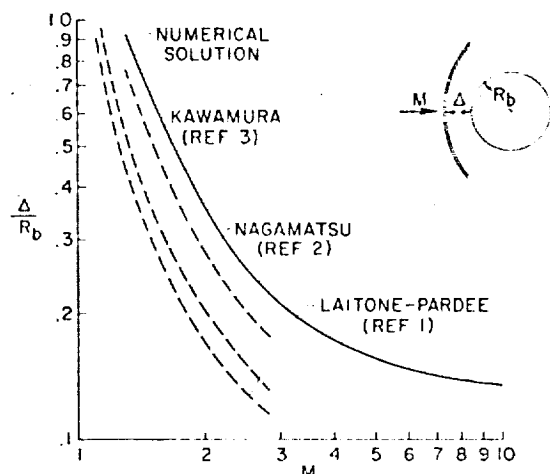
FIG. 1. Potential flow approximations for standoff distance of shock from sphere with $\gamma = 7/5$

The accuracy is seen to be mediocre, particularly in hypersonic flow (and is still worse for plane flow). Closest agreement is given by the theory of Kawamura,[3] who makes a straightforward match of streamline slopes behind the vertex of the shock wave with those of the incompressible potential flow. His results have been reproduced by Heybey[1] who also attempts to estimate a correction for compressibility. However, it will be seen in section (1.3) that vorticity rather than compressibility is the chief factor neglected at high Mach Numbers and that Heybey's estimate of the compressibility effect is too large. In any case, these theories are of no value for predicting such quantities as surface pressures (which by assumption have the form corresponding to incompressible potential flow).

### (1.2) Taylor Series Expansion From Shock

If the form of a detached shock wave is known or assumed, the flow variables (pressure, density, velocity) just behind it are given by the oblique shock relations, and their first derivatives can be found by substituting into the equations of motion. Higher derivatives can be found by first differentiating the equations of motion. According to the Cauchy-Kowalewski theorem (see, e.g., reference 33) the flow field is analytic somewhat downstream of the shock wave, and there is physically no reason to doubt that the region of analyticity extends to the body. One may therefore attempt to represent the flow layer between the shock and body by a few terms of a Taylor series expansion starting from the shock wave. This idea, introduced by Lin and Rubinov,[5] has been applied to plane,[8] axisymmetric,[6, 7, 10, 11] and three-dimensional[9] flows.

The expansion has been pursued furthest by Cabannes for axisymmetric flow. Taking the shock wave to be described in Cartesian coordinates by $x = \Sigma a_n r^n$, he gives the coefficients in the double Taylor series for the various flow variables out to $x^4$, $x^2 r^2$, $r^4$ (and of Stokes' stream function to $x^6$, $x^4 r^2$, ...) for $\gamma = 7/5$ and general free-stream Mach Number $M$ (reference 10), and the stream function to two addi-

tional terms in the special case $M = 2$ (reference 11). The variation of Stokes' stream function along the axis of revolution behind a paraboloidal shock wave is compared in Fig. 2(a) with the accurate numerical solution. Successive terms of the Taylor series are seen to meander with no clear indication of either convergence or divergence.

The expansion procedure can be simplified by introducing the natural curvilinear coordinates associated with the shock wave—parabolic coordinates for a paraboloidal shock wave, etc. The Taylor series have then the advantage of being not double but only single expansions (in the coordinate leading away from the shock). It may also be anticipated that the convergence properties of the series will show up more clearly in the natural coordinates. It is easy to recast Cabannes' series in parabolic coordinates. The result
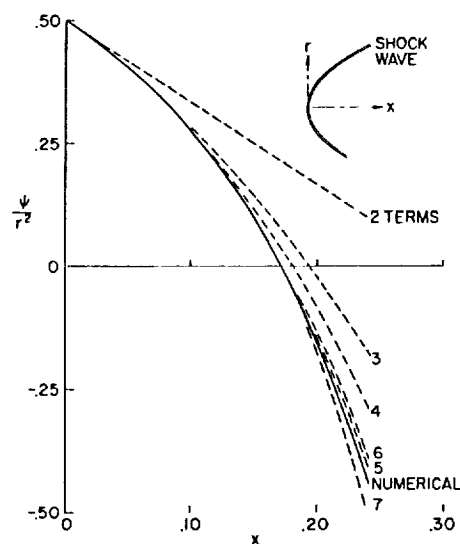


(a) Cartesian coordinates.
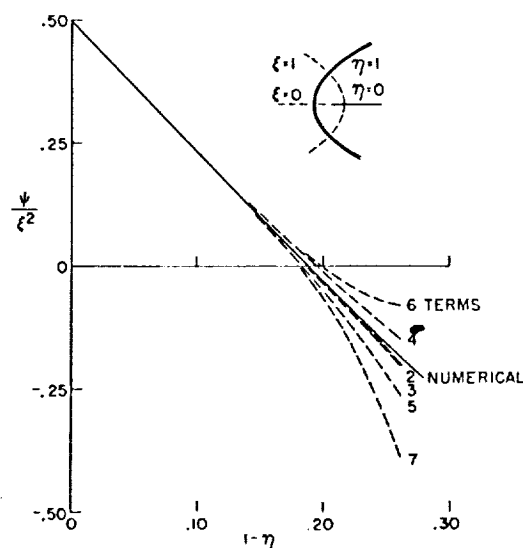


(b) Parabolic coordinates.

FIG. 2. Variation of stream function along axis behind paraboloidal shock wave at $M = 2$ with $\gamma = 7/5$.

corresponding to Fig. 2(a) is shown in Fig. 2(b), and it is now clear that at the nose of the body the series diverges.

The probable source of the divergence has been suggested in reference 34. The Taylor series expansion describes not only the flow downstream of the shock wave but also its analytical continuation upstream. As indicated in Fig. 3, this fictitious flow will contain a limiting line which intersects the axis at the sonic point and in the supersonic region is the envelope of outgoing characteristics. (Such a line exists also in the well known Taylor-McColl flow past a circular cone; its location is, in fact, tabulated by Kopal.[35]) The flow variables are nonanalytic at the limiting line where they vary as half powers of the distance. Hence if the shock wave is closer to the limiting line than to the body, the Taylor series will not include the body in its radius of convergence. This suggestion has been verified by running the numerical procedure backward to calculate the fictitious flow in the example of Fig. 2. On the axis, the limiting line was found to lie only three-fourths as far from the shock wave as does the body nose.

The situation is comparably bad for other shapes and Mach Numbers and worse away from the axis or in plane flow. Hence the method of Taylor series expansion from the shock wave cannot be expected to succeed. Nevertheless, the first three terms of the series (in natural coordinates) can serve as a useful qualitative model in the case of axisymmetric flow.[34] For a paraboloidal shock wave at $M = \infty$ (and $\gamma = 7/5$) the model predicts the ratio of standoff distance to body nose radius correct to within 0.8 per cent, so that it may also have some quantitative value. However, it deteriorates away from the axis and does not predict a real body out to the sonic point.

### (1.3) Incompressible Approximation

At high supersonic Mach Numbers the density varies only slightly between the shock wave and the body in the vicinity of the stagnation point. It therefore seems appropriate to solve the equations of rotational incompressible flow together with the exact conditions just behind the shock wave. Thus Lighthill[13] has obtained the solution in closed form for the special case of a spherical shock wave at infinite Mach Number (that is, in the "strong shock" approximation), the body being found as a concentric sphere. Similarly, Whitham[14] and Hayes[15] have shown that in plane flow a circular shock leads to a concentric circular body.

To assess this approximation, numerical solutions have been carried out for a spherical and a circular shock wave in a stream of infinite Mach Number (all solutions for $M = \infty$ were actually carried out at $M = 10,000$) with $\gamma = 7/5$. In axisymmetric flow the resulting body shape, shown in Fig. 4(a), lies close to the sphere of the incompressible approximation out roughly halfway to the sonic point. In plane flow, as might be expected, the agreement is poorer (though it

would improve in either case as $\gamma \to 1$). The body is roughly the front portion of a 4:1 ellipse standing on end rather than a circle.

For the flow near the axis, these results were given earlier by Hida.[12] His analysis is more general in that all supersonic Mach Numbers are considered. Fig. 4(b) shows that his results for standoff distance are fairly accurate throughout the Mach Number range, the remaining discrepancy being presumably attributable to compressibility. Thus at infinite Mach Number the approximation of irrotational incompressible flow[3,4] gives 0.094 as the standoff distance for a sphere in air; the increment due to rotation is 0.026 according to the Hida-Lighthill theory and the remaining difference of 0.008 from the value 0.128 of the numerical solution must represent the effect of compressibility. (Heybey's estimate of the compressibility effect[4] is 0.024 in this case.) It might be possible to include compressibility by iteration in the style of the Janzen-Rayleigh approximation for subsonic flow. If so, this would seem the most promising of the analytic theories.

### (1.4) Newtonian Approximation and Improvements Thereon

In simple Newtonian theory, fluid particles are imagined to lose their normal component of momentum upon striking the surface of the body. The local pressure coefficient is then given by $2 \sin^2 \theta$, where $\theta$ is the angle that the surface makes with the stream direction. Lees[36] has proposed a modified Newtonian theory which consists merely in scaling down this result so as to be exact at the stagnation point where the correct value is known. He suggests that because of compensating effects, this will be more accurate than the shock-layer or "Newtonian-plus-centrifugal" approximation[16,17] which is the actual limit of the solution for $M \to \infty$ and $\gamma \to 1$.

The surface pressures on a sphere and circular cylinder at $M = \infty$ with $\gamma = 7/5$ according to these three approximations are compared in Fig. 5 with numerical solutions. The modified Newtonian result is seen to fall either above or below the accurate solution, depending on Mach Number and body shape, but to be remarkably accurate when $\gamma = 7/5$.

Chester[23] and Freeman[24] have taken the shock-layer or Newtonian-plus-centrifugal solution as a first step and sought to improve it systematically by successive approximations. The result is a double series expansion of the flow quantities for small $\delta = (\gamma - 1) \div (\gamma + 1)$ and $M^{-2}$ (a single series expansion in the work of Freeman, who considers only the "strong shock" case, corresponding to $M = \infty$).

Unfortunately, the series appears to converge slowly for practical values of $\gamma$, and worse in axisymmetric than plane flow. This is illustrated in Fig. 6 for the standoff distance in Chester's example of a paraboloidal shock wave. By appeal to the model mentioned at the end of section (1.2), the present writer has suggested[34] that Chester's series actually converges for $\gamma > 2.2$ (corresponding to $\delta < 3/8$), whereas for real
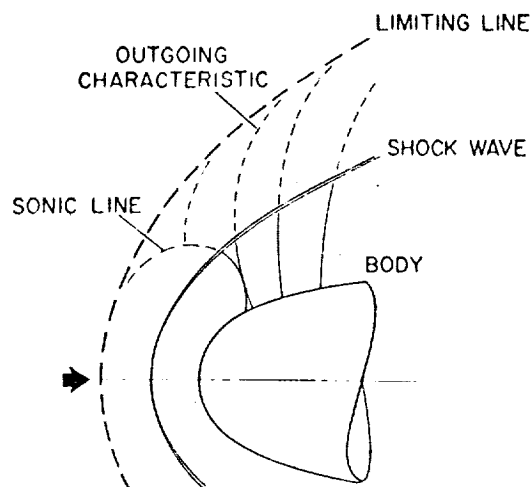
FIG. 3. Schematic sketch of analytical continuation of flow field upstream through shock wave, showing limiting line (from reference 34).
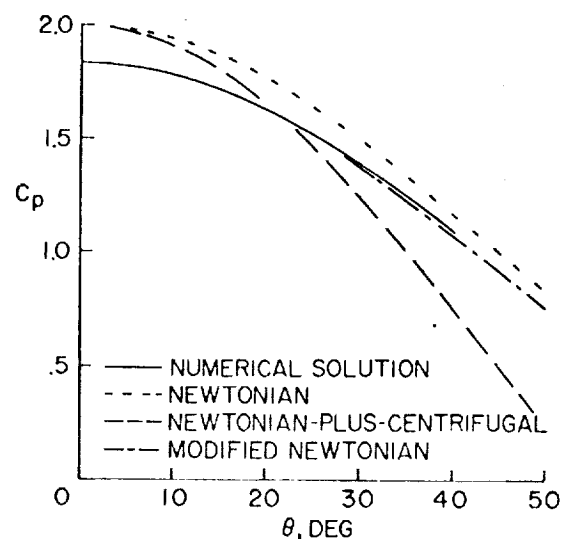


(a) Circular cylinder.
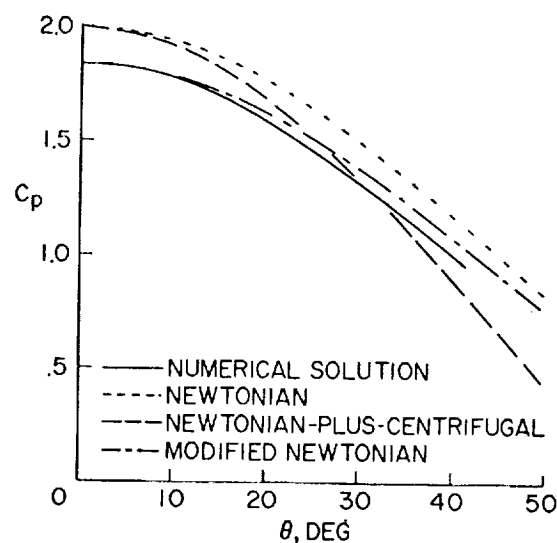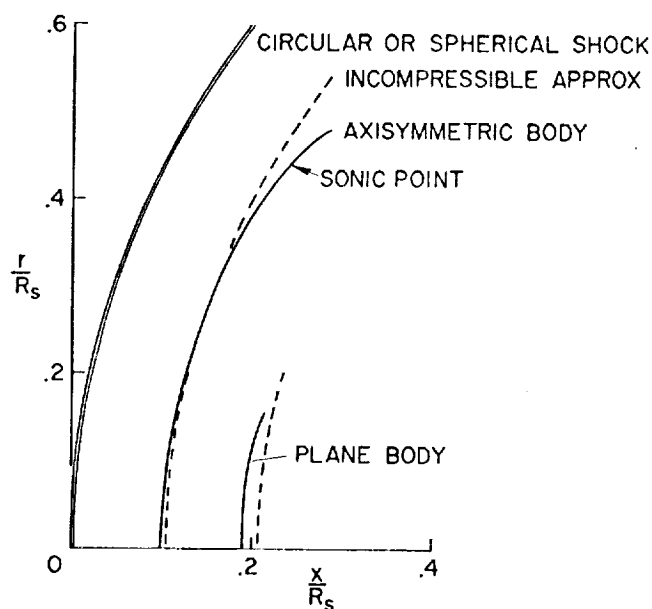




(b) Sphere.

FIG. 5. Surface pressure distributions at $M = \infty$, $\gamma = 7/5$.
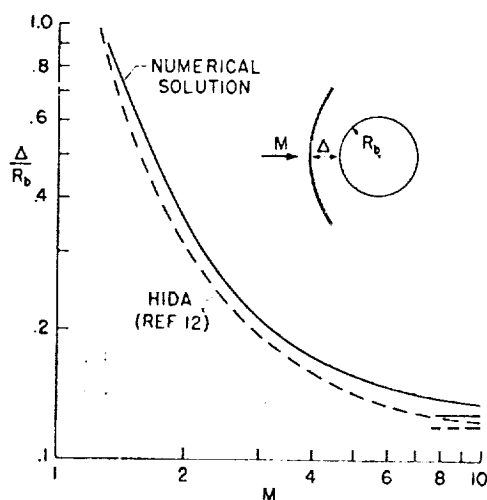


FIG. 4. Accuracy of incompressible approximation. (a) Plane and axisymmetric bodies that support circular and spherical shock at $M = \infty$, $\gamma = 7/5$. (b) Standoff distance of shock from sphere with $\gamma = 7/5$.
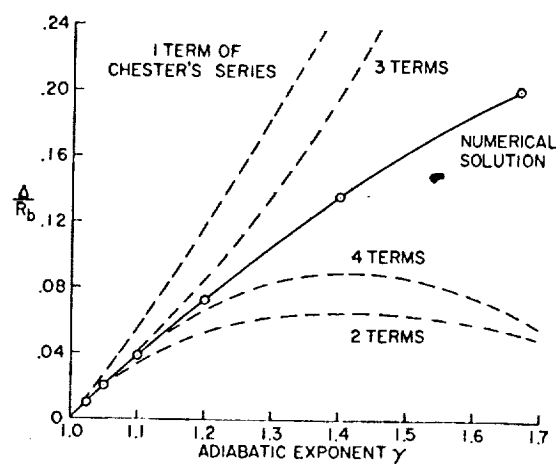


FIG. 6. Variation with $\gamma$ of standoff distance for bodies that support paraboloidal shock at $M = \infty$.

gases $\gamma$ does not exceed 1.67; but it is clearly not useful for $\gamma$ above 1.1. In the same note it was shown how, by comparison with the model, the convergence of Chester's series for the standoff distance can apparently be accelerated. Thus at $\gamma = 1.667$ in the example of Fig. 6, five terms of the modified series give $\Delta R_b = 0.198$, which differs from the accurate numerical result by only 4 per cent. The convergence of the series is even worse for surface pressure, and there no useful modification has been found.

## (2)  DESCRIPTION OF NUMERICAL METHOD

The preceding survey shows that none of the existing analytic treatments is adequate for calculating the details of flow near a blunt nose. One must turn instead to numerical solution of the full equations. A relatively simple numerical scheme will be described which has been programed for a medium-sized electronic computer.

### (2.1)  Coordinate System

It is convenient to assume a family of detached shock waves of known shape. The resulting simplification more than offsets the disadvantage of having to accept whatever body shapes result. Another possible objection will be dealt with in section (3.4). Schlieren pictures show that the shocks produced by simple shapes such as spheres, paraboloids, and ellipsoids (or their plane counterparts) are themselves nearly conic sections. Accordingly, the present method has been applied to the family of plane and axisymmetric bodies that support detached shock waves described by conic sections—hyperbola, parabola, prolate ellipse, circle, or oblate ellipse. It could, however, be extended to other analytic shock shapes.

In Cartesian coordinates originating from its vertex (Fig. 7), any conic section is described by

$$r^2 = 2Rx - Bx^2 \qquad (1)$$

Here $R$ is the nose radius, and $B$ the bluntness, which is a convenient parameter that characterizes the eccentricity of the conic section. (The bluntness $B$ is $b^2/a^2$ for an ellipse but $-b^2/a^2$ for a hyperbola.) As shown in Fig. 8, the bluntness is zero for a parabola, negative for hyperbolas, positive for ellipses, and unity for a circle.

It is advantageous to choose a natural coordinate system that contains the shock wave as one of its surfaces. The conventional hyperbolic, parabolic, elliptic, and polar coordinates are unsatisfactory because their definition changes at $B = 0$ and again at $B = 1$ whereas conic sections clearly form a single continuously varying family. A suitable unified orthogonal system that covers the entire range is introduced by setting

$$\left. \begin{aligned} x &= (R/B_s) \left[ 1 - \sqrt{(1 - B_s\xi^2)(1 - B_s + B_s\eta^2)} \right] \\ r &= R\xi\eta \end{aligned} \right\} \quad (2)$$

The shock wave of bluntness $B_s$ is described by $\eta = 1$; the downstream axis by $\eta = 0$; and the upstream axis

by $\xi = 0$ (Fig. 7). Special cases are

$$x/R = (1/2)(1 + \xi^2 - \eta^2), \quad \text{for parabola } (B_s = 0)$$

$$x/R = 1 - \sqrt{1 - \xi^2}\eta, \quad \text{for circle } (B_s = 1)$$

For ellipses, Eq. (2) gives only the left half which is the part that may form a shock wave. The right half of the ellipse is obtained by taking a plus instead of a minus sign ahead of the radical in Eq. (2).

In this coordinate system the line element is given by

$$ds^2 = h_1^2 d\xi^2 + h_2^2 d\eta^2 + \nu h_3^2 d\varphi^2 \qquad (3a)$$

where $\nu = 0$ for plane flow and $\nu = 1$ for axisymmetric flow, so that the last term (involving the azimuthal angle $\varphi$) appears only in the latter case, and

$$h_1^2 = (C\xi^2 + \eta^2)/(1 - B_s\xi^2),$$

$$h_2^2 = (C\xi^2 + \eta^2)/(C + B_s\eta^2), \quad h_3^2 = \xi^2\eta^2 \qquad (3b)$$

where $C \equiv 1 - B_s$.

### (2.2)  Equations of Motion

Let $\vec{V}$ be the velocity referred to the free-stream speed $V_\infty$, $\rho$ the density referred to its free-stream value $\rho_\infty$, and $p$ the pressure referred to $\rho_\infty V_\infty^2$. Then the
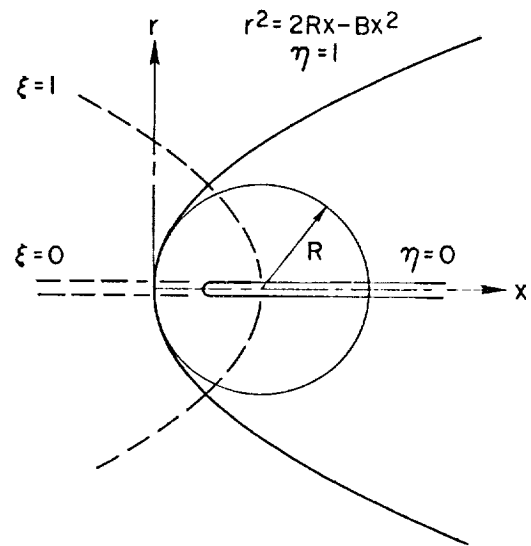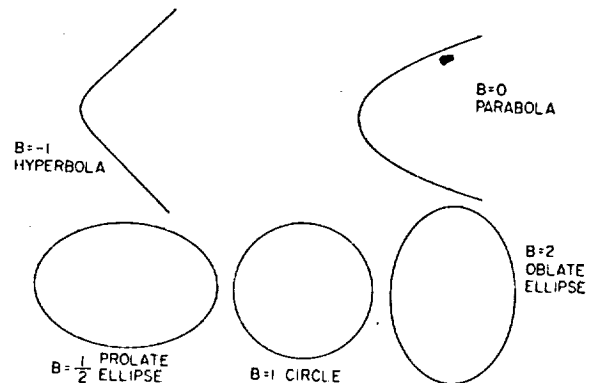


FIG. 7.  Coordinates for conic section.



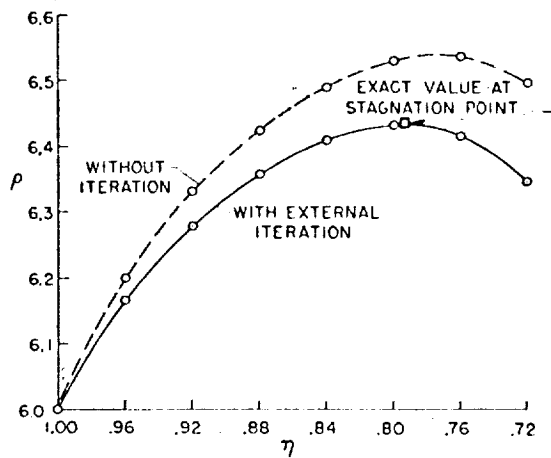FIG. 8.  Conic sections of varying bluntness.

Fig. 9. Variation of density along axis behind parabolic shock wave at $M = \infty$, $\gamma = 7/5$.

equations of continuity, motion, and energy are, in vector form,

$$\operatorname{div}(\rho \vec{V}) = 0, \quad \rho(\vec{V} \cdot \operatorname{grad}) \vec{V} + \operatorname{grad} p = 0,$$

$$\vec{V} \cdot \operatorname{grad}(p/\rho^\gamma) = 0 \quad (4)$$

where $\gamma$ is the adiabatic exponent. Transforming these to the $(\xi, \eta)$ coordinate system (using Eq. (3), and dropping the subscript on $B_s$ for simplicity) gives

$$[(\xi\eta)^\nu \sqrt{(C\xi^2 + \eta^2)}\,(C + B\eta^2)\rho u]_\xi +$$
$$[(\xi\eta)^\nu \sqrt{(C\xi^2 + \eta^2)}\,(1 - B\xi^2)\rho v]_\eta = 0 \;\Big\}$$

$$\rho\big(uu_\xi - [C\xi v^2/(C\xi^2 + \eta^2)] +$$
$$\sqrt{(C + B\eta^2)/(1 - B\xi^2)}\; v\{u_\eta +$$
$$[\eta u'/(C\xi^2 + \eta^2)]\}\big) + p_\xi = 0 \;\Bigg\} \quad (5)$$

$$\rho\big(vv_\eta - [\eta u^2/(C\xi^2 + \eta^2)] +$$
$$\sqrt{(1 - B\xi^2)/(C + B\eta^2)}\; u\{v_\xi +$$
$$[C\xi v'/(C\xi^2 + \eta^2)]\}\big) + p_\eta = 0 \;\Big\}$$

$$u\sqrt{1 - B\xi^2}\,(p/\rho^\gamma)_\xi +$$
$$v\sqrt{C + B\eta^2}\,(p/\rho^\gamma)_\eta = 0 \;\Big\}$$

where $u$, $v$ are the components of $\vec{V}$ in the $\xi$, $\eta$ directions.

The first (continuity) equation is satisfied by introducing the stream function $\Psi$ according to

$$\Psi_\eta = (\xi\eta)^\nu \sqrt{(C\xi^2 + \eta^2)/(C + B\eta^2)}\rho u \;\Bigg\}$$
$$\Psi_\xi = -(\xi\eta)^\nu \sqrt{(C\xi^2 + \eta^2)/(1 - B\xi^2)}\rho v \;\Bigg\} \quad (6)$$

Then the last (energy) equation simply states that

$$p = \rho^\gamma f(\Psi) \quad (7)$$

Using this to eliminate the pressure from the equations of motion gives

$$\Psi_\xi\Psi_{\xi\eta} - \Psi_\eta\Psi_{\xi\xi} - \Psi_\xi\{\Psi_\xi[(\rho_\eta/\rho) + (\nu/\eta)] - \Psi_\eta[(\rho_\xi/\rho) + (\nu/\xi)]\} - [\eta/(C\xi^2 + \eta^2)]\,\{\Psi_\xi^2 +$$
$$[(C + B\eta^2)/(1 - B\xi^2)]\Psi_\eta^2\} + [B\xi/(1 - B\xi^2)]\Psi_\xi\Psi_\eta +$$
$$(\xi^2\eta^2)^\nu\,[(C\xi^2 + \eta^2)/(1 - B\xi^2)]\,(\gamma\rho^\gamma f\rho_\eta + \rho^{\gamma+1}f'\Psi_\eta) = 0 \;\Bigg\}$$

$$\Psi_\eta\Psi_{\xi\eta} - \Psi_\xi\Psi_{\eta\eta} + \Psi_\eta\{\Psi_\xi[(\rho_\eta/\rho) + (\nu/\eta)] - \Psi_\eta[(\rho_\xi/\rho) + (\nu/\xi)]\} - [C\xi/(C\xi^2 + \eta^2)] \times \;\Bigg\} \quad (8)$$
$$\{[(1 - B\xi^2)/(C + B\eta^2)]\Psi_\xi^2 + \Psi_\eta^2\} - [B\eta/(C + B\eta^2)]\Psi_\xi\Psi_\eta +$$
$$(\xi^2\eta^2)^\nu\,[(C\xi^2 + \eta^2)/(C + \beta\eta^2)]\,(\gamma\rho^\gamma f\rho_\xi + \rho^{\gamma+1}f'\Psi_\xi) = 0 \;\Bigg\}$$

### (2.3) Initial Conditions

Values of $u$, $v$, $p$, $\rho$ just behind the shock wave (at $\eta = 1$) are found from the oblique shock relations—e.g., reference 37—in terms of the slope of the bow wave, $\sqrt{1 - B\xi^2}/\xi$. Expressed in terms of the stream function, these give the initial conditions

$$\rho = (\gamma + 1)M^2(1 - B\xi^2)/[2(1 + C\xi^2) + \;\Big\}$$
$$(\gamma - 1)M^2(1 - B\xi^2)], \;\Bigg\} \quad (9)$$
$$\Psi = \xi^{1+\nu}/(1 + \nu), \quad \Psi_\eta = \rho\xi^{1+\nu}, \quad \text{at } \eta = 1 \;\Big\}$$

and for the function $f(\Psi)$

$$f(\Psi) = \frac{2\gamma M^2(1 - Bs^2) - (\gamma - 1)(1 + Cs^2)}{\gamma(\gamma + 1)M^2(1 + Cs^2)} \times$$
$$\left[\frac{2(1 + Cs^2) + (\gamma - 1)M^2(1 - Bs^2)}{(\gamma + 1)M^2(1 - Bs^2)}\right]^\gamma, \quad s^2 = [(1 + \nu)\Psi]^{2/(1+\nu)} \quad (10)$$

### (2.4) Form of Problem for Numerical Computation

For numerical work it is advantageous to use $(1 + \nu)\Psi/\xi^{1+\nu}$, which is constant on the shock and elsewhere more nearly independent of $\xi$ than is $\Psi$ and vanishes only on the body rather than also on the axis of symmetry. Hence set

$$\Psi(\xi, \eta) = [\xi^{1+\nu}/(1 + \nu)]\omega(\xi, \eta) \quad (11)$$

Then the initial conditions become

$$\rho = (\gamma + 1)M^2(1 - B\xi^2) / [2(1 + C\xi^2) + (\gamma - 1)M^2(1 - B\xi^2)], \quad \omega = 1, \quad \omega_\eta = (1 + \nu)\rho, \quad \text{at } \eta = 1 \quad (12)$$

and the equations of motion

$$\left[\gamma\left(\rho^{\gamma+1}f\eta^{2\nu}\frac{C\xi^2 + \eta^2}{1 - B\xi^2}\right) - \left(\omega + \frac{\xi\omega_\xi}{1 + \nu}\right)^2\right]\frac{\rho_\eta}{\rho} = \frac{\omega_\eta}{1 + \nu}\left[\frac{2 + \nu}{1 + \nu}\xi\omega_\xi - \left(\omega + \frac{\xi\omega_\xi}{1 + \nu}\right)\left(\frac{B\xi^2}{1 - B\xi^2} + \frac{\xi\rho_\xi}{\rho}\right) + \frac{\xi^2\omega_{\xi\xi}}{1 + \nu}\right] - $$

$$\left(\omega + \frac{\xi\omega_\xi}{1 + \nu}\right)\left(\omega_\eta + \frac{\xi\omega_{\xi\eta}}{1 + \nu}\right) + \frac{\nu}{\eta}\left(\omega + \frac{\xi\omega_\xi}{1 + \nu}\right)^2 + \frac{\eta}{C\xi^2 + \eta^2}\left[\left(\omega + \frac{\xi\omega_\xi}{1 + \nu}\right)^2 + \frac{C + B\eta^2}{1 - B\xi^2}\left(\frac{\xi\omega_\eta}{1 + \nu}\right)^2\right] - $$

$$\left(\rho^{\gamma+1}f\eta^{2\nu}\frac{C\xi^2 + \eta^2}{1 - B\xi^2}\right)\left(\xi^{\nu-1}\frac{f'}{f}\right)\frac{\omega_\eta}{1 + \nu}\xi^2 \quad (13a)$$

$$\left(\omega + \frac{\xi\omega_\xi}{1 + \nu}\right)\left(\omega_{\eta\eta} - \omega_\eta\frac{\rho_\eta}{\rho}\right) = \omega_\eta\left[\frac{\omega_\eta + \xi\omega_{\xi\eta}}{1 + \nu} + \left(\frac{\nu}{\eta} - \frac{B\eta}{C + B\eta^2}\right)\left(\omega + \frac{\xi\omega_\xi}{1 + \nu}\right) - \frac{\omega_\eta}{1 + \nu}\frac{\xi\rho_\xi}{\rho}\right] - $$

$$(1 + \nu)C\frac{1 - B\xi^2}{C\xi^2 + \eta^2}\left[\frac{1 - B\xi^2}{C + B\eta^2}\left(\omega + \frac{\xi\omega_\xi}{1 + \nu}\right)^2 + \left(\frac{\xi\omega_\eta}{1 + \nu}\right)^2\right] + (1 + \nu)\rho^{\gamma+1}f\eta^{2\nu}\frac{C\xi^2 + \eta^2}{C + B\eta^2}\left[\gamma\frac{\rho_\xi}{\xi\rho} + \xi^{\nu-1}\frac{f'}{f}\left(\omega + \frac{\xi\omega_\xi}{1 + \nu}\right)\right] \quad (13b)$$

where
$$f = \frac{2\gamma M^2(1 - Bs^2) - (\gamma - 1)(1 + Cs^2)}{\gamma(\gamma + 1)M^2(1 + Cs^2)}\left[\frac{2(1 + Cs^2) + (\gamma - 1)M^2(1 - Bs^2)}{(\gamma + 1)M^2(1 - Bs^2)}\right]^\gamma, \quad s^2 = \xi^2\omega^{2/(1+\nu)} \quad (13c)$$

## (2.5) Numerical Integration

The initial value problem of Eqs. (12) and (13) has been solved numerically by forward integration from the shock wave ($\eta = 1$) toward smaller values of $\eta$. Over each interval ($\Delta\eta$), $\rho$ and $\omega_\eta$ are extrapolated linearly. At each new value of $\eta$ the $\xi$-derivatives are evaluated by 11-point numerical differentiation.[38] The procedure may be summarized as follows:

(0) Calculate initial values at $\eta = 1$ from Eq. (12).

(1) Calculate $\xi$-derivatives $\rho_\xi$, $\omega_\xi$, $\omega_{\xi\xi}$, $\omega_{\xi\eta}$ by 11-point numerical differentiation.

(2a) Calculate $\rho_\eta$ from Eq. (13a).

(2b) Calculate $\omega_{\eta\eta}$ from Eq. (13b).

(3a) Extrapolate $\rho$ and $\omega_\eta$ linearly to next smaller value of $\eta$:

$$\rho^{(m+1)} = \rho^{(m)} - (\Delta\eta)\rho_\eta^{(m)}, \quad \omega_\eta^{(m+1)} = \omega_\eta^{(m)} - (\Delta\eta)\omega_{\eta\eta}^{(m)}$$

(3b) Extrapolate $\omega$ using averaged value of $\omega_\eta$:

$$\omega^{(m+1)} = \omega^{(m)} - (1/2)(\Delta\eta)(\omega_\eta^{(m)} + \omega_\eta^{(m+1)})$$

(4) Repeat steps (1) to (4) at new value of $\eta$ and continue until $\omega$ is negative.

After completion of the integration, the accuracy of $\rho$ (and hence of $p$) can be greatly increased by recomputing it using the averaged value of $\rho_\eta$ over each interval $\Delta\eta$, so that the value after the $m$th step is given by

$$\rho^{(m)} = \rho^{(0)} - (\Delta\eta)[(1/2)\rho_\eta^{(0)} + \rho_\eta^{(1)} + \rho_\eta^{(2)} + $$
$$\ldots + \rho_\eta^{(m-1)} + (1/2)\rho_\eta^{(m)}] \quad (14)$$

Fig. 9 shows in a typical case the improvement obtained from this "external iteration."

This procedure has been coded for machine computation on the IBM 650 electronic digital computer with floating decimal attachment. For each value of $\eta$ the flow quantities are calculated at the 20 equally spaced values $\xi = (n + 1/2)(\Delta\xi)$, $0 \le n \le 19$, which straddle the axis of symmetry $\xi = 0$ in order to avoid the indeterminate form $\rho_\xi/\xi\rho$ in Eq. (13). The mesh

dimensions $\Delta\xi$ and $\Delta\eta$ are arbitrary (but equal for all steps). One prescribes the parameters

| | | |
|---|---|---|
| $M$ | = | free-stream Mach Number |
| $B_s$ | = | bluntness of conic section describing shock |
| $\nu$ | = | 0 for plane, 1 for axisymmetric flow |
| $\gamma$ | = | adiabatic exponent |
| $\Delta\xi$, $\Delta\eta$ | = | mesh dimensions |

Flow variables (and their $\eta$-derivatives) are printed for each mesh point. The body shape and surface pressures can then be found by interpolation. Machine computing time is $1\frac{1}{4}$ minutes per value of $\eta$. It will be seen that 4 to 8 steps in $\eta$ yield ample accuracy so that a typical case requires 5 to 10 minutes computing time.

## (2.6) Instability

In the subsonic region the initial value problem is unstable. This means that small errors (such as arise from rounding to the 8 significant figures used) grow in geometric progression. The instability has been tested in a typical case by perturbing the initial data, changing $\omega$ from 1.000 0000 to 1.000 0010 at the point on the shock wave nearest to the axis (where the equation is most elliptic and hence most unstable). Fig. 10 shows that in 11 steps (last step interpolated) from shock to body a unit error grows by a factor of 160. This means that rounding errors of $\pm1/2$ in the last place can amplify to invalidate no more than 2 of the 8 significant figures used. Near the stagnation point the error grows by a factor of about 3 in each step. (This may be compared with the maximum factor of 5.8284 for Laplace's equation in a semi-infinite domain.[39]) Hence the error would swamp all 8 significant figures if it were necessary to take as many as 24 steps from shock to body. Fortunately, many fewer steps than even 11 suffice, so that instability is of no practical concern.

Another type of instability peculiar to the particular differentiation scheme used is more serious and, in practice, limits the downstream extent of flow field that can be calculated. The 11-point differentiation scheme uses central differences where possible, but the largest 5 values of $\xi$ must use progressively more noncentral schemes. These involve large differences of small numbers and so produce instability which is more severe in the hyperbolic than the elliptic region. It eventually causes oscillations of flow variables for the highest few values of $\xi$, and stops the computation by producing negative values of $\rho$. This difficulty has been alleviated by using 7- and 5-point differentiation schemes at the highest two values of $\xi$. It is to be entirely eliminated by recoding the program to use only central-difference schemes, starting with more values of $\xi$ and dropping the highest 5 in each step in $\eta$.

A second imperfection in the present procedure appears when the factor $\{\omega + [\xi\omega_\xi{}'(1 + \nu)]\}$ in Eq. (13) vanishes, leading to a singularity in $\omega_{\eta\eta}$. This can happen only inside the body (for $\omega < 0$) but, because of the instability illustrated in Fig. 10, its effect occasionally spreads so rapidly as to affect the actual flow field.

### (2.7) Accuracy Comparison With Garabedian-Lieberstein Method

The accuracy of the numerical method has been tested both internally, by refining the mesh size, and externally, by comparing with experiment and with the numerical procedure of Garabedian and Lieberstein.[29]

The Garabedian-Lieberstein method is like that proposed here in starting from a given analytic shock shape (and conic sections were actually used) and solving the initial-value problem with electronic computers. It differs in that it avoids the instability in the subsonic region by continuing the initial data analytically into a fictitious third dimension where the equation is hyperbolic rather than elliptic. The solution is carried out by the numerical method of characteristics on a number of planes in the fictitious three-dimensional space that intersect the real physical plane along curved lines. Thanks to known uniqueness proofs for the numerical method of characteristics, the Garabedian-Lieberstein method possesses a degree of mathematical rigor seldom attained in aerodynamic research.

The price paid for eliminating instability is a large increase in the computing time (and cost) compared with the present method. Also the solution is artificially restricted to the subsonic region (though another solution can be carried out for the supersonic region).

It can be shown that the present procedure converges as the mesh size is refined, despite its instability. Indeed, it differs only in degree from any stable numerical procedure, in which one must strike a balance between the truncation error resulting from too few steps and the round-off error resulting from too many; here the accumulated error simply grows in geometric rather than arithmetic progression. What is lacking is a proof that the solution to which the present method converges is the correct one. (The question of whether a real body exists for any given shock wave is an open question in either method.) However, it reproduces the results of the Garabedian-Lieberstein method to four significant figures, as shown for one case in Figs. 11 and 12. Fig. 12 indicates that the present method is the more accurate near the sonic line.

In general, as in the example of Fig. 11, four to six steps in $\eta$ along the axis are found to yield the standoff distance correct to within 1 per cent, with comparable accuracy in the other flow quantities. It was thought worthwhile to carry out the solutions discussed below only to this standard of accuracy.

### (3) EXAMPLES AND DISCUSSION

Some 50 examples have been calculated, covering a wide range of shock bluntness, Mach Number, and $\gamma$ in both plane and axisymmetric flow. Only axisymmetric flow will be considered henceforth as being of more practical interest. A complete compilation of both plane and axisymmetric solutions will be issued later as an NACA publication by the writer and Helen Gordon, who carried out the coding and machine computation.*

### (3.1) The Family of Bodies

At each Mach Number (and $\gamma$) the family of conic-section shock waves leads to a one-parameter family of bodies. Fig. 13 shows various members of the family for $M = \infty$. The downstream extent of the body was limited in each case by the end instability discussed in section (2.6), which could be eliminated.

Except possibly for the very bluntest, the bodies can all be accurately described by conic sections back at least to the sonic point or limiting characteristic. Thereafter the solution could be continued, or modified, by the method of characteristics. However, it is a virtue of the present method that it gives the subsequent shape. The sonic line and the change of type from elliptic to hyperbolic play no significant role. From this point of view it may be said that the blunt-body problem is not a transonic problem.

### (3.2) Comparison With Experiments on Spheres

Because the bodies are found all to be represented closely by conic sections, it is possible to consider a fixed shape over a range of Mach Numbers. Enough experience has been accumulated at $\gamma = 7/5$ that a desired body can be produced in one or two attempts. Thus the sphere has been solved for a number of Mach Numbers from 1.30 to $\infty$ (and values closer to 1 would offer even less difficulty). The standoff distance is compared in Fig. 14 with experimental results from references 40 to 44. The surface pressure distribution is compared in Fig. 15 with experiments at $M = 1.30$ (reference 45) and $M = 5.8$ (reference 41).

---

* We are indebted to Marcelline Chartz for continued guidance through the mysteries of machine computation.

|      |      |      |      |      |      |      | .16  | 1.8  | STOP |
|------|------|------|------|------|------|------|------|------|------|
|      |      |      |      |      |      |      | -.05 | .27  | -1.9 |
|      |      |      |      |      |      |      | .01  | 0    | -.55 |
|      |      |      |      |      |      |      | -.01 | 0    | .47  |
|      |      |      |      |      |      |      | .01  | .01  | -.20 |
|      |      |      |      |      |      |      | 0    | -.01 | .21  |
|      |      |      |      |      |      |      | 0    | .03  | -.50 |
|      |      |      |      |      |      |      | -.01 | -.15 | .15  |
|      |      |      |      |      |      |      | -.04 | .17  | 1.8  |
|      |      |      |      |      |      | -.01 | .10  | -.97 | -3.3 |
|      |      |      |      |      |      | .02  | .02  | -.55 | 1.5  |
|      |      |      |      |      |      | 0    | -.11 | .30  | 1.1  |
|      |      |      |      |      | .02  | 0    | -.01 | .09  | -.07 | -1.8 |
|      |      |      |      | .01  | -.01 | 0    | .03  | -.03 | .22  | 3.8 |
|      |      |      |      | 0    | 0    | -.04 | .05  | -.13 | -.10 |
|      |      |      |      | -.01 | -.03 | -.02 | -.35 | -1.8 | 9.0  |
| .01  | .02  | .02  | .02  | .05  | .16  | .25  | 1.0  | 5.9  | 29   |
| 0    | -.01 | -.01 | .04  | .14  | .37  | 1.3  | .24  | 11   | 20   |
| .01  | .02  | .03  | -.11 | -.60 | -1.7 | -4.5 | -12  | -33  | -141 |
| 1.0  | .97  | .93  | .89  | .26  | -1.4 | -5.8 | -18  | -46  | -120 | -320 |

SHOCK WAVE    AXIS OF SYMMETRY    NOSE OF BODY    $\eta$

FIG. 10. Growth of unit error along axis behind parabolic detached shock wave at $M = \infty$, $\gamma = 7/5$.



FIG. 11. Variation with mesh size of standoff distance for body that supports hyperboloidal shock wave asymptotic to Mach cone at $M = 5.8$, $\gamma = 7/5$.



FIG. 12. Surface pressure distribution over body that supports hyperboloidal shock wave asymptotic to Mach cone at $M = 5.8$, $\gamma = 7/5$.



FIG. 13. Family of axisymmetric bodies that support detached shock waves of conic-section shape at $M = \infty$, $\gamma = 7/5$ (drawn for equal shock radii $R_s$).



FIG. 14. Standoff distance for sphere in air.



(a) $M = 1.30$



(b) $M = 5.8$

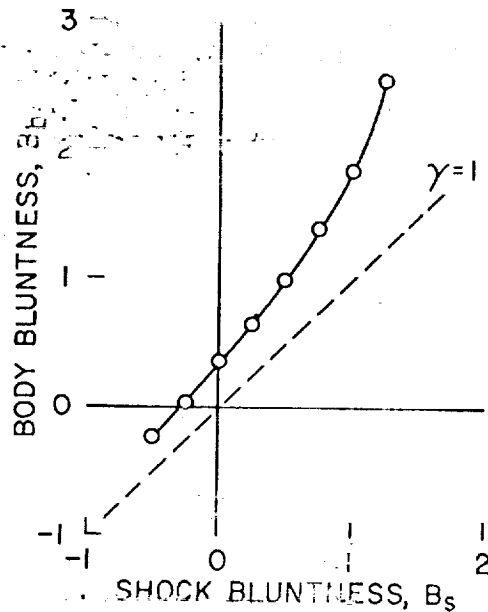FIG. 15. Pressure distribution on sphere in air.

FIG. 16. Variation of body bluntness with shock wave bluntness at $M = \infty$, $\gamma = 7/5$.

### (3.3) Comparison With Other Numerical Methods

After developing the present numerical procedure, the author learned of two other independent treatments by essentially the same method. Priority clearly goes to K. Mangler, of the Royal Aircraft Establishment, although his work is not yet published.* At a meeting in Holland in June 1957, he reported a hand computation of the plane flow behind a parabolic shock wave at $M = 7$ (with $\gamma = 7/5$). The body was found to be circular within half a per cent to behind the sonic line (in conformity with results of the present method) and was continued to a semicircle by the numerical method of characteristics.

More recently, Zlotnick and Newman[30] have applied a similar procedure to the spherical shock wave at several high Mach Numbers. The accuracy of their examples is low (the pressure at the stagnation point being off by some 3 per cent and the standoff distance low by 10 per cent), at least partly because the thickness of the layer between shock and body is neglected at one point. They apparently attempt to suppress the instability by filtering out high harmonics (which are the most unstable). The present author believes such attempts to be dangerous as well as unnecessary.

In contrast with these indirect methods (that start from an assumed shock wave), Belotserkovsky[31] and Uchida and Yasuhara[32] have described methods for solving the direct problem of a given body. Following the so-called integral method of Dorodnitsyn, Belotserkovsky divides the layer between shock and body into $n$ strips (2 or 3 in practice) across each of which the flow variables are approximated by polynomials. Integrating the equations of motion analytically across

* ADDENDUM: Mangler's work is now available in: Mangler, K. W., and Evans, M. E., *The Calculation of the Inviscid Flow Between a Detached Bow Wave and a Body*, R.A.E. Tech. Note Aero 2536, October, 1957.

the various strips yields a system of ordinary differential equations that are integrated on an electronic digital computer. As in the Garabedian-Lieberstein method, the sonic line assumes a spurious significance which necessitates special treatment in its vicinity. Belotserkovsky has published results for a circular cylinder at $M = 3, 4, 5$ (with $\gamma = 7/5$) which agree well with those from the present method; and it would seem reasonable to assume that he has also considered more practical axisymmetric bodies.

Uchida and Yasuhara have given a very tedious method of successive approximations which does not seem suited to machine computation. Their one published example of a circular cylinder at $M = 2$ ($\gamma = 7/5$) agrees fairly well with results from the present method.

### (3.4) Shock Insensitivity

An objection sometimes raised against the inverse method of starting from an assumed shock wave is that its shape is insensitive to changes in the body shape. A near nonuniqueness is implied according to which essentially the same shock wave would correspond to various bodies. However, no such difficulty exists within the family of shapes considered here. Fig. 16 shows that for shapes sharper than a parabola the
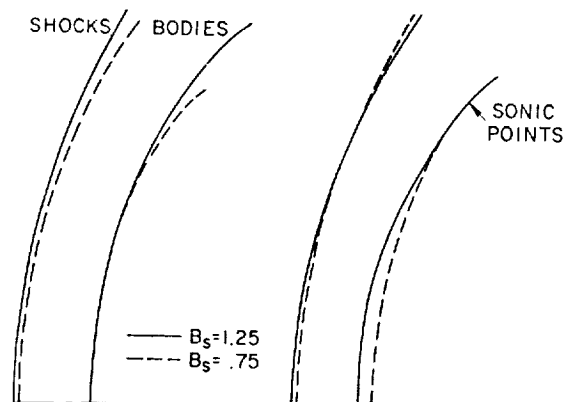


FIG. 17. Axisymmetric bodies at $M = \infty$, $\gamma = 7/5$ matched with same nose radius and with same sonic point.
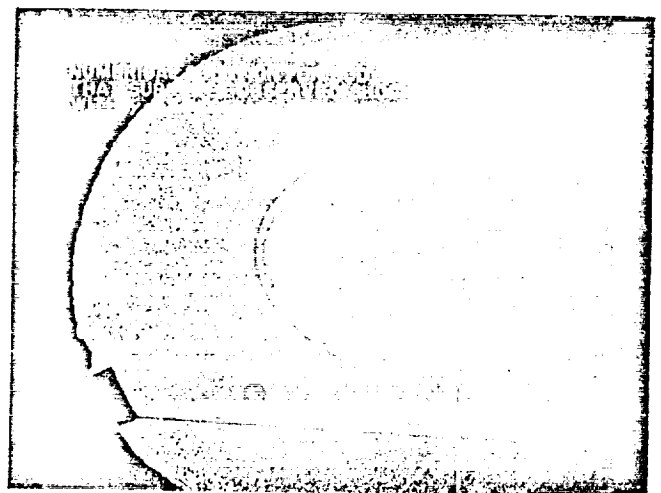


FIG. 18. Result of trying constant effective $\gamma$ to simulate real gas effects, $M = 14.2$.

hardness of shock and body change at the same rate; and although the shock insensitivity increases for blunter shapes, it by no means approaches infinite slope which would imply complete insensitivity.

### (3.5) Shoulder Choking

Increasing shock insensitivity for blunt bodies is related to the phenomenon of shoulder choking pointed out by Busemann[16] and Hayes.[18] According to this, the standoff distance and the shock shape in the subsonic region are determined mainly by the shape of the body near the sonic point. This is illustrated in Fig. 17 by superposing first the vertices and then the sonic points of two different bodies. The effect would become even more pronounced for blunter shapes (and in plane flow).

### (3.6) Possibility of Treating Real Gases

The present numerical method is suitable for the inclusion of real gas effects assuming equilibrium thermodynamics. Hand calculation would probably be necessary if the standard tables were to be used, but they could be approximated analytically for purposes of machine computation.

Several investigators have suggested the use of a constant effective $\gamma$ to account roughly for real gas effects. This idea was tested by starting from the observed shock for a hemisphere flying at $M = 14.2$ (reference 17), which clearly involves significant gas imperfections, and attempting to reproduce the body. The observed standoff distance is obtained by choosing $\gamma = 1.35$ which according to section (3.5) must be the effective value in the vicinity of the sonic line. Fig. 18 shows that the body shape is then closely reproduced. At least in this case of mild gas imperfections, the idea shows promise.

### REFERENCES

*Potential Flow Approximations*

[1] Laitone, Edmund V., and Pardee, Otway O'M., *Location of Detached Shock Wave in Front of a Body Moving at Supersonic Speeds*, NACA RM A7B10, 1947.

[2] Nagamatsu, Henry T., *Theoretical Investigation of Detached Shock Waves*, GALCIT Pub., 1949.

[3] Kawamura, T., *On the Detached Shock Wave in Front of a Body Moving at Speeds Greater Than That of Sound*, Univ. of Kyoto, College of Science, Memoirs, Ser. A, Vol. XXVI, No. 3, pp. 207–232, 1950.

[4] Heybey, W. H., *Shock Distances in Front of Symmetrical Bodies*, NAVORD Rep. 3594, December 24, 1953.

*Taylor Series Expansions From Shock*

[5] Lin, C. C., and Rubinov, S. I., *On the Flow Behind Curved Shocks*, J. Math. and Phys., Vol. 27, No. 2, pp. 105–129, July, 1948.

[6] Dugundji, John, *An Investigation of the Detached Shock in Front of a Body of Revolution*, Journal of the Aeronautical Sciences, Vol. 15, No. 12, pp. 699–705, December, 1948.

[7] Lin, C. C., and Shen, S. F., *An Analytic Determination of the Flow Behind a Symmetrical Curved Shock in a Uniform Stream*, NACA TN 2506, 1951.

[8] Meßkus, H., *Über den abgelösten Verdichtungsstoss*, Ingenieur-Archiv, Vol. 19, No. 3, pp. 208–227, 1951.

[9] Cabannes, M. Henri, *Contribution a l'étude théorique des fluides compressibles, Écoulements transsoniques, Ondes de choc*. Chapitre III. Étude de l'onde de choc détachée au voisinage de son sommet. École Normale Superieure, Annales Scientifique, Ser. 3, Vol. 69, pp. 31–46, 1952.

[10] Cabannes, Henri, *Détermination théorique de l'écoulement d'un fluide derrière une onde de choc détachée*, ONERA note technique no. 5, 1951.

[11] Cabannes, H., *Tables pour la détermination des ondes de choc détachées*, La Recherche Aéronautique, No. 49, pp. 11–15, Jan.-Feb., 1956.

*Incompressible Approximations*

[12] Hida, Kinzo, *An Approximate Study on the Detached Shock Wave in Front of a Circular Cylinder and a Sphere*, J. Phys. Soc. of Japan, Vol. 8, No. 6, pp. 740–745, Nov.-Dec., 1953. (Also Vol. 10, No. 1, pp. 79–81, January, 1955.)

[13] Lighthill, M. J., *Dynamics of a Dissociating Gas, Part I, Equilibrium Flow*, J. Fluid Mech., Vol. 2, Pt. 1, pp. 1–32, January, 1957.

[14] Whitham, G. B., *A Note on the Stand-Off Distance of the Shock in High Speed Flow Past a Circular Cylinder*, Comm. on Pure and Applied Math., Vol. 10, No. 4, pp. 531–535, November, 1957.

[15] Hayes, W. D., *Constant-Density Solutions*. Circular Cylinder. Ch. 4 of Hypersonic Flow Theory, by Hayes, Wallace D., and Probstein, Ronald F.; Academic Press. (To be published).

*Newtonian Approximations and Improvements Thereon*

[16] Busemann, A., *Flüssigkeits und Gasbewegung*, Second Ed., pp. 275–277; Handwörterbuch der Naturwissenschaften, Gustav Fischer, Jena, 1933.

[17] Ivey, H. Reese, Klunker, E. Bernard, and Bowen, Edward N., *A Method for Determining the Aerodynamic Characteristics of Two- and Three-Dimensional Shapes at Hypersonic Speeds*, NACA TN 1613, 1948.

[18] Hayes, Wallace D., *Some Aspects of Hypersonic Flow*, Ramo-Wooldridge Corp., January 4, 1955.

[19] Hayes, Wallace D., *Hypersonic Flow Fields at Small Density Ratio*, Ramo-Wooldridge Corp., May 12, 1955.

[20] Serbin, H., *Hypersonic, Non-Viscous Flow Around A Circular Disk Normal to the Stream*, RM-1713, Rand Corp., May 3, 1956.

[21] Serbin, H., *Hypersonic, Non-Viscous Flow Around a Sphere*, RM-1772, Rand Corp., August 13, 1956.

[22] Probstein, Ronald F., *Inviscid Flow in the Stagnation Point Region of Very Blunt-Nosed Bodies at Hypersonic Flight Speeds*, Brown Univ., Div. of Eng., September, 1956. (Also pub. as WADC TN 56-395, 1956.)

[23] Chester, W., *Supersonic Flow Past a Bluff Body With a Detached Shock, Part I: Two-Dimensional Body, Part II: Axisymmetrical Body*, J. Fluid Mech., Vol. 1, Pt. 4, pp. 353–365, October, 1956; Vol. 1, Pt. 5, pp. 490–496, November, 1956.

[24] Freeman, N. C., *On the Theory of Hypersonic Flow Past Plane and Axially Symmetric Bluff Bodies*, J. Fluid Mech., Vol. 1, Pt. 4, pp. 366–387, October, 1956.

[25] Li, Ting-Yi, and Geiger, Richard E., *Stagnation Point of a Blunt Body in Hypersonic Flow*, Journal of the Aeronautical Sciences, Vol. 24, No. 1, pp. 25–32, January, 1957.

*Explosion and Similarity Approximation*

[26] Lees, Lester, and Kubota, Toshi, *Inviscid Hypersonic Flow Over Blunt-Nosed Slender Bodies*, Journal of the Aeronautical Sciences, Vol. 24, No. 3, pp. 195–202, March, 1957.

[27] Cherny, G. G., *Hypersonic Flow Past an Aerofoil With a Slightly Blunted Leading Edge*, Doklady, Akad. Nauk SSSR, Vol. 114, No. 4, June, 1957 (Russian)

*Numerical Methods*

[28] Garabedian, P. R., *Numerical Construction of Detached Shock Waves*, J. Math. and Phys., Vol. 36, No. 3, pp. 192–205, October, 1957. See also: Lin, C. C., *Note on Garabedian's Paper "Numerical Construction of Detached Shock Waves,"* pp. 206–209.

[29] Garabedian, P. R., and Lieberstein, H. M., *On the Numerical Calculation of Detached Bow Shock Waves in Hypersonic Flow*, Journal of the Aeronautical Sciences, Vol. 25, No. 2, pp. 109–118, February, 1958.

[30] Zlotnick, Martin, and Newman, Donald J., *Theoretical Calculation of the Flow on Blunt-Nosed Axisymmetric Bodies in a Hypersonic Stream*, AVCO Mfg. Co., Rep. RAD-TR-2-57-29, September 19, 1957.

[31] Belotserkovsky, O. M., *Flow Past a Circular Cylinder With a Detached Shock Wave*, Doklady, Akad. Nauk SSSR, Vol. 113, No. 3, pp. 509–512, 1957 (Russian).

[32] Uchida, Shigeo, and Yasuhara, Michiru, *The Rotational Field Behind a Curved Shock Wave Calculated by the Method of Flux Analysis*, Journal of the Aeronautical Sciences, Vol. 23, No. 9, pp. 830–845, September, 1956.

**Other References**

[33] Courant, R., and Hilbert, D., *Methoden der Mathematischen Physik*, Vol. 2, p. 39; Julius Springer, Berlin, 1937. (Also pub. by N. Y. Univ. Inst. for Math. and Mech., 1950–1951; and pub. by Interscience Publishers, 1953. English text.)

[34] Van Dyke, M. D., *A Model of Supersonic Flow Past Blunt Axisymmetric Bodies, With Application to Chester's Solution*, J. Fluid Mech, Vol. 3, Pt. 5, pp. 515–522, February, 1958.

[35] Staff of the Computing Section (Under the direction of Zdeněk Kopal), *Tables of Supersonic Flow Around Cones*, Tech. Rep. No. 1, Center of Analysis, M.I.T., 1947.

[36] Lees, Lester, *Hypersonic Flow*, IAS Preprint No. 554, 1955. (Also C.I.T. pub. 404.)

[37] Ames Research Staff, *Equations, Tables, and Charts for Compressible Flow*, NACA Rep. 1135, 1953.

[38] Bickley, W. G., *Formulae for Numerical Differentiation*, Math. Gazette (London), Vol. 25, pp. 19–27, 1941.

[39] Hyman, Morton A., *Noniterative Numerical Solutions of Boundary-Value Problems*, Appl. Sci. Research, Vol. B2, No. 5, pp. 325–351, 1952. (Also pub. as NAVORD Rep. 1813, Aeroballistic Res. Rep. 26.)

[40] Heberle, Juergen W., Wood, George P., and Gooderum, Paul B., *Data on Shape and Location of Detached Shock Waves on Cones and Spheres*, NACA TN 2000, 1950.

[41] Oliver, Robert Earl, *An Experimental Investigation of Flow About Simple Blunt Bodies at a Nominal Mach Number of 5.8*, Journal of the Aeronautical Sciences, Vol. 23, No. 2, pp. 177–179, February, 1956. (Also available as GALCIT Pub. 386 and Memo 26, June 1955.)

[42] Crawford, Davis H., and McCauley, William D., *Investigation of the Laminar Aerodynamic Heat-Transfer Characteristics of a Hemisphere-Cylinder in the Langley 11-Inch Hypersonic Tunnel at a Mach Number of 6.8*, NACA TN 3706, 1956.

[43] Ladenburg, R., Winckler, J., and Van Voorhis, C. C., *Interferometric Studies of Faster Than Sound Phenomena, Part I. The Gas Flow Around Various Objects in a Free, Homogeneous, Supersonic Air Stream*, Physical Review, Vol. 73, No. 11, pp. 1359–1377, June 1, 1948.

[44] Love, Eugene S., *A Re-examination of the Use of Simple Concepts for Predicting the Shape and Location of Detached Shock Waves*, NACA TN 4170, 1957.

[45] Gooderum, Paul B., and Wood, George P., *Density Fields Around a Sphere at Mach Numbers 1.30 and 1.62*, NACA TN 2173, 1950.

[46] Busemann, Adolf, *A Review of Analytical Methods for the Treatment of Flows With Detached Shocks*, NACA TN 1858, 1949.

[47] Seiff, Alvin, *The Use of Gun-Launched Models for Experimental Research at Hypersonic Speeds*, AGARD Report 138, July, 1957.

# Theory of Stagnation Point Heat Transfer in Dissociated Air[†]

## J. A. FAY* AND F. R. RIDDELL**

*Avco Research Laboratory*

### SUMMARY

The boundary-layer equations are developed in general for the case of very high speed flight where the external flow is in a dissociated state. In particular the effects of diffusion and of atom recombination in the boundary layer are included. It is shown that at the stagnation point the equations can be reduced exactly to a set of nonlinear ordinary differential equations even when the chemical reactions proceed so slowly that the boundary layer is not in thermochemical equilibrium.

Two methods of numerical solution of these stagnation point equations are presented, one for the equilibrium case and the other for the nonequilibrium case. Numerical results are correlated in terms of the parameters entering the numerical formulation so as not to depend critically on the physical assumptions made.

For the nonequilibrium boundary layer, both catalytic (to atom recombination) and noncatalytic wall surfaces are considered. A solution is represented which shows the transition from the "frozen" boundary layer (very slow recombination rates) to the equilibrium boundary layer (fast recombination rates). A recombination rate parameter is introduced to interpret the nonequilibrium results, and it is shown that a scale factor is involved in relating the equilibrium state of a boundary layer on bodies of different sizes.

It is concluded that the heat transfer through the equilibrium stagnation point boundary layer can be computed accurately by a simple correlation formula [see Eq. (63)] and that the heat transfer is almost unaffected by a nonequilibrium state of the boundary layer provided the wall is catalytic and the Lewis Number near unity.

### SYMBOLS

$c_i$ = mass fraction of component $i$

$c_{pi}$ = specific heat per unit mass at constant pressure of component $i$, Eq. (19)

$c$ = $\bar{c}_p/\bar{c}_{pw}$, Eq. (A-11)

$\bar{c}_p$ defined by Eq. (19)

$C_1$ = recombination rate parameter, Eq. (57)

$C_2$ = $h_D/\bar{c}_{pw}T_s$

$C_3$ defined by Eq. (A-14)

$d$ defined by Eqs. (A-4), and (A-7)

$D$ = diffusion coefficient

$D^T$ = thermal diffusion coefficient

$e$ defined by Eq. (A-13)

$e_i$ = internal energy per unit mass of component $i$

$f$ defined by Eq. (24)

$F$ defined by Eq. (A-9)

$g$ defined by Eq. (25)

$h$ = enthalpy per unit mass of mixture, Eq. (16)

$h_i$ = perfect gas enthalpy per unit mass of component $i$, Eq. (10)

$h_i^0$ = heat evolved in the formation of component $i$ at 0°K. per unit mass

$h_A^0$ = dissociation energy per unit mass of atomic products, Eq. (59)

$h_D$ = average atomic dissociation energy times atom mass fraction in external flow, Eq. (61)

$k$ = thermal conductivity

$K_1$ = recombination rate constant, Eq. (50)

$K_2$ = dissociation rate constant, Eq. (51)

$l$ defined by Eqs. (33), (A-5), and (A-9)

$L_i$ = $D_i\rho c_p/k$, Lewis Number

$L_i^T$ = $D_i^T\rho c_p/k$, thermal Lewis Number

$L$ = Lewis Number for atom-molecule mixture

$M$ = molecular weight of molecules in atom-molecule mixture

$N$ = number density, moles per unit volume

$Nu$ = Nusselt Number, Eq. (43)

$p$ = pressure

$q$ = heat flux

$\vec{q}$ = vector mass velocity

$\vec{q}_i$ = vector diffusion velocity, Eq. (2)

$r$ = cylindrical radius of body

$R$ = body nose radius

$Re$ = Reynolds Numbers, Eq. (44)

$R_i$ = gas constant of component $i$
$R_m$ = gas constant of mixture
$\mathfrak{R}$ = universal gas constant
$s$ = defined by Eq. (27)
$T$ = absolute temperature
$T_V$ = vibrational temperature for molecules, taken as 800° K.
$u$ = $x$ component of velocity
$v$ = $y$ component of velocity
$w_i$ = mass rate of formation of component $i$ per unit volume and time
$x$ = distance along meridian profile
$y$ = distance normal to the surface
$\alpha_1, \alpha_2$ defined by Eq. (A-5)
$\beta_1, \beta_2$ defined by Eq. (A-7)
$\gamma_1, \gamma_2$ defined by Eq. (A-6)
$\eta$ defined by Eq. (22)
$\theta$ defined by Eq. (26)
$\mu$ = absolute viscosity
$\nu$ = kinematic viscosity
$\xi$ = defined by Eq. (23)
$\rho$ = mass density
$\sigma$ = Prandtl Number $c_p\mu/k$, taken as 0.71 in numerical calculations
$\Phi$ = dissipation function

**Subscripts**

$A$ = atom
$i$ = $i$th component of mixture
$e$ = external flow conditions
$w$ = wall
$s$ = stagnation point in external flow
$M$ = molecule
$m$ = mixture
$E$ = equilibrium

## (1) INTRODUCTION

THE PROCESS of aerodynamic heat transfer at hypersonic velocities is complicated by two features not normally present at low velocities. The first is the possible dissociation and ionization of air due to high static temperatures encountered where the air is decelerated by shock waves, by viscous forces in the boundary layer, or at a stagnation point. Because dissociation and ionization (and their reverse processes, recombination) proceed at finite rates, thermochemical equilibrium is not necessarily achieved throughout the flow field, and such rates are therefore an essential ingredient of the flow process. Secondly, diffusion of atoms and ions, which subsequently recombine with a high specific energy release, may appreciably add to the heat transferred by normal molecular conduction. While there may be other physical phenomena also present, such as radiative effects, it is the purpose of the present analysis to include only the two effects previously noted in an otherwise classical viscous flow problem.

Some aspects of this problem have already received attention. Moore[1] considered a dissociated laminar boundary layer on a flate plate in air with a local composition determined by the thermochemical equilibrium—i.e., a recombination rate constant sufficiently great to maintain local equilibrium. Hansen[2] noted that Moore had miscalculated the Prandtl Number for dissociated air and an analysis similar to Moore's but

following Hansen's suggestion was made by Romig and Dore.[3] Beckwith[4] considered the heat transfer to the stagnation region of a blunt nosed body, using integral methods.* Crown[5] also considered the stagnation point problem, using a modified Crocco method for solving the boundary-layer equations. Finally, Mark[6] treated the stagnation point equilibrium boundary layer with variable fluid properties.†

In all these analyses no detailed distinction is made between the roles of atomic diffusion and molecular conduction in transporting energy to the wall.‡ If one considers the energy transport through a motionless dissociated gas with temperature and concentration gradients, the energy flux is approximately

$$q = k \operatorname{grad} T + h_A{}^0 D\rho \operatorname{grad} c_A$$

where $k$ is the ordinary thermal conductivity, $T$ is the temperature, $h_A{}^0$ is the dissociation energy per unit mass of atomic products, $D$ is the atomic diffusion coefficient, $\rho$ the density, and $c_A$ the atomic mass fraction. The first term is the usual transport of kinetic, vibrational and rotational energy and the second is the transport of potential (recombination) energy. Even in the "equilibrium" boundary layer, the latter term should be taken into account in the energy equation, and will constitute a significant contribution where the atom concentration and diffusional velocities are noticeable.

These distinctions were first pointed out by Fay.[13] Subsequently, Lees[7] considered in detail the laminar heat-transfer problem in dissociated air, including the effects of atomic diffusion, and suggested several approximations to facilitate the solution of the boundary-layer equations. He considered the limiting extremes of the recombination rate constant which (as discussed below) lead to simpler solutions than the general case, and suggested expressions for the heat transfer for both cases. Similar arguments, but in less detail, are advanced by Kuo.[14]

Apart from the physical mechanism of heat transfer, there are several relevant aerodynamic considerations, the foremost of which is the question of shock-wave boundary-layer interaction at a sharp leading edge. From a mechanical point of view, it does not appear possible to maintain sharp leading edges with their attendant high heat-transfer rates, so that a finite radius of curvature appears mandatory. Under these conditions a distinct layer will exist independent of the detached bow shock wave if the boundary-layer thickness is much less than the shock detachment distance.

---

* It is noted that the variation of viscosity through the boundary layer, which materially affects the heat-transfer rate, cannot be accounted for by the integral method.

† For a more detailed discussion of numerical results, see Fay, Riddell, and Kemp.[12]

‡ Crown,[5] for example, assumes that the potential energy of dissociation (which is actually carried by diffusion of atoms) is transported in the same manner as the internal energy of the molecules, which implies equal diffusivities of molecules and atoms.

Since the former varies as the inverse square root of the Reynolds Number and the latter is independent of Reynolds Number, there is a minimum Reynolds Number below which the shock wave and boundary layer merge. However, since low Reynolds Numbers at hypersonic velocities can only be attained by reducing the density (and hence increasing the mean free path), this limit may not be reached before free molecule flow ensues. It thus appears that stagnation point boundary layers are quite relevant to hypersonic continuum flows.

Boundary layers at locations other than the stagnation point are also of interest, but will not be considered herein in detail. There are certain difficulties inherent in such solutions when the recombination rate is finite which will be discussed more fully below.

For any boundary-layer calculation, the behavior of the free stream outside the boundary layer must be known. If the boundary-layer thickness is small compared with the nose (and also detached shock wave) radius of curvature, then only fluid which has passed through the normal shock wave close to the axis (or plane) of symmetry will enter the boundary layer, and this constitutes the "free stream." If it is assumed that this stream has attained thermochemical equilibrium by the time it reaches the stagnation point, then the free-stream conditions for the stagnation point boundary layer are those of an equilibrium gas. This would appear to be the case most likely to be encountered.*

Whether the free stream in regions other than the stagnation point remains at equilibrium again depends upon the recombination rate since, in flowing to regions of lower pressure, the gas is expanded and cooled. Again, there will be no general solution which will include all possible situations.

The two extremes of recombination rate give rise to simpler solutions than the general case. For sufficiently small recombination rate, the concentration of atoms (or ion pairs) is determined by the diffusive flow from the free stream to the wall where recombination would occur, and would bear no relation to the thermochemical equilibrium concentration corresponding to the local temperature. In such a "frozen" boundary layer, the temperature and concentration distributions are practically independent of one another. On the other hand, for a sufficiently large recombination rate, constant thermochemical equilibrium would prevail throughout and either the temperature or concentration distribution is a sufficient description of the thermodynamic state of the boundary layer. It is, therefore, to be expected that the distribution of atoms in the

"frozen" and "equilibrium" boundary layers will be quite different.

Despite the importance of the processes of dissociation and recombination in determining the thermodynamic state of the air throughout the flow field, their effect on heat transfer is secondary. This is most easily seen by again considering the heat flux through a stagnant gas as given above, and replacing grad $T$ by $(1/c_p)$ grad $h$, where $h$ is the perfect gas enthalpy. If we also make the approximation that $D\rho c_p/k$ (Lewis number) is unity, the heat flux becomes

$$q = (k/c_p) \text{ grad } (h + c_A h_A{}^0)$$

that is, the heat flux is determined by the chemical enthalpy (perfect gas enthalpy plus enthalpy of formation) difference between free stream and wall. Whether atoms recombine in the boundary layer or on the wall makes no great difference since the energy is conducted about as readily by normal conduction as by diffusion when the Lewis Number is approximately one. On the other hand, if the heat transfer is to be known more exactly, then such relevant effects as variation of transport coefficients with temperature, variation in heat capacities, actual Lewis Number, etc., must be accounted for properly. It will be seen that it is the influence of these effects which constitutes the principal departure from an extrapolation of the classical theory.

Since a considerable fraction of the heat may be transported by atomic diffusion toward the wall followed by recombination on the surface, it would be possible to eliminate this fraction of the heat transfer by using a noncatalytic surface. However, such a scheme is useful only if the atoms do not first recombine in the gas before reaching the wall. The flight conditions under with the gas phase recombination is slow enough to permit atoms to reach the wall, and the resulting heat transfer with both catalytic and noncatalytic surface, have been determined for the stagnation point flow.

For a discussion of experimental techniques and results of shock tube measurements of stagnation point heat transfer in dissociated air, see reference 15.

## (2) Laminar Boundary-Layer Equations in a Dissociated Gas

The general equation of continuity for any species $i$ is

$$\text{div}\{\rho(\vec{q} + \vec{q}_i)c_i\} = w_i \qquad (1)$$

where $\rho$ is the mixture density, $c_i$ is the mass fraction of species $i$, $w_i$ is the mass rate of formation of species $i$ per unit volume, $\vec{q}$ is the mass averaged velocity and $q_i$ the diffusional velocity of species $i$ measured with respect to $\vec{q}$. $\vec{q}_i$ may be given by

$$\vec{q}_i = -(D_i/c_i) \text{ grad } c_i - (D_i{}^T/T) \text{ grad } T \qquad (2)$$

where $D_i$ and $D_i{}^T$ are, respectively, the molecular and thermal diffusion coefficients of species $i$, and $T$ is the temperature. The first term on the right of Eq. (2) is

---

* The time for the gas to come to equilibrium behind the normal shock wave depends upon the kinetics of the dissociation process. It is merely noted here that immediately behind the shock wave, before dissociation begins, the translational temperature is extremely high and thereby promotes high dissociation rates. Even at high temperatures equilibrium may not be attained soon enough if the density is sufficiently low, but this would probably occur only near the free molecule flow regime.

due to concentration diffusion and the second is due to thermal diffusion (pressure diffusion is neglected).

The use of the gradient of mass fraction instead of mole fraction is particularly useful since, in the case of a bimolecular mixture, $D_i$ becomes the bimolecular diffusion coefficient $(D_{12})$ which is practically independent of composition. For multicomponent mixtures, the diffusional velocity of any one component depends, in general, upon the concentration gradients of all the components, and a method for determining the diffusional velocities has been suggested by Hirschfelder, Curtiss, and Bird.[5] In such a case Eq. (2) is not exact (except for equal diffusivities and molecular weights of all components), but is a useful approximation. A dissociated gas (such as air) in which all the molecules (or atoms) have nearly the same molecular weight and probably similar collision diameters may be considered primarily a two-component mixture with atoms and molecules as species, for which Eq. (2) is adequate.

In order to conserve mass in any chemical change it is necessary that

$$\Sigma w_i = 0 \qquad (3)$$

and from the definition of the mass averaged velocity it follows that

$$\Sigma \vec{q}_i c_i = 0 \qquad (4)$$

Hence, Eq. (1) summed over all species gives the usual form for the continuity equation,

$$\text{div}\,(\rho \vec{q}) = 0 \qquad (5)$$

The energy equation may be written for a moving element of fluid

$$\rho \vec{q} \cdot \text{grad}(\Sigma c_i e_i) = \text{div}(k\,\text{grad}\,T) - \\ \text{div}(\Sigma \rho \vec{q}_i c_i h_i) + \Sigma w_i h_i^0 + p\,\text{div}\,\vec{q} + \Phi \qquad (6)$$

where $e_i$, $h_i$, and $h_i^0$ are, respectively, the specific internal energy, enthalpy, and heat of formation of species $i$, $k$ is the thermal conductivity for transport of kinetic, rotational, and vibrational energy, $p$ is the pressure, and $\Phi$ is the dissipation function.

The first term on the right of Eq. (6) is the internal energy increase due to normal heat conduction, the second that due to fluid diffusing across the boundary of the element, the third that due to chemical reaction,[*] and the fourth and fifth that due to the work of the pressure and the viscous forces, respectively.

It will be assumed that the gas is a mixture of perfect gases, so that for each component

$$p_i = \rho_i R_i T \qquad (7)$$

where $R_i$ is the gas constant for species $i$, and for the mixture

$$p = \rho R_m T \qquad (8)$$

where the gas constant for the mixture $(R_m)$ is given by

$$R_m = \Sigma c_i R_i \qquad (9)$$

It then follows that the enthalpy and internal energy are related by

$$h_i = c_i + R_i T \qquad (10)$$

By combining Eqs. (5) and (7) through Eq. (10) with Eq. (6), the steady-state energy equation reduces to

$$\rho \vec{q} \cdot \text{grad}(\Sigma c_i h_i) = \text{div}(k\,\text{grad}\,T - \\ \Sigma \rho \vec{q}_i c_i h_i) + \Sigma w_i h_i^0 + \vec{q} \cdot \text{grad}\,p + \Phi \qquad (11)$$

A further simplification occurs by combining Eqs. (1) and (11) to eliminate the term $\Sigma w_i h_i^0$:

$$\rho \vec{q} \cdot \text{grad}\{\Sigma c_i (h_i - h_i^0)\} = \text{div}\{k\,\text{grad}\,T - \\ \Sigma \rho \vec{q}_i c_i (h_i - h_i^0)\} + \vec{q} \cdot \text{grad}\,p + \Phi \qquad (12)$$

By making the usual boundary-layer assumptions, Eqs. (1), (5), and (12) reduce to the following form for a body of revolution, if the boundary-layer thickness is small compared with the radius of curvature and centrifugal forces are neglected:[†]

$$(\rho r u)_x + (\rho r v)_y = 0 \qquad (13)$$

$$\rho u c_{ix} + \rho v c_{iy} = \{D_i \rho c_{iy} + D_i^T \rho c_i T_y / T\}_y + w_i \qquad (14)$$

$$\rho u h_x + \rho v h_y = (k T_y)_y + u p_x + \\ \mu(u_y)^2 + \{\Sigma D_i \rho (h_i - h_i^0) c_{iy} + \\ \Sigma D_i^T \rho c_i (h_i - h_i^0) T_y / T\}_y \qquad (15)$$

where $r$ is the radial distance of the body surface from the axis of revolution, $u$ and $v$ are the velocity components in the $x$ and $y$ directions (tangential and normal to the surface, respectively), $\mu$ is the absolute viscosity, and the enthalpy for the mixture is

$$h = \Sigma c_i (h_i - h_i^0) \qquad (16)$$

The corresponding equation of motion is

$$\rho u u_x + \rho v u_y = -p_x + (\mu u_y)_y \qquad (17)$$

Since the transport coefficients are, in general, functions of temperature and composition, it may be desirable to use $T$ rather than $h$ as the dependent variable in the energy equation. Noting that $h_i$ is a function of temperature alone, we have

$$\text{grad}\,h = \{\Sigma c_i (dh_i / dT)\}\,\text{grad}\,T + \\ \Sigma (h_i - h_i^0)\,\text{grad}\,c_i \qquad (18)$$

Letting

$$\bar{c}_p \equiv \Sigma c_i (dh_i / dT) = \Sigma c_i c_{pi} \qquad (19)$$

where $c_{pi}$ is the constant pressure specific heat for translation, rotation, and vibration, the energy equation (15), in combination with Eq. (14), becomes

$$\bar{c}_p \{\rho u T_x + \rho v T_y\} = \\ (k T_y)_y + u p_x + \mu(u_y)^2 + \Sigma w_i (h_i^0 - h_i) + \\ \Sigma c_{pi} (D_i \rho c_{iy} + D_i^T \rho c_i T_y / T) T_y \qquad (20)$$

For a gas at equilibrium, on the other hand, it is found

---

[*] The heat of formation $h_i^0$ may be taken as zero for the molecules and negative for the atoms, in which case the enthalpy $h$ [see Eq. (16)] is always positive.

[†] Subscripts $x$ and $y$ (or $\xi$ and $\eta$ below) are used to denote partial differentiation.

more convenient to use the enthalpy as a variable rather than temperature, in which case by combining Eqs. (17) and (18) with Eq. (15), we obtain

$$\rho u(h + u^2/2)_x + \rho v(h + u^2/2)_y = \{(k/\bar{c}_p) \times \\ (h + u^2/2)_y\}_y + \{(1/2)[\mu - (k/\bar{c}_p)](u^2)_y\}_y + \\ \{\Sigma[D_i\rho - (k/\bar{c}_p)](h_i - h_i^0)c_{iy} + \\ \Sigma(D_i^T\rho c_i'/T)(h_i - h_i^0)T_i\}_y \quad (21)$$

Eqs. (13), (14), (17), and (20) or (21) thus constitute the system whose solution is required.

### (3) SIMILAR SOLUTIONS

As is usual in boundary-layer problems, one first seeks solutions of restricted form which permit reducing exactly the partial differential equations to ordinary differential form. An easily recognizable case is that of the stagnation point flow, where, because of symmetry, all the dependent variables are chosen to be functions of $y$ alone, except $u$ which must be taken proportional to $x$ times a function of $y$. This also appears to be the *only case* for which exact ordinary differential equations may be obtained regardless of the recombination rate. For the flat plate and cone, exact solutions exist only for the extreme values of the recombination rate constant, that is, when the boundary layer is either "frozen" or in the thermodynamic equilibrium.

For all other cases, certain degrees of approximation are required. Following standard procedures, one first tries solutions for which the velocity and enthalpy profiles remain similar to themselves, at least for an appreciable distance along the body. Such "locally similar" approximate solutions may be obtained for the "frozen" or "equilibrium" boundary layer, and also for an arbitary recombination rate in certain restricted cases.

The existence of a finite recombination rate is not the only hindrance to obtaining exact solutions in regions other than the stagnation point. In general, the variation of the velocity, thermodynamic variables and transport coefficients in the free stream and along the wall of the body of arbitrary shape preclude exact solutions (except for the cone and flat plate). An important aspect of the locally similar solutions is a proper accounting for these variations such that the heat transfer may be determined for any point of the body of arbitrary (but regular) shape. Although this problem will not be treated in this paper, we will start with a transformation suitable for locally similar solutions.

With this in mind, we choose the following transformation of the independent variables $x$ and $y$, which includes the usual Howarth and Mangler transformations, as proposed by Lees.[7]

$$\eta \equiv (ru_e/\sqrt{2\xi}) \int_0^y \rho dy \qquad (22)*$$

$$\xi \equiv \int_0^x \rho_w\mu_w u_e r^2 dx \qquad (23)*$$

where $u_e$ is the velocity at the outer edge of the boundary layer. In addition, the following dimensionless dependent variables are chosen:

$$\partial f/\partial \eta \equiv u/u_e; \quad f = \int_0^\eta (\partial f/\partial \eta)d\eta \qquad (24)$$

$$g = (h + u^2/2)/h_s \qquad (25)$$

$$\theta = T/T_e \qquad (26)$$

$$s_i = c_i/c_{ie} \qquad (27)$$

where the subscript $e$ refers to values in the local free stream, and $s$ to values in the free stream at the stagnation point. Substituting in Eqs. (13), (14), (17), (20), and (21), there results

$$\rho v = -r^{-1}[(\sqrt{2\xi} f_\xi + f/\sqrt{2\xi})\xi_x + \sqrt{2\xi} f_\eta\eta_x] \qquad (28)$$

$$[(l/\sigma)(L_i s_{i\eta} + L_i^T s_i\theta_\eta/\theta)]_\eta + fs_{i\eta} + [2\xi w_i/\rho u_e c_{ie}(d\xi/dx)] = 2\xi(f_\eta s_{i\xi} - f_\xi s_{i\eta}) + 2f_\eta s_i[d(\ln c_{ie})/d(\ln \xi)] \qquad (29)$$

$$(lf_{\eta\eta})_\eta + ff_{\eta\eta} + 2[d(\ln u_e)/d(\ln \xi)][(\rho_e/\rho) - f_\eta^2] = 2\xi(f_\eta f_{\eta\xi} - f_\xi f_{\eta\eta}) \qquad (30)$$

$$[(\bar{c}_p/\bar{c}_{pw})(l/\sigma)\theta_\eta]_\eta + (\bar{c}_p/\bar{c}_{pw})f\theta_\eta + \Sigma[2\xi w_i/\rho u_e(d\xi/dx)][(h_i^0 - h_i)/\bar{c}_{pw}T_e] + (u_e^2/\bar{c}_{pw}T_e)lf_{\eta\eta}^2 + \\ \Sigma(c_{pi}/\bar{c}_{pw})(c_{ie}l/\sigma)(L_i s_{i\eta} + L_i^T s_i\theta_\eta/\theta)\theta_\eta = f_\eta\{2(\bar{c}_p/\bar{c}_{pw})\theta[d(\ln T_e)/d(\ln \xi)] + \\ (2u_e^2/\bar{c}_{pw}T_e)(\rho_e/\rho)[d(\ln u_e)/d(\ln \xi)]\} + 2(\bar{c}_p/\bar{c}_{pw})\xi(f_\eta\theta_\xi - f_\xi\theta_\eta) \qquad (31)$$

$$[(l/\sigma)g_\eta]_\eta + fg_\eta + (u_e^2/h_s)\{(1 - \sigma^{-1})lf_\eta f_{\eta\eta}\}_\eta + \\ \{(l/\sigma)\Sigma(c_{ie}/h_s)(h_i - h_i^0)[(L_i - 1)s_{i\eta} + L_i^T s_i\theta_\eta/\theta]\}_\eta = 2\xi(f_\eta g_\xi - f_\xi g_\eta) \qquad (32)$$

where $l \equiv \rho\mu/\rho_w\mu_w$

and where $\sigma$ and $L_i$ are the Prandtl Number ($\bar{c}_p\mu/k$) and Lewis Number ($D_i\rho\bar{c}_p/k$), respectively. The subscript $w$ refers to values of the variables at the wall.

For the dependent variables $f$, $g$, $\theta$, and $s_i$ to be functions of $\eta$ alone, it is first necessary that the thermodynamic state variables be unchanging in the free stream and along the wall as $\xi$ increases, a condition satisfied at a stagnation point, or along a cone or flat plate. It is further necessary that the source term—i.e., the term

involving $w_i$—in Eqs. (29) and (31) depend upon $\eta$ alone. Since the chemistry of the recombination process is believed to depend only upon the local thermodynamic variables—that is, $w_i$ is a function of $\rho$, $T$, and $s_i$—this second condition may be satisfied in three different ways: (a) $w_i = 0$ (frozen boundary layer), (b) $u_e d(\ln \xi)/dx = $ constant, which is satisfied at a stagnation point, or (c) the recombination rate is sufficiently

* For two-dimensional flows let $r = $ constant.

large to maintain thermodynamic equilibrium,* in which case $w_i$ is determined through Eq. (29) from the

$$[(l/\sigma)(L_i s_{i\eta} + L_i^T s_i T_\eta/T)]_\eta + f s_{i\eta} + \{2(du_e/dx)_s\}^{-1}(w_i/\rho c_{is}) = 0 \qquad (34)$$

$$(lf_{\eta\eta})_\eta + ff_{\eta\eta} + (1/2)\{(\rho_s/\rho) - f_\eta^2\} = 0 \qquad (35)$$

$$[(\bar{c}_p/\bar{c}_{pw})(l/\sigma)]_\eta + (\bar{c}_{p_i}/\bar{c}_{pw})f\theta_\eta + \{2(du_e/dx)_s\}^{-1}\Sigma(w_i/\rho)[(h_i^0 - h_i)/\bar{c}_{pw}T_s] + \\ \Sigma(c_{p_i}/\bar{c}_{pw})(c_{is}l/\sigma)(L_i s_{i\eta} + L_i^T s_i\theta_\eta'/\theta)_\eta\theta_\eta = 0 \quad (36)$$

$$[(l/\sigma)g_\eta]_\eta + fg_\eta + ((l/\sigma)\Sigma[c_{is}(h_i - h_i^0)/h_s]\{(L_i - 1)s_{i\eta} + L_i^T s_i\theta_\eta/\theta\})_\eta = 0 \qquad (37)$$

where it has been assumed that $u^2 \ll h_s$.

For a "locally similar" solution away from the stagnation point it is required that the terms on the right-hand side of Eqs. (29) through (32) all be negligible compared with those on the left, and thus the equations may be integrated with respect to $\eta$. The dependence upon $\xi$ of $f$, $g$, $\theta$, and $s_i$ is thereby implicitly determined by the variation of $\rho$, $T$, $s_i$, $u$, and the transport coefficients in the free stream and along the wall, this variation being determined by the aerodynamics of the external flow.

For Newtonian flow the distribution around the body of the relevant quantities is easily found, all quantities except $du_e/dx$ being determined by the local body slope— i.e., local pressure. Since $du_e/dx$ depends upon the pressure gradient and hence body curvature in the meridian plane, there is introduced an extra parameter in the locally similar solutions. Lees[7] points out that in the equation of motion (30) the pressure gradient affects only a single term, that this term is generally small, and that neglecting this term in the equation of motion will only slightly affect the solutions for $g$, $\theta$, and $s_i$. This appears to be a greatly desirable simplification in determining the heat transfer at other than the stagnation point.

The use of locally similar solutions can only be justified a posteriori in each particular case by determining from such a solution the magnitude of the terms in Eqs. (29) through (32) which were neglected. Presumably an iterative scheme could be devised to improve on such solutions. It does not appear possible to formulate a general criterion for determining the limit of applicability of the locally similar solutions except a loose physical argument that conditions in the free stream and along the body must change only slightly in a distance of many boundary-layer thicknesses.

### (4) HEAT TRANSFER

The local heat-transfer rate to the body $q$ is determined by the sum of the conductive and diffusive transports, the latter being included only when the atoms recombine on the wall. Thus,

$$q = [k(\partial T/\partial y)]_{y=0} + [\Sigma\rho(h_i - h_i^0) \times \\ \{D_i(\partial c_i/\partial y) + (D_i^T c_i/T)(\partial T/\partial y)\}]_{y=0} \quad (38)$$

solution of Eqs. (28), (30), and (32).

For the stagnation point, then, Eqs. (29) to (32) reduce to

or

$$q = [(k'/\bar{c}_p)(\partial h/\partial y)]_{y=0} + [\Sigma(k/\bar{c}_p)(h_i - h_i^0) \times \\ \{(L_i - 1)(\partial c_i/\partial y) + (L_i^T c_i/T)(\partial T/\partial y)\}]_{y=0} \quad (39)$$

In terms of the dimensionless temperature and enthalpy distributions, this becomes

$$q = (rk_w\rho_w u_e T_e'/\sqrt{2\xi})\{\theta_\eta + \Sigma c_{ie} \times \\ [(h_i - h_i^0)/\bar{c}_p T_e](L_i s_{i\eta} + L_i^T s_i\theta_\eta/\theta)\}_{\eta=0} \quad (40)$$

or

$$q = (rk_w\rho_w u_e h_s/\sqrt{2\xi}\,\bar{c}_{pw}) \times \\ \{g_\eta + \Sigma c_{ie}[(h_i - h_i^0)/h_s] \times \\ [(L_i - 1)s_{i\eta} + L_i^T s_i\theta_\eta/\theta]\}_{\eta=0} \quad (41)$$

For stagnation point heat transfer we note that

$$r\rho_w u_e/\sqrt{2\xi} = \{(2/\nu_w)(du_e/dx)_s\}^{1/2} \quad (42)$$

where $\nu_w$ is the kinematic viscosity at the wall.

It is also possible to define local Nusselt and Reynolds Numbers based on the local coordinate $x$. Thus, defining[†]

$$Nu = qx\bar{c}_{pw}/k_w(h_s - h_w) \quad (43)$$

$$Re = u_e x/\nu_w \quad (44)$$

the heat transfer at the stagnation point may be written as

$$q = (Nu/\sqrt{Re})\sqrt{\rho_w\mu_w(du_e/dx)_s}[(h_s - h_w)/\sigma] \quad (45)$$

where

$$Nu/\sqrt{Re} = [\sqrt{2}\,\bar{c}_{pw}T_s/(h_s - h_w)] \times \\ \{\theta_\eta + \Sigma c_{is}[(h_i - h_i^0)/\bar{c}_p T_s] \times \\ (L_i s_{i\eta} + L_i^T s_i\theta_\eta/\theta)\}_{\eta=0} \quad (46a)[‡]$$

$$Nu/\sqrt{Re} = [\sqrt{2}/(1 - g_w)] \times \\ \{g_\eta + \Sigma c_{is}[(h_i - h_i^0)/h_s] \times \\ [(L_i - 1)s_{i\eta} + L_i^T s_i\theta_\eta/\theta]\}_{\eta=0} \quad (46b)[‡]$$

It should be emphasized that the heat transfer is independent of the particular choice of reference density and viscosity $(\rho_w\mu_w)$ which appears in the definition of Eq. (23). The use of wall values of $\rho$ and $\mu$ for this pur-

---

\* Strictly speaking, the fluid cannot be exactly in thermodynamic equilibrium, for if this were so, there could be no net rate of change of composition following a particle path. For large enough rate constants, the fluid will be very close to equilibrium.

[†] It is clear from the expressions (40) and (41) that the enthalpy difference between wall and free stream, not the temperature difference, is the proper "driving force" for heat transfer.

[‡] For conical or flat plate flows, the factor $\sqrt{2}$ in Eq. (46) should be replaced by $\sqrt{3/2}$ or $1/\sqrt{2}$, respectively, when the reference dimensions for $Nu$ and $Re$ are the distances from the apex or leading edge, respectively, measured along the surface.

$\dots$ is merely a convenience, but a logical choice in that it ensures that $l = 1$ [Eq. (33)] at the wall ($\eta = 0$). However, another choice, such as free-stream $\rho$ and $\mu$, or even $\rho\mu$ equal to an arbitrary function of $x$, could also be used. In each such case, however, the solutions of the boundary-layer equations give different $g(\eta)$, $\theta(\eta)$, etc. It is clear from an examination of these equations that each such solution may be transformed into another by a simple change of scale of $\eta$ and $f$ defined by

$$\sqrt{\rho_w\mu_w}\,\eta = \sqrt{\rho_0\mu_0}\,\eta_0 \qquad (47)$$

$$\sqrt{\rho_w\mu_w}\,f = \sqrt{\rho_0\mu_0}\,f_0 \qquad (48)$$

and

$$g(\eta) = g_0(\sqrt{\rho_0\mu_0 / \rho_w\mu_w}\,\eta_0), \quad \text{etc.} \qquad (49)$$

and where $\rho_0\mu_0$ is the new reference value used in defining $\eta_0$. As a consequence the heat transfer [see Eqs. (38) and (39)] can be seen to be independent of the choice of $\rho_0\mu_0$.

On the other hand, if one attempts to estimate $g_\eta(0)$ for the case of $\rho\mu$ not constant from a solution for $\rho\mu$ constant,* which is the problem considered by Lees,[7] the reference state ($\rho_0\mu_0$) is quite relevant since by its proper (and arbitrary) selection the wall gradient of $g$ may be made to equal numerically that for the case of $\rho\mu$ constant. A discussion of this point has been given by Probstein,[9] and by Fay, Riddell, and Kemp.[12]

### (5) TRANSPORT PROPERTIES

To obtain a numerical solution of the boundary-layer equations it is necessary to know the viscosity, Prandtl Number, Lewis Number, and thermal diffusivity as functions of the local temperature, density, and composition. For the high temperatures under consideration, these properties have been estimated,† the principal uncertainty resulting from lack of knowledge of atom-molecule interaction potentials. The particular results of this study which are pertinent to the boundary-layer calculation may be summarized as follows.

(a) The viscosity of equilibrium air, determined by assuming that all particles possess the same interaction potentials, does not vary more than 10 per cent from Sutherland's formula below 9,000°K.

(b) Both Prandtl and Lewis Numbers do not change appreciably with temperature (below 9,000°K.), the value of the latter being uncertain, but estimated as about 1.4.

In light of the uncertainties in viscosity and Lewis Number, it is clear that the calculated heat transfer using these estimates is also uncertain. However, the numerical solutions of the boundary-layer equations may be obtained for a range of possible Lewis Number and viscosity variation, such solutions being generally valid when expressed explicitly in terms of the property

variations. Thus for the numerical solutions, the Prandtl Number was held fixed at 0.71, the Lewis Number was assumed constant through the boundary layer at values ranging from one to two, and the viscosity variation was determined by Sutherland's law for the equilibrium air and as calculated by Penner and Litvak for nonequilibrium composition.‡

It is easily shown that thermal diffusion is unimportant for the equilibrium boundary layer at stagnation temperatures less than 10,000°K. For the frozen boundary layer this is no longer necessarily the case; however, thermal diffusion was neglected in all the numerical solutions reported in this paper.

### (6) RECOMBINATION RATE

As suggested by Davidson,** the recombination rate of atoms is determined by a three-body collison:

atom + atom + particle → molecule + particle
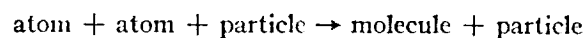
For this process the rate of disappearance of atoms may be written as

$$dN_A/dt = -K_1 N_A{}^2 N T^{-1.5} \qquad (50)$$

where the temperature dependence is as suggested by Davidson, who also estimated $K_1 T^{-1.5}$ to be $5 \times 10^{14}$ cc.² mole⁻² sec.⁻¹ for oxygen recombination when $T = 300°K$.†† $N_A$ and $N$ are the number of moles per cm.³ of atoms and particles, respectively.

Atoms will be produced by the reverse of the above reaction, so that the net rate of production may be written as

$$dN_A/dt = -K_1 N_A{}^2 N T^{-1.5} + K_2(T) N_M N \qquad (51)$$

Since under equilibrium conditions, there is no net production of atoms, $K_2(T)$ may be solved for in Eq. (51) in terms of the equilibrium atom and molecule concentrations which would exist at the local temperature $T$ and pressure. Substituting this value of $K_2$ in Eq. (51), there results

$$dN_A/dt = -K_1 N_A{}^2 N T^{-1.5} \times$$
$$\left\{ 1 - (N_M/N_{ME})(N_{AE}/N_A)^2 \right\} \qquad (52)$$

where the subscript $E$ refers to the concentrations which would exist at thermodynamic equilibrium at the local pressure and temperature, and $N_M$ is the number of moles of molecules per cm³.

Considering a gas mixture of diatomic molecules of

---

* As, for example, the solutions of Cohen and Reshotko.[10]

† These estimates were made by Dr. S. Penner of California Institute of Technology and M. M. Litvak of Cornell University.

‡ Results of the experiments of reference 15 indicate good agreement with the present estimates of transport properties with Prandtl Number 0.71 and Lewis Number 1.4.

** Dr. Norman Davidson, California Institute of Technology (private communication).

†† Recent experiments reported by J. Camm and J. Keck (see Bulletin of the American Physical Society, Series II, Vol. 2, No. 4, p. 216, 1957) indicate that the recombination rate at 6,000°K. may be higher than that obtained by extrapolating Davidson's estimate to such a temperature. There is nothing known concerning this rate at the low wall temperatures pertinent to the boundary-layer problem.

molecular weight $M$ and atoms of weight $M/2$, the atom mass fraction and total density are, respectively,

$$c_A = N_A/(N_A + 2N_M) \qquad (53)$$

and

$$\rho = M(N_M + N_A/2) \qquad (54)$$

The net mass rate of formation of atoms ($w_A$) may now be determined in terms of these quantities to give

$$\left. \begin{array}{l} w_A = (M/2)(dN_A/dt) \\ \quad = -(2K_1\rho^3 T^{-1.5}/M^2) \times \\ \qquad [(1 + c_A)(c_A^2 - c_{AE}^2)/(1 - c_{AE}^2)] \end{array} \right\} \qquad (55)$$

Neglecting the term $(1 - c_{AE}^2)$, which does not vary by 25 per cent in the cases considered, the relevant source term in the diffusion equation (34) for atoms reduces to

$$\{2(du_e/dx)_s\}^{-1}(w_i/\rho) = -[K_1\rho_s^2 T_s^{-3.5}/\Re^2(du_e/dx)_s] \times \{\theta^{-3.5}(c_A^2 - c_{AE}^2)/(1 + c_A)\} \qquad (56)$$

where $\Re$ is the universal gas constant. The coefficient of the term in braces on the right of Eq. (56) contains all the dimensional effects of the finite recombination rate problem, and will be termed the *recombination rate parameter* ($C_1$)—i.e.,

$$C_1 \equiv K_1\rho_s^2 T_s^{-3.5}\Re^{-2}(du_e/dx)_s^{-1} \qquad (57)$$

The term $(du_e/dx)_s^{-1}$ is approximately the time for a particle in the free stream to move a distance equal to the nose radius, and thus also the time for a particle to diffuse through the boundary layer at the stagnation point. The factor which multiplies it in Eq. (57) is the reciprocal of the lifetime of an atom, so that the recombination rate parameter is the ratio of the diffusion time to the lifetime of an atom. Because the diffusion time contains the body nose radius while the lifetime does not, a scale effect is introduced by the chemical change which is not accounted for in the Reynolds Number. Thus, similar flows require equal Reynolds Numbers and recombination rate parameters.

A term similar to the left side of Eq. (56) appears in the energy equation (36) except that it is multiplied by a dimensionless dissociation energy. A part of this term, $\Sigma w_i h_i$, is negligible since $\Sigma w_i = 0$ and $h_i$ per unit mass for vibrationally excited molecules and atoms are nearly equal, being in the ratio 9/10.

### (7) NUMERICAL SOLUTIONS

The boundary-layer equations derived above [Eqs. (34) through (37)] can be put in a form suitable for numerical integration. The details of how this was done are given in the Appendix. Numerical solutions were obtained by use of an IBM 650 digital computer.

Many combinations of the parameters $\sigma$, $L$, and $C_1$ are possible, as well as extreme ranges in the free-stream (stagnation point) and wall boundary values. It was therefore decided to restrict the solutions to the following values:

(a) $\sigma = 0.71$

(b) $L = 1.0, 1.4, 2.0; L^T = 0$

(c) $0 \leq C_1 \leq \infty$

(d) Stagnation point conditions corresponding to thermodynamic equilibrium at velocities between 5,800 ft. per sec. and 22,800 ft. per sec. and at altitudes of 25,000 ft. to 120,000 ft. (Equilibrium air properties were determined from the tables prepared by the National Bureau of Standards[11].)

(e) Wall temperatures from 300° K. to 3,000°K.

Wherever possible, only one parameter or boundary condition was varied in a series of calculations in order to determine its individual effect. It was not believed necessary to establish such effects for all possible combinations of the remaining parameters. Tables giving the values of the parameters and the boundary conditions for each computation may be obtained directly from the authors.

The heat-transfer parameter ($Nu/\sqrt{Re}$) determined from each integration depends not only upon the parameters and boundary values of the dependent variables involved, but also upon the assumed variation of viscosity with temperature and composition. In addition, further simplifications as explained below for the individual cases were also made. In order to make the results less dependent upon the specific assumptions made, the heat-transfer parameter was numerically correlated with the parameters and boundary values in what seemed to be a suitable manner. It is believed that not too widely different assumptions would give results which would fall within the same correlation.

### (8) THE EQUILIBRIUM BOUNDARY LAYER

A first series of equilibrium boundary layers was computed by solving Eqs. (35) and (37) simultaneously (hereafter denoted as Method 1). The solution requires specifying $\rho_s/\rho$ and $l = \rho\mu/\rho_w\mu_w$ as functions of $g$, typical variations of these quantities being shown in Fig. 1. The calculated values at various altitudes of interest are compared with the fitted curves used in the computing program, from which it was concluded that there was a negligible effect of altitude variation on these functions. Specific details of the method of calculation are given in the Appendix. It was found that moderate changes in the distribution for identical end values resulted in negligible changes in the heat-transfer parameter.

For $L_i = 1$, the equations are similar in form to those solved by Cohen and Reshotko,[10] and become identical at low enough stagnation temperatures when $l$ is approximately constant. Solutions were obtained for the range of velocities and wall temperatures given above, and the heat-transfer parameter was found to depend only upon the total variation in $\rho\mu$ across the boundary layer, in accordance with the relation

$$Nu/\sqrt{Re} = 0.67(\rho_s\mu_s/\rho_w\mu_w)^{0.4} \qquad (58)$$

The numerical correlation leading to Eq. (58) is shown in Fig. 2. The solution of Cohen and Reshotko[10] for $l = 1$ is also plotted, after correcting for Prandtl Number by multiplying their result by $(0.71)^{0.4}$.
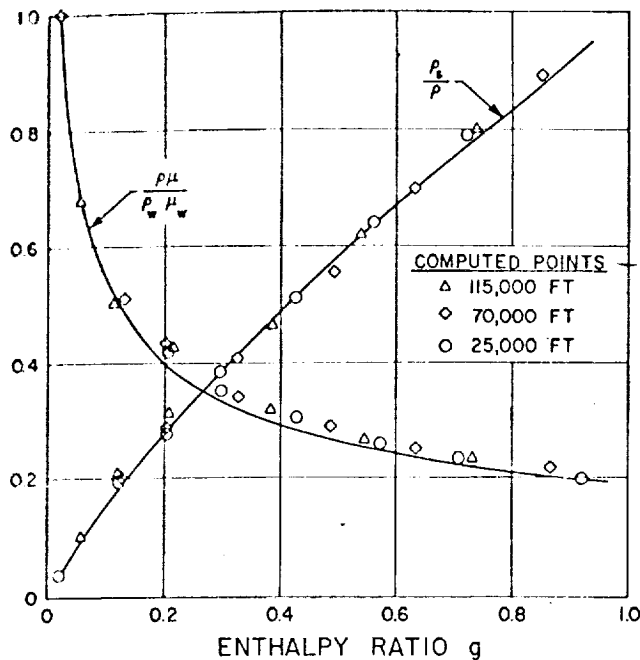
FIG. 1. Variation of $\rho\mu/\rho_w\mu_w$ and $\rho_s/\rho$ through a stagnation point boundary layer, shown as a function of enthalpy ratio $g$. Stagnation conditions are for a flight velocity of 19,700 ft. per sec. at various altitudes. $T_w = 300°K$.

An alternative procedure for the equilibrium boundary layer is to solve Eqs. (34), (35) and (36) simultaneously (hereafter denoted as Method 2). An appreciable simplification results if we consider air to be composed of only "air" molecules and "air" atoms having an average heat of formation given by

$$h_A{}^0 = \sum_{\text{atoms}} c_{is}(-h_i{}^0) / \sum_{\text{atoms}} c_{is} \qquad (59)$$

where the summation extends over atomic oxygen and nitrogen only. Thus only one diffusion equation (34) is needed for the diffusion of air atoms. With this simplification the equilibrium boundary layer may be treated by eliminating the term involving $w_i$ between Eq. (34) and (36). A solution is then possible when $\bar{c}_p$ and $l$ are specified as functions of $s_A$ and $\theta$, and $s_A$ is specified as a function of $\theta$ through the known equilibrium atom fraction as a function of temperature. (Details of the approximations made are given in the Appendix.)

This alternative solution was found to give very closely the same results as the Method 1 for a Lewis Number of unity, and the results are compared with Eq. (58) in Fig. 2. For a Lewis Number of unity, Method 2 is believed to be less accurate than Method 1, since it involves more approximations to the real gas properties.

For other values of the Lewis Number, the effect of Lewis Number on the heat-transfer parameter was found by Method 2 to be best given by

$$(Nu/\sqrt{Re}) (Nu'/\sqrt{Re})_{L=1} = 1 + \qquad (L^{0.52} - 1) (h_D/h_s) \qquad (60)$$

where the "dissociation enthalpy" $h_D$ is defined as

$$h_D = \sum c_{is}(-h_i{}^0) = h_A{}^0 \sum_{\text{atoms}} c_{is} \qquad (61)$$

i.e., $h_D$ is the dissociation enthalpy per unit mass of air in the external flow. The numerical results are plotted in Fig. 3 for comparision with Eq. (60).

It was also possible to determine the effect of Lewis Number from the Method 1 computations by evaluating the additional term in Eq. (37) involving $(L - 1)$ from the equilibrium properties of air. (The approximation for this evaluation is discussed in the Appendix.) Two such cases were computed, and the results are plotted in Fig. 3 for comparison with Eq. (60). While there is some disagreement with the results of Method 2, it is not too unreasonable considering the many different approximations involved in fitting curves to the functions $l$, $\bar{c}_p$, etc. It is the authors' opinion that the Method 2 solutions give a better indication of the Lewis Number effect for the equilibrium boundary layer, as embodied in Eq. (60). However, for Lewis Number unity the effect of $\rho\mu$ variation is believed to be better given by the results of Method 1 [Eq. (58)], so that the total effect may be obtained by combination of Eqs. (58) and (60) in the form

$$Nu/\sqrt{Re} = 0.67(\rho_s\mu_s/\rho_w\mu_w)^{0.4} \times \{1 + (L^{0.52} - 1)(h_D/h_s)\} \qquad (62)$$

The stagnation point heat-transfer rate for $\sigma = 0.71$ thus becomes, by virtue of Eq. (45),*

$$q = 0.94(\rho_w\mu_w)^{0.1}(\rho_s\mu_s)^{0.4} \times \{1 + (L^{0.52} - 1)(h_D/h_s)\}(h_s - h_w)\sqrt{(du_e/dx)_s} \qquad (63)$$

It is interesting to note that the external flow properties are much more important than the wall values in determining the heat-transfer rate, so that the uncertainty in the heat transfer is about 40 per cent of the un-

---

* For $\sigma$ not equal to 0.71, it is recommended that the factor 0.94 be replaced by $(0.76\ \sigma^{-0.6})$.
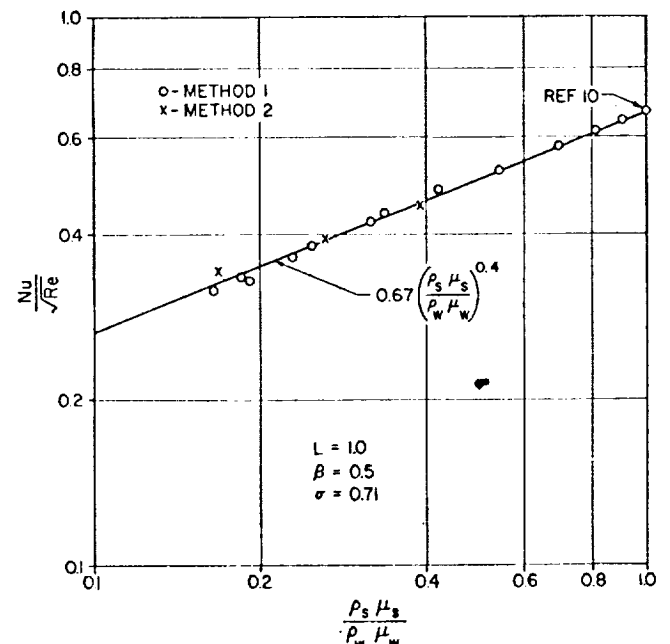


FIG. 2. Correlation of the heat-transfer parameter $Nu/\sqrt{Re}$ as a function of the $\rho\mu$ ratio across the boundary layer, $\rho_s\mu_s/\rho_w\mu_w$, for the equilibrium stagnation point boundary layer with $L = 1$.

certainty in the external viscosity. The physical reason for the importance of the external viscosity is that the growth of the boundary layer, and hence the heat transfer to the wall, depends mostly upon the external properties. The analogy with turbulent boundary layers is easily seen.

For a modified Newtonian flow, the stagnation point velocity gradient is

$$(du_e/dx)_s = (1/R)\sqrt{2(p_s - p_\infty)/\rho_s} \qquad (64)$$

where $R$ is the nose radius and $p_\infty$ is the ambient pressure.

## (9) The "Frozen" Boundary Layer

When atomic gas phase recombination is negligible ($C_1 = 0$), atoms diffusing from the free stream will reach the wall. If the wall is *noncatalytic* to surface recombination, the atom fraction at the wall will build up to the free-stream value. On the other hand, if the wall is *catalytic*, the atom concentration will be reduced to its equilibrium value at the wall temperature. Intermediate cases of wall catalyticity are of course possible, but only these extremes were computed.

Eqs. (34), (35), and (36) were solved with $C_1 = 0$ for various stagnation conditions and Lewis Numbers as discussed in the Appendix (Method 2).

For Lewis Number unity, the effect of the $\rho\mu$ variation was very close to that found for the equilibrium boundary layer by Method 2, and could suitably be expressed by Eq. (58). For other values of $L$, the dependence could best be given by*

$$(Nu/\sqrt{Re})/(Nu/\sqrt{Re})_{L=1} = 1 + (L^{0.63} - 1)(h_D/h_s) \qquad (65)$$

The calculated values are compared with Eq. (65) in Fig. 4.

The difference in the exponent of $L$ for the frozen as compared with the equilibrium boundary layer [Eqs. (60) and (65)] is quite certain since exactly the same property variations were used in both cases, and also seems reasonable in view of the greater importance of diffusion throughout the whole of the frozen boundary layer. It can be seen, however, that for a Lewis Number not too far from unity there is little difference in heat transfer for the frozen as opposed to the equilibrium boundary layer.

A few cases for noncatalytic wall were also computed. The resultant heat-transfer parameter could be given approximately by Eq. (62) with $L = 0$—i.e., the heat transfer becomes proportional to $h_s - h_D$.

A comparison of the distributions of enthalpy, temperature, and atom concentration for an equilibrium and a frozen boundary layer with identical catalytic wall and free-stream conditions is shown in Figs. 5 and 6. Both cases give very nearly the same heat transfer; however, the enthalpy distributions are slightly different (since $L = 1.4$) and the temperature and concentration

* Note that Lees [see reference 7, Eq. (19)] suggested that, for the frozen boundary layer, the exponent of $L$ in Eq. (65) be 2/3.

distributions are markedly different, as is the mechanism of heat transfer.

## (10) Finite Recombination Rate

This most general case was solved using Method 2 with values of the recombination rate parameter ($C_1$) varying from zero (frozen) to infinity (equilibrium). As for the frozen boundary layer, the wall may be either catalytic or noncatalytic, and both of these alternatives were calculated. It is to be expected, of course, that for large values of $C_1$ (near equilibrium) there should be little effect of wall catalysis, since few atoms reach the wall.

The heat-transfer parameter for one flight condition and wall temperature is plotted in Fig. 7 for the complete range of $C_1$. The solid lines are the total heat transfer for both catalytic (upper curve) and noncatalytic (lower curve) surfaces. For the catalytic wall, the fraction of heat transfer by conduction alone is shown by the dotted curve, so that the freezing of the boundary layer as recombination slows down ($C_1$ decreasing) is easily evident.

For either wall condition, $C_1$ must change by a factor of $10^4$ in order for the boundary layer to change from substantially frozen to equilibrium throughout. Within this region of variation of $C_1$, the boundary layer will be partly frozen (near the outer edge) and partly in equilibrium (near the wall). Since the recombination term [Eq. (56)] varies as $T^{-3.5}$, and the temperature changes by a factor of twenty between wall and external flow for the case considered, large variations in the recombination rate are possible across the boundary layer, thus permitting it to be partly frozen and partly in equilibrium.

For the noncatalytic wall, the distributions of atom mass fraction for several recombination rate parameters are shown in Fig. 8. For $C_1$ very large, no atoms reach the wall, all having recombined in the gas. For lower values of $C_1$, some atoms reach the wall and, because none recombine on the wall, a finite atom concentration builds up. For $C_1$ approaching zero, there is no recombination and hence no concentration gradients exist.

It can be seen in Fig. 7 that a much lower value of $C_1$ is necessary to "freeze" the boundary layer when a noncatalytic wall is used than would be the case otherwise. This is caused by the "damming up" of the atoms at the noncatalytic wall, resulting in greater recombination because of high local concentrations.

From Eqs. (57) and (63) it can be seen that, for a given flight velocity (hence $T_s$), $C_1$ varies as the square of the stagnation point density (and thus for strong shock waves, as the square of the ambient density), and also as the nose radius. Thus the boundary layer would become frozen at a high enough altitude, this altitude being less for small nose radii than for large. In order to change from a frozen to an equilibrium boundary layer, $C_1$ must change by $10^4$, and thus the density by $10^2$, which is an altitude change of about 100,000 ft.
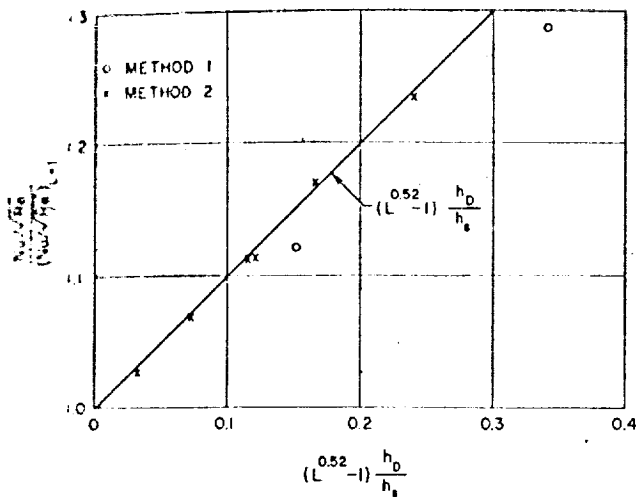
FIG. 3. Correlation of Lewis Number effects on the heat-transfer parameter $Nu/\sqrt{Re}$ for the equilibrium stagnation point boundary layer with $L = $ constant $\neq 1$.
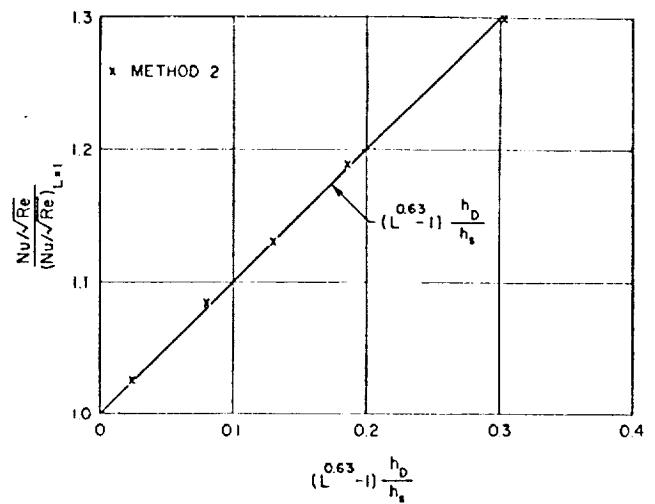


FIG. 4. Correlation of Lewis Number effects on the heat-transfer parameter $Nu/\sqrt{Re}$ for the frozen stagnation point boundary layer, $L = $ constant $\neq 1$.
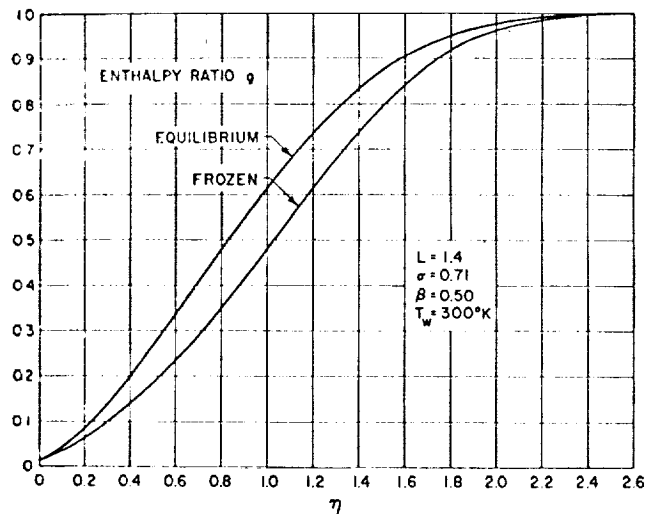


FIG. 5. Comparison of enthalpy distributions for an equilibrium and a frozen stagnation point boundary layer with the same external flow and wall conditions, $g_w = 0.0123$, $c_{AS} = 0.499$.
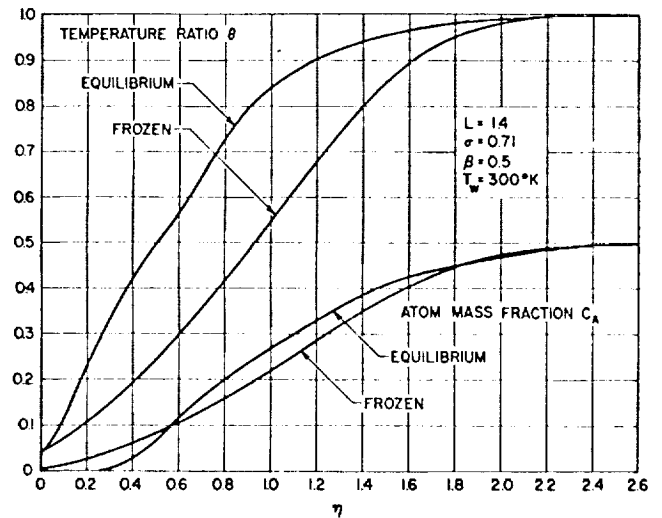


FIG. 6. Comparison of temperature and atom concentration distributions for an equilibrium and a frozen boundary layer with the same external flow and wall conditions, $g_w = 0.0123$, $c_{AS} = 0.499$.
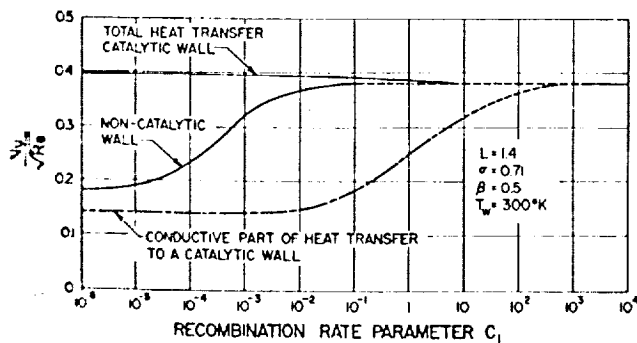


FIG. 7. Heat-transfer parameter $Nu/\sqrt{Re}$ for a boundary layer with finite recombination rates i.e., various values of the recombination rate parameter $C_1$, $g_w = 0.0123$, $c_{AS} = 0.536$. Note the reduction of heat transfer to a noncatalytic wall for low values of $C_1$.
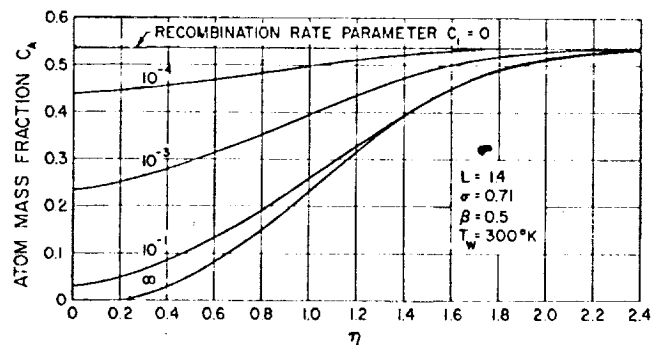


FIG. 8. Distributions of atom mass fraction in a stagnation point boundary layer on a noncatalytic wall for several values of the recombination rate parameter $C_1$, $g_w = 0.0123$, $c_{AS} = 0.536$.

## (11) Conclusions

The laminar stagnation point heat transfer in dissociated air can be given by Eqs. (63) and (65) for the equilibrium and frozen boundary layers, respectively. These results were computed for a Prandtl Number of 0.71 and for a Lewis Number which was constant throughout the boundary layer.

The major deviation in the heat-transfer parameter from the low temperature, perfect gas value is due to the variation of $\rho\mu$ across the boundary layer. The heat transfer [Eq. (63)] is mainly dependent upon the value of $\rho\mu$ at the outer edge of the boundary layer.

If the wall catalyzes atomic recombination, the total heat transfer is not much affected by a nonequilibrium state of the boundary layer if the Lewis Number is near unity.

If the wall is noncatalytic, the heat transfer may be appreciably reduced when the boundary layer is frozen throughout—i.e., when the recombination reaction time becomes much longer than the time for a particle to diffuse through the boundary layer. Since the ratio of these times depends upon altitude and nose radius, there is a scale effect which determines the chemical state of the boundary layer.

## Appendix—Details of the Numerical Solutions

### Method 1

The momentum equation for the stagnation point boundary layer is given by Eq. (35)—namely,

$$(lf_{\eta\eta})_\eta + ff_{\eta\eta} + (1/2)[(\rho_s/\rho) - f_\eta^2] = 0 \quad \text{(A-1)}$$

If thermal diffusion is neglected (i.e., $L_i{}^T = 0$) then the energy equation in terms of the enthalpy becomes, from Eq. (37),

$$[(l/\sigma)g_\eta]_\eta + fg_\eta + \{(l/\sigma)\Sigma[c_{is}(h_i - h_i^0)/h_s](L_i - 1)s_{i\eta}\}_\eta = 0 \quad \text{(A-2)}$$

or

$$[(l/\sigma)(1 + d)g_\eta]_\eta + fg_\eta = 0 \quad \text{(A-3)}$$

where

$$d \equiv \Sigma[c_{is}(h_i - h_i^0)/h_s](L_i - 1)(\partial s_i/\partial g)_p \\ = (L - 1)\Sigma(h_i - h_i^0)(\partial c_i/\partial h)_p \quad \text{(A-4)}$$

where the subscript $p$ denotes that the differentiation is at constant pressure and it is assumed $L_i = L = $ constant for all species.

In Method 1, which is suitable only for the equilibrium boundary layer, Eqs. (A-1) and (A-3) were solved simultaneously with the boundary conditions

$$f(0) = 0, \quad f_\eta(0) = 0, \quad f_\eta(\infty) = 1$$

$$g(0) = g_w, \quad g(\infty) = 1$$

The functions $l$, $\rho_s/\rho$ and $d$ were evaluated from the calculated equilibrium properties of air[11] and by taking the viscosity to vary according to Sutherland's formula [see Section (5) above]. For given external (stagnation point) flow conditions these quantities were plotted as functions of $g$. For numerical computation it was convenient to use analytic expressions of the following form:

$$l \equiv \rho\mu/\rho_w\mu_w = (\alpha_1/\sqrt{g}) - (\alpha_2 g) \quad \text{(A-5)}$$

$$\rho_s/\rho = 1 - \gamma_1(1 - g) - \gamma_2(1 - g)^4 \quad \text{(A-6)}$$

$$d = (L - 1)\Sigma(h_i - h_i^0)(\partial c_i/\partial h)_p = \beta_1 e^{-\beta_2/g} \quad \text{(A-7)}$$

The constants $\alpha$, $\gamma$, $\beta$ in each expression were determined by fitting these expressions to the equilibrium air calculations (see Fig. 1).

Numerical solutions for this problem were obtained on an IBM 650 computer. The method of solution was to pick values of $f_{\eta\eta}(0)$ and $g_\eta(0)$ and integrate the equations directly, recording the resultant asymptotic values of $f_\eta$ and $g$ for large values of $\eta$. After three such integrations an interpolation will produce better values of $f_{\eta\eta}(0)$ and $g_\eta(0)$. The interpolation procedure was repeated until the required conditions at "infinity" were met—i.e., $f_\eta \to 1$ and $g \to 1$. This interpolation was made an integral part of the numerical program so by starting with three initial guesses for $f_{\eta\eta}(0)$ and $g_\eta(0)$ the program would run automatically to completion.

It should be noted that Eqs. (A-1) and (A-3) are formally identical with the stagnation point equations solved by Cohen and Reshotko[10] except for the function $d$ [Eq. (A-4)]. If $L = 1$, however, $d \equiv 0$; thus by specifying $L = 1$, $\sigma = 1$, $l = 1$ and $\rho_s/\rho = g$, the stagnation point solutions given by Cohen and Reshotko could be duplicated. (A table giving the specific values of the parameters for which solutions were obtained by the method described above may be obtained directly from the authors.)

### Method 2

This method is a more general formulation in that it allows computation of the nonequilibrium boundary layer. As may be expected, however, it involves more approximations than the rather straightforward procedure of Method 1.

In the nonequilibrium case, the concentration of the various species is not determined by the enthalpy and the (known) pressure. It is necessary, therefore, to add a continuity equation for each species. Furthermore, it is convenient to express the thermodynamic properties in terms of the temperature and the concentrations of the species. The energy equation should, therefore, be written in terms of the temperature. To make this problem tractable it was assumed that air is a diatomic gas composed of "air" molecules and "air" atoms with properties properly averaged between oxygen and nitrogen. The dissociation energy of an air atom was taken to be the average dissociation energy in the external flow [see Eq. 59)]. With this assumption the problem is reduced to the simultaneous solution of three equations (momentum, energy and atom concentration) and the thermodynamic properties are to be expressed in terms of the temperature and atom concentration.

The momentum equation is still Eq. (A-3), with

$$\rho_s'/\rho = [(1 + c_A)/(1 + c_{As})]\theta \qquad (A-8)$$

$$l \equiv \rho\mu'/\rho_w\mu_w = [1/(1 + c_A)]^{3/2}(\theta_w/\theta)F(\theta) \quad (A-9)$$

where

$$F(\theta) \equiv (T_s\theta/300)^{3/2}[413/(T_s\theta + 113)] +$$
$$3.7(T_s\theta/10,000)^2 - 2.35(T_s\theta/10,000)^4$$

and the stagnation temperature $T_s$ is given in degrees Kelvin. The function $F(\theta)$ is a fitted curve giving the temperature dependence of the viscosity under the assumption that the atoms and molecules have the same collision cross-sections.

The energy equation in terms of the temperature is, from Eq. (36) with $L_i^T = 0$,

$$[(cl/\sigma)\theta_\eta]_\eta + cf\theta_\eta + (l/\sigma)\theta_\eta \times$$
$$\Sigma(c_{pi}/\bar{c}_{pw})L_i c_{i_s} s_{i\eta} + \{2(du_e/dx)_s\}^{-1} \times$$
$$\Sigma(w_i/\rho)[(h_i^0 - h_i)/\bar{c}_{pw}T_s] = 0 \quad (A-10)$$

where $c \equiv \bar{c}_p/\bar{c}_{pw}$

With the assumption of a simple diatomic gas and taking $L_i = L =$ constant, the third term may be rewritten as

$$(Ll/\sigma)\theta_\eta c_{A\eta}[(c_{pA} - c_{pM})/\bar{c}_{pw}]$$

and the fourth term, using Eqs. (56), (57), and (61), and taking $h_A = h_M$, becomes

$$C_1(h_D/\bar{c}_{pw}T_s)[(c_A^2 - c_{AE}^2)/\theta^{3.5}(1 + c_{As})]$$

Now $\quad c_{pM} \approx (\Re/M)\{(7/2) + e^{-(Tv/T)^2}\}$

where the exponential is the vibrational heat capacity and $T_V \approx 800°K.$ for air; also

$$c_{pA} = (5/2)[\Re/(M/2)]$$

Hence,

$$c \equiv \bar{c}_p/\bar{c}_{pw} = (10/7)c_A + \{1 + (2/7)e^{-(\theta v/\theta)^2}\}(1 - c_A) \qquad (A-11)$$

$$(c_{pA} - c_{pM})/\bar{c}_{pw} = (3/7) - (2/7)e^{-(\theta v/\theta)^2} \quad (A-12)$$

For computation then the energy equation becomes

$$[(cl/\sigma)\theta_\eta]_\eta + cf\theta_\eta + e(Ll/\sigma)\theta_\eta c_{A\eta} + C_1 C_2 m = 0 \quad (A-13)$$

where

$$l \equiv \rho\mu/\rho_w\mu_w = [1/(1 + c_A)]^{3/2}(\theta_w/\theta)F(\theta),$$
$$\text{see Eq. (A-9)}$$

$$e \equiv (c_{pA} - c_{pM})/\bar{c}_{pw} = (3/7) - (2/7)e^{-(\theta v/\theta)^2}$$

$$c \equiv \bar{c}_p/\bar{c}_{pw} = (10/7)c_A +$$
$$\{1 + (2/7)e^{-(\theta v/\theta)^2}\}(1 - c_A)$$

$C_1 =$ parameter, see Eq. (57)

$C_2 \equiv h_D/\bar{c}_{pw}T_s =$ parameter, see Eq. (61)

$m \equiv (c_A^2 - c_{AE}^2)/\theta^{3.5}(1 + c_A)$

The equilibrium atom mass fraction $c_{AE}$ can be determined from reference 11. For computation $c_{AE}$ was approximated by

$$c_{AE} = c_{As}e^{C_3(1 - 1/\theta)} \qquad (A-14)$$

where $C_3$ is a constant.

The continuity equation for atoms was written in terms of the atom mass fraction $c_A$ instead of the normalized atom mass fraction $s$. Thus Eq. (34) becomes

$$[(lL/\sigma)c_{A\eta}]_\eta + fc_{A\eta} -$$
$$\{2(du_e/dx)_s\}^{-1}\Sigma(w_i/\rho) = 0 \quad (A-15)$$

or

$$[(lL/\sigma)c_{A\eta}]_\eta + fc_{A\eta} - C_1 m = 0 \qquad (A-16)$$

Method 2 for the nonequilibrium boundary layer is the simultaneous solution of Eqs. (A-1), (A-13) and (A-16) with the boundary conditions

$$f(0) = 0, \quad f_\eta(0) = 0, \quad f_\eta(\infty) = 1$$
$$\theta(0) = \theta_w, \quad \theta(\infty) = 1$$

$c_A(0) = 0$ for catalytic wall $\quad\big\}$
$c_{A\eta}(0) = 0$ for noncatalytic wall $\quad$ $c_A(\infty) = c_{As}$

Solutions were obtained on a digital computer using an iterative procedure similar to that used in Method 1.

The limiting case of the equilibrium boundary layer was obtained by Method 2 by eliminating the term $C_1 m$ between Eqs. (A-13) and (A-16) and solving the resulting equation simultaneously with Eq. (A-1), taking the equilibrium atom concentration as a known quantity in the form of Eq. (A-14). The limiting case of the frozen boundary was obtained by putting $C_1 \equiv 0.$*

### REFERENCES

[1] Moore, L. L., *A Solution of the Laminar Boundary Layer Equations for a Compressible Fluid with Variable Properties, Including Dissociation,* Journal of the Aeronautical Sciences, Vol. 19, No. 8, pp. 505-518, August, 1952.

[2] Hansen, C. F., *Note on the Prandtl Number for Dissociated Air,* Journal of the Aeronautical Sciences, Vol. 20, No. 11, pp. 789-790, November, 1953.

[3] Romig, M. F., and Dore, F. J., *Solutions of the Compressible Laminar Boundary Layer Including the Case of a Dissociated Free Stream,* Convair Report No. ZA-7-012, San Diego, Calif., 1954.

[4] Beckwith, I. E., *The Effect of Dissociation in the Stagnation Region of a Blunt-Nosed Body,* Journal of the Aeronautical Sciences, Vol. 20, No. 9, pp. 645-646, September, 1953.

[5] Crown, J. C., *The Laminar Boundary Layer at Hypersonic Speeds,* Navord Report 2299, U.S. Naval Ordnance Lab., 1952.

[6] Mark, R., *Compressible Laminar Heat Transfer Near the Stagnation Point of Blunt Bodies of Revolution,* Convair Report No. ZA-7-016, San Diego, Calif., 1955.

[7] Lees, L., *Laminar Heat Transfer Over Blunt-Nosed Bodies at Hypersonic Flight Speeds,* Jet Propulsion, Vol. 26, No. 4, pp. 259-269, 1956.

[8] Hirschfelder, J. O., Curtiss, C. F., and Bird, R. B., *Molecular Theory of Gases and Liquids,* John Wiley and Sons, Inc., New York, 1954.

[9] Probstein, R. F., *Methods of Calculating the Equilibrium Laminar Heat Transfer Rate at Hypersonic Flight Speeds,* Jet Propulsion, Vol. 26, No. 6, pp. 497-499, 1956.

[10] Cohen, C. B., and Reshotko, E., *Similar Solutions for the Compressible Laminar Boundary Layer with Heat Transfer and Pressure Gradient,* NACA TN 3325, 1955.

[11] Hilsenrath, J. and Beckett, C., *Tables of Thermodynamic Properties of Argon-Free Air to 15,000°K,* AEDC-TN-56-12, Arnold Engineering Development Center, USAF, September, 1956 (ASTIA Document No. AD-98974).

*Numerical results of these calculations may be obtained directly from the authors.

[12] Fay, J. A., Riddell F. R., and Kemp, N. H., *Stagnation Point Heat Transfer in Dissociated Air Flow*, Technical Notes, Jet Propulsion, Vol. 27, pp. 672–674, 1957.

[13] Fay, J. A., *The Laminar Boundary Layer in a Dissociating Gas*, Avco Research Laboratory TM-13, June, 1955.

[14] Kuo, Y. H., *Dissociation Effects ir Hypersonic Viscous Flows*, Journal of the Aeronautical Sciences, Vol. 24, No. 5, pp. 345 350, May, 1957.

[15] Rose, P. H., and Stark, W. I., *Stagnation Point Heat-Transfer Measurements in Dissociated Air*, Journal of the Aeronautical Sciences, Vol. 25, No. 2, pp. 86–97, February, 1958.

# RADIATION HEAT TRANSFER TO HYPERSONIC VEHICLES

ROLAND E. MEYEROTT
Lockheed Missile Systems Division
Palo Alto, California

*A survey is made of what is known about the emission characteristics of air at temperatures and densities of interest for radiation heating in hypersonic flight. The problem is illustrated by considering two examples which should cover the range of interest: a locally hemispherical ballistic missile nose re-entering the atmosphere, and a sphere used as a circumlunar carrier under extreme re-entry conditions. These examples are followed by a survey of the existing theory of emissivity of air and an analysis of recent experimental data.*

## INTRODUCTION

THE so-called "aerodynamic heating" associated with vehicle re-entry into the atmosphere has received wide attention of late. Temperatures have been reached which produce considerable luminosity in the surrounding air and which, in fact, require consideration of the radiative transport as one of the factors determining the temperature balance of the re-entry vehicle.

Since the radiation heat transfer is determined by the emission properties of heated air, the present paper is designed to be a survey of what is known about the emission characteristics of hot air. Our knowledge of the emission properties of air is derived from only a limited amount of experimental data, supplemented and interpreted by a considerable amount of theory, so that a reasonably complete discussion of the problem becomes lengthy and involved. In order to preserve the continuity of thought in the paper, the introductory discussion of heat transfer by convection and radiation will be followed by conclusions as to their relative importance for two examples which should bracket the range of interest. The results of the remainder of the paper will be employed in making this comparison. The remainder of the paper will attempt to summarize our present state of knowledge of the emission and absorption properties of hot air.

### AEROTHERMODYNAMICS OF HYPERSONIC BLUNT BODIES

When a blunt-nosed vehicle passes through the air at hypersonic speeds, an overall pattern of air flow results as shown in *Fig. 1*. The intense compressional heating and acceleration of the air are accomplished by the detached bow shock wave. Upon traversing this shock, the air enters the shock layer, which is, in fact, the high-temperature environmental source for the heat transfer. Since the radiation heat transfer is greatest at the stagnation point, we shall limit our discussion to that region. The thickness of the shock layer

at the stagnation point, i.e. the stand-off distance $\delta$, depends upon the radius of the curvature $R$ of the nose cone and $\rho_1/\rho_2$, the air density ratio across the shock. It has been shown to be approximately

$$\delta \simeq R\rho_1/\rho_2 \tag{1}$$

The temperature in the shock region is reasonably uniform across the shock layer except for the extremely thin boundary-layer profiles immediately adjacent to the surface. The temperature and density of the air in the shock
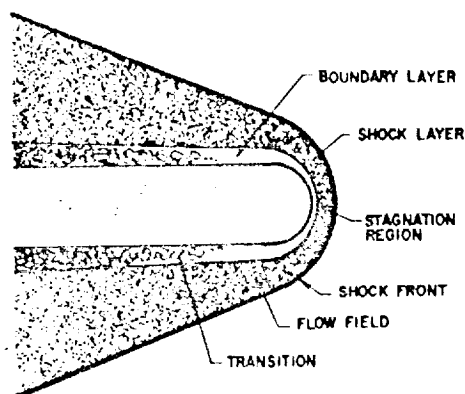


*Fig. 1. Flow pattern around hypersonic vehicle nose*

layer depend upon the velocity of the missile and the temperature and density of the ambient air. The convective and radiative heat transfer depend on density and missile velocity in a different manner. At the stagnation point, the convective heat flux, assuming a laminar boundary layer $\dot{q}_c$, depends to a good approximation on air density $\rho$, missile velocity $U$, and radius of curvature $R$, as

$$\dot{q}_c \sim (\rho/R)^{1/2}U^3 \tag{2}$$

while a fit to the emissivity of air data gives for the radiative heat transfer at the stagnation point

$$\dot{q}_r \sim \rho^{3/2}RU^{10} \tag{3}$$

We see here that the radiative heat transfer will be relatively more important for blunt bodies, high velocities, and high densities.

The situation in which one is most likely to be concerned with the radiative heat transfer occurs during re-entry of vehicles into the atmosphere. Under re-entry conditions, the radiation contribution is likely to be largest at intermediate altitudes (70,000–200,000 ft) where the velocity of the missile is still high but where the ambient density of air is appreciable.

In order to be more specific, we shall consider two examples to illustrate the problem and the magnitude of the radiation heating contribution.

*Example 1:* A locally hemispherical ballistic missile nose of radius of curvature 2 ft with a re-entry velocity around 25,000 ft/sec at 120,000 ft altitude. We shall only consider the heat load for typical weight/drag situations.

*Example 2:* A sphere used as a circumlunar instrument carrier of 18 in. radius re-entering the atmosphere at normal incidence with a speed of 35,000 ft/sec. This case has been treated by GAZLEY and MASSON[1] and illustrates the magnitude of the heat load for extreme re-entry conditions.

For the ballistic missile example, typical shock-layer conditions at the stagnation point for peak heating are temperature and density in the range 8000°K, 0·075 of normal atmospheric density to 7800°K, 0·295 of normal
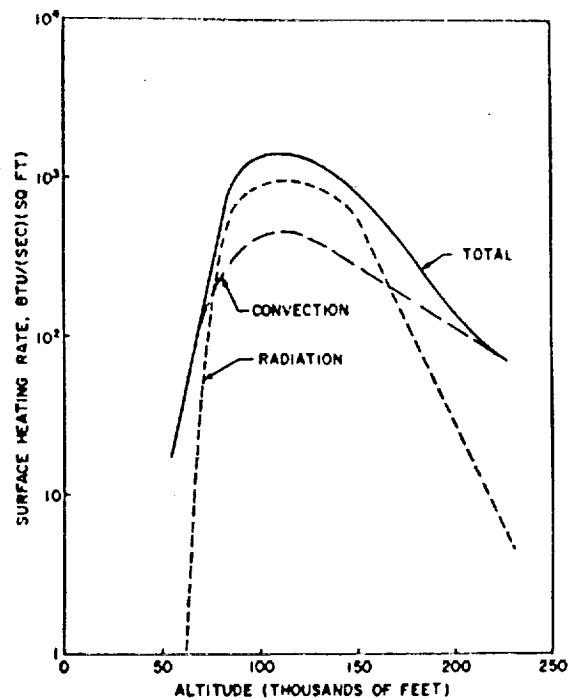
Fig. 2. *Heating rate during direct re-entry of circumlunar vehicle*

atmospheric density respectively with stand-off distance of about 1·6 in. for the spherical nose of 24 in. radius of curvature. For the circumlunar instrument carrier, the corresponding conditions are temperature and density in the range 11,000°K, 0·014 of normal atmospheric density to 7500°K, 0·43 of normal atmospheric density with stand-off distance of about 1·2 in. for the sphere of 18 in. radius.

For the ballistic missile case, the peak heating occurs for typical conditions at altitudes in the neighborhood of 100,000 ft. Typical convective heat flux for a laminar boundary layer at the stagnation point is 775 B.t.u./ft$^2$ sec while the radiation heat-transfer flux is 75 B.t.u./ft$^2$ sec. The radiation heat flux contributes only about 10 per cent to the heat load for this case.

For the circumlunar vehicle, the surface heating rates as computed by GAZLEY and MASSON[1] are shown in *Fig. 2*. At altitude from 70,000 to 150,000 ft, the principle contribution to the heat load is that due to radiation.

The results quoted in the above examples are based on the experiments and theories discussed in the remainder of the present paper. It can be said that, for the ballistic missile case, the radiation heat transfer is sufficiently well known that its relative unimportance can be demonstrated. For the circumlunar vehicle case where, as we have seen, the radiation heat transfer predominates, there is still enough uncertainty in our knowledge of the emission coefficients of air to limit the accuracy of that calculation. At the higher temperatures and lower densities there may be uncertainties of as much as a factor of 2 in the emissivities and hence the radiation heat transfer.

## CALCULATION OF THE RADIATION HEAT TRANSFER
### FROM THE ABSORPTION COEFFICIENTS

We shall consider the radiation heat transfer at the stagnation point only, where the radiation heat load is greatest. The radiating gas will be considered to be an infinite slab of thickness equal to the stand-off distance $\delta$, of uniform temperature $T_s$, and density $\rho_s$, equal to the stagnation temperature and density of the gas. It will be assumed that the collision frequencies will be sufficiently high so that a true particle temperature exists, i.e. local thermodynamic equilibrium.

If $I_\nu(\theta)$ is the energy in the frequency range between $\nu$ and $\nu + d\nu$ incident per unit area into a solid angle $d\omega$ making an angle $\theta$ with the normal to the slab, then $I_\nu$ is given by

$$I_\nu(0) = B_\nu(T_s) [1 - \exp(-\mu'_\nu \, \delta \sec \theta)] \tag{4}$$

$$\mu'_\nu = \mu_\nu [1 - \exp(h\nu/kT_s)]$$
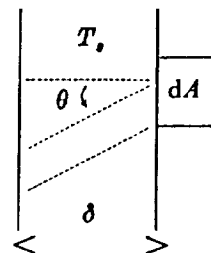
where

$\mu_\nu$ is the absorption coefficient at frequency $\nu$,

$h$ is Planck's constant,

$B_\nu(T)$ is the specific intensity for a black body

$$B_\nu(T) \, d\nu = (\sigma/\pi) \, T^4 P(u) \, du,$$

$$\text{where } u = h\nu/kT,$$

$\sigma$ is the Stephan–Boltzmann constant,

$P(u) \, du$ is the fraction of the energy of the Planck spectrum which lies in the frequency range between $u$ and $u + du$.

The total energy $\dot{q}_r$ transferred per second to a unit area of the surface is

$$\dot{q}_r = 2\pi \int_0^\infty d\nu \int_0^{\pi/2} A_\nu(\theta) I_\nu(\theta) \cos\theta \sin\theta \, d\theta \tag{5}$$

where

$A_\nu(\theta)$ is the absorption coefficient of surface at the angle of incidence $\theta$ and frequency $\nu$. Using Eq. (4), Eq. (5) becomes

$$\dot{q}_r = 2\pi \int_0^\infty B_\nu(T_s) \, d\nu \int_0^{\pi/2} A_\nu(\theta)[1 - \exp(-\mu'_\nu \, \delta \sec\theta)] \cos\theta \sin\theta \, d\theta \tag{6}$$

For points on a missile other than the stagnation point, the present treatment does not approximate the true situation since $I_\nu$ depends upon the azimuth angle $\Phi$ as well as $\theta$ considered here.

The expression for the total radiation flux $F$ incident on the surface can be obtained by putting the reflexion coefficient $A_\nu(\theta)$ equal to unity. When $\mu'_\nu \delta \ll 1$, the expression for the flux $F$ is approximately

$$F \simeq 2\pi\delta \int_0^\infty \mu'_\nu B_\nu(T) \, d\nu \tag{7}$$

According to the definition of $B_\nu(T)$,

$$F \simeq 2\delta \, \sigma T^4 \int_0^\infty \mu'_u \, P(u) \, du \tag{8}$$

Hence, we see that for $\mu'_\nu \delta \ll 1$, the emissivity $\epsilon$ becomes

$$\epsilon = 2\delta \int_0^\infty \mu'_u \, P(u) \, du \tag{9}$$

As can be seen from Eq. (6), the radiation heat transfer can be evaluated provided one knows the absorption coefficient $\mu_\nu$ for all frequencies at the required temperature and density. Most of the remainder of this paper will be concerned with a discussion of our present knowledge of the absorption and emission coefficients of air.

## ABSORPTION AND EMISSION PROPERTIES OF AIR

### Theory

There are a large number of constituents present in dry air in the temperature and density range of interest for the present problem. The most important of these according to abundance are $N_2$, $O_2$, NO, $NO_2$, N, O, $O^-$, $N_2^+$, $O_2^+$, $NO^+$, $N^+$, $O^+$, $CO_2$, CO and CN. The contribution to the absorption coefficient made by each constituent at a given temperature and density is determined by its concentration at that temperature and density and by its radiation properties. The concentrations of the important species are now well known from the work of GILMORE;[2] thus the problem is reduced to that of determining the radiation properties of each species.

The contributions to the total absorption coefficient can be conveniently divided into two classes: those arising from the continuous absorption transitions and those arising from the discrete transitions, i.e. line spectra. The contributions from the continuous transitions depend only on the

$f$-number for the transition, while those from the discrete transitions depend upon the line width and spacing as well as the $f$-number.

*Continuous absorption cross-sections*—The contributors to the continuous absorption coefficient of importance are $NO_2$, photoelectric absorption by O, N and $N_2$, and free-free absorption by electrons in the field of both positive ions and oxygen and nitrogen atoms. Only those species will be considered which are of importance for temperatures in the neighborhood of 8000°K of interest for radiation heat transfer in hypersonic flight.

$O^-$ *Photoelectric cross-section*—The photoelectric cross-section of $O^-$ has been measured by BRANSCOMB and SMITH.[3] They used an analyzed beam of $O^-$ ions in a mass spectrometer and have measured the photo cross-section from the apparent threshold of 1·45 –3 eV. A fit to their experimental cross-section, $\sigma$ in cm², in this energy range is

$$10^{18}\sigma = -26\cdot4 + 23\cdot7\epsilon - 3\cdot82\epsilon^2 \tag{10}$$

where $\epsilon$ is the photon energy in electron volts. This experimental cross-section is in rough agreement with that computed by BATES and MASSEY.[4] Unfortunately, neither the experimental nor the theoretical values are available for $\epsilon > 4$ eV. The theoretical work of BATES and MASSEY indicates a flattening off of the cross-section at around 4 eV. At very high energy, by analogy with other photo cross-sections, one would expect that the cross-section would vary approximately as $\epsilon^{-3}$. We have available an approximate sum rule stating that, for one electron transitions, $\Sigma f \simeq 1$. This may be expected to be the order of magnitude of the sum in this case, although since considerable polarization is involved in the $O^-$ binding energy, the sum may even exceed unity.

A reasonable estimate of the entire cross-section can be made by using Eq. (10) from 1·45 to 3 eV, assuming a constant cross-section from 3 eV to some point $\epsilon_1$ and one varying as $\epsilon^{-3}$ from $\epsilon_1$ to $\infty$. One can use the sum rule to evaluate $\epsilon_1$ which turns out to be 7·5 eV, making the cross-section for $\epsilon$ greater than 7·5 eV

$$10^{17}\sigma = (7\cdot3)^3\epsilon^{-3}$$

*O, N, $N_2$ Photoelectric cross-sections*—The photoelectric absorption by O, N and $N_2$ in their excited states lies in the frequency range of interest for the present problem. The photoelectric cross-section can be written

$$\sigma_{PE} = \frac{4\pi^2\alpha a_0^2}{Z_e^2}\frac{df}{d\nu} \tag{11}$$

where

$\alpha$ = fine structure constant

$a_0$ = Bohr radius for hydrogen

$Z_e$ = effective charge (to be taken as unity in the present application)

$df/d\nu$ = change in $f$-number per Rydberg

For the present application, we are interested in transitions from the excited states of O, N and $N_2$ from levels that would correspond to principal quantum number $n = 3$ or higher in hydrogen. Since the excited states more nearly approximate the hydrogen-like situation than the ground state, $df/d\nu$ is estimated by comparison with the hydrogen-like case. The photoelectric cross-section varies approximately as $\nu^{-3}$ from any particular photoelectric edge, which implies the same variation in $df/d\nu$. For hydrogen, levels of principal quantum number $n \sim 3$ have a total $f$-number in the continuum of about 0·2. We use these facts to evaluate $df/d\nu$. This gives

$$df/d\nu = 0\cdot4\ \nu_i^2/\nu^3 \tag{12}$$

where $\nu_i$ is the frequency corresponding to the ionization energy of that level expressed in Rydberg units. The photoelectric absorption coefficient is then

$$\mu_{PE} = N_i\ 1\cdot6\pi^2\ \alpha a_0^2\ (\nu_i^2/\nu^3) \tag{13}$$

where $N_i$ is the number of atoms or molecules per cubic centimeter in the state $i$, and $\nu$ is the frequency expressed in Rydberg units. Expression (13) predicts the absorption coefficient of neon in the ground state for a frequency of 1 Rydberg above the absorption edge to within a factor of 2.

$f$-number for the transition, while those from the discrete transitions depend upon the line width and spacing as well as the $f$-number.

*Continuous absorption cross-sections*—The contributors to the continuous absorption coefficient of importance are $NO_2$, photoelectric absorption by $O^-$, O, N, and free-free absorption by electrons in the field of both positive ions and oxygen and nitrogen atoms. Only those species will be considered which are of importance for temperatures in the neighborhood of 8000°K of interest for radiation heat transfer in hypersonic flight.

$O^-$ *Photoelectric cross-section*—The photoelectric cross-section of $O^-$ has been measured by BRANSCOMB and SMITH.[3] They used an analyzed beam of $O^-$ ions in a mass spectrometer and have measured the photo cross-section from the apparent threshold of $1 \cdot 45 - 3$ eV. A fit to their experimental cross-section, $\sigma$ in cm$^2$, in this energy range is

$$10^{18}\sigma = -26 \cdot 4 + 23 \cdot 7\epsilon - 3 \cdot 82\epsilon^2 \tag{10}$$

where $\epsilon$ is the photon energy in electron volts. This experimental cross-section is in rough agreement with that computed by BATES and MASSEY.[4] Unfortunately, neither the experimental nor the theoretical values are available for $\epsilon > 4$ eV. The theoretical work of BATES and MASSEY indicates a flattening off of the cross-section at around 4 eV. At very high energy, by analogy with other photo cross-sections, one would expect that the cross-section would vary approximately as $\epsilon^{-3}$. We have available an approximate sum rule stating that, for one electron transitions, $\Sigma f \simeq 1$. This may be expected to be the order of magnitude of the sum in this case, although since considerable polarization is involved in the $O^-$ binding energy, the sum may even exceed unity.

A reasonable estimate of the entire cross-section can be made by using Eq. (10) from $1 \cdot 45$ to 3 eV, assuming a constant cross-section from 3 eV to some point $\epsilon_1$ and one varying as $\epsilon^{-3}$ from $\epsilon_1$ to $\infty$. One can use the sum rule to evaluate $\epsilon_1$ which turns out to be $7 \cdot 5$ eV, making the cross-section for $\epsilon$ greater than $7 \cdot 5$ eV

$$10^{17}\sigma = (7 \cdot 3)^3\epsilon^{-3}$$

O, N, $N_2$ *Photoelectric cross-sections*—The photoelectric absorption by O, N and $N_2$ in their excited states lies in the frequency range of interest for the present problem. The photoelectric cross-section can be written

$$\sigma_{PE} = \frac{4\pi^2\alpha a_0^2}{Z_e^2}\frac{df}{d\nu} \tag{11}$$

where

$\alpha$ = fine structure constant

$a_0$ = Bohr radius for hydrogen

$Z_e$ = effective charge (to be taken as unity in the present application)

$df/d\nu$ = change in $f$-number per Rydberg

For the present application, we are interested in transitions from the excited states of O, N and $N_2$ from levels that would correspond to principal quantum number $n = 3$ or higher in hydrogen. Since the excited states more nearly approximate the hydrogen-like situation than the ground state, $df/d\nu$ is estimated by comparison with the hydrogen-like case. The photoelectric cross-section varies approximately as $\nu^{-3}$ from any particular photoelectric edge, which implies the same variation in $df/d\nu$. For hydrogen, levels of principal quantum number $n \sim 3$ have a total $f$-number in the continuum of about $0 \cdot 2$. We use these facts to evaluate $df/d\nu$. This gives

$$df/d\nu = 0 \cdot 4\,\nu_i^2/\nu^3 \tag{12}$$

where $\nu_i$ is the frequency corresponding to the ionization energy of that level expressed in Rydberg units. The photoelectric absorption coefficient is then

$$\mu_{PE} = N_i\,1 \cdot 6\pi^2\,\alpha a_0^2\,(\nu_i^2/\nu^3) \tag{13}$$

where $N_i$ is the number of atoms or molecules per cubic centimeter in the state $i$, and $\nu$ is the frequency expressed in Rydberg units. Expression (13) predicts the absorption coefficient of neon in the ground state for a frequency of $\nu = 1$ Rydberg above the absorption edge to within a factor of 2.

*Free-free absorption in the field of positive ions*—For the free-free absorption due to electrons absorbing radiation in the presence of ions, we use the Kramer formula for hydrogen ions with the effective charge $Z_e = 1$. The absorption coefficient for free-free transitions, $\mu_{ff}$ can be approximated by[5]

$$\mu_{ff} = \frac{16\pi^2 Z_e^2}{3\sqrt{3}} \frac{e^6}{hc(2\pi m)^{3/2}} \frac{N_e}{(kT)^{1/2}} \frac{N^+}{\nu^3} \tag{14}$$

where

$Z_e$ is the effective charge $= 1$

$N_e$ is the number of electrons per cm$^3$

$N^+$ is the number of positive ions per cm$^3$

$e$, $h$, $m$, $c$ and $k$ are respectively the electronic charge, Planck's constant, mass of electron, the velocity of light and the Boltzmann constant.

*The line absorption coefficient*—The line spectrum of importance for this temperature and density region in air is the many-line spectra associated with the electronic transitions in the diatomic molecules of $N_2$, $N_2{}^+$, NO and $O_2$.

The absorption coefficient $\mu_{mn,v''v',J''J'}$ corresponding to a transition in the molecule from electronic state $m$ to $n$, from vibrational level $v''$ to $v'$, and from rotational level $J''$ to $J'$ can be expressed as[6]

$$\mu_{mn,v''v',J''J'} = \frac{8\pi^3}{3hc} \nu_{mn,v''v',J''J'} N_{m,v'',J''} \frac{\sum\limits_{M'M''} |D|^2 \mathfrak{F}}{2J''+1} \tag{15}$$

where

the summation is over all values of magnetic quantum numbers $M'$ and $M''$, $\nu_{mn,v''v',J''J'}$ is the light frequency,

$N_{m,v'',J''}$ is the number of molecules per cubic centimetre in the initial state $m$, $v''$, $J''$,

$h$ and $c$ are respectively Planck's constant and the velocity of light,

$\mathfrak{F}$ is a shape factor for the line such that $\int_{line} \mathfrak{F}\, d\nu = 1$ and,

$D$ is the dipole matrix element.

When the total wave function is expressed as a product of an electronic function, a vibrational function, and a rotational function, the dipole matrix element $D$, can be written

$$R = D_e^{nm} \cdot D_{vib}^{v'v''} \cdot D_{rot}^{J'J''} \tag{16}$$

The following sum rules hold

$$\sum_{J'} \sum_{M'M''} \frac{|D_{rot}^{J'J''}|^2}{2J''+1} = 1 \tag{17}$$

and

$$\sum_{v'} |D_{vib}^{v'v''}|^2 = 1 \tag{18}$$

F2

If $\mu_{mn,v''v',J''J'}$ in Eq. (15) is multiplied by $d\nu$ and integrated over each line, summed over final rotational states $J'$, and summed over all initial rotational states $J''$, we obtain the absorption coefficient integrated over the band, $\mu_{mn,v''v'}$, which is

$$\mu_{mn,v''v'} = \frac{8\pi^3}{3hc} \nu_{mn,v''v'} N_{mv''} |D_e^{nm}|^2 \cdot |D_{vib}^{v'v''}|^2 \tag{19}$$

$\nu_{mn,v''v'}$ is some average value of $\nu_{mn,v''v',J''J'}$. Since rotational energies are very small compared to electronic excitation energies, this result is insensitive to the particular average chosen to evaluate this quantity. $N_{mv''}$ is the total number of molecules per cubic centimeter in the electronic states $m$ and vibrational states $v''$,

$$N_{mv''} = \sum_{J''} N_{m,v'',J''} \tag{20}$$

If $\mu_{mn,v''v'}$ in Eq. (19) is summed over final vibrational states $v'$, and then over all initial vibrational states $v''$, we obtain the absorption coefficient integrated over the entire band system $\mu_{mn}$,

$$\mu_{mn} = \frac{8\pi^3}{3hc} N_m \nu_{mn} |D_e^{nm}|^2 \tag{21}$$

Where $\nu_{mn}$ is the same average frequency for the electronic transition, and $N_m$ is the number of molecules per cubic centimeter in the initial electronic state $m$,

$$N_m = \sum_{v'} N_{mv'}.$$

(22)

By analogy with atomic transitions, one can define an $f$-number for the electronic transition as

$$f_{nm} = \frac{8\pi^2 m}{3he^2}\, \nu_{nm} \,|D_e^{nm}|^2$$

(23)

where
   $m$ is the electronic mass and
   $e$ is the electronic charge
$\mu_{mn}$ becomes

$$\mu_{mn} = N_m \frac{\pi e^2}{mc} f_{nm}$$

(24)

which is the usual expression for the integrated absorption for line spectrum in atoms. As in the case of atoms, for one electron spectrum

$$\sum_n f_{nm} \simeq 1$$

(25)

*The average absorption coefficient*—The absorption coefficient averaged over a frequency interval $\Delta\nu$ can be written

$$\bar{\mu}^{\Delta\nu} = \frac{1}{\Delta\nu} \int_{\Delta\nu} \mu \, d\nu$$

(26)

If the region in question contains lines, the integral in Eq. (26) will be converted to an integral over each line and a sum over all the lines in the interval. According to Eq. (15), the integral over the line gives unity from the definition of $\mathfrak{F}$, so that $\bar{\mu}^{\Delta\nu}$ becomes for the case of lines

$$\bar{\mu}^{\Delta\nu} = \frac{1}{\Delta\nu} \sum_{\Delta\nu} \int_{\text{line}} \mu \, d\nu$$

(27)

Using Eqs. (17) to (23) the absorption coefficient averaged over a band of width, $\Delta\nu_b$ is

$$\bar{\mu}^{\Delta\nu_b} = \frac{\pi e^2}{mc} \frac{f_{nm}}{\Delta\nu_b} N_{mv'} \,|D_{\text{vib}}^{v'v''}|^2$$

(28)

The average over a frequency interval that contains many bands can be written approximately as

$$\bar{\mu}^{\Delta\nu} = \frac{1}{\Delta\nu} \sum \frac{\pi e^2}{mc} f_{nm} N_{mv'} \,|D_{\text{vib}}^{v'v''}|^2$$

(29)

where the sum is over all bands that lie in the frequency range $\Delta\nu$. Equation (29) is only approximate as the boundary of the interval $\Delta\nu$ may not coincide with one end of a band.

The average absorption coefficient is a significant quantity only when the region in question is optically thin, e.g. so that there is no self-absorption of the radiation in any of the lines. In such sources, this average can be used to predict the emissivity. In other cases, this average is useful in determining the conditions under which the particular band system will be observable. If the average absorption coefficient for a band system is not less than, say, an order of magnitude smaller than the continuous background, the system may be observable if the lines are sharp. This point will be discussed further in the section on line widths and spacing.

The average absorption coefficient for most of the important diatomic molecules can be computed to within a constant (the electronic $f$-number) with fair accuracy over most of the frequency range of interest. Through the work of NICHOLLS and co-workers[7] the vibrational transition probabilities, $|D_{\text{vib}}^{v'v''}|^2$, are reasonably well known. For the NO $\beta$- and $\gamma$-band systems, extensive calculation of this quantity has also been made by KIVEL et al.[8] The electronic $f$-numbers, however, are not known from theory, and recourse to experiment is needed for their evaluation. They are expected to be of the same order of magnitude as the atomic $f$-numbers for similar transitions, 0·1–0·2, for allowed transitions.

74

The preceding theoretical and experimental results formed the basis of the work by Meyerott.[9] In that work, 0·2 was taken for the electronic $f$-numbers for all molecular electronic transitions. With the observation by Teller[10] that $f$-numbers of this order of magnitude would make the radiation heat transfer of importance, this work received new impetus. At around 8000°K and normal air density, the most important single contributor appeared to be the $\beta$- and $\gamma$-band systems of NO. The $N_2$ first and second positive systems and $N_2^+$ first negative system also appeared to be worthy of consideration. Possible contributors to the continuous absorption of importance were photoelectric absorption by $O^-$, O, N and $N_2$ and free–free absorption by electrons in the fields of both positive ions and O.

Analysis of the work by Marmo[11] using absorption techniques with room temperature NO indicated that the $f$-numbers for the $\beta$- and $\gamma$-bands were considerably less than 0·1. Further work by Weber and Penner[12] and also by Hurowitz[13] using similar techniques has established the electronic $f$-numbers for both the $\beta$- and $\gamma$-band systems of NO to be of the order of 0·002. Weber and Penner obtain a value of 0·0025 for the electronic $f$-number of the $\gamma$-bands and Weber has shown that the electronic $f$-number for the $\beta$-bands is greater than 0·008. As we shall see, this is also in fair agreement with high-temperature results.

No reliable estimate existed for the free–free cross-section for absorption by electrons in the presence of neutral atoms of O and N. This has now been computed by Hammerling et al.[14] This contribution is appreciable at wavelengths longer than the photoelectric edge of $O^-$.

The remaining species make contributions to the absorption coefficient by absorptions from excited states so that some other techniques must be employed to evaluate their contribution. The most promising are those used by the AVCO Research Laboratory[15] which center around the use of the shock tube. The shock tube is used to obtain a sample of gas at a known temperature and density which can be used as a source to make emissivity measurements. Such a sample is prepared by creating a shock wave which is reflected off the end of the shock tube. This creates a gas sample of essentially constant temperature and density which are known from hydrodynamic considerations and whose thickness increases linearly with time. The measurements reported by the AVCO group are for air at a temperature of 8000°K, a density of 0·85 that of normal atmospheric density and of thickness up to 3 cm. These measurements include time-resolved emission spectra taken with a drum camera and absolute intensity measurements as a function of time and frequency made with phototubes and a monochromator. The results of the absolute intensity measurements are shown in *Fig. 3.* The intensities shown are for a gas sample 1 cm thick. The measured intensities show a linear increase with time which is due to the linear increase of reflected shock thickness with time. This implies that there is little self-absorption in the sample and that Eq. (9) for small $\mu, \delta$ is valid.

The theoretical emissivity is also shown in *Fig. 3.* The various contributions to the emitted intensity are shown in *Fig. 4.* The major contribution to continuous absorption is due to photoelectric absorption of $O^-$. At wavelengths longer than the $O^-$ photoelectric edge, the O and N free–free transitions are the predominant absorbers in the continuum. For the discrete spectra, the NO $\beta$- and $\gamma$-bands have been computed with an electronic $f$-number of 0·008 and 0·0025 respectively. Subtracting these contributions, the remainder of the absorption is due to $N_2$ first and second positive bands, $N_2^+$ first negative bands, and $O_2$ Schuman–Runge bands. In order to fit the data, the electronic $f$-number for the $N_2$ first and second positive bands were estimated by the AVCO group to be 0·07 and 0·02, respectively. The electronic $f$-number of the $O_2$ Schuman–Runge bands is known to be 0·259 from the work of Ditchburn and Heddle.[16]
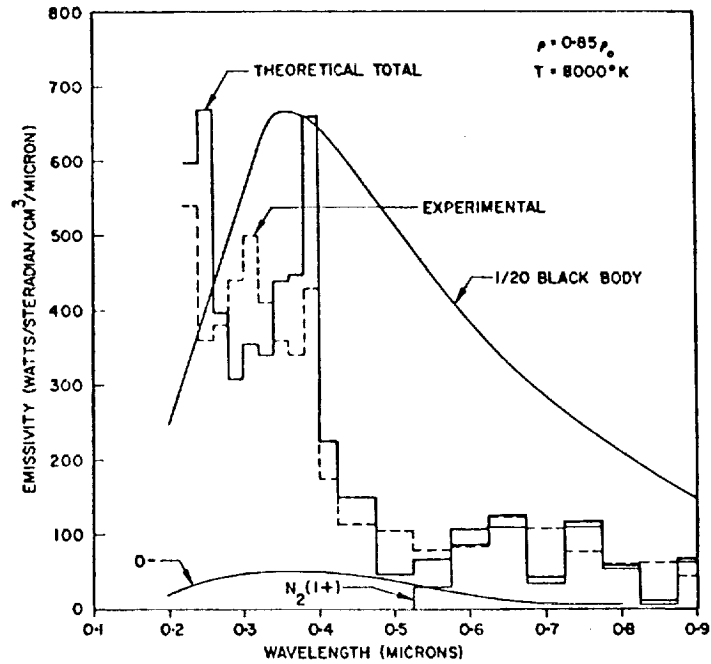
*Fig. 3. Theoretical and experimental emissivity at $T = 8000°K$ and $\rho = 0.85\,\rho_0$ showing theoretical contributions $N_2(1+)$ and $O^-$*
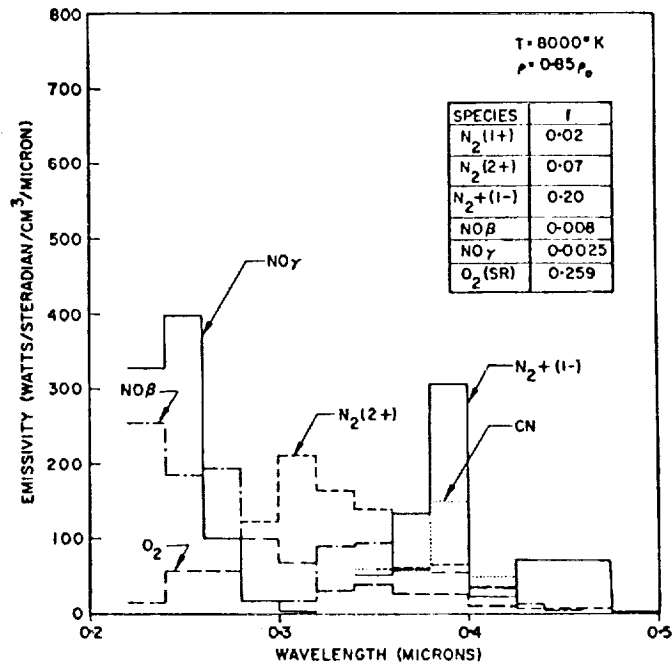


*Fig. 4. Theoretical contributions to emissivity $0.2$–$0.5\,\mu$*

The presence of the CN red and violet bands in the spectra is expected, since there is carbon present in normal air in the form of $CO_2$. However, since the normal concentration of carbon is only about two carbon atoms in $10^4$ air atoms, a small amount of oil impurity could easily contribute unknown amounts of carbon much in excess of that occurring naturally.
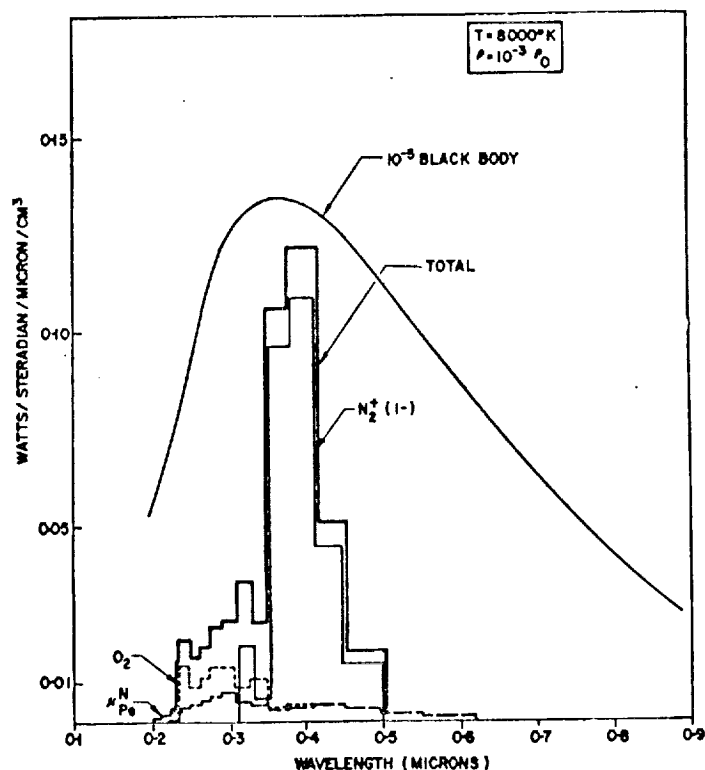


Fig. 5. Theoretical emissivity at $T = 8000°K$ and $\rho = 10^{-3} \rho_0$

Unfortunately, the CN violet band system overlaps the $N_2^+$ first negative system, so that the possible carbon impurity eliminates a good evaluation of the $f$-number for the $N_2^+$ first negative band system. The contribution from the $N_2^+$ first negative bands has been computed using an $f$-number of 0·2 and is also shown in Fig. 4.

For the purpose of scaling to other temperatures and densities, the emission characteristics of air at 8000°K and $10^{-3}$ normal density, and 12,000°K and normal density and $10^{-3}$ normal density are shown in Figs. 5, 6 and 7, respectively. It can be seen that the relative importance of the various species changes. At 8000°K and $10^{-3}$ normal density, the relative importance of $N_2^+$ first negative bands increases, $O^-$ becomes unimportant, and the photoelectric absorption from the excited states of N and O appears to be a contributing factor. The CN violet band system will be unimportant at this density. At 12,000°K normal density in addition to the $N_2$ first positive and

second positive band systems, the $N_2^+$ first negative system, and $O^-$ photo-electric absorption, the photoelectric absorption from the excited states of N and O as well as free–free absorption by electrons in the field of positive ions contribute to the absorption. At 12,000°K and $10^{-3}$ normal density, the molecules are dissociated and the only remaining contributors are free–free
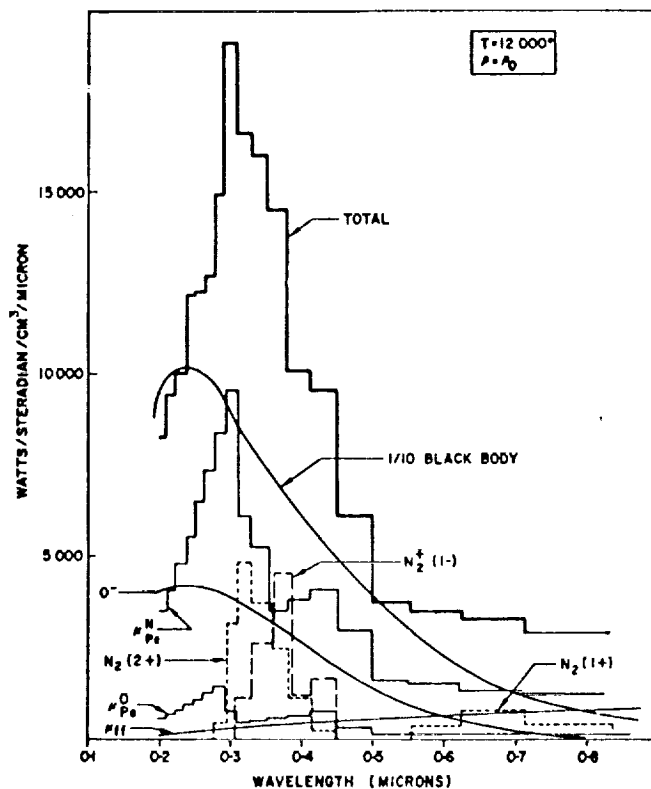


Fig. 6. *Theoretical emissivity at $T = 12,000°K$ and $\rho = \rho_0$*

absorption by electrons in the field of positive ions and photoelectric absorption from the excited states of N and O.

While the work by the AVCO group has answered some of the most important questions about the absorption properties of air in this tempera-ture and density range, it seems clear that measurements at more than one temperature and density and on mixtures to isolate particular contributors are needed to complete our understanding. The contributions of $O^-$ photo-electric absorption, $N_2^+$ first negative bands and CN bands are not evaluated, or only poorly evaluated, at normal density and 8000°K. At lower density and higher temperature the contributions due to the photoelectric absorption of O and N in their excited states as well as free–free transitions from electrons in fields of positive ions are only poorly known by the theory outlined here. There is also the possibility that some constituent other than those presently considered might be a dominant one.
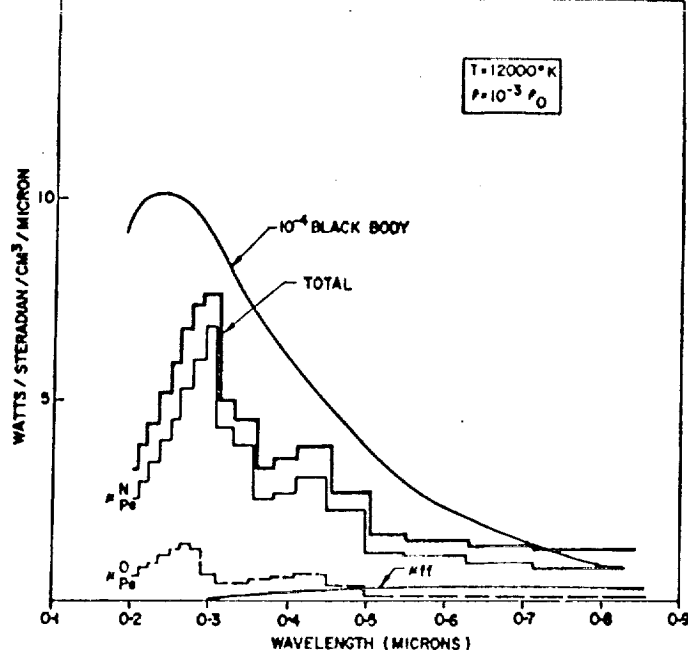
Fig. 7. *Theoretical emissivity at* $T = 12,000°K$ *and* $\rho = 10^{-3} \rho_o$

## LINE WIDTHS AND LINE SPACINGS FOR
### THE DISCRETE TRANSITIONS

The energy emitted by a hot sample of air is proportional to the thickness of the gas sample provided that $\mu_\nu' \delta$ in Eq. (4) is small. The results so far for the discrete transitions refer to some average absorption coefficient which results from an average over the lines, as indicated in Eq. (29). In estimating the emissivity from thick gas sample, one needs to have the absorption coefficient for each line, which depends upon the line width through the factor $\mathfrak{F}$ in Eq. (15). An estimate can be obtained for the average absorption coefficient in each line from the average absorption coefficient $\bar{\mu}^{\Delta\nu}$ in the following manner.

If $W$ is the width of the lines at one-half maximum intensity and $S$ is the mean line spacing, the fraction of the space covered by lines will be $W/S$, and the average absorption coefficient of a line will be $(S/W)\mu^{\Delta\nu}$. Conversely, the emissivity in each can be computed for thin samples by multiplying the local average emissivity by the factor $W/S$. If this approaches the black body result, saturation effects set in, and the sample can no longer be considered thin.

The line spacing depends on the temperature and the nature of the transition for each species. This can be obtained by estimating the spacing at the peak intensity for the rotational lines. In *Table 1* the spacings are estimated for several of the band systems. Overlapping from adjacent vibrational bands has also been included.

The line widths depend on the temperature, density, the states involved in the transitions, and the gas mixture. At low density the width is due to the Doppler effect; at high density the width is due to pressure broadening. MARGENAU[17] has estimated the pressure broadening of the NO-band lines due to $N_2$ and obtains $W = 0.3$ cm$^{-1}$/atm of $N_2$. This is expected to be of the order of magnitude of the widths for the other systems considered here. Line width measurements on cold NO have been made by WEBER;[18] he

Table 1. *Line spacing, Doppler widths, and ratio at 8000°K*

|  | Band system | $S$(cm$^{-1}$) | $W$(cm$^{-1}$) | $S/W$ |
|---|---|---|---|---|
| NO | $\beta$-bands | 2·60 | 0·36 | 7·2 |
| NO | $\gamma$-bands | 1·00 | 0·48 | 2·0 |
| $N_2$ | first positive | 0·47 | 0·18 | 2·6 |
| $N_2$ | second positive | 0·60 | 0·36 | 1·7 |
| $N_2^+$ | first negative | 1·40 | 0·30 | 4·7 |

$S$ = Mean line spacing
$W$ = Width of lines at half maximum intensity

finds the width at half maximum to be $0.10$ cm$^{-1}$/atm at 298°K for the $\gamma$-bands. He also finds, for the vibration rotation bands a width of $0.08$ cm$^{-1}$/atm. Using micro wave techniques, BERINGER and CASTLE[19] obtain a width of $0.11$ cm$^{-1}$/atm for the rotational lines. There are no data on the line widths for the band systems of $N_2$ and $N_2^+$. The calculations of Margenau would indicate that the line widths of lines in these band systems should be of the same order as those of NO.

The contribution to the width of the lines due to the Doppler effect at 8000°K is $0.12$ cm$^{-1}$, $0.24$ cm$^{-1}$, $0.38$ cm$^{-1}$ and $0.48$ cm$^{-1}$ at $1.0$, $0.5$, $0.33$ and $0.25$ $\mu$, respectively. It would appear that at normal density the Doppler width might be taken as a fair estimate of the width. These widths and the ratio $S/W$ are also included in *Table 1*. Since the strongest bands may be of the order three times as intense as the average intensity from any band system the peak absorption from these band lines may be as much as $3(S/W)\mu^{\Delta\nu}$.

## CONCLUSION

The progress made in the determination of the absorption and emission coefficients of air in the past 2 years is encouraging. Preliminary values of the most important $f$-numbers for several molecular transitions are now known.

For thick gas samples when $\mu_v'\delta$ is not small, one must use Eq. (4) to determine the intensity of radiation. Calculations of the emissivity of NO have been made by KIVEL, MAYER and BETHE,[8] and by THOMSON.[20] No calculations for thick samples exist which include the other important species contributing to the emissivity of air. A continuation and extension of present techniques will certainly yield the remaining values of importance to radiation problems. Sources are now available for the study of line widths of molecular lines. In the next year or so these line widths will probably be well determined. When this is done, reliable tables can be derived for the radiation heat-transfer problem.

## SOMMAIRE

*On passe en revue ce que l'on connaît actuellement sur les caractéristiques d'émission de l'air à des températures et des densités de l'ordre de grandeur de celles intéressant l'étude de l'échauffement par rayonnement au cours du vol à des vitesses hypersoniques. On illustre le problème en étudiant deux problèmes particuliers couvrant l'ensemble du domaine intéressant: le nez d'un engin balistique, localement hémisphérique, rentrant dans l'atmosphère et un véhicule sphérique circumlunaire rentrant dans l'atmosphère sous des conditions très sévères. Ces exemples sont suivis par une revue des théories existantes sur le coefficient d'émission de l'air et une analyse des résultats expérimentaux les plus récents.*

## REFERENCES

[1] GAZLEY, C. Jr. and MASSON, D. J. "Recovery of Circum-Lunar Instrument Carrier" Presented under the auspices of the American Rocket Society, 8th International Astronautical Congress, Barcelona, Spain, Report 488–57, pp. 1–22, 6–12 October 1957.

[2] GILMORE, F. R. "Equilibrium Composition and Thermodynamic Properties of Air to 24,000°K" U.S. Air Force Project, Rand Research Memorandum RM-1543, August 1955, The Rand Corporation, Santa Monica, California, U.S.A.

[3] BRANSCOMB, L. M. and SMITH, S. J. "Electron Affinity of Atomic Oxygen" *Phys. Rev.* Vol. 98, No. 4, p. 1127, 1955.

[4] BATES, D. R. and MASSEY, H. S. W. "The Basic Reaction in the Upper Atmosphere, II Theory of Recombination in the Ionized Layers" *Phil. Trans.* A, Vol. 192 1, pp. 1–16, 1947; also *Proc. roy. Soc.* A, Vol. 239, p. 269, 1943.

[5] CHANDRASEKHAR, S. *An Introduction to the Study of Stellar Structure* p. 263, Chicago University Press, 1939.

[6] HERTZBERG, G. *Spectra of Diatomic Molecules* p. 38; Van Nostrand, New York, 1950.

[7] JARMAIN, W. R., FRASER, P. A. and NICHOLLS, R. W. "Vibrational Transition Probabilities of Diatomic Molecules—Collected Results $N_2$ $N_2^+$ NO $O_2^+$" *Astrophys. J.* Vol. 118, pp. 228–233, 1953.

JARMAIN, W. R., FRASER, P. A. and NICHOLLS, R. W. "Vibrational Transition Probabilities of Diatomic Molecules—Collected Results, $N_2$ NO $O_2$ $O_2^+$ OH CO $CO^+$" *Astrophys. J.* Vol. 122, pp. 55–61, 1955.

JARMAIN, W. R. and NICHOLLS, R. W. "Vibrational Transitional Probabilities to High Quantum Numbers for $N_2$, First Positive and Second Positive Systems" *Canad. J. Phys.* Vol. 32, pp. 201–204, 1954.

TURNER, R. G. and NICHOLLS, R. W. "An Experimental Study of Band Intensities in the First Positive System of $N_2$. Vibrational Transition Probabilities" *Canad. J. Phys.* Vol. 32, pp. 468–474, 1954.

FRASER, P. A. "A method of Determining the Electronic Transition Moment for Diatomic Molecules" *Canad. J. Phys.* Vol. 32, pp. 515–521, 1954.

NICHOLLS, R. W. "An Experimental Study of Band Intensities in the First Positive System of $N_2$. Quantitative Treatment of Eye Estimates" *Canad. J. Phys.* Vol. 32, pp. 722–725, 1954.

[8] KIVEL, B., MAYER, H. and BETHE, H. "Radiation from Hot Air, Part 1, Theory of Nitric Oxide Absorption" *Ann. Phys., LpZ.* Vol. 2, No. 1, 1957. pp. 57–80,

[9] MEYEROTT, R. E. "Absorption Coefficients of Air from 6000°K to 18,000° K" U.S. Air Force Project, Rand Research Memorandum RM-1554, September 1955. The Rand Corporation, Santa Monica, California; "Absorption Coefficients of Air from 2000°K to 18,000°K" Conference on Chemical Aeronomy, Geophysics Research Directorate of the Air Force, Cambridge Research Center, ARDC, June 1956.

ZELIKOFF, M. (Edit.) "The Threshold of Space" Pergamon Press, London, June 1956, p. 259.

[10] TELLER, E. Private Communication.

[11] MARMO, F. F. "Absorption Coefficients of NO in the Vacuum Ultraviolet" *J. opt. Soc. Amer.* Vol. 47, pp. 1186–1190, 1953.

[12] WEBER, D. "Approximate Intensity Estimates for Several Ultraviolet $\beta$-Bands of NO" California Institute of Technology, Report No. 23, March 1957; WEBER, D. and PENNER, S. S., Report No. 18, April 1956, Pasadena, California, U.S.A.

WEBER, D. and PENNER, S. S. "Absolute Intensities for the UltraViolet $\gamma$-bands of NO" *J. chem. Phys.*, Vol. 26, No. 4, p. 860, April, 1957.

[13] HUROWITZ, H. Private Communication.

[14] HAMMERLING, P., SHINE, W. W. and KIVEL, B. "Low Energy Elastic Scattering of Electrons by Oxygen and Nitrogen" AVCO Research Laboratory, Report Note 31, March 1957, Everett 49, Massachusetts, U.S.A.

[15] KECK, J., KIVEL, B. and WINTINK, T. Jr. "Emissivity of High-Temperature Air" AVCO Research Laboratory Report 8, April 1957, Everett 49, Massachusetts, U.S.A.

[16] DITCHBURN, R. W. and HEDDLE, D. W. O. "Absorption Cross-Sections in the Vacuum Ultraviolet I. Continuous Absorption of $O_2$ (1800–1300 Å)" *Proc. roy. Soc.* A Vol. 220, p. 61, 1953; also Vol. 226, p. 509, 1954.

[17] MARGENAU, HENRY, "Estimate of Pressure Effects on NO—Band Lines" U.S. Air Force Project, Rand Research Memorandum RM-1669, April 1956, The Rand Corporation, Santa Monica, California, U.S.A.

[18] WEBER, D. "Absolute Intensities and Line-Width Measurements" California Institute of Technology, Report No. 23, March 1957, Pasadena, California, U.S.A.

WEBER, D. and PENNER, S. S. "Rotational Line-Width Measurements on NO, HCl, HBr" *J. chem. Phys.* Vol. 21, No. 9, p. 1503, September 1953.

[19] BERINGER, R. and CASTLE, J. G. Jr. "Magnetic Resonance Absorption in Nitric Oxide" *Phys. Rev.* Vol. 78, No. 5, 1950.

[20] THOMSON, A. "Emissivity Estimates for Heated NO" Technical Report No. 6 Contract AF81(603)-2 California Institute of Technology, Pasadena, 1957.

# THE COUPLING OF RADIATION AND CONVECTION IN DETACHED SHOCK LAYERS*

R. Goulard†

Purdue University, Lafayette, Indiana

Abstract—Recent studies have shown that for sufficiently high re-entry speeds, radiation energy transfer from high temperature air becomes an appreciable part of the total energy transfer to the nose of the re-entry body. This note is concerned with the effects of this fluid energy loss on the energy distribution in the shock layer and, therefore, on the convective and radiative fluxes at the wall. A nondimensional parameter is shown to govern the resulting coupling between radiative and convective fluxes. The first approximation which consists in assuming a constant stagnation temperature layer is shown to be acceptable for most ballistic and earth satellite re-entry problems. For larger velocities or dimensions (e.g., planetary probes and heavy meteors), radiation losses become important and it is necessary to include the radiation terms into the equations which determine the flow field.

## LIST OF SYMBOLS

| | |
|---|---|
| $a$ | radial velocity gradient in the shock layer (equation 1) |
| $c_p$ | specific heat at constant pressure |
| $E$ | $\rho_\infty U_\infty h_{es}$, energy flux across the shock (equation 13) |
| $F$ | equation 14 |
| $h$ | specific enthalpy |
| $\Gamma$ | energy ratio (equation 13) |
| $q_c$ | convective heat flux to the wall |
| $\bar{q}_c$ | dimensionless convection heat flux to the wall $q_c/q_e^\circ$ |
| $q_R$ | radiant heat flux to the wall |
| $\bar{q}_R$ | dimensionless radiant heat flux to the wall $q_R/q_R^\circ$ |
| $r$ | radial coordinate (Fig. 1) |
| $R$ | nose radius |
| $t, t_o$ | time, initial time |
| $T$ | absolute temperature |
| $\bar{T}$ | $T/T_{es}$ |
| $u$ | radial component of the air velocity (Fig. 1) |
| $U_\infty$ | flight velocity |

| $V_E$ | maximum flight velocity during re-entry |
|---|---|
| $w$ | air velocity component, normal to the wall (Fig. 1) |
| $W/C_DA$ | weight–drag ratio |
| $z$ | coordinate perpendicular to the wall (Fig. 1) |
| $\bar{z}$ | $z/\delta$ |
| $\alpha, \beta$ | constant exponents (equation 15) |
| $\delta$ | shock layer thickness |
| $\theta_E$ | angle between the re-entry trajectory and the horizontal plane |
| $\varkappa$ | mass absorption coefficient |
| $\rho$ | density |
| $\sigma$ | Stefan–Boltzman constant |

*Subscripts and superscripts*

| $e$ | condition at the boundary layer edge |
|---|---|
| $es$ | stagnation conditions |
| $\infty$ | upstream conditions |
| $\delta$ | conditions immediately behind the shock |
| $^{o}$ | stagnation approximation (constant properties across the boundary layer) |

## INTRODUCTION

THE advent of space flight has brought about the possibility of very high speed penetration of planetary atmospheres[1]. Such maneuvers communicate considerable energy to the gas particles lying in the path of the vehicle and radiative processes of appreciable intensity are likely to occur in the flow fields past the body. These radiation fluxes have been estimated for the stagnation flow of such man-made objects as ballistic missiles and planetary probes[2, 3].

In these estimates it was assumed that the radiation losses were only a small fraction of the total energy in the shock layer and that consequently, taking them into account would not appreciably affect the flow field. The properties of this flow field, notably temperature and density, were therefore determined on the basis of the familiar conservation equations, neglecting the radiation terms, and the calculation of the radiation losses was based on their value.

It is apparent, however, that for increasing velocities, the radiation losses from any group of particles streaming past the body are becoming an increasing fraction of their total energy. As a result of this cooling effect, one can expect lower flow field temperatures and consequently lower radiation fluxes than calculated for an adiabatic (loss-less) shock layer. The purpose of this note is to try to estimate this effect.

## THE INCOMPRESSIBLE SHOCK LAYER MODEL

An accurate estimate of the stagnation flow field, cumbersome as it is for nonradiative media[4, 5], becomes quite intricate when radiation fluxes are included. In general, the difficulty lies in the integral character of the radiation term that must be included into the already complex set of coupled differential equations of mass, momentum and energy.

Physically, this means that the energy balance of each elementary volume of the flow field is conditioned by long range contributions from all other elementary volumes throughout the shock layer.

In this paper, radiation losses will be considered only as a perturbation to the exact
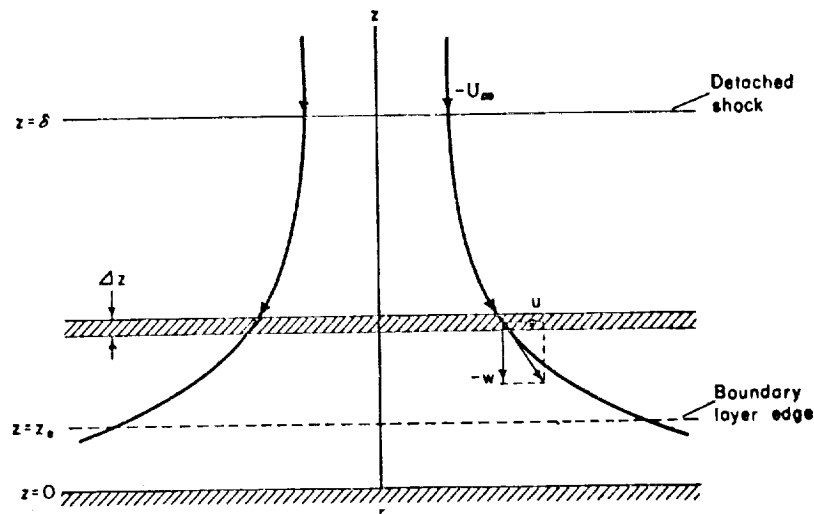


FIG. 1. Detached shock layer flow at stagnation.

nonradiant shock layer solutions[4-6]; we will make use of three important features of these solutions in the stagnation area (Fig. 1)*:

a) The shock layer thickness $\delta$ is much smaller at very high speeds than the radius $R$ of the body $\left(\dfrac{\delta}{R} \simeq \dfrac{1}{20}\right)$.

The shock layer will therefore be considered as a plane parallel layer in the stagnation zone.

b) The shock layer is nearly incompressible in the stagnation area:

$$\rho_{es} = \text{const.}$$

c) The velocity component along the axis of the body is nearly proportional to the distance from the surface of the body[4, 6]:

$$w \equiv \frac{dz}{dt} = -2\,az. \tag{1}$$

The value of the parameter $a$ will be chosen to satisfy the conservation of mass principle in the $z$ direction across the shock:

$$a = -\frac{w_\delta}{2\delta} = -\frac{1}{2}\frac{\rho_\infty U_\infty}{\rho_{es}\delta} \tag{2}$$

This value of $a$ is in fair agreement with exact calculated values[6] and in particular with those of VAGLIO-LAURIN and FERRI[4]. We also note the close similarity between actual shock layer flow at stagnation and the classical potential flow.

## THE TEMPERATURE DISTRIBUTION IN THE SHOCK LAYER

An interesting property of this incompressible stagnation flow model, from the standpoint of the mathematics of radiation (and also of those of chemical kinetics), is that for both inviscid and viscous cases[7], the time history of the particles is dependent on the coordinate $z$ and *not* on the coordinate $r$ (equation 1).

Therefore, all particles entering the shock layer at a time $t_0$ will be at $z$ at a time $t$, such that:

$$t - t_0 = -\frac{1}{2a} \ln \frac{z}{\delta} \tag{3}$$

These particles form a thin infinite layer of thickness $\Delta z$ which loses its energy at the rate: $(\rho \Delta z)\frac{dh}{dt}$ per unit area. The radiative losses are made of the fluxes *towards* the wall and *away* from it. Their total value per unit area[8] is $2(2\rho \times \sigma T^4)\Delta z$ where $\times$ is the mass absorption coefficient of the gas.* No self-absorption is expected from this optically thin medium[8].

Also a look at hypersonic flow charts[9] shows that for body velocities higher than 20 kft/sec, the kinetic energy in the shock layer is always a small fraction ($< 4\%$) of the total energy, decreasing further[9] when the velocity of the body increases to values of interest in this study (35 kft/sec).

For the inviscid flow in the stagnation area (kinetic energy neglected), the principle of conservation of energy is therefore satisfied if the following two fluxes compensate† each other:

$$-\rho \frac{dh}{dt} = 4 \rho \times \sigma T^4 \tag{4}$$

Elimination of the time variable between equations (1) and (4) yields:

$$\frac{dz}{z} = \frac{2 a \rho \, dh}{4 \rho \times \sigma T^4} \tag{5}$$

Since for any gas in chemical equilibrium, the enthalpy $h$ is a known function of the temperature $T$, equation (5) gives implicitly a distribution $T(z)$ across the shock layer. It is also possible to bring out the shock layer thickness $\delta$ into equation (5) by using equation (2):

$$\frac{dz}{z} = \frac{\rho_\infty U_\infty \, dh}{4 \rho_{es} \times \delta \sigma T^4} \tag{6}$$

Equation (6) can be rearranged as follows:

$$\frac{dz}{z} = \frac{\rho_\infty U_\infty h_{es}}{4 \rho_{es} \times_{es} \delta \sigma T^4_{es}} \frac{\times_{es}}{\times} \frac{T^4_{es}}{T^4} \frac{c_p dT}{h_{es}} \tag{7}$$

---

* Note that $2\rho \times = \frac{\varepsilon}{L}$, this latter quantity being tabulated for air in [13].

† Since, in all practical cases, the wall is assumed much cooler than the gas, its radiative emission to the gas layer will be neglected, regardless of its emissivity coefficient.

and after integration and determination of the integration constant at the shock:

$$\bar{T} = [1 + (\alpha - \beta - 3)\,\Gamma\,\ln \bar{z}]^{\frac{1}{\alpha-\beta-3}} \tag{12}$$

The total heat flux to the wall is the summation of the fluxes from all the elementary layers of thickness $dz$:

$$q_R = \int_0^\delta dq_R = \int_0^\delta 2\,\rho\,\varkappa\,\sigma\,T^4\,dz \tag{13}$$

or, in nondimensional form:

$$q_R = 2\,\rho_{es}\,\varkappa_{es}\,\delta\,\sigma\,T^4_{es} \int_0^1 \frac{\rho\,\varkappa}{\rho_{es}\,\varkappa_{es}} \left(\frac{T}{T_{es}}\right)^4 d\bar{z}$$

$$= q^\circ_R \int_0^1 \bar{T}^{\beta+3}\,d\bar{z}$$

Introducing a dimensionless flux $\bar{q}_R = q_R/q^\circ_R$ and replacing $\bar{T}$ by its value from equation (12):

$$\bar{q}_R = \frac{q_R}{q^\circ_R} = \int_0^1 [1 + (\alpha - \beta - 3)\,\Gamma\,\ln \bar{z}]^{\frac{\beta+3}{\alpha-\beta-3}}\,d\bar{z} \tag{14}$$

Since $\Gamma$ is assumed to be small, we can expand both equation (12) and the integrand of equation (14) as Newton polynomials, and neglect the terms in powers of $\Gamma$ higher than one. Equation (14) becomes.

$$\bar{q}_R = 1 + (\beta + 3)\,\Gamma\,[\lim_{\bar{z}\to 0} \int_{\bar{z}}^1 \ln \bar{z}\,d\bar{z}]$$

and the nondimensional radiation flux and temperature (equations 12 and 14) can finally be written:

$$\bar{q}_R = 1 - (\beta + 3)\,\Gamma \tag{15}$$

$$\bar{T} = 1 + \Gamma\,\ln \bar{z} \tag{16}$$

Another convenient formulation is that of the nondimensional deviations from the stagnation values:

$$\Delta\bar{q}_R = \frac{q_R - q^\circ_R}{q^\circ_R} = -(\beta + 3)\,\Gamma \tag{17}$$

$$\Delta\bar{T} = \frac{T - T_{es}}{T_{es}} = (\ln \bar{z})\,\Gamma \tag{18}$$

which are both clearly proportional to $\Gamma$.

## CONVECTION AND RADIATION FLUXES

Equation (16) shows that because of the continuing radiation losses, the closer the particles get to the wall, the lower their temperature is. The temperature at the outer edge

of the viscous boundary layer must then be lower than the stagnation temperature. As a result, the convective heat transfer is expected to be reduced because of the presence of radiation.

As a first estimate, since radiation is proportional to the mass of the radiant medium, and even more dependent on temperature, the thin and cool boundary layer can be treated as if it were nonradiant.* Its calculated thickness $z_e$ in the case of a nonradiant gas (see for instance[14], can also be used in equation (16) to determine the outer edge temperature. The convective energy transfer can then be estimated on this basis.

Both radiative fluxes $q_R$ and boundary layer edge temperature $T_e$ have been calculated in four typical re-entry trajectories. These trajectories are shown on Fig. 3. The values of $\bar{q}_R$ and $T_e$ corresponding to the maximum value of $\Gamma$ for each trajectory, are shown on Table 1 for a nose radius of one foot ($\beta \simeq 7$, $\bar{z}_e \simeq 0.04$ and $\ln \bar{z}_e \simeq -3.2$). Also shown is the dimensionless convection heat flux to the wall $\bar{q}_c = q_c/q°_c$. The flux $q_c$ is roughly proportional to the enthalpy $h_e$ at the boundary layer edge[6] and its deviations from the stagnation value $q°_c$ can therefore be readily calculated† from those of $T_e$ with the help of a Mollier Chart for air[9].

TABLE 1.

| Re-entry trajectory ($R = 1$ ft) | $\Gamma_{max}$ | $\bar{q}_R$ | $T_e$ | $\bar{q}_c$ |
|---|---|---|---|---|
| $\theta_E = 20°$, $V_E = 23,000$ ft/sec, $W/C_D A = 900$ lbs ft$^{-2}$ (ICBM) | $2 \times 10^{-3}$ | 0.98 | 0.994 | 0.986 |
| $\theta_E = 90°$, $V_E = 35,000$ ft/sec, $W/C_D A = 32$ lbs ft$^{-2}$ (moon probe) | $10^{-2}$ | 0.90 | 0.97 | 0.93 |
| $\theta_E = 90°$, $V_E = 35,000$ ft/sec, $W/C_D A = 160$ lbs ft$^{-2}$ ("iron sphere") | $5 \times 10^{-2}$ | 0.50 | 0.84 | 0.75 |
| $\theta_E = 90°$, $V_E = 45,000$ ft/sec, $W/C_D A = 32$ lbs ft$^{-2}$ (Mars probe) | assumption $\Gamma \ll 1$ not applicable | | | |

## CONCLUSION

Three conclusions can be drawn from Table 1 and from the form of equations (15) to (18):

1) The radiation flux in the forward direction and to the wall is, in principle, less than the quantity $q°_R$ calculated in first approximation assuming $T = T_e$, throughout the layer.
2) The temperature at the edge of the boundary layer is, in principle, less than the stagnation temperature. A smaller convective flux at the wall is therefore expected. This coupling between radiation and convection is also apparent in static[8] and viscous[15] cases.
3) Calculation of radiative and convective transfer rates by assuming the temperature of the inviscid shock layer constant throughout ($\bar{q}_R = 1$, $\bar{T} = 1$), is a first order approximation to the result (equations (15) and (16)); the extent of this overestimation depends on the magnitude of $\Gamma$ and on the boundary layer thickness.

---

* Flow contamination by the wall is not considered here.
† To help interpret the nondimensional data in Table 1, the reader is reminded that, according to estimates[2], $q°_R \simeq \frac{1}{10} q°_c$ for the first case in the table, $q°_R \simeq q°_c$ for the second case and $q°_R > q°_c$ for the last two cases.

In the case of air, large values of $\Gamma$ correspond to high velocities, large nose radii and low altitudes. From the estimates of this paper, it appears that for ballistic and earth satellite trajectories, MEYEROTT's and KIVEL's first approximations[2,3] are justified for nose radii of the order of one foot or less. The study of the atmospheric penetration of most planetary probes and heavy meteors present more difficulty: it will be necessary to include the radiation terms into the equations which determine the flow past the body, in order to account for radiation losses and self-absorption. For intermediate cases, such as that of a moon probe, the approximation suggested in this paper should be adequate.

## REFERENCES

1. C. GAZLEY, Jr., The Penetration of Planetary Atmospheres, Transactions of the ASME, *J. Heat Transfer* **81**, Series C, No. 4, p. 315 (1959).
2. R. E. MEYEROTT, *Radiation Heat Transfer to Hypersonic Vehicles*, Third AGARD Combustion and Propulsion Panel Colloquium, Palmermo, Sicily (1958).
3. B. KIVEL, Radiation from Hot Air and Stagnation Heating, *J. Aero. Sci.* **28**, 2 (1961).
4. R. VAGLIO-LAURIN and A. FERRI, Theoretical Investigation of the Flow Field about Blunt Nosed Bodies in Supersonic Flight, *J. Aero. Sci.* **25**, 12 (1958).
5. F. G. GRAVALOS, et al., *The Supersonic Flow about a Blunt Body of Revolution for Gases at Chemical Equilibrium*, Ninth International Astronautical Congress (Amsterdam 1958), Springer Verlag, Vienna (1959).
6. W. D. HAYES and R. F. PROBSTEIN, *Hypersonic Flow Theory*, p. 238–240, Academic Press, New York (1959).
7. H. SCHLICHTING, *Boundary Layer Theory*, p. 73, McGraw-Hill, New York (1955).
8. R. and M. GOULARD, One-Dimensional Energy Transfer in Radiant Media, *Int. J. Heat Mass Transfer*, **1**, 81–91 (1960).
9. S. FELDMAN, *Hypersonic Gas Dynamic Charts for Equilibrium Air*, AVCO Research Report 40 (1957).
10. A. UNSÖLD, *Physik der Sternatmosphären*, Springer Verlag, Vienna (1955).
11. V. N. ADRIANOV and S. N. SHORIN, Radiative Transfer in the Flow of a Radiating Medium, *Izv. Akad. Nauk SSSR. OTN*, 1958, 5, 46. (Translation available from Purdue University, School of Aeronautical and Engineering Sciences, Lafayette, Indiana).
12. H. SERBIN, Supersonic Flow Around Blunt Bodies, *J. Aero. Sci.*, Readers' Forum, **25**, 58 (1958).
13. B. KIVEL and H. BAILEY, *Tables of Radiation from High Temperature Air*, AVCO Research Laboratory RR 21 (1957).
14. S. M. SCALA and C. W. BAULKNIGHT, Transport and Thermodynamic Properties in a Hypersonic Laminar Boundary Layer—Part II—Applications, *Amer. Roc. Soc. J.*, **30**, no. 4, p. 329 (1960).
15. J. P. GUIRAUD, Ecoulement plan de Couchette d'un gaz rayonnant, *C. R. Acad. Sci.*, Paris, **250**, 2997 (1960).

# Ablation in Hypersonic Flows

## LESTER LEES

## Summary

Ablation is the process of absorbing heat energy by removal of surface material, either by melting (possibly accompanied by vaporization of the molten material), or by sublimation. Recent theoretical investigations have contributed to our understanding of the fluid mechanics of ablation. The large increase in effective heat capacity produced by gaseous ablation is attributed partly to the well-known "heat blockage" effect of mass addition, and partly to infrared radiation from the gas-liquid or gas-solid interface. Results of some experimental studies of ablation in hypersonic wind tunnels and electric-arc driven tunnels are discussed, and the application of ablating materials to spacecraft entering a planetary atmosphere is treated briefly in order to illustrate the flexibility of ablating heat-sink systems.

## Symbols

$A$ = maximum frontal area

$B$ = $\dot{m}_i/\rho_e u_e C_{H_0}$ $\Big\}$ mass addition parameters
$B'$ = $\dot{m}_i/\rho_e u_e C_H$

$c_p$ = specific heat at constant pressure

$C_D$ = drag coefficient

$C_H$ = local Stanton number, $\dot{q}_w/[(\rho_e u_e \Delta h_s)]$.

$\bar{c}_s$ = average value of specific heat of solid material up to the melting point

$\Delta d$ = width of entry corridor

$f$ = fraction of melted material evaporated

$h_s$ = stagnation enthalpy

$\Delta h_s$ = $h_{s_e} - h_{s_i}$

$\mathfrak{IC}$ = effective heat capacity

$k$ = coefficient of thermal conductivity

$K_E$ = mass fraction of vaporizing or subliming material

$L_m$ = heat of fusion

$L_T$ = internal heat capacity of solid material up to sublimation temperature; or, $L_T = \mathfrak{IC}_0$, if melting plus vaporization occurs

$m$ = geometric index

$\dot{m}_i$ = rate of mass addition to gas boundary layer

$\dot{m}_L$ = melting rate

$\mathfrak{M}$ = molecular weight

$p$ = static pressure

$p_0'$ = stagnation pressure behind normal shock

$P_r$ = Prandtl number, $c_p\mu/k$

$\dot{q}$ = local heat-transfer rate

$\dot{q}_R$ = net radiative heat transfer rate away from interface

$\Delta Q_c$ = heat released in chemical reaction per unit mass

$r_0$ = radius of cross-section of body of revolution

$R_E$ = radius of the earth

$R_0$ = nose radius
$Re_0$ = Reynolds number, $u_\infty R_0/(\nu_e)_{g,0}$
$Re_\infty$ = $u_\infty R_0/\nu_\infty$
$t$ = time
$T$ = absolute temperature
$T_m$ = melting temperature
$T_0$ = internal solid temperature; also initial internal temperature
$u, v$ = components of velocity parallel and normal to gas liquid or gas-solid interface
$W$ = gross weight
$w_A$ = axial ablation velocity
$x$ = axial distance, measured from nose
$y$ = distance normal to interface
$\alpha$ = proportionality factor
$\beta$ = slope of curve $C_H/C_{H_O} = 1 - \beta B$
$\delta$ = boundary layer thickness
$\delta_T$ = thermal thickness, $\rho_e \mathcal{K}/\dot{m}$
$\epsilon$ = turbulent exchange coefficient; also emissivity
$\mathcal{K}$ = $k/\rho c_p$, thermal diffusivity
$\mu$ = absolute viscosity
$\nu$ = $\mu/\rho$, kinematic viscosity
$\rho$ = density
$\sigma$ = Stefan-Boltzmann constant, $5.672 \times 10^{-5}$ erg cm.$^{-2}$ deg.$^{-4}$ sec.$^{-1}$
$\tau$ = shear stress; also duration of heat pulse
$\theta_E$ = entry angle

### Subscripts

$e$ = flow quantities evaluated at outer edge of gas boundary layer
$g$ = gas
$i$ = gas-liquid or gas-solid interface
$L$ = liquid
$0$ = zero mass addition; also stagnation point (except $T_0$)
$s$ = solid
$\infty$ = free stream ahead of bow shock wave

## I.  Introduction

TECHNOLOGICAL ADVANCES in aeronautics and propulsion are almost always accompanied by increased power levels and heat-transfer rates. In aircraft internal-combustion engines the heat-transfer rates to the cooling air are of the order of 10 to 100 B.t.u./ft.²/sec. In earlier liquid-fuel rockets the heat-transfer rates at the nozzle throat were about 400 B.t.u./ft.²/sec., but values as high as 1,000 B.t.u./ft.²/sec. are attained in modern liquid rockets of high specific impulse. Peak heat-transfer rates of this same order are encountered on the "nose cone" of a ballistic missile with a high drag/weight ratio during re-entry into the earth's atmosphere. For a ballistic missile with a low drag/weight ratio, peak re-entry heat-transfer rates are of the order of 2,500 to 3,000 B.t.u./ft.²/sec., which amounts to a power input of 15 kw. over an area about the size of a 4-cent United States postage stamp.

When the peak heat-transfer rate is sufficiently low, a heat pulse* of given

---

\* A triangular timewise distribution of heat-transfer rate is a good approximation to the heat pulse during re-entry.

duration applied to one face of a solid slab produces a nearly uniform temperature increase throughout the material. In other words, the material behaves like a capacitor in this regime, and the slab thickness required to prevent the temperature from exceeding a certain prescribed maximum value is proportional to the peak heat-transfer rate. When the maximum heat-transfer rate is increased, the material nearer the exposed surface heats up more rapidly than the material farther away, and the required slab thickness increases faster than the peak rate. At some critical value of the peak heat-transfer rate ($\dot{q}_{max}$), the maximum allowable temperature ($T_{max}$) is reached even if the slab is very thick. In fact, at this point the material behaves like a semi-infinite slab, and $\dot{q}_{max} \sim T_{max} \sqrt{\rho_s k c_p / \tau}$, where $\rho_s$, $k$, and $c_p$ are the density, thermal conductivity and specific heat of the solid, and $\tau$ is the duration of the heat pulse. Even for a good thermal conductor such as copper, the peak heat-transfer rate is limited to a value of about 1,000 B.t.u./ft.$^2$/sec. for a triangular heat pulse of 30 sec. duration and a maximum allowable temperature of 1,500°F.

The strong influence of the heat-rate limitation imposed by a nonmelting solid heat sink on ballistic missile nose cone design and re-entry performance is brought out very clearly by G. Solomon.[1] These considerations led to the development of ablating materials that absorb heat energy by melting, and possibly vaporizing, or by undergoing sublimation directly to the vapor phase. Although ablation is a relatively new process to the engineer, it has been occurring in nature for millions of years. Because of their tremendous kinetic energy, all but the very smallest and very largest meteorites are almost completely vaporized during their passage through the earth's atmosphere. Of course, the engineer hopes to bring this rather violent natural process under careful control.
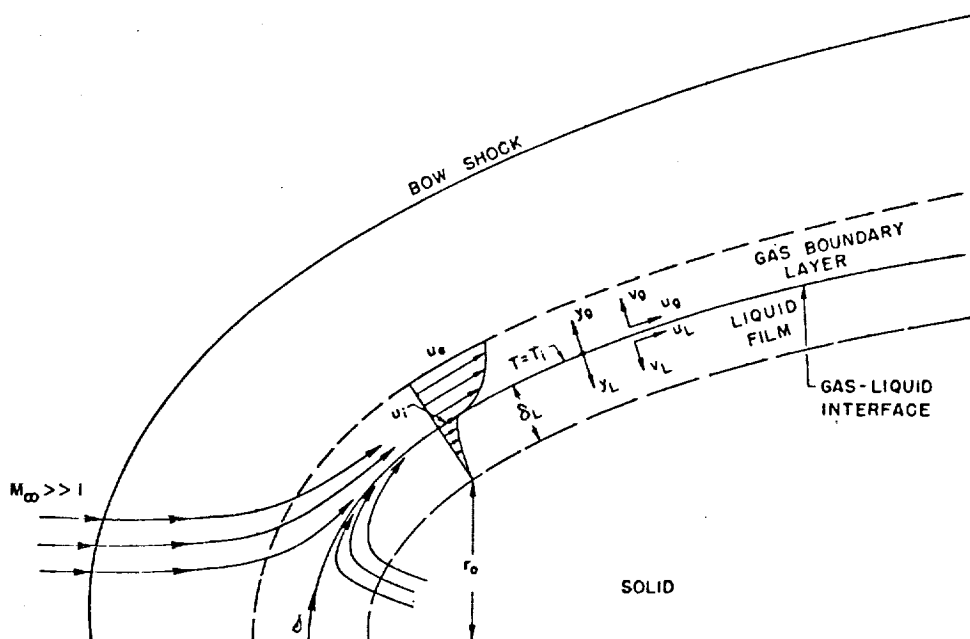


Fig. 1. Schematic diagram of a 2-phase boundary layer over melting blunt-nosed body at high velocity.

Before we can discuss the ablation process itself, we must outline briefly the main mechanisms of heat transfer from the gas to the ablating liquid or solid surface.[2] At hypersonic speeds, the hot gas in the "shock layer" between the body and the bow shock wave (Fig. 1) is partly or fully dissociated. When this mixture of atoms and molecules enters the boundary layer, strong concentration gradients are produced and heat energy is transported toward the surface, partly by diffusion and partly by ordinary heat conduction. Recombination reactions occur in the boundary layer and some of the gas components may react chemically with vaporizing surface material. Of course, the details are extraordinarily complicated, but it turns out[2-5] that the convective heat-transfer rate at the gas-liquid or gas-solid interface depends primarily on the total enthalpy difference across the gas boundary layer, and not on these details, provided that the ratio of mass diffusivity to thermal diffusivity of the gas is nearly unity. The maximum effect of chemical reactions on heat-transfer rate corresponds to the rate of energy transfer that would occur if all the oxygen atoms at the outer edge of the boundary layer that could possibly diffuse to the surface combined with the surface material.[5]

At hypersonic speeds, heat energy is transported to the body surface also by radiation from the hot gas in the shock layer. Theoretical and experimental research[6] has shown that the emissivity per centimeter of "air" in equilibrium at temperatures of the order of 10,000°K. is less than one per cent for gas densities in the shock layer less than ten per cent of sea level density. For most entry trajectories, the gas radiative heat-transfer rate is much smaller than the convective heat-transfer rate, but for direct entry into a planetary atmosphere at near-normal incidence, gas radiation may be dominant. Radiation from the shock layer to the body occurs mostly in the ultraviolet to near infrared portion of the spectrum, while radiation away from the much cooler gas-liquid or gas-solid interface occurs mostly in the infrared to far-infrared. Thus, the gas in the shock layer is nearly transparent to infrared radiation, and this mode of heat transfer is important for high-temperature ablators.

With this summary as a background, the physical mechanisms of ablation are discussed in Section II. The emphasis here is on the main processes and not on the detailed theoretical analyses; for these, the interested reader should consult the numerous references cited. Some experimental studies of ablation are discussed in Section III. Applications of ablating materials to spacecraft entering a planetary atmosphere are treated briefly in Section IV, in order to illustrate the flexibility of ablating heat-sink systems.

## II. Physical Mechanisms of Ablation

### II. 1. Melting Ablation

To AN OBSERVER fixed in the gas-liquid interface, molten material appears to be flowing toward him, as well as along the body surface (Fig. 1), and the heat energy absorbed and carried away by this countercurrent of material against the main direction of heat flux is the chief mechanism of ablation. The most important physical property of a melting ablator is the viscosity of the liquid film, as shown

originally by Sutton.[7] The larger the viscosity, the greater is the film thickness, the temperature rise across the film and the magnitude of the heat energy absorbed by the ablator. For the highly viscous substances of interest, the velocity at the interface in the direction parallel to the body surface ($u_i$) is negligibly small compared with the velocity at the outer edge of the gas-phase boundary layer ($u_e$). As long as vaporization does not occur, the gas boundary layer is virtually independent of the presence of the liquid film, and the heat transfer rate and shear stress at the gas-liquid interface are very nearly equal to their values at a *solid* boundary at the enthalpy level $h_{s_i} = h_i(T_i)$. This statement applies equally well to laminar and turbulent gas boundary layers.

Certain glassy substances do not possess a definite melting temperature, and therefore do not have a definite liquid film thickness.[8] Nevertheless, it is helpful to visualize the process of melting ablation in terms of an effective thickness, $\delta_L$, and a corresponding effective temperature rise, $T_i - T_m$, across this film. The countercurrent of molten material absorbs heat energy at a rate given by

$$\int_0^{\delta_L} \rho v c_{p_L}(\partial T/\partial y)dy = \int_{T_m}^{T_i} \rho v c_{p_L} dT = (\overline{\rho v}) c_{p_L}(T_i - T_m) = \dot{q}_i - \dot{q}_s \qquad (1)$$

where $(\overline{\rho v})$ is the average mass flux. A detailed calculation[9] shows that $(\overline{\rho v}) = 0.60\,\dot{m}_L$, so that

$$\dot{q}_s = \dot{q}_i - 0.60 \dot{m}_L c_{p_L}(T_i - T_m) \qquad (2)$$

In other words, in addition to its heat capacity up to the melting temperature, the ablating material absorbs an amount of energy equivalent to that required to heat about 60 per cent of the melt from the melting temperature up to the interface temperature. When ablation reaches a steady state

$$\dot{q}_s \cong \dot{m}_L[L_m + \bar{c}_s(T_m - T_0)] \qquad (3)$$

where $L_m$ is the heat of fusion* (if any). By utilizing Eqs. (2) and (3), one obtains the effective heat capacity, $\mathcal{3C}$, of the ablating material, as follows:

$$\mathcal{3C} = \dot{q}_i/\dot{m}_L = L_m + \bar{c}_s(T_m - T_0) + 0.60 c_{p_L}(T_i - T_m) \qquad (4)$$

Now what factors determine the magnitude of the temperature rise across the liquid film? Without going into details,[9] we remark that this temperature rise is given very closely by the "thin film" relation

$$\dot{q}_i = \dot{q}_0 = [\bar{k}_L(T_i - T_m)]/\delta_L \qquad (5)$$

and some estimate of the effective film thickness $\delta_L$ is required. By utilizing the approximate relation $\tau_{L_i} = \tau_{0_i} = \mu_L(u_i/\delta_L)$, recognizing that the liquid mass flux at any station

$$\int_0^{\delta_L} \rho_L u_L dy = \alpha \rho_L u_i \delta_L$$

---

* Here we are assuming that the heat energy stored in the material by conduction is small compared with the heat absorbed by ablation.

is proportional to the integral of the melting rate around the body up to that station, and employing Eq. (4) and the modified Reynolds analogy

$$(\dot{q}_g)_i/(\tau_g)_i = (h_{s_e} - h_{s_i})/(u_e)\,(\overline{Pr}_g)^{-2/3}$$

one obtains

$$\delta_L/R_0 \sqrt{Re_0} \sim \sqrt{(\nu_L)_i/(\nu_e)_{g,\,0}} \sqrt{h_{s_e} - h_{s_i}/\mathfrak{K}} \tag{6}$$

From Eqs. (5) and (6),

$$T_i - T_m \sim [\sqrt{(\rho_i\mu_i)_{g,\,0}}\,(h_{s_e} - h_{s_i})][\sqrt{(h_{s_e} - h_{s_i})/\mathfrak{K}}\,\sqrt{(\nu_L)_i}](N^{1/2}/\bar{k}_L) \tag{7}$$

where the first bracket in Eq. (7) arises from the heat transfer rate $\dot{q}_g$, and the second bracket contains the film thickness. Since the viscosity of the liquid is a sensitive function of the temperature, Eq. (7) is an implicit relation for the temperature rise. For example, for Corning No. 7740 glass, $(\mu_L)_i = 0.0672\ \exp\ [(8720/T_i)^{1.612}]$, where $(\mu_L)_i$ is expressed in lb./ft.-sec. and $T_i$ is in °F. absolute.

The function $N(s)$ depends on the local heat-transfer rate and also on the heat-transfer rate history over the body surface up to the point in question.[9] At the forward stagnation point of a blunt-nosed body $N = 2^{-m}$ for laminar gas flow, where $m = 0$ for two-dimensional flow and $m = 1$ for axially symmetric flow. Elsewhere on the body surface $N \cong 2^{-m}(p/p_0')$, so long as the gas boundary layer remains laminar. On the other hand, when laminar-turbulent transition occurs in the gas boundary layer near the forward stagnation point the value of $N$ at the sonic point on the body surface (for example) is given[†] by

$$N \cong 1.11Q_t^*[0.18 + 0.35Q_t^*] \tag{8}$$

where

$$Q_t^* = 0.050/2^{m/2}(\rho_\infty/\rho_{e_g,\,c})^{c.15}(Re_\infty)^{0.30} \tag{8a}$$

Of course, these rough estimates cannot be regarded as a substitute for a detailed theoretical treatment[7, 8, 10-12] but they furnish the following important conclusions about melting ablation:

(1) The temperature rise across the liquid film is strongly dependent on the liquid viscosity and the driving enthalpy potential $(h_{s_e} - h_{s_i})$. At the forward stagnation point, this temperature rise is completely independent of the body nose radius, while for a turbulent gas boundary layer $(T_i - T_m)$ is weakly dependent on body dimensions through the factor $Re_\infty^{0.30}$ in Eq. (8a).

(2) . Evidently, the enthalpy increase across the liquid film is much smaller than the enthalpy difference across the gas boundary layer, because the thermal conductivity of the liquid is so much larger than that of the gas, while $\delta_L$ and $\delta_g$ are of the same order of magnitude. Nevertheless, at hypersonic flight velocities of the order of 18,000 fps. the additional energy absorbed by the countercurrent

---

† Here $Q_t^*$ is the ratio of the turbulent heat transfer rate at the sonic point to the laminar heat transfer rate at the stagnation point; e. g., for $Re_\infty = 10^7$ and $m = 1$, $Q_t^* \cong 3.2$.

flow of liquid across this film amounts to about 70 per cent of the heat capacity up to melting for a laminar gas boundary layer, and to about 100 per cent for a turbulent gas boundary layer (Fig. 2, for example).

(3) For a typical melting ablator, the total heat capacity is about 1,200 B.t.u./lb. for laminar gas flow and about 1,500 B.t.u./lb. for turbulent gas flow. The restrictions on maximum heat-transfer rate imposed by a nonmelting solid heat sink are removed, and the effective heat-absorbing capacity is comparable with that of a high-temperature metallic heat shield such as beryllium. In certain cases, infrared radiation may increase the effective heat capacity, because of the high temperature at the gas-liquid interface (Fig. 2).

### II. 2. *Vaporization or Sublimation*

When vaporization occurs at the gas-liquid interface, or when sublimation takes place directly from the solid phase, the countercurrent of gas away from the surface takes up a large fraction of the enthalpy difference across the gas boundary
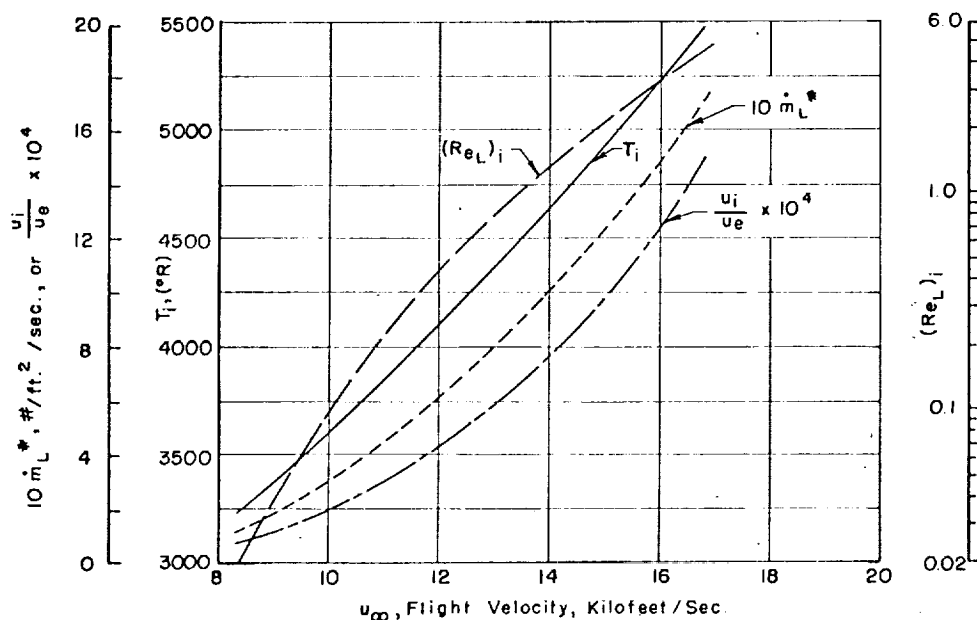


Fig. 2. Liquid film properties at gas-liquid interface and peak surface melting rate—turbulent gas boundary layer at sonic point, altitude = 60,000 ft., $R_o$ = 2 ft., Corning glass No. 7740, $T_m$ = 3,000°R.

layer. A rough estimate of this heat blockage by mass addition is obtained by considering the countercurrent mass flux $\rho v = \dot{m}_i$ to be constant across a layer of uniform thickness in the main flow direction. Then

$$\dot{m}_i(dh_s/dy) \cong -(d\dot{q}/dy) \tag{9}$$

where $\dot{q} = -F(y)(dh_s/dy)$, and $F(y) = k/\bar{c}_p$ for laminar gas flow, while $F(y) = \rho\epsilon$ for turbulent flow: here, $\epsilon$ is the turbulent exchange coefficient, or effective turbulent thermal diffusivity.[5] By defining a new variable

$$Y = \int_0^y dy/F(y)$$

and integrating Eq. (9) across the layer, one obtains

$$(h_s - h_{s_i})/(h_{s_e} - h_{s_i}) = (e^{\dot{m}_i Y} - 1)/(e^{\dot{m}_i \Delta} - 1) \tag{10}$$

(The stagnation enthalpy distribution is indicated schematically in Fig. 3.) According to Eq. (10),

$$(\dot{q}_0)_i = \dot{m}_i \Delta h_s/(e^{\dot{m}_i \Delta} - 1) \tag{11}$$

But this expression must reduce to the heat-transfer rate for zero mass addition when $\dot{m}_i \to 0$; therefore,

$$\Delta = (\rho_e u_e C_{H_O})^{-1} \qquad \frac{(\dot{q}_0)_i}{[(\dot{q}_0)_i]_{\dot{m}_i = 0}} = C_H/C_{H_O} = B/(e^B - 1) \tag{12}$$

where $B$ is the mass addition parameter $\dot{m}_i/\rho_e u_e C_{H_O}$. For small values of $B$, $C_H/C_{H_O} \cong 1 - B/2$. In Fig. 4, the blocking effect of mass addition on heat transfer for air injection into an air boundary layer is illustrated for laminar flow at the forward stagnation point, and for turbulent flat-plate experiments at supersonic speeds. Evidently, the rough estimate given by Eq. (12) somewhat overestimates
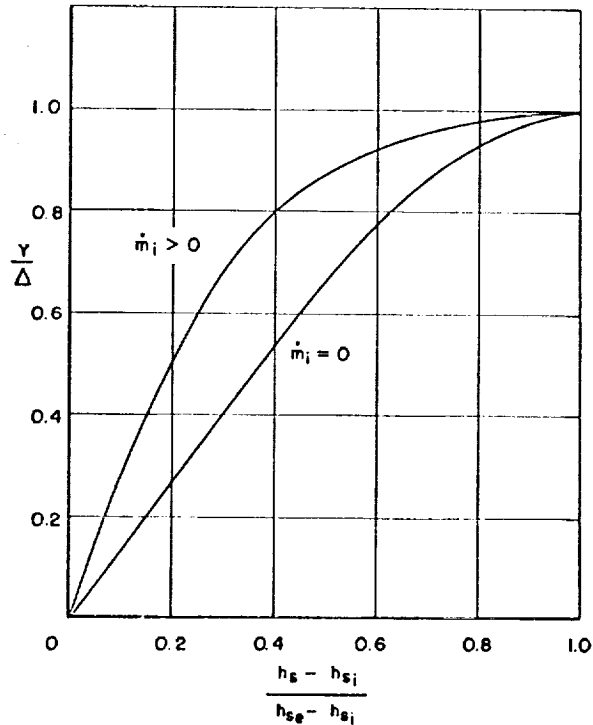


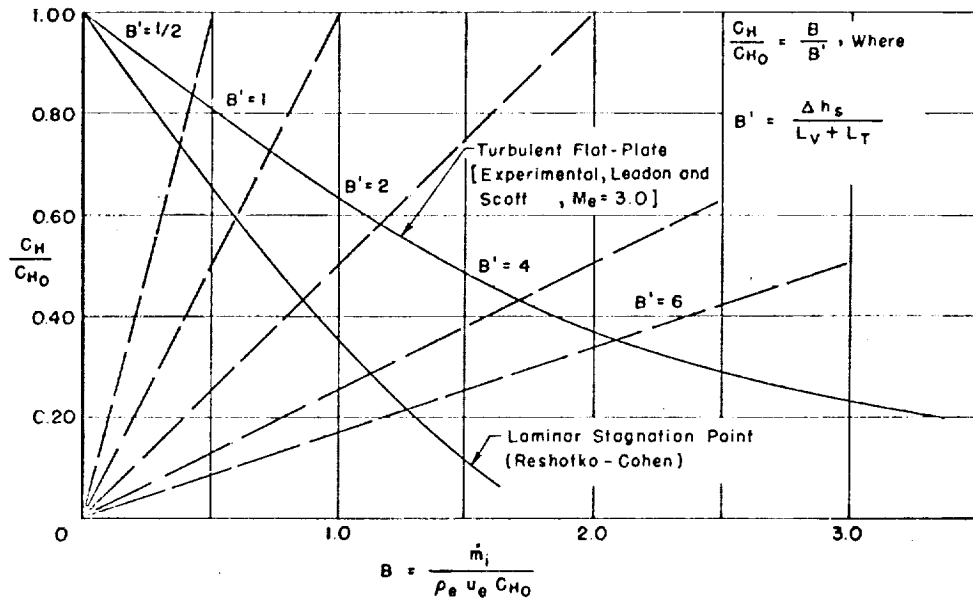Fig. 3. Effect of mass addition on enthalpy distribution (schematic).

Fig. 4. Effect of mass addition on heat-transfer rate (air to air).

this effect for turbulent flow, but underestimates the effect for laminar flow because the laminar boundary layer thickness is actually increased by mass addition.

Now the significant feature of gaseous ablation is the interaction or "feedback" mechanism between the rate of mass addition and the net rate at which heat energy is supplied to the gas-liquid or gas-solid interface. When ablation reaches a steady state $\dot{q}_{NET} = \dot{m}_L L_T$, where $L_T = \mathcal{K}_0$ (Section II. 1) if melting plus vaporization occurs, or $L_T$ is the thermal capacity of the solid material up to sublimation temperature if sublimation occurs. But $\dot{q}_{NET} = (\dot{q}_0)_i - (f\dot{m}_L)L_V$,* where $f$ is the fraction vaporized; of course, $f = 1$ for a sublimation process. In other words, $(\dot{q}_0)_i = \dot{m}_L(L_T + fL_V)$. If a new mass addition parameter $B'$ is defined by the relation

$$B' = \dot{m}_i / \rho_e u_e C_H = f\dot{m}_L / \rho_e u_e C_H$$

then

$$B' = f(\dot{q}_0)_i / (\rho_e u_e C_H)(L_T + fL_V) = f\Delta h_s / (L_T + fL_V) \tag{13}$$

where $\Delta h_i$ is the total enthalpy difference $(h_{s_e} - h_{s_i})$. By definition

$$C_H / C_{HO} = B / B' \tag{14}$$

and the intersection of the straight line for a given $B'$ defined by Eq. (14) with the curve of $C_H / C_{HO}$ vs. $B$ in Fig. 4 gives the value of $B$, or the normalized rate of mass loss in terms of known conditions for zero mass addition. In Fig. 4, $f = 1$; when melting plus vaporization occurs $f$ is a function of $\Delta h_s / L_V$ (Ref. 8). In any event,

---

* The quantity $L_V$ must include the heat of dissociation of the gaseous ablating material if dissociation occurs right at the gas solid or gas-liquid interface, or if the dissociated gas is able to diffuse back to the interface and the interface is not catalytic for recombination.[3] Otherwise, $L_V$ is simply the usual heat of vaporization or sublimation per gram of material.

the most important parameter is again the total enthalpy difference across the layer.

A correlation[13] of theoretical and experimental results for mass addition into a laminar gas boundary layer shows that $C_H/C_{H_0} \cong 1 - \beta B$, where $\beta \cong 0.84$ $(\mathfrak{M}_1/\mathfrak{M}_2)^{1/3}$, and $\mathfrak{M}_1$ and $\mathfrak{M}_2$ are the molecular weights of the original gas in the boundary layer and the injected vapor, respectively. According to Eq. (14), for laminar gas flow

$$B \cong B'/(1 + \beta B') \tag{15}$$

or

$$B = f\dot{m}_L/\rho_e u_e C_{H0} = f\Delta h_s/[L_T + f(L_V + \beta\Delta h_s)] \tag{16}$$

The effective ablation heat capacity $\mathfrak{K}_{eff}$ defined by $(\dot{q}_o)_0 = \dot{m}_L\mathfrak{K}_{eff}$ is given by the relation

$$\mathfrak{K}_{eff} = (L_T + fL_V)\Delta h_{s_0}/\Delta h_s + f\beta\Delta h_{s_0} \tag{17}$$

where $(\dot{q}_o)_0$ and $\Delta h_{s_0}$ are the heat-transfer rate and the enthalpy difference across the gas boundary layer without mass addition, respectively. As discussed in Section I, the effect of combustion (if any) of the gaseous ablated material appears as an added driving potential, or

$$\Delta h_s/\Delta h_{s_0} = 1 + \Delta Q_c/\Delta h_{s_0}$$

where $\Delta Q_c$ is the heat released by combustion per gram of air. According to Eq. (17) the heat energy blocked by gaseous ablation amounts to a fraction $f\beta$ of the enthalpy difference across the gas boundary layer.

When sublimation occurs, or when $T_t$ is close to the local boiling temperature, $f \to 1$, and the problem is considerably simplified.* Here

$$B' = \Delta h_s/(L_V + L_T) \qquad B = \Delta h_s/(L_V + L_T + \beta\Delta h_s) \tag{18}$$

and

$$\mathfrak{K}_{eff} = (L_T + L_V)[1 + (\Delta Q_c/\Delta h_{s_0})]^{-1} + \beta\Delta h_{s_0} \tag{19}$$

Thus, the effective heat of ablation increases linearly with the driving enthalpy difference across the boundary layer, and the relative importance of combustion steadily decreases. To state the result another way, for laminar flow $B \to 1/\beta$ as $B' \to \infty$, or the normalized rate of mass loss approaches a constant as $\Delta h_{s_0}$ increases. If one utilizes Eq. (12) for a turbulent gas boundary layer then $B = \log_e (B' + 1)$; Fig. 5 illustrates this "self-regulating" property of gaseous ablation.**

Just as in the case of melting ablation, infrared radiation can make a significant contribution to the effective heat capacity of a high-temperature ablator.[14] The

---

* When $L_V \gg L_T$ a similar simplification occurs even for relatively low values of $f$, as in the case of $H_2O$.

** A rough approximation for turbulent gas boundary layers is $\beta_T \cong 1/3 \beta_L$ (Ref. 14).
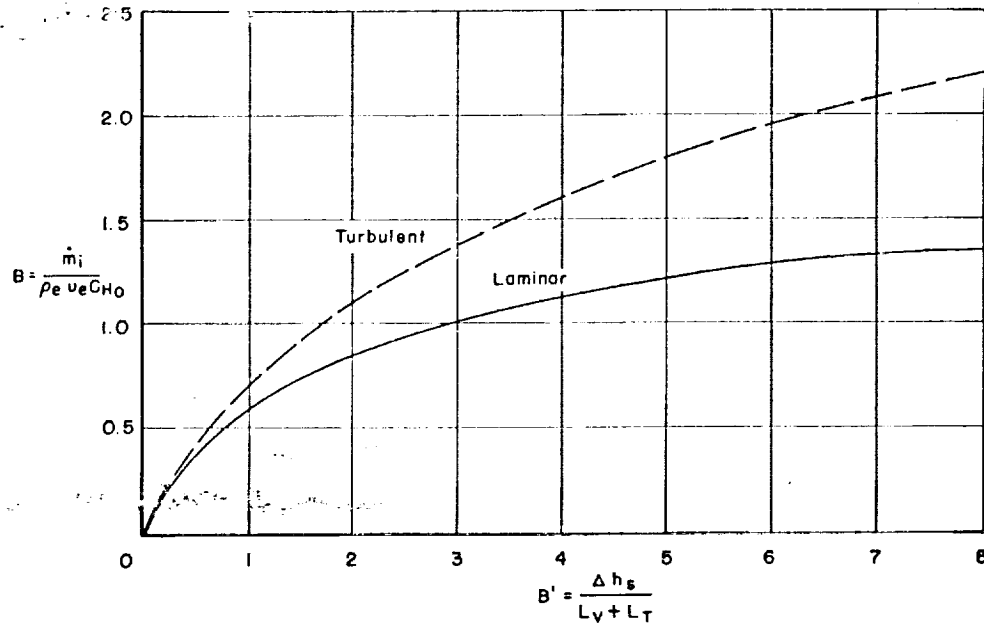
Fig. 5. Normalized ablation rate as a function of driving enthalpy difference.

enthalpy difference $\Delta h_s$ in the expression for the mass addition parameter $B'$ [Eq. (13)] is reduced by the factor

$$\left[1 - \frac{q_R}{(\dot{q}_o)_0} C_{H_o}/C_H \left(1 + \frac{\Delta Q_c}{\Delta h_{s_o}}\right)^{-1}\right]$$

where $\dot{q}_R$ is the *net* radiative heat-transfer rate away from the interface. When radiation from the hot gas in the shock layer to the interface is negligible (Section I), $\dot{q}_R = \epsilon\sigma T_i^4$. For laminar gas flow with $C_H/C_{H_o} = 1 - \beta B$, one finds

$$B = \frac{f\Delta h_s\{1 - [\dot{q}_R/(\dot{q}_o)_0][1 + (\Delta Q_c/\Delta h_{s_c})]^{-1}\}}{L_T + f(L_V + \beta\Delta h_s)} \qquad (20)$$

and the effective heat capacity given by Eqs. (17) and (19) is increased by the factor in brackets appearing in the numerator of Eq. (20).

In general, the interface temperature must be determined by iteration between the energy balance expressed by Eq. (20) and the equilibrium vapor pressure-temperature curve of the material. At the interface, the mass flux of material injected into the gas boundary layer is carried away partly by the mean countercurrent flux and partly by diffusion. The analysis given in Ref. 5 shows that

$$(K_E)_i = B'/(B' + 1) \qquad (21)$$

where $(K_E)_i$ is the mass fraction of the vaporizing material at the interface.* For laminar gas flow [Eq. (15)]

---

* As shown in Ref. 5, chemical reactions can be included in the analysis.

$$B' = B/(1 - \beta B) \tag{22}$$

Now

$$(p_E)/p = \{1 + [(1/K_E) - 1]\mathfrak{M}_E/\mathfrak{M}_{air}\}^{-1} \tag{23}$$

where $p_E$ is the partial pressure of the vapor, and $K_E$ is the mass fraction of the ablating material itself.

When $f \rightarrow 1$ and the radiative heat transfer rate is small compared to the convective heat-transfer rate the value of $B$ [Eq. (20)] is not very sensitive to $T_i$ at hypersonic speeds. A good first approximation to $B$ can be obtained by making a reasonable estimate of $T_i$. Then a much better approximation to $T_i$ is obtained by utilizing this value of $B$ and Eqs. (21) through (23). It appears that $T_i$ adjusts

Fig. 6. Stagnation-point heat of ablation measurements for Teflon, compared with theory.
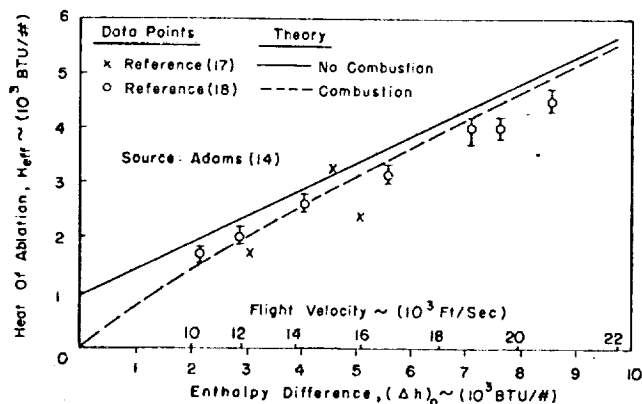
itself at hypersonic speeds to a value determined mainly by the energy balance and the blockage effect of mass addition on heat transfer.

*To summarize*, gaseous ablation produces a substantial increase in the effective heat capacity of the material by means of the blocking effect of mass addition on heat transfer to the interface. In fact, the effective ablation heat capacity increases almost linearly with the external stagnation enthalpy, and can reach values of 5,000 B.t.u./lb. for laminar flow and 2,500 B.t.u./lb. for turbulent flow at flight speeds of the order of 20,000 fps. To put it another way, the normalized rate of ablation $\dot{m}_i/\rho_e u_e C_{H_0}$ becomes virtually independent of the driving enthalpy difference across the gas boundary layer when this enthalpy is large compared to the intrinsic heat capacity $(L_V + L_T)$ of the material.

## III. Experimental Studies of Ablation

BECAUSE OF THE SEVERE CONDITIONS encountered during ballistic missile re-entry, most of the earlier experimental investigations of ablation were concerned with the mechanical properties of ablating materials. These studies were carried out with the aid of high-temperature sources that could readily be made available, including oxy-acetylene torches, solar furnaces, and rocket exhaust jets. Although such tests provided much valuable practical information, it soon became evident

that one must duplicate, or at least take into account, important parameters like

$$\Delta h_s/(L_V + L_T) \qquad \dot{q}_R/\dot{q}_\theta$$

duration of the heat pulse compared with time required to reach steady-state ablation, etc., before experimental results could safely be extrapolated to hypersonic flight conditions.

Experimental investigations of ablation, guided by theoretical considerations, have been conducted in air plasma jets, or arc-jets, capable of providing a wide range of stagnation enthalpies up to satellite-entry conditions.[15, 16] Adams[14] has given an excellent review and evaluation of such studies. Perhaps the most striking result is the experimental confirmation of the blocking effect of gaseous ablation on heat transfer (Section II. 2), at least for laminar flow. In Fig. 6, we reproduce Adams' plot of $\mathcal{3C}_{eff}$ for Teflon vs the driving enthalpy difference $\Delta h_{s_0}$,
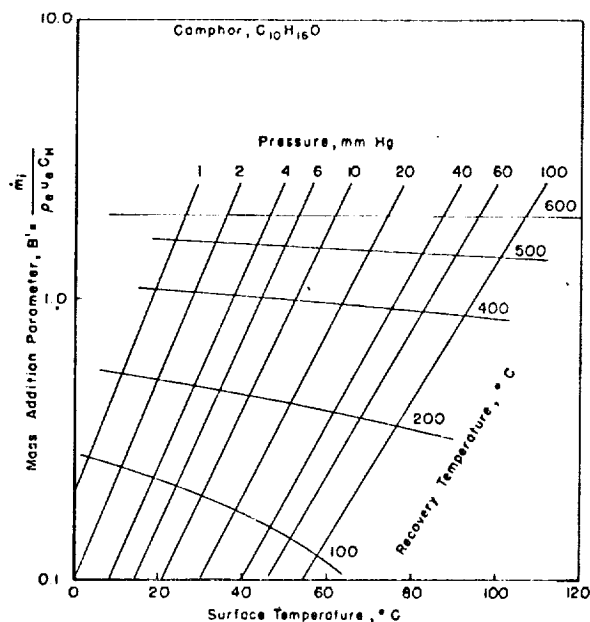


Fig. 7.  Mass addition parameter vs surface temperature

as obtained by General Electric[17] and AVCO.[18] Even the slope of the experimental curve is in good agreement with the theoretical prediction when proper account is taken of the molecular weight of Teflon ($C_2F_4$). Another important result is the experimental confirmation of the Bethe-Adams[8] predictions of $\mathcal{3C}_{eff}$ vs $\Delta h_s$ for a melting-evaporating, highly viscous substance, such as quartz. As Adams[14] points out, it is essential to estimate or measure the high temperatures at the gas-liquid interface (or the net radiative heat-transfer rate), before the data can be interpreted. If proper allowance is made for radiation, the results of the earlier tests on quartz and reinforced plastics[19] in rocket exhausts correlate fairly well with arc-jet experiments, in terms of the parameter $\Delta h_s/(L_V + L_T)$.

By developing and extending the arc-jet facility to provide higher supply (or test section) pressures and larger model sizes, ablation experiments can be

performed with a turbulent gas boundary layer; the results of such experiments at AVCO should be available shortly. Ablation studies are also required at the high stagnation enthalpies corresponding to super-satellite speeds (Section IV), where electronic heat transfer may enter the problem, and in gases other than air, in order to simulate the atmospheres of other planets.

Ablation experiments in a high-temperature facility usually consist of measurements of mass loss in a certain time interval, and the hot jet is calibrated in terms of the melting time of a known sample, such as a copper hemisphere-cylinder.[15, 16] For certain purposes, such measurements are sufficient, but it would be desirable to study the fluid-mechanical aspects of ablation in some detail under carefully controlled conditions. Kubota[13] has examined the possibility of providing a sufficiently wide range of the ablation similarity parameters (Section II) in a moderate-temperature, continuously operating, hypersonic wind tunnel. Since the driving enthalpy difference is much lower than in flight, materials with relatively low values of intrinsic heat capacity $(L_V + L_T)$ must be selected. In addition, the vapor pressure of such materials at low-to-moderate temperatures must be of the same order as the local static pressure at the outer edge of the boundary layer. By employing relations similar to Eqs. (18), (21) and (23) (Section II), Kubota prepared charts of the mass addition parameter $B'$ vs surface temperature under hypersonic wind-tunnel conditions for $H_2O$ (ice), $CO_2$ (dry ice), and $C_{10}H_{16}O$ (camphor). Fig. 7 shows one such plot for camphor. According to this chart values of $B'$ larger than unity can be attained in the GALCIT hypersonic tunnel (Leg 2) operating at stagnation temperatures of around 400 to 500°C. Under these conditions, the mass fraction of the vapor at the gas-solid interface is larger than 0.50.

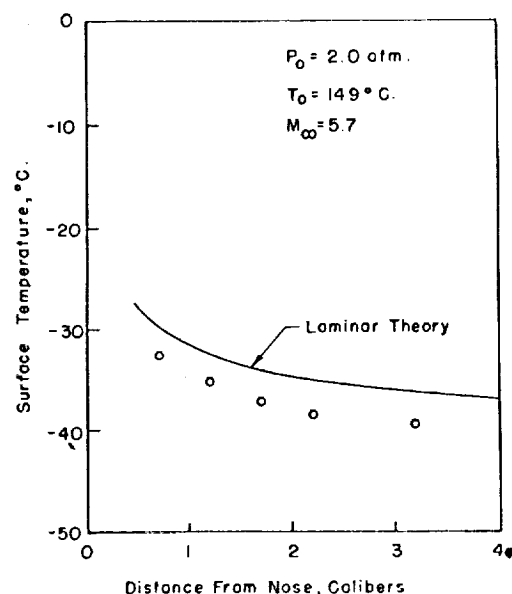At sufficiently low local static pressures, $H_2O$ (ice) does not melt, but sublimes,[13]



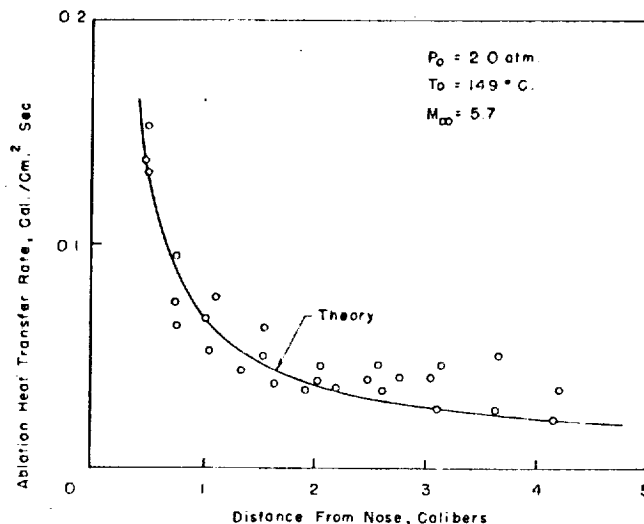Fig. 8. Surface temperature in $H_2O$ (ice), hemisphere-cylinder.

Fig. 9. Ablation heat-transfer rate along cylindrical surface, $H_2O$ (ice) model.

and the heat of ablation is about 1,000 B.t.u./lb.; thus $B'$ is very low in the GALCIT hypersonic tunnel. Ablation measurements on $H_2O$ (ice) can be regarded as a convenient "base-line" for evaluating experimental techniques. Kubota[13] measured the ablation rates and surface temperatures on a water-ice hemisphere cylinder model at the stagnation point and also on the cylindrical afterbody (Figs. 8 and 9). Agreement between laminar theory and experiment is encouraging, and indicates that useful information about the ablation process can, in fact, be obtained. Similar experiments on camphor models are now in progress. Detailed measurements of such quantities as vapor concentration in the gas boundary layer should also be feasible.

Because of the comparatively low heat-transfer rates obtained on models in a moderate-temperature hypersonic tunnel, the ablation process is "stretched out" in time, and studies of the time required to reach steady-state ablation can be made. Another interesting question suitable for investigation on this longer time scale is the feed-back mechanism between the changes in body shape brought about by ablation, and the distribution of static pressure and heat transfer rate around the body surface. For example, one would expect that a hemispherical nose becomes "flatter" with time, until the heat transfer rate is nearly uniform across the face.* On the other hand, along the cylindrical afterbody the pressure is nearly independent of local body shape, and decays inversely with distance from the nose, according to blast-wave theory. If $r_0(x)$ denotes the radius of the body cross section, the condition for a steady "equilibrium shape" is

$$(\partial r_0/\partial t) + w_A(\partial r_0/\partial x) = 0$$

where $w_A$ is the constant axial "velocity" of ablation. But

$$\rho_s(\partial r_0/\partial t) = -(\dot{q}_{y_a}/\mathcal{K}_{eff})$$

* Radiative heat transfer and internal heat conduction must also be taken into account.

so that

$$\partial r_0 / \partial x = (\dot{q}_0)_0' / \rho_s w_A \mathcal{K}_{eff}$$

In general $(\dot{q}_0)_0$ is a complicated function of static pressure distribution and body shape. Suppose we make the rough approximation that $(\dot{q}_0)_0 \sim \sqrt{p}$. Then $\partial r_0 / \partial x \sim \sqrt{p} \sim \sqrt{1/x}$, or $r_0 \sim \sqrt{x}$; in other words, according to this rough calculation, the equilibrium afterbody shape is a parabola of revolution, provided the nose is quite blunt. A somewhat more careful theoretical and experimental study of this interesting problem would be worthwhile.

## IV.   Some Applications and Future Developments

BECAUSE OF THE high stagnation enthalpies associated with the entry of manned or unmanned satellite vehicles and spacecraft into a planetary atmosphere, the effective heat of ablation should be large (Sections II and III), but the requirements imposed on ablating materials for this application are quite different than for ballistic missile re-entry. For example, when re-entry is initiated from a circular satellite orbit the entry angle is normally very low ($<2°$), because of the prohibitively large retrorocket weight required for a steeper descent. The maximum convective heat-transfer rates for a typical nonlifting vehicle[20] are about 65 B.t.u./ft.$^2$/sec., or less than one tenth the values encountered by a ballistic missile, and the duration of the heat pulse is about 250 sec., or ten times longer. Under these conditions, a high-temperature ablator will radiate rather than ablate, so that a moderate- or low-temperature ablator is required. Even such a material reaches steady-state ablation only after a certain time interval.[21] If the countercurrent mass flux of liquid or solid material is regarded as a constant, the effective thermal depth[8, 16] $\delta_T$ is proportional to $\mathcal{K}/v = \rho_s \mathcal{K}/\dot{m}$, where $\mathcal{K} = k/\rho_s c_p$ is the thermal diffusivity of the material. The time $\tau$ required for the heat pulse to penetrate this distance is proportional to $\delta_T^2/\mathcal{K}$, or

$$\tau \sim (\rho_s k/c_p)[1/(\dot{m})^2] = (\rho_s k/c_p)[(\mathcal{K}_{eff})^2/(\dot{q}_0)_0^2]$$

The low values of $(\dot{q}_0)_0$ and high $\mathcal{K}_{eff}$ encountered along a grazing entry trajectory dictate a low-density, low-temperature ablator that is also a poor thermal conductor. Of course, these physical properties are precisely those that are required to minimize the problem of heat conduction to the interior during relatively long "soak" times. For example, if the gas-solid or gas-liquid interface remains at a constant temperature $T_i$ for a period $\tau'$, and the inner wall must be kept below a certain prescribed maximum temperature $T_{max}$, then the weight/area of insulation material required is proportional to the quantity

$$\sqrt{(\rho_s k/c_p)\tau'} \qquad \{\log_e[(T_i - T_0)/(T_i - T_{max})]\}^{-1/2}$$

where $T_0$ is the initial temperature of the inner wall.

Teflon (Section III) meets these requirements to a remarkable degree. When lift is employed, however, the duration of the heat pulse increases roughly as the

lift-drag ratio for a given (shallow) re-entry angle, and both insulation weight and weight of ablated material will increase. Thus, there is a strong incentive to develop materials that ablate at even lower temperatures than Teflon.

Because of the low heat-transfer rates experienced in grazing entry, radiation from the body surface is always an attractive alternative. Of course, the various proposed heat-protection systems are by no means mutually exclusive. One possible combination is a material that radiates most of the heat over part of the trajectory, and ablates only over the portion of the flight where the convective heat-transfer rate exceeds the radiating capacity of the surface.

The situation is quite different for entry from highly elliptical orbits or from outer space. In these cases, a steeper entry angle is an attractive means of alleviating the difficult guidance and control problem associated with grazing entry and multiple-pass drag braking. For low entry angles, the width of the entry "corridor" in earth radii is given by

$$\Delta d/R_E \cong 1/2(\theta_{E_2}{}^2 - \theta_{E_1}{}^2)$$

where $\theta_{E_1}$ and $\theta_{E_2}$ are the minimum and maximum allowable entry angles, respectively. On the one hand, a vehicle returning from outer space at the "ideal" approach velocity of 35,000 fps.[*] skips out of the earth's atmosphere if the entry angle (at 400,000 ft. altitude) is less than about 4.5°. On the other hand, the peak deceleration experienced by a nonlifting, constant-drag vehicle is already 20 g's when $\theta = 6°$. Thus, for manned vehicles, the entry "corridor" is only about 10 miles high. By employing aerodynamic lift during entry,[22] the peak deceleration is held to 10 g's for a maximum lift-drag ratio of 2.0 and an entry angle of 10.5°, so that the allowable entry "corridor" is now about 60 miles high.[**] For such a trajectory, the maximum stagnation-point heat-transfer rate is (800 B.t.u./ft.²/sec.)$/\sqrt{R_0}$, for a value of $W/C_D A = 100$, where $R_0$ is the nose radius in feet, and the total heat energy transferred to the vehicle is about (40,000 B.t.u./ft.²)$/\sqrt{R_0}$. Because of the relatively high convective heat-transfer rates and the high-stagnation enthalpy along the trajectory, a gaseous ablator should have an effective heat capacity of at least 6,000 B.t.u./lb. Again, the comparatively long duration of the heat pulse dictates a low or moderate temperature, low density ablating material that is also a poor thermal conductor.

Employment of ablating materials during entry into a planetary atmosphere is attractive also for unmanned vehicles.[24] A typical space probe, entering the atmosphere of Venus at a velocity of about 40,000 fps. and near-normal incidence, experiences a peak deceleration of about 400 g's, a peak radiative heat-transfer rate from the hot gas in the nose region of about 7,000 B.t.u./ft.²/sec. and a peak convective heat-transfer rate of about 1,000 B.t.u./ft.²/sec., for $W/C_D A = 60$. Gaseous ablation is incapable of "blocking" the radiative heat transfer from the

---

[*] The actual approach velocity is likely to be of the order of 40,000 fps.

[**] Grant[23] has recently shown that the corridor width can be increased to 100 miles by employing combined drag and lift modulation.

gas to the body surface,* but an ablating material is fully capable of absorbing the heat-transfer rates and heat-energy loadings that would be involved.

Even this brief discussion should illustrate the inherent flexibility of ablating heat-sink systems. Ablating materials are certain to be developed and utilized far beyond our present conceptions.

---

\* Perhaps one could select (or invent) a gaseous ablator with a low absorptivity with respect to the energy spectrum of the gas radiation.

# References

[1] Solomon, G., *The Nature of Re-Entry*, Astronautics, Vol. 4, No. 3, pp. 20–21, 98, 100, March, 1959.

[2] Lees, L., *Recovery Dynamics—Heat Transfer at Hypersonic Speeds in a Planetary Atmosphere*, Chapt. 12, "Space Technology," pp. 12–01 to 12–20, John Wiley & Sons, New York, N. Y., 1959.

[3] Fay, J. A. and Riddell, F. R., *Theory of Stagnation Point Heat Transfer in Dissociated Air*, J. of the Aero. Sci., Vol. 25, No. 2, pp. 73–85, February, 1958.

[4] Lees, L., *Laminar Heat Transfer over Blunt-Nosed Bodies at Hypersonic Flight Speeds*, Jet Propulsion, Vol. 26, No. 4, pp. 259–269, April, 1956.

[5] Lees, L., *Convective Heat Transfer with Mass Addition and Chemical Reactions*, Third Combustion and Propulsion Colloquium, Advisory Group for Aeronautical Research and Development, NATO, Palermo, Italy, March 17–21, 1958, pp. 451–98, Pergamon Press, 1958.

[6] Kivel, B., *Radiation from Hot Air and Stagnation Heating*, AVCO Everett Research Laboratory, Research Report No. 79, October, 1959.

[7] Sutton, G., *The Hydrodynamics and Heat Conduction of a Melting Surface*, J. of the Aero. Sci., Vol. 25, No. 1, pp. 29–32, 36, January, 1958; also, Scala, S. M. and Sutton, G. W., *The Two-Phase Laminar Boundary Layer—A Study of Surface Melting*, Aerophysics Laboratory, Missile and Ordnance Systems Department, General Electric Company, Technical Memorandum 23, February 14, 1958.

[8] Bethe, H. A. and Adams M. C., *A Theory for the Ablation of Glassy Materials*, J. of the Aero/Space Sci., Vol. 26, No. 6, pp. 321–28, 350, June, 1959.

[9] Lees, L., *Similarity Parameters for Surface Melting of a Blunt-Nosed Body in a High Velocity Gas Stream*, ARS Journal, Vol. 29, No. 5, pp. 345–54, May, 1959.

[10] Roberts, L., *On the Melting of a Semi-Infinite Body of Ice Placed in a Hot Stream*, Department of Mathematics, Massachusetts Institute of Technology, June, 1957, ONR Contract Nonr-1841(12); also, J. Fluid Mech., Vol. 4, Part 5, pp. 505–28, September, 1958.

[11] Roberts, L., *Stagnation-Point Shielding by Melting and Vaporization*, NASA Report No. 10, April, 1959.

[12] Lew, H. G. and Fanucci, J. B., *A Study of Melting Surfaces*, General Electric Co., Missile and Space Vehicle Dept., Aerophysics Research Memorandum No. 38, April, 1959.

[13] Kubota, T., *Study of Ablation with Ice Model at $M = 5.8$*, Paper presented at the ARS Semi-Annual Meeting, San Diego, Calif., June, 1959.

[14] Adams, Mac C., *Recent Advances in Ablation*, ARS Journal, Vol. 29, No. 9, pp. 625–32, September, 1959.

[15] Brogan, T. R., *Electric Arc Gas Heaters for Re-entry Simulation and Space Propulsion*, AVCO Research Laboratory, Research Report No. 35, September, 1958; also, *The Electric Arc Wind Tunnel—A Tool for Atmospheric Re-Entry Research*, ARS Journal, Vol. 29, No. 9, pp. 648–53, September, 1959.

[16] Adams, Mac C., Powers, W. E., and Georgiev, S., *An Experimental and Theoretical Study of Quartz Ablation at the Stagnation Point*, AVCO Research Laboratory, Research Report No. 57, June, 1959.

[17] Steg, L., *Materials for Re-entry Heat Protection of Satellites*, Paper presented at the ARS Semi-Annual Meeting, San Diego, Calif., June, 1959.

[18] Georgiev, S., Hidalgo, H., and Adams Mac C., *On Ablation for the Recovery of Satellites*, AVCO Research Laboratory, Research Report No. 47, March 6, 1959.

[19] Sutton, G. W., *The Ablation of Reinforced Plastics in Supersonic Flow*, General Electric Co., Missile and Ordnance Systems Dept., Aerophysics Operation Research Memorandum No. 3, July 26, 1957.

[20] Eggers, A. J., Jr., *Recovery Dynamics—Possibility of Nondestructive Landing*, Chapt. 13, "Space Technology," pp. 13-01 to 13-53, John Wiley & Sons, New York, N. Y., 1959.

[21] Roberts, L., *An Approximate Analysis of Unsteady Vaporization Near the Stagnation Point of Blunt Bodies*, NASA Technical Note No. D-41, September, 1949.

[22] Lees, L., Hartwig, F. W., and Cohen, C. B., *The Use of Aerodynamic Lift during Entry into the Earth's Atmosphere*, Space Technology Laboratories, Inc., Report No. GM-TR-0165-00519, November 20, 1958; also, ARS Journal, Vol. 29, No. 9, pp. 634-41, September, 1959.

[23] Grant, F. C., *Analysis of Low-Acceleration Lifting Entry from Escape Speed*, NASA Technical Note No. D-249, June, 1960.

[24] Gazley, C., Jr., and Masson, D. J., *Recovery of a Circum-lunar Instrument Carrier*, Rand Corporation, Report No. P-1119, August 19, 1957; also presented at the 8th Congress of the International Astronautical Federation, Barcelona, Spain, October 6-12, 1957.

# PROGRESS AND PROBLEMS IN ATMOSPHERE ENTRY[1]

By Alfred J. Eggers, Jr., and Nathaniel B. Cohen
Office of Advanced Research and Technology
National Aeronautics and Space Administration
Washington, D.C.

## ABSTRACT

Problems of entry vehicle motion, heating, and heat protection are discussed in the context of current and possible future space flight missions, including unmanned probes of the atmospheres of Mars, Venus, and Jupiter, and manned vehicles appropriate for controlled planetary entry at velocities from orbital to hyperbolic. Recent advances in reentry physics, including both theoretical and experimental work in flow-field analysis, convective and radiative heating, and combined effects, have enhanced our ability to predict aerodynamic heating. Problems in reentry physics which remain, such as transition to turbulent flow, turbulent heat transfer at hypervelocities, and complex radiation flow-field interactions and their possible influence on vehicle configuration are discussed. Attention is also given to ground simulation facilities, such as the expansion tunnel, ballistic shock tunnel, and high enthalpy arc jet, which are particularly useful in the solution of problems in reentry physics and heat shield materials behavior. Finally, some consideration is given to the comparative features of rocket braking and maneuvering as contrasted to atmosphere braking and maneuvering for the spectrum of speeds and mission profiles of future interest.

## INTRODUCTION

Significant advances have been accomplished in the science and technology appropriate to atmosphere entry of spacecraft during the 8 years since the launching of Sputnik I. This progress is no better illustrated than by the successful entry from earth orbit of the manned Vostok, Mercury, Voskhod, and Gemini spacecraft, for which the problems inherent in orbital entry, such as high convective heating rate and load and communication blackout, were successfully overcome. For the past 4 years, atmosphere entry research activities in the United States were concentrated upon the problems appropriate to return from lunar missions which are characterized, for the Apollo vehicle, by nonnegligible radiative heating rates and a highly nonsymmetric flow field, as well.

Although the first Apollo vehicle entry has yet to be demonstrated, the next few years are expected to bring successful accomplishment of first earth orbital and then lunar return entries with this vehicle. Much engineering work for this vehicle remains to be done; however, the fundamental research activity associated with Apollo is being reduced in favor of that associated with missions and vehicles of the more distant future. Already certain new problems arising in such missions have been investigated in the various laboratories, resulting in important new knowledge. It is the purpose of this paper to discuss some of the more interesting missions of the future, to describe those mission characteristics pertinent to atmosphere entry, to review some related research

accomplishments in the recent literature, and to point out some of the many problems remaining to be solved.

References cited throughout the paper are merely representative of the wealth of literature available on the topics discussed. An extensive bibliography was provided by Love (ref. 1). Additional material may be found in the reference lists of the cited papers.

## FUTURE MISSIONS

The post-Apollo era is likely to provide a variety of new entry opportunities which introduce a number of phenomena considerably different from those related to near-ballistic entries at orbital or escape velocities into the Earth's atmosphere. The establishment of long-duration earth-orbital laboratories may well lead to a requirement for logistic vehicles capable of generating a sufficient lift/drag ratio to provide for reduced entry decelerations, maneuvering during entry for longitudinal and lateral ranging, and horizontal landing capability. Such vehicles would, of necessity, be relatively slender and nonsymmetric in order to provide the required lift; the economics of such vehicles might call for required reuse. While the gross entry environment for these vehicles will be little different from that previously encountered, their configurations will result in flow fields of a somewhat different character.

We are presently fast approaching the capability of launching unmanned probes of the atmospheres of Mars and Venus, for which a whole host of new entry problems will be encountered. The atmospheres of these two planets are at this time not fully determined, but both are thought to contain significant fractions of $CO_2$ and $N_2$, leading us to expect radiation heat transfer of major proportion from cyanogen formed in the shock layer, especially at the moderate velocities associated with Mars entry. Characteristic entry velocities for such probes are shown in Figure 1.

Because Mars is thought to be that planet in the solar system, other than Earth, most likely to have an environment suitable for the evolution of life, it may be the subject of extensive exploration, first by unmanned systems, and then, if warranted, by man. The mounting of a manned exploration program will be accompanied by major new problems in atmosphere entry associated with the three types of entry vehicles contemplated for use in such a mission; namely, a large vehicle capable of hyperbolic entry into the Martian atmosphere as alternative to a propulsive maneuver, an excursion module for landing on the surface from orbit if the Mars Orbital Rendezvous mode is used, and a hyperbolic earth reentry module. The entry velocity range associated with each of these maneuvers is shown in Figure 1. Earth return velocities shown presuppose use of trajectories shaped by passage close to Venus during the mission. For direct trajectories, earth return velocities up to about 23 km/sec are appropriate.

---

Also listed in the figure is the entry velocity associated with atmosphere probes of Jupiter, provided that no propulsive braking is utilized. Today's entry technology clearly does not permit such an entry and much work must be done if such a mission is to be attempted. Because Jupiter entry probes are so far in the future, no further consideration will be given to them here.

## FLIGHT MECHANICS AND MOTION

Among the primary problems in flight mechanics and motion appropriate to entry vehicle technology are determination of the permissible entry corridor, range capability, the ability to deploy decelerators such as parachutes, and the ability to land horizontally. Each of these places certain requirements upon vehicles, and influences the reentry physics phenomena through their dependence upon both entry trajectory and vehicle configuration. The implications of these will be discussed for Earth and Mars entry.

### Earth Entry

The entry corridor is defined for supercircular entry as the range of entry angle permitted to a vehicle between the boundaries representing skipout (overshoot) and excessive deceleration (undershoot). The allowable corridor is frequently described by a linear dimension, the corridor depth, defined by Chapman (ref. 2) as equal to the difference in the vacuum perigees for the corresponding overshoot and undershoot trajectories. The corridor available to a vehicle depends upon the planet, its atmosphere, the entry velocity, and vehicle aerodynamic characteristics, and must be sufficiently deep to accommodate approach guidance tolerances.

A very thorough discussion of earth entry flight mechanics was given by Love (ref. 1). It was shown there that the available corridor decreased rapidly with increasing entry velocity, increased with increasing lift/drag ratio, and was further increased if the modulation of lift through vehicle attitude change was permitted. For entry velocities characteristic of return from a mission to Mars, these trends are graphically illustrated by Figure 2, a plot of available corridor depth as a function of maximum hypersonic lift/drag ratio for two velocities and two lift modulation schemes. These data are cross-plotted from the data of Pritchard (ref. 3). For the roll-modulated case, the vehicle flies at a fixed attitude corresponding to a fixed ratio of the resultant lift to drag; however, the vertical component of lift may be modulated through rolling the vehicle about the flight path axis. Lateral translation will result, but this may be compensated by later maneuvers, if desired. The entry through pullout is at maximum positive lift-to-drag ratio. For this case, the overshoot boundary is defined by the minimum entry angle permitting constant altitude flight with negative lift/drag ratio after pullout (i.e., the vehicle rolls 180° at pullout), and the undershoot boundary is defined by a 12g limit on resultant deceleration.

Angle-of-attack changes are permitted in the pitch modulated case in addition to roll. For this case the overshoot criterion is the same as for the previous case, but the undershoot boundary is somewhat different. In undershoot, pitch modulation is employed when the 12g deceleration limit is reached such that this deceleration is maintained as the lift coefficient decreases through zero and to maximum negative $L/D$. Roll modulation at constant altitude is then assumed.

For the roll-modulated vehicle, large increases in maximum lift/drag ratio beyond a value of about one, offer only a small increase in available corridor depth. If the guidance accuracy is assumed to be typically about 15 km, the roll-modulated vehicle provides a sufficient corridor depth for $L/D$ greater than 1/2 at 15.2 km/sec, typical of the entry velocities for return trajectories from Mars, but provides a maximum of only about 10 km at the extreme high energy return velocity of 21.3 km/sec. In contrast, the pitch-modulated vehicle not only provides sufficient corridor depth at $L/D = 1$ for the higher velocity, but can more profitably employ higher $L/D$ if required. The penalty one must pay for pitch modulation is in vehicle weight and complexity. Movable control surfaces will be required to provide pitch modulation, and these must project well into the high energy airstream to be effective, thus creating an aerodynamic heating problem of major proportions. In addition, undershoot entries are steeper for the pitch-modulated vehicle and higher radiative heating rates and loads are encountered compared to the roll-modulated vehicle of equal maximum $L/D$. However, for a given corridor depth, lower $L/D$ is required for the pitch-modulated vehicle and this trend is reversed (see ref. 3).

The preceding discussion has shown a requirement for $L/D$ ranging from about 1/2 to 1 for earth return from Mars, depending upon return velocity and lift modulation scheme utilized. Vehicles providing such a capability will be necessarily relatively slender compared to today's operational manned entry vehicles. Such a family of vehicles is the so-called lifting body, with a lift/drag ratio ranging from about 1/2 in the blunter vehicles to about $1\frac{1}{2}$ for the more slender vehicles (refs. 4 and 5). It will be shown later that the relatively slender vehicles are also compatible with requirements resulting from consideration of radiation heat transfer at hyperbolic velocities.

Once the requirement for hypersonic $L/D$ of the order of one is established to meet entry corridor requirements, significant longitudinal and lateral range capability is afforded for selection of the landing point, and the possibility of having conventional landing capability is established. For the latter capability, a subsonic $L/D$ of from three to five appears desirable, depending upon vehicle wing loading. Such a subsonic $L/D$ appears feasible for a vehicle with hypersonic $L/D$ of about one, and glide tests of a research entry vehicle of this type, shown in Figure 3, will soon begin at the NASA Flight Research Center.

### Mars Entry

Many of the same considerations discussed for earth entry are of interest for entry into the atmosphere of Mars. In addition, the problem of ballistic entry of unmanned probes or landers and the complication of an uncertain atmospheric composition and structure are introduced. Estimates of the surface pressure at Mars, which had ranged from about 10 to 85 mb in recent years, have been

revised downward to more nearly 10 mb, based upon the results of the recent Mariner IV flyby. Atmosphere composition is still not established with any certainty. Definition of the atmosphere structure and composition with sufficient accuracy for detailed design of optimum vehicles may not be possible until direct measurements by unmanned probes or landers are made. Until that time, design of Mars entry vehicles will, of necessity, be sufficiently conservative to permit successful entry (and soft landing, if appropriate) for the range of likely atmospheres. Levin, Evans, and Stevens (ref. 6) provide a list of references proposing models of the Martian atmosphere and, corresponding to the recent measurements of Kaplan, et al. (ref. 7) and Kuiper (ref. 8), have generated three tentative engineering models useful for deceleration and heating calculations. The effect of Martian atmospheric uncertainties upon flight mechanics parameters will be discussed in the subsequent paragraphs.

Hyperbolic entry at Mars of ballistic vehicles is of interest in terms of unmanned atmosphere probes and landers. Because deceleration tolerances of instruments tend to be significantly greater than those of man, entry corridor considerations for such systems are not usually critical. However, to ensure landing at tolerable impact velocities, such vehicles must decelerate sufficiently in the atmosphere to allow for the deployment of decelerators such as parachutes. If the atmosphere is as tenuous as suggested by Kaplan and Kuiper, as well as by the Mariner IV results, vehicles will have to be quite blunt and lightly loaded in order that deployment velocities are reached at sufficiently high altitude. The degree to which the atmosphere influences the vehicle design for this case may be seen from the following simple calculation.

The expression

$$\frac{V}{V_E} = e^{-\left(C_D A \rho H_\rho / 2m \sin \gamma_E\right)} \tag{1}$$

from reference 9, defines the velocity of a ballistic entry vehicle during its entry for conditions of an isothermal atmosphere with constant density scale height $H_\rho$ and decelerations large with respect to the local gravity. $V$ is the velocity, $V_E$ the entry velocity, $m/C_D A$ the ballistic parameter, $\rho$ the ambient density, and $\gamma_E$ the entry angle. The stratosphere of each of the three model atmospheres of reference 6 is isothermal and has an approximately constant density scale height. They have each been approximated by an idealized isothermal atmosphere, with the density relation

$$\frac{\rho}{\rho_{ref}} = e^{-\left(h/H_\rho\right)} \tag{2}$$

where $h$ is the altitude, and the constants are as given in the table.

| Model | 1 | 2 | 3 |
|---|---|---|---|
| $\rho_{ref}$ (gm/cm³) | $5.28 \times 10^{-5}$ | $5.69 \times 10^{-5}$ | $1.09 \times 10^{-4}$ |
| $H_\rho$ (km) | 20.9 | 14.0 | 6.5 |
| Model surface pressure $p_o$ (mb) | 40 | 25 | 10 |
| Idealized surface pressure $p_{ref}$ (mb) | 39.6 | 28.6 | 25.4 |
| Tropopause altitude (km) | 22 | 18 | 10 |

Thus, the idealized atmospheres are good fits to the respective models above the tropopause and equation (1) is approximately valid here.

Equations (1) and (2) may be solved for the altitude at which the velocity is reduced to a specified fraction of the entry velocity. This has been done for $V/V_E = 0.05$, corresponding to reasonable velocities for deployment of conventional parachutes and for vertical entry, and the results are plotted in Figure 4 as a function of $m/C_D A$ for each of the three idealized atmospheres. The dashed portions of the curves represent altitudes below the corresponding tropopause and the results are invalid here. If a minimum deployment altitude of about 10 km is assumed, the figure shows that values of the ballistic parameter somewhat greater than 6 gms/cm² are tolerable for Model 1, while a value of about 2.5, about as low as can be attained in practice, is required for Model 3. Entry at some angle other than vertical would alleviate these results somewhat, but would still require low values of $m/C_D A$. Without better definition of the atmosphere, Model 3 would necessarily be the design model for parachute deployment, and would require extremely blunt, lightly loaded, entry vehicles. This restriction, coupled with the associated high levels of radiative heating, results in rather small payload to gross weight ratios. Related aspects of this problem were discussed by Roberts (ref. 10) and Seiff (ref. 11).

The aforementioned atmospheric uncertainties could have major impact on hyperbolic manned entry vehicles as well. Such entries would be appropriate if atmosphere braking were to be used either for direct landing on the planet surface from a hyperbolic approach trajectory or for capture of an approaching vehicle. The latter maneuver is part of a mission mode called Mars Orbit Rendezvous in which the mission vehicle enters hyperbolically, is decelerated aerodynamically to approximately circular satellite velocity, and then, through a maneuver utilizing lift, exits the atmosphere. When an appropriate altitude is reached, a moderate propulsive maneuver is used to establish an orbit. From this orbit, an excursion module may be dispatched to the surface and, upon return, rendezvous with the parent vehicle prior to departure for Earth. In either case, direct entry or entry to orbit, atmosphere braking can be more efficient than the corresponding propulsion maneuver in terms of equivalent specific impulse, as is shown later.

For such hyperbolic entries, the concept of an entry corridor may be used to define lift requirements as a function of entry velocity and atmospheric characteristics. Consideration was given to such entry corridors by McKenzie (ref. 12) and Napolin and Mendez (ref. 13), and Figure 5, cross-plotted from McKenzie's data, illustrates the available corridor for atmospheres of two different scale heights within the range of the models of reference 6. In this figure, the lift/drag ratio is constant at ±1/2, undershoot is defined by a resultant deceleration of 10g with the lift vector directed outward, and overshoot by capture requirements with the lift vector directed towards the planet. As can be seen, if a guidance accuracy of 15 km is assumed, sufficient corridor would be provided even for the smaller value of scale height for the full range of velocities of interest. For a given scale height, surface pressure level is not a factor in determining available corridor because this pressure tends only to fix the altitude at which maneuvers take place. In the case of Figure 5, the minimum altitudes for undershoot are above surface level even for a surface pressure as low as 11 mb.

Atmospheric uncertainties introduce a more subtle effect in available corridor depth, however. Scale height, as well as surface pressure, influences the altitude at which the corridor is placed. Without precise determination of these parameters, an approaching vehicle would be limited to that corridor defined by the lowest overshoot boundary and the highest undershoot boundary appropriate for the range of postulated atmospheres. The curve labeled COMPOSITE in Figure 5 represents the result of this consideration as influenced only by scale height uncertainty in the range specified, and shows that for velocities above 9 km/sec in this case, the available corridor is decreased rapidly with increasing velocity and vanishes at about 10.5 km/sec. Consideration of a range of possible surface pressures would reduce the corridor still further. Clearly a vast improvement in our knowledge of the Martian atmosphere is important in order that the full benefits afforded by atmosphere braking can be realized. As for earth entry, increasing the lift/drag ratio and providing lift modulation capability both increase the available entry corridor and, for Mars, reduce the impact of atmospheric uncertainties.

The provision of lifting capability for hyperbolic Mars entry vehicles utilizing the Mars Orbit Rendezvous mode has an additional benefit, that of permitting plane change during entry. Such a maneuver would allow greater flexibility in incoming trajectory parameters while still permitting post-entry orbits consistent with possible landing locations and subsequent desirable Mars escape trajectories. This aspect of atmosphere braking at Mars was considered by Napolin and Mendez (ref. 13), and Figure 6 herein displays a representative result. The plane change capability for an entry velocity of 8.4 km/sec is plotted against lift-to-drag ratio with undershoot defined by 5g resultant decelerations and overshoot by maintenance of level flight with maximum negative L/D (roll modulation). For an L/D of 1/2, a modest plane change of about 10° is afforded, but for L/D of one, this capability has increased to about 25°, permitting considerable flexibility in trajectory selection.

The entry velocities for a Mars excursion module capable of entry from an orbiting parent spacecraft are considerably lower than those appropriate to hyperbolic entry. One study of such a vehicle, described by Dixon (ref. 14), has determined that a half-cone vehicle with L/D of about one is feasible from a motion and heating point of view, with the heat protection afforded through reradiation. The lift capability of such a vehicle is particularly important for lateral range capability.

Entry flight mechanics, because they are not sensitive to atmosphere composition, are expected, for Venus entry, to be very much like those at Earth. For ballistic probes, the major problems are expected to be those related to entry heating at velocities greater than 11 km/sec in a possibly dense atmosphere with appreciable concentration of $CO_2$.

## FLOW FIELDS AND HEATING

It has been established from our considerations of flight mechanics and motion that relatively slender lifting vehicles are appropriate for hyperbolic entry at Earth and Mars for manned vehicles, and that extremely blunt ballistic probes appear to be required for unmanned Mars landers. A brief summary of the problems and progress in understanding flow fields and heating of such vehicles is now given. Except where noted, the discussion is limited to a reacting gas mixture in chemical equilibrium because, in general, nonequilibrium effects on radiative and convective heating have been shown to be of less over-all importance (e.g., ref. 15).

### Inviscid, Adiabatic Shock Layer

Although for earth entry at velocities much above parabolic the effects of shock-layer radiation and conduction are important in the determination of shock-layer structure, it is instructive to consider the inviscid, adiabatic shock layer both for direct application at lower velocities and for comparison with shock layers determined including these energy transfer mechanisms at the high velocities. Seiff (ref. 16) reviewed the status of flow-field analysis in 1962. Since that time, further advances have been accomplished, including the further development of two methods which appear capable of analyzing the flow about a blunt nose at large angle of attack. The first method, a direct, essentially exact numerical method, avoids the usual complexity of attempting to integrate the elliptic equations in the subsonic portion of the flow field by treating the problem as one in unsteady aerodynamics. The unsteady equations are hyperbolic with well-defined initial conditions and can be integrated to arbitrarily large times such that the steady-state flow is approached as closely as desired. Such a method is that of Bohachevsky, Rubin, and Mates (ref. 17). Further development of this approach should make possible the treatment of the flow about arbitrary bodies with realistic high-temperature gas properties.

The second method discussed here is the approximate method of Kaattari (ref. 18) in which mass-flow continuity in the shock layer and empirical correlations were used to define the shock shape and shock-layer properties for blunt bodies at large angles of attack. The method is appropriate

for flow of an ideal gas or reacting gas mixtures at equilibrium. Some interesting results were given by Katzen and Kaattari (ref. 19) and are reproduced here as Figures 7 and 8. It was determined that stagnation point shock stand-off distance for equilibrium flow could be correlated as a function of normal shock density ratio for a fixed geometry. The curves of Figure 7 show such correlations for spherically blunted cylinders of various nose radii as derived by Katzen and Kaattari. Also shown for a hemisphere-cylinder is the stand-off distance correlation derived by Lomax and Inouye (ref. 20) by an inverse method. Agreement of the two methods is good. Except for the recent work of Bohachevsky, et al., this family of shapes (other than the hemisphere-cylinder) has not been amenable to calculation before.

Shock shapes for a flat-faced cylinder at angle of attack are shown in Figure 8(a) and compared to experimental data at 30° angle of attack for a density ratio of 0.25. Pressure distribution for the same shape is compared to experiment at 20° angle of attack in Figure 8(b). In both cases, agreement between experiment and prediction is extremely good, and this method should prove extremely versatile. It has also been extended successfully to the calculation of stand-off distance for nonequilibrium flows and for flows with gases injected into the shock layer (ref. 19).

### Convective Heat Transfer

Any discussion of the laminar heat transfer in air at hyperbolic velocities must begin with consideration of the transport properties of ionized air. Predictions of stagnation point heat transfer to date have been based on transport properties predicted by simplifications of the Chapman-Enskog formulation (see refs. 21 and 22). Typical of such calculations are those of reference 23 based upon the transport properties of Hansen (ref. 24). While agreement between heat-transfer prediction and experiment has been satisfactory up to equivalent flight velocities of about 15 km/sec, corresponding to about 50 percent ionization of air, we realize now that this is a result of the relative insensitivity of surface heat-transfer rate to thermal conductivity outside the boundary layer. Figure 9, a plot of total thermal conductivity as a function of temperature, was used by Ahtye (ref. 22) to demonstrate the inability of the simplified theory to predict the experimentally observed values of Maecker (ref. 25) for nitrogen when ionization becomes important. Ahtye has utilized the rigorous second order theory for partially ionized argon in references 21 and 22, and these results should give some indication of the importance of the previously neglected effects in more complex gases. An example of this effect is given in Figure 10, wherein the translational thermal conductivity is plotted as a function of temperature, at a pressure of $10^{-1}$ atm, for both the simplified and more rigorous second order theories. The latter values are greater by some 30 to 50 percent when ionization is appreciable.

Heat transfer for equilibrium mixtures depends upon reactive and thermal diffusive components of conductivity, as well as on the translational component. The first two components are dependent upon multicomponent and thermal diffusion coefficients. These coefficients have been calculated for partially ionized argon by Ahtye (ref. 22).

However, the reactive and thermal diffusive components depend also upon macroscopic concentration gradients for ions and electrons and the charge-separation field which may affect these gradients. These effects have not yet been determined, and thus the accurate prediction of convective heat transfer in highly ionized gases is not yet possible.

Some indication of how important an order of magnitude change in total thermal conductivity might be to convective heat transfer in air is given by Figures 11 and 12, from Howe and Sheaffer (ref. 26). Figure 11 shows assumed thermal conductivity curves (and Maecker's data) as a function of temperature. Curve I is the prediction of Yos (ref. 27) which fits the data quite well until ionization becomes important; curve II corresponds to an arbitrary increase of roughly an order of magnitude over Yos' curve in the region of important ionization; and curve III approximates the prediction of Hansen up to 15,000° K and then is faired into the Yos curve. Stagnation point heating rates were calculated by Howe and Sheaffer for each of these assumed conductivity functions and the results are shown in Figure 12. Although these values were calculated for a viscous, conducting shock layer with radiation transfer, the Reynolds numbers are sufficiently high and the radiant transfer sufficiently low that the results correspond closely to a more classical boundary-layer calculation. It is evident that the order of magnitude difference in conductivity appears as only a factor of two in heat-transfer rate at the highest enthalpy level shown, and then only for equivalent velocities greater than about 20 km/sec. Shown also is the prediction of Howe and Viegas (ref. 28) wherein Hansen's properties (to 15,000° K) were used. If this is extrapolated linearly to higher velocity, it lies roughly halfway between the two extremes shown. Because experiments have been limited to conditions corresponding to a maximum of about 15 km/sec, the reason that no discrepancies between experiment and theory have been noted, even with 50 percent ionization, is the relative insensitivity of heat transfer to thermal conductivity external to the boundary layer for these velocities. It is evident that, should the second order total conductivity predictions, when established, show even an order of magnitude increase over the current approximations above 10,000° K, experiments at equivalent velocities greater than 20 km/sec will be required to confirm the effect upon heat-transfer rate. Nevertheless, such velocities are at the upper end of those appropriate for direct return from Mars, and these effects may well have an important influence on vehicle selection and design.

The relative insensitivity of heat transfer to high-temperature gas properties for relatively cold walls was shown by Marvin (ref. 29) for various other pure gases at velocities up to about 10 km/sec. It was found that a single correlation could be established for all the gases considered ($CO_2$, Air, $N_2$, $H_2$, A) in terms of low-temperature transport properties. These results are shown in Figure 13, wherein all the numerical results are within ±16 percent of the correlation function. Plotted is a convective heat-transfer parameter against enthalpy ratio. $\varphi_D$ is the ratio of density-viscosity product at the onset of dissociation (or ionization in the case of argon) to that at the wall, $h_D$ is the corresponding static enthalpy, and $g$ is the ratio of total enthalpy to

that outside the boundary layer. Marvin also found that the laminar heating rate distribution to blunt bodies, as calculated from local similarity principles, was little affected by composition, and, as for air, can be obtained with reasonable accuracy from the inviscid flow alone so long as the pressure gradients are not too large (ref. 30) and from ideal gas boundary-layer solutions when pressure gradients are high (ref. 31).

Unfortunately, our understanding of transition and turbulent heat transfer at reentry velocities has not advanced to the same degree as has that for laminar flow in the past few years. The mechanisms leading to transition are not well defined and hence theoretical predictions can not be derived. Empirical transition criteria have been derived from low velocity ground facility and small scale flight experiments, but how they can be extrapolated to flight conditions at moderate to high local Mach numbers, small ratios of wall to total enthalpy, and in the presence of ablation, has not yet been well established. Much the same situation holds for turbulent flow at reentry flight conditions. Turbulent skin friction and heating predictions are also based upon relatively low velocity data with corrections for high temperatures, enthalpy ratios, and Mach number through a variety of estimation techniques (see refs. 32 and 33). One can show that a requirement for a significant increase in our ability to predict transition and turbulent flow phenomena exists for the hyperbolic lifting entry vehicles appropriate for future missions. For example, typical boundary trajectories for earth entry at velocities appropriate to return from Mars are shown on an altitude-velocity plot on Figure 14. The vehicle is assumed to have a maximum $L/D$ of one with modulation by roll control, a ballistic parameter $(m/C_D A)$ of 49 $gm/cm^2$, and enters at a velocity of 15.2 km/sec. Plotted also are lines of constant free-stream Reynolds number based on a length of 10 meters, typical of the over-all length of contemplated vehicles. The vehicle would experience maximum free-stream Reynolds numbers of about $3 \times 10^6$ based upon vehicle length during the undershoot trajectory; local Reynolds numbers based upon conditions outside the boundary layer and the length of the vehicle would be roughly an order of magnitude lower, or of the order of $10^5$. Reynolds numbers based upon local conditions and laminar momentum thickness would be roughly 500. Each of these values is sufficiently large that transition must be considered a distinct possibility, particularly in the presence of the mass transfer and surface roughness associated with ablation.

### Radiative Heating

It has become apparent in the past few years that as contemplated entry velocities were increased above parabolic escape speed at Earth, the contribution of radiative energy transfer from the hot shock layer would have to be considered in vehicle design along with that from conduction in the boundary layer. In fact, for very blunt vehicles (as appropriate to satellite reentry and lunar return) the radiative input would dominate even for velocities at the lower end of the Mars return velocity spectrum. Detailed consideration of both mechanisms of energy transport has led to the concept of more slender vehicles to compensate for the potentially dominant radiative transfer; these will be described in a subsequent section. In

this section, some recent radiative research results will be briefly discussed.

The principal radiators and the corresponding radiative intensities for high-temperature air and gases thought to be representative of the atmospheres of Mars and Venus are reasonably well established for conditions corresponding to velocities up to approximately 8 km/sec. In this flight regime, the dominant radiation sources are molecules undergoing radiative transitions from excited states to states of lower energy. Some recent data obtained in a free-flight facility by Arnold, Reis, and Woodward (ref. 34) for mixtures of $CO_2$ and $N_2$ are shown in Figure 15. These data are appropriate for flow fields in chemical equilibrium and the emission is seen to correlate with a function of density and velocity in much the same manner as does that for dissociated air. Shown also is the prediction for air of Kivel and Bailey (ref. 35) and it is apparent that at the lower velocities radiation from the $CO_2$-$N_2$ mixture exceeds that for air by as much as an order of magnitude. This effect is attributed to the radiation from the CN-violet band system which dominates the emission for the former case. Other shock tube and free-flight data and predictions (refs. 36, 37, and 38) are shown in the figure as indicated. At velocities above about 10 km/sec, radiation resulting from recombination of ions and electrons, bremsstrahlung, and atomic line radiation become the dominant factors, and in this region the $CO_2$-$N_2$ mixtures and air behave in a similar manner. This is expected since few molecules exist at the correspondingly high temperatures (about 10,000° K and above).

Not properly accounted for in this work is the increasingly important contribution to the continuum radiation of sources at wavelengths shorter than 2,000 $\overset{o}{A}$ for air and $CO_2$-$N_2$ mixtures. Recent work by Biberman, et al. (ref. 39), Nardone, et al. (ref. 40) and Hahne (ref. 41) has demonstrated the importance of this region of the spectrum for velocities much above 10 km/sec. The intensity of this radiation is such that the radiating gas layer must be treated as self-absorbing for these wavelengths, complicating the heretofore conceptually simple scaling relations. The impact of this recent work is yet to be fully determined.

Although the simple model of an adiabatic, optically-thin shock layer has been generally appropriate for the calculation of radiation heat transfer to vehicles of moderate size entering planetary atmospheres at velocities up to about 15 km/sec (provided the vacuum ultraviolet contribution is not considered), higher velocity applications require that the effects of energy transfer, both by radiation and conduction, be considered in determining the shock layer. Wilson and Hoshizaki considered the effect of large radiation transfer upon the inviscid flow field of hemisphere-shaped bodies by an integral method (ref. 42), and determined the resulting radiation relative to that for an assumed adiabatic shock layer. The gas was considered optically thin. For the stagnation point flow, the radiation was found to decrease significantly when the energy radiated from a mass of gas traversing the stagnation region (as calculated for adiabatic flow) became as large as the order of 1/10 of its initial total energy. This is shown in

Both Howe and Viegas (ref. 28) and Hoshizaki and
Wilson (ref. 43) analyzed the radiating viscous
shock layer. In the former, only the stagnation
region was considered for a grey gas. It was found
that the convective heat transfer was significantly
reduced for cases where radiant heat transfer
caused the enthalpy outside the edge of the viscous
layer to be reduced, although a simple correlation
in these terms was not possible. These results are
plotted in Figure 17 at 1 atmosphere pressure and
for various nose radii. Because of the relatively
strong dependence of radiation upon gas density,
the decrease in the convective heating parameter
would be greater for higher pressures. The effect
of radiation cooling on the radiant heat transfer
itself was found to be essentially independent of
the inclusion of heat conduction (for the Reynolds
numbers considered), and the results are in agree-
ment with those of Wilson and Hoshizaki, as shown
in Figure 16.

Hoshizaki and Wilson (ref. 43) retained the
optically thin assumption in extending the inte-
gral method to the viscous shock layer. Two dif-
ferent estimates of the emissivity of air were
used, one corresponding to the estimates of
Meyerott, et al. (ref. 44), and the other to the
somewhat higher estimates of Kivel and Bailey
(ref. 35). For the stagnation point, the results
were found to be in general agreement with those
of Howe and Viegas. Distribution of both convec-
tive and radiative heat-transfer rates about a
hemisphere were again found to be roughly inde-
pendent of the level of radiation, provided they
were plotted in terms of the ratio of local to
corresponding stagnation point values. These
results are shown in Figures 18(a) and 18(b).
Note, however, that the level of heating, both
convective and radiative, depended upon the magni-
tude of the radiation transfer.

The influence of the intense radiation in the
vacuum ultraviolet upon these results must now be
determined. One cannot say a priori that the
stagnation point correlation of Figure 16 and the
invariance of distribution with radiation cooling
level, as shown in Figures 18(a) and 18(b), will
remain unchanged because self-absorption of the
UV radiation will tend to influence the convec-
tive heat transfer through heating of the gas
adjacent to the surface, and the influence may be
a function of local conditions on the body. This
should be a fruitful area of investigation.

## VEHICLE CONFIGURATION ASPECTS

The performance of heat protection systems,
whether operating by ablation, reradiation, tran-
spiration, film cooling, or simply by energy stor-
age, must be determined along with the flow-field
and energy-transfer characteristics external to
the vehicle in order that efficient vehicle con-
cepts be derived. Reradiative systems are appro-
priate, with the present high-temperature materials

technology, to the low levels of heating sustained
over long durations, such as for lifting vehicles
(L/D $\approx$ 2 or more) entering the Earth's atmosphere
at satellite velocity. For higher velocities, or
when heating pulses are of large magnitude and
short duration, ablation, transpiration, or film
cooling systems are more appropriate, with ablation
having been used almost exclusively in recent years.
The inefficient heat-sink type of system is gen-
erally not competitive except perhaps for special
applications.

Heat-protection-system performance per se will
not be discussed here in any detail; rather, some
simple models of ablation will be used to demon-
strate the importance of the convective and radia-
tive heating inputs upon vehicle configuration for
super-satellite entry velocities at Earth.

The apparent dominance of radiative heating over
convective heating for blunt bodies at velocities
greater than parabolic escape speed at Earth (for
example, refs. 45 and 46), has led to the study of
moderately slender cones with a pointed rather than
a blunt nose for such reentry conditions. Allen,
Seiff, and Winovich (ref. 15) analyzed a family of
such cones for hypervelocity ballistic earth entry
and some pertinent results are shown here. Two
ablators were considered, one a low-temperature
ablator having the assumed characteristics of sub-
liming teflon, and the other a high-temperature
ablator having the assumed characteristics of vapor-
izing quartz. The cone was assumed to remain sharp;
the details of the analysis are given in the refer-
ence. In the analysis, optimum cone angles were
computed for minimum absorbed energy fraction as a
function of entry velocity for both all-laminar and
all-turbulent flow. The results for laminar flow,
both with the teflon and quartz ablators, are shown
in Figure 19. Corresponding results for turbulent
flow are shown in Figure 20. In these figures, $\eta$
is the absorbed energy fraction (ratio of absorbed
energy to initial kinetic energy) and $\theta_c$ is the
semivertex angle of the cone. The parameter B is
a ballistic parameter defined by

$$B = \frac{C_D A}{m} \frac{\rho_o H_\rho}{\sin \gamma_E}$$

where $\rho_o$ is the atmospheric density at the sur-
face and the other parameters are as defined
previously.

One important point to note from these results is
that for each optimum condition, convection con-
tributes approximately 85 to 90 percent of the
total energy absorbed, and for the radiative models
used, equilibrium radiation accounts for most of
the balance (nonequilibrium radiation input is gen-
erally negligible). At first glance, this behavior
appears somewhat anomalous when the tendency
towards dominance of radiative transfer over con-
vective transfer at such velocities is considered.
For stagnation flows, for example, optimum nose
radii were calculated for minimum energy transfer
by Howe and Sheaffer (ref. 47) and for these cases,
radiation transfer exceeded net convective transfer
by factors of from two to nine. No real anomaly
exists, however; for given flows over sharp cones,
convection decreases slowly and radiation increases
rapidly with increasing cone angle, while for
increasing nose radius in stagnation flow, convec-
tion decreases almost as rapidly as radiation

116

...... .... As a result, the optima are shifted with respect to one another. In either case, for a given configuration (cone angle or nose radius) radiation would tend towards dominance for velocities greater than that corresponding to the optimum. Note also that reference 15 considered total energy transfer while reference 47 calculated minimum heating rate.

Optimum cone semivertex angles tend to be rather large, from 25° to 50°, for the range of parameters shown, both for laminar and turbulent flow. For turbulent flow, the absorbed energy fractions are nearly an order of magnitude greater than for laminar flow, a result of the aforementioned dominance of the convective energy absorbed. This result is graphically illustrated in Figure 21, a plot of laminar and turbulent optimum energy fractions as a function of ballistic parameter for various entry velocities. The laminar curves are assumed valid for local Reynolds numbers less than $10^7$, and the dashed portions of the curves represent arbitrary fairings to join with the turbulent curves. One can conclude that important areas for future research should be those associated with determination of transition criteria, maintenance of laminar flow, and determination with greater confidence of the turbulent heating levels for reentry conditions.

The analysis described above neglected the effect of shape change. If shape change were permitted, the sharp cones would rapidly blunt, radiative transfer would be much enhanced in the nose region, and the resulting surface recession in the nose regions would tend to continually accelerate the blunting effect during an entry. This suggests that some means of providing nonablative tips should be sought. Transpiration or film cooling may be appropriate means of providing such protection. Such nonablative heat-protection techniques may also be desirable for entry vehicles which are designed for reuse.

The results just described were derived specifically for ballistic entry. No equivalent parametric analysis has been performed for lifting entry; such an analysis would be much more complex. However, a conceptual lifting entry vehicle design study for one set of entry conditions was carried out and is reported by Hearne, Chin, and Lefferdo (ref. 48). The vehicle configuration consisted of a spherically-blunted circular cone aligned with its axis parallel to the direction of flight, and with its base raked off at an angle to provide the desired lift. An elliptic cone afterbody was fitted to the raked-off base to provide useful volume. The vehicle studied had a lift/drag ratio of 0.6, and a ballistic parameter ($m/C_DA$) of about 100 gm/cm². For given gross weight and volume (including afterbody), a cone semivertex angle of about 40° was found to yield minimum heat-shield weight for entry into the Earth's atmosphere at 19.8 km/sec with a phenolic-nylon ablative heat shield assumed.

Two levels of radiative heating were assumed; the large (nominal) corresponding roughly to the estimates of Nardone, et al. (ref. 40), and the smaller equal to 1/10 that amount. Heat-shield mass is plotted for each case as a function of cone angle for these two estimates in Figure 22. For the larger emission, the optimum angle is about 43°, and when the radiative input is reduced an order of magnitude, the optimum shifts to an angle above 45° while the heat-shield mass is reduced to a value estimated to be about one-half that for nominal emission. The fact that the heat-shield masses are not in proportion to the emission levels is attributed to the influence of convective heating, radiative cooling of the shock layer, reradiation from the heat-shield surface, and the presence of unaffected heat-shield insulation.

The effect of transition Reynolds number is shown in Figure 23, a plot of heat-shield mass against cone angle for three values of transition Reynolds number based upon momentum thickness. As expected, an increase in transition Reynolds number results in a decreased optimum cone angle and a total heat-shield mass reduction of a factor of about two for the values shown. This again demonstrates the importance of the determination of transition criteria and turbulent heat transfer.

## RELATIVE MERITS OF AERODYNAMIC AND PROPULSIVE BRAKING

Allen (ref. 49) considered the relative merits of propulsive and aerodynamic braking for deceleration at earth return. This comparison was based upon the results for ballistic entry of sharp, ablating cones described previously (ref. 15). Plotted in Figure 24 is the equivalent specific impulse for the teflon and quartz ablators as a function of entry velocity, for laminar flow. Shown also are typical specific impulse values appropriate to chemical and nuclear rockets. Equivalent specific impulse values for the aerodynamic braking case with turbulent flow would be about one order of magnitude lower than for laminar flow, and for teflon would be of the same order as the propulsion systems, while quartz would still be more effective. More complete comparisons making use of estimated engine, propellant tank, and structure weights for propulsive systems, and insulation and structure weights for atmosphere braking systems, should be investigated. So long as laminar flow can be maintained, however, it is expected that the advantage would remain with atmosphere braking.

Much the same advantage was shown by Tauber and Seiff (ref. 50) for atmosphere braking from hyperbolic approach velocities to orbital velocity at Mars, compared to the equivalent propulsive maneuver. In the reference, initial mass required in earth orbit to launch the missions was considered the measure by which relative advantage was determined, and systems utilizing rocket propulsion at Mars to perform the capture maneuver were approximately twice as massive as those utilizing atmosphere braking. Thus atmosphere braking to orbit at Mars for manned missions appears to offer a significant advantage over propulsive braking from a vehicle weight standpoint. Its ultimate selection, however, will depend upon many factors, such as the level of heat shielding technology, ability to store and insulate cryogenic fluids from the entry heating loads, and residual uncertainties in the Martian atmosphere.

## GROUND SIMULATION AND FACILITIES

Ground facilities capable of simulation of one or more of the parameters characteristic of reentry flight have advanced considerably in the past few years. Although the shock tube will continue as

the primary tool for the determination of high-temperature properties of gases and for measurements of phenomena which are essentially independent of free-stream simulation, such as convective heat transfer to the forebody of blunt configurations, new facility concepts which hold much promise have been or are being developed.

For the simulation of free-stream velocity, Mach number, and Reynolds number, extensive development of ballistic shock tunnels has been pursued. In this type of facility, a small model is fired from a light gas gun into a countercurrent gas stream generated by a shock tunnel. Relative velocities of about 13 km/sec have been attained with models of about 1/2 cm diameter (ref. 51).

Roughly similar capabilities with a model fixed relative to the laboratory should be possible with a new concept, the expansion tunnel (ref. 52). The tunnel is essentially a double diaphragm shock tube with the cross-sectional area increased downstream of the second diaphragm. The test gas is placed between the two diaphragms and is first compressed and accelerated by the shock wave generated through rupture of the first diaphragm. This gas subsequently undergoes expansion and further acceleration by both the unsteady expansion wave generated by rupture of the second diaphragm and the steady expansion as it passes through the region of increasing area. The gas, by this time at low temperature and high velocity, then passes over the fixed, instrumented model. The expansion tunnel is a modification of an earlier concept, the expansion tube (ref. 53), with potentially greater utility.

Neither of the aforementioned types of facilities is capable of providing sufficiently long test times for research with high-temperature charring ablators, and most work of this type has been carried out in various arc-heated wind tunnels. The recently developed constricted arc tunnel (ref. 54) has been operated at enthalpies up to about $24 \times 10^3$ cal/gm, corresponding to a velocity of 14 km/sec, and may be appropriate for development of such ablation materials suitable for the next generation of entry vehicles.

The simultaneous attainment of reentry flight velocity, Mach number, Reynolds number, and heating history in ground facilities does not appear possible at this time. Investigation of these phenomena, shown to be important in the previous discussion, will have to be carried on with partial simulation, as in the past, and supplemented with well chosen reentry flight tests.

## CONCLUDING REMARKS

Some recent advances in atmosphere entry have been reviewed against a background of the requirements of missions of the future. The requirements of unmanned and manned Mars missions have been emphasized, but some brief consideration was given to unmanned Venus and Jupiter missions and to manned near-earth missions.

Although the entry velocities characteristic of Mars entries are low by earth entry standards, problems somewhat different will be experienced. Unmanned ballistic probes must be of extremely high drag in order that they can decelerate to sufficiently low velocities for parachute deployment. Thus, the blunt entry configuration is still of pertinence. Manned entry vehicles for both Mars and earth entry, on the other hand, may well tend to the less blunt configurations compatible with lift/drag ratios of the order of one and reduced radiative heating. The current uncertainty in the definition of the Martian atmosphere has serious implications for both unmanned and manned entry at Mars.

The prediction of laminar convective heat transfer and radiative heat transfer for velocities up to those corresponding to dissociation of molecules appears to be well in hand. The prediction of transition and turbulent heat transfer for high reentry velocities and the prediction of laminar convective and radiative heating at velocities inducing significant ionization is, at present, unsatisfactory. Critical to the improved prediction of laminar convective and radiative heating are the determination of second and higher order effects in thermal conductivity and the effects of radiation in the vacuum ultraviolet portion of the spectrum, respectively.

Finally, it is instructive to compare some of the conclusions reached in a review of atmosphere entry technology presented in 1961 (ref. 5) with those of the present paper. In the previous review, the tendency of radiation heating to dominate the heating problem during hyperbolic entry was cited as a potential major problem, and this tendency still exists today. However, it has been determined during the intervening period that nonequilibrium radiation is not a major factor at high super-satellite velocities, and that radiative cooling alleviates, to a degree, the tendency of equilibrium radiation to dominate the convective heat transfer. Radiation in the extreme ultraviolet portion of the spectrum, not previously considered, has now been determined to be of major importance. However, self-absorption of this emission may tend to reduce the impact of this component of the radiation.

The situation with regard to transition and turbulent heating remains little changed from 1961. Of particular importance is the consideration of transition, because large lifting and nonlifting vehicles experience rather large Reynolds numbers during atmosphere entry. The existence of extensive regions of turbulent flow has been shown to result in an increase of an order of magnitude in heat-protection requirements for a class of conical, ballistic, ablating configurations.

## REFERENCES

1. Love, Eugene S.: Factors Influencing Configuration and Performance of Multipurpose Manned Entry Vehicles. J. Spacecraft Rockets, vol. 1, no. 1, Jan.-Feb. 1964, pp. 3-12.

2. Chapman, Dean R.: An Analysis of the Corridor and Guidance Requirements for Supercircular Entry Into Planetary Atmospheres. NASA TR R-55, 1960.

3. Pritchard, E. Brian: Velocity Requirements and Re-Entry Flight Mechanics for Manned Mars Missions. J. Spacecraft Rockets, vol. 1, no. 6, Nov.-Dec. 1964, pp. 605-610.

4. Eggers, A. J., Jr.: The Possibility of a Safe Landing. Space Technology, Edited by Howard Seifert, John Wiley and Sons, Inc., 1959.

5. Eggers, A. J., Jr., and Wong, T. J.: Motion and Heating of Lifting Vehicles During Atmosphere Entry. ARS Journal, vol. 31, no. 10, October 1961, pp. 1364-1375.

6. Levin, George M., Evans, Dallas E., and Stevens, Victor, ed.: NASA Engineering Models of the Mars Atmosphere for Entry Vehicle Design. NASA TN D-2525, 1964.

7. Kaplan, Lewis D., Munch, Guido, and Spinrad, Hyron: An Analysis of the Spectrum of Mars. Astrophys. J., vol. 139, no. 1, Jan. 1964.

8. Kuiper, Gerard P.: Fifth Semiannual Status Report to National Aeronautics and Space Administration Lunar and Planetary Laboratory, University of Arizona Research Grant No. NsG 161-61, Dec. 1963.

9. Allen, H. Julian, and Eggers, A. J., Jr.: A Study of the Motion and Aerodynamic Heating of Ballistic Missiles Entering the Earth's Atmosphere at High Supersonic Speeds. NACA Rept. 1381, 1958. (Supersedes NACA TN 4047.)

10. Roberts, Leonard: Entry Into Planetary Atmospheres. Aeronautics and Astronautics, Oct. 1964, pp. 22-29.

11. Seiff, Alvin: Developments in Entry Vehicle Technology. Presented at the AIAA First Annual Meeting and Technical Display, June 29-July 2, 1964, Washington, D.C.

12. McKenzie, Robert L.: Some Effects of Uncertainties in Atmosphere Structure and Chemical Composition on Entry Into Mars. NASA TN D-2584, 1965.

13. Napolin, A. L., and Mendez, J. C.: Target Orbit Selection for Mars Missions Using Aerodynamic Maneuvering. Presented at the AIAA Aerospace Sciences Meeting, Jan. 20-22, 1964, New York, N.Y. (AIAA Preprint No. 64-14).

14. Dixon, Franklin P.: An Early Manned Mars Landing Mission Using the Mars Excursion Module. Presented at the NASA/AIAA Third Manned Space Flight Conference, Nov. 4-6, 1964, Houston, Texas.

15. Allen, H. Julian, Seiff, Alvin, and Winovich, Warren: Aerodynamic Heating of Conical Entry Vehicles at Speeds in Excess of Earth Parabolic Speed. NASA TR R-185, 1963.

16. Seiff, Alvin: Recent Information on Hypersonic Flow Fields. Proc. NASA-University Conference on the Science and Technology of Space Exploration, vol. 2, no. 55, NASA SP-11, 1962, pp. 269-282.

17. Bohachevsky, Ihor O., Rubin, Ephraim L., and Mates, Robert E.: A Direct Method for Computation of Nonequilibrium Flows With Detached Shock Waves. Presented at the AIAA Second Aerospace Sciences Meeting, Jan. 25-27, 1965, New York, N.Y. (AIAA Paper No. 65-24).

18. Kaattari, George E.: Shock Envelopes of Blunt Bodies at Large Angles of Attack. NASA TN D-1980, 1963.

19. Katzen, Elliott D., and Kaattari, George E.: Flow Around Blunt Bodies Including Effects of High Angles of Attack, Nonequilibrium Flow, and Vapor Injection. Presented at the AIAA Entry Technology Conference, Oct. 12-14, 1964, Williamsburg, Va. (AIAA Publication CP-9, pp. 106-117).

20. Lomax, Harvard, and Inouye, Mamoru: Numerical Analysis of Flow Properties About Blunt Bodies Moving at Supersonic Speeds in an Equilibrium Gas. NASA TR R-204, 1964.

21. Ahtye, Warren F.: A Critical Evaluation of Methods for Calculating Transport Coefficients of a Partially Ionized Gas. Proc. 1964 Heat Transfer and Fluid Mechanics Institute, Stanford Univ. Press, 1964, pp. 211-225.

22. Ahtye, Warren F.: A Critical Evaluation of Methods for Calculating Transport Coefficients of Partially and Fully Ionized Gases. NASA TN D-2611, 1965.

23. Cohen, Nathaniel B.: Boundary-Layer Similar Solutions and Correlation Equations for Laminar Heat-Transfer Distribution in Equilibrium Air at Velocities up to 41,000 Feet/Second. NASA TR R-118, 1961.

24. Hansen, C. Frederick: Approximations for the Thermodynamic and Transport Properties of High-Temperature Air. NASA TR R-50, 1959.

25. Maecker, H.: The Properties of Nitrogen to 15,000° K. Presented at Meeting on Properties of Gases at High Temperature, AGARD, Aachen, Sept. 21-23, 1959. AGARD Rept. 324.

26. Howe, John T., and Sheaffer, Yvonne S.: Effects of Uncertainties in the Thermal Conductivity of Air on Convective Heat Transfer for Stagnation Temperature up to 30,000° K. NASA TN D-2678, 1965.

27. Yos, Jerrold M.: Transport Properties of Nitrogen, Hydrogen, Oxygen, and Air to 30,000° K. Avco Rept. RAD TM-63-7, 1963.

28. Howe, John T., and Viegas, John R.: Solutions of the Ionized Radiating Shock Layer, Including Reabsorption and Foreign Species Effects, and Stagnation Region Heat Transfer. NASA TR R-159, 1963.

29. Marvin, Joseph G., and Deiwert, George S.: Convective Heat Transfer in Planetary Gases. Prospective NASA TR R-224, 1965.

30. Lees, Lester: Laminar Heat Transfer Over Blunt-Nose Bodies at Hypersonic Flight Speeds. Jet Propulsion, vol. 26, no. 4, April 1956, pp. 259-269, 274.

31. Beckwith, Ivan E., and Cohen, Nathaniel B.: Application of Similar Solutions to Calculation of Laminar Heat Transfer on Bodies With Yaw and Large Pressure Gradient in High-Speed Flow. NASA TN D-625, 1961.

...........g, D. B., and Chi, S. W.: The Drag of a Compressible Turbulent Boundary Layer on a Smooth Flat Plate With and Without Heat Transfer. J. Fluid Mech., vol. 18, Part I, Jan. 1964, pp. 117-143.

... Bertram, Mitchel H., and Neal, Luther, Jr.: Recent Experiments in Hypersonic Turbulent Boundary Layers. Presented at the AGARD Specialists Meeting on Recent Developments in Boundary-Layer Research, May 10-14, 1965, Naples, Italy.

34. Arnold, James O., Reis, Victor H., and Woodward, Henry T.: Theoretical and Experimental Studies of Equilibrium and Nonequilibrium Radiation to Bodies Entering Postulated Martian and Venusian Atmospheres at High Speeds. Presented at the AIAA Second Aerospace Sciences Meeting, Jan. 25-27, 1965, New York, N.Y. (AIAA Paper No. 65-116).

35. Kivel, B., and Bailey, K.: Tables of Radiation From High Temperature Air. AVCO-Everett Res. Lab., Res. Rept. 21, Dec. 1957.

36. James, Carlton S.: Experimental Study of Radiative Transport From Hot Gases Simulating in Composition the Atmospheres of Mars and Venus. AIAA Journal, vol. 2, no. 3, March 1964, pp. 470-475.

37. Gruszczynski, J. S., and Warren, W. R., Jr.: Experimental Heat-Transfer Studies of Hypervelocity Flight in Planetary Atmospheres. AIAA Journal, vol. 2, no. 9, Sept. 1964, pp. 1542-50.

38. Thomas, G. M., and Menard, W. A.: Experimental Measurements of Nonequilibrium and Equilibrium Radiation From Planetary Atmospheres. Presented at the AIAA Entry Technology Conference, Oct. 12-14, 1964, Williamsburg, Virginia (AIAA Publication CP-9, pp. 170-185).

39. Biberman, L. M., Iakubov, I. T., Norman, G. E., and Vorobyov, V. S.: Radiation Heating Under Hypersonic Flow. Astronautica Acta, vol. X/fasc. 3-4, 1964, pp. 238-252.

40. Nardone, M. C., Breene, R. G., Zeldin, S. S., and Riethof, T. R.: Radiance of Species in High Temperature Air. General Electric Co., Space Sciences Lab. Rept. R 63 SD3, June 1963.

41. Hahne, Gerhard E.: The Vacuum Ultraviolet Radiation from $N^+$- and $O^+$-Electron Recombination in High-Temperature Air. Prospective NASA TN D-2794, 1965.

42. Wilson, K. H., and Hoshizaki, H.: Inviscid, Nonadiabatic Flow About Blunt Bodies. Presented at the AIAA Aerospace Sciences Meeting, Jan. 20-22, 1964 (AIAA Preprint No. 64-70).

43. Hoshizaki, H., and Wilson, K. H.: The Viscous, Radiating Shock Layer About a Blunt Body. Presented at the AIAA Entry Technology Conference, Oct. 12-14, 1964, Williamsburg, Va. (AIAA Publication CP-9, pp. 65-76).

44. Meyerott, R. E., et al.: Absorption Coefficients of Air. AFCRL, Geophysics Research Paper, No. 68, 1960.

45. Trimpi, Robert L., Grant, Frederick C., and Cohen, Nathaniel B.: Aerodynamics and Heating Problems of Advanced Reentry Vehicles. Vol. 2, Proc. NASA-University Conference on Science and Technology of Space Exploration. NASA SP-11, no. 53, 1962, pp. 235-248.

46. Allen, H. Julian: Gas Dynamics Problems of Space Vehicles. Vol. 2, Proc. NASA-University Conference on the Science and Technology of Space Exploration. NASA SP-11, no. 54, 1962, pp. 251-267.

47. Howe, John T., and Shaeffer, Yvonne S.: Mass Addition in the Stagnation Region for Velocity up to 50,000 Feet/Second. NASA TR R-207, 1964.

48. Hearne, L. F., Chin, Jin H., and Lefferdo, J. M.: Reentry Heating and Thermal Protection of a Mars-Mission Earth-Reentry Module. Presented at the AIAA Entry Technology Conference, Oct. 12-14, 1964, Williamsburg, Va. (AIAA Publication CP-9), pp. 118-135.

49. Allen, H. Julian: The Aerodynamic Heating of Atmosphere Entry Vehicles - A Review. Presented at the Symposium on Fundamental Phenomena in Hypersonic Flow, June 25-26, 1964, Buffalo, N.Y.

50. Tauber, Michael E., and Seiff, Alvin: Optimization Analysis of Conical Bodies Making Lifting Hyperbolic Entries Into the Atmospheres of Earth and Mars. Presented at the AIAA Entry Technology Conference, Oct. 12-14, 1964, Williamsburg, Va. (AIAA Publication CP-9, pp. 13-21).

51. Canning, Thomas N., and Page, William A.: Measurements of Radiation From the Flow Fields of Bodies Flying at Speeds up to 13.4 Kilometers per Second. Presented to the Fluid Mechanics Panel of AGARD, April 3-6, 1962, Brussels, Belgium.

52. Trimpi, Robert L., and Callis, Linwood B.: A Perfect-Gas Analysis of the Expansion Tunnel, a Modification to the Expansion Tube. NASA TR R-223, 1965.

53. Trimpi, Robert L.: A Preliminary Theoretical Study of the Expansion Tube, A New Device for Producing High-Enthalpy Short-Duration Hypersonic Gas Flows. NASA TR R-133, 1962.

54. Vorreiter, John W., and Shepard, Charles E.: Performance Characteristics of the Constricted-Arc Supersonic Jet. Proceedings of the 1965 Heat Transfer and Fluid Mechanics Institute, Stanford University Press, 1965, pp. 42-49.

| PLANET | VELOCITY, km/sec | ENTRY MODE | VELOCITY, km/sec |
|--------|------------------|------------|------------------|
| VENUS | 11 OR GREATER | DIRECT MARS ENTRY | 6 TO 11 |
| MARS | 6 OR GREATER | MARS ENTRY FROM ORBIT | 3.6 TO 5.2 |
| JUPITER | APPROX 60 | EARTH ENTRY | 12 TO 16 |

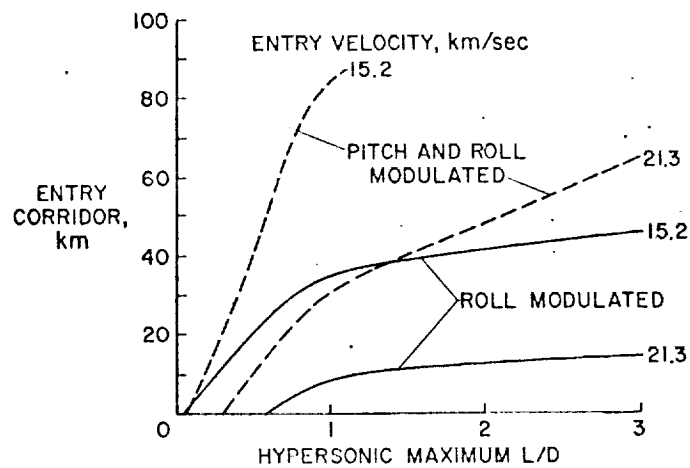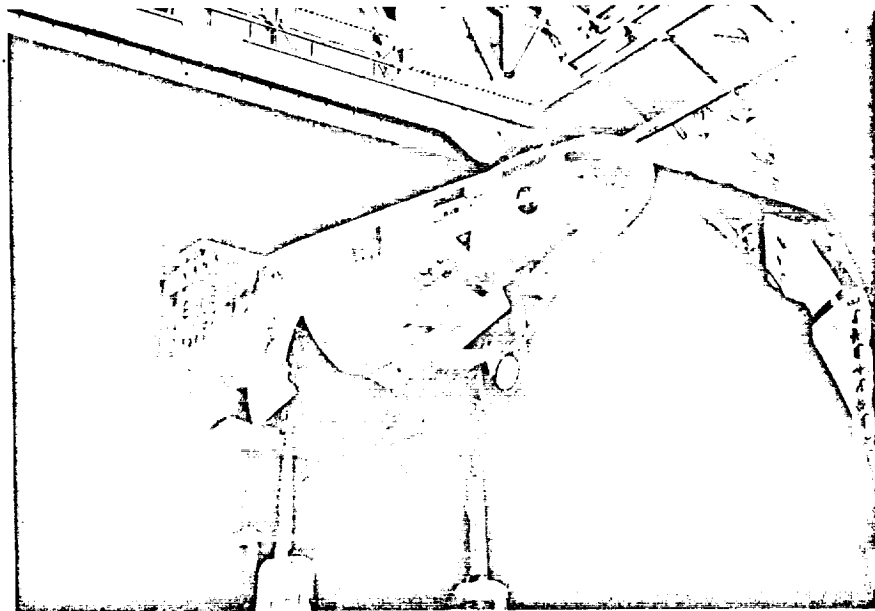Figure 1.- Characteristic entry velocities for future missions.



Figure 2.- Earth entry corridor as a function of hypersonic maximum lift-drag ratio.



A-35069

Figure 3.- Low-speed lifting reentry research vehicle.
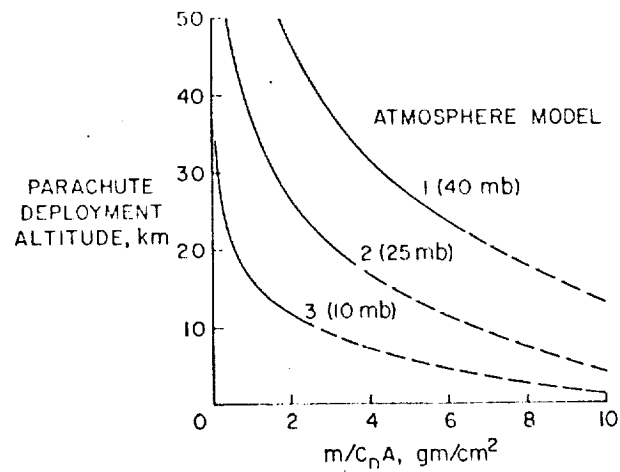
Figure 4.- Parachute deployment altitude as a function of ballistic parameter for three model atmospheres of Mars, $V/V_E$ = 0.05.
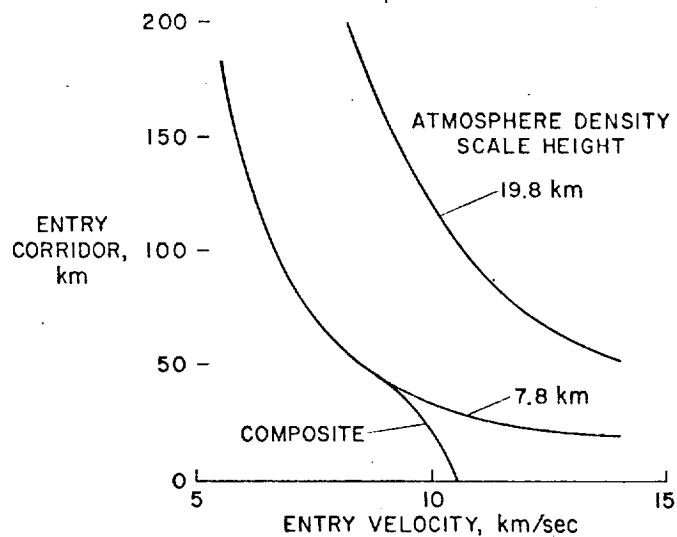


Figure 5.- Mars entry corridor as a function of entry velocity for various scale heights, L/D = 1/2.
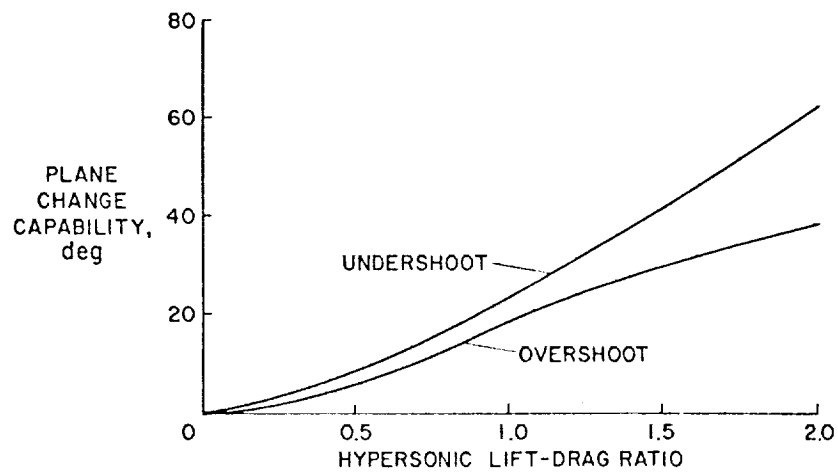


Figure 6.- Aerodynamic plane change capability for Mars entry and skip out to orbit as a function of hypersonic lift-drag ratio, $V_E$ = 8.4 km/sec.
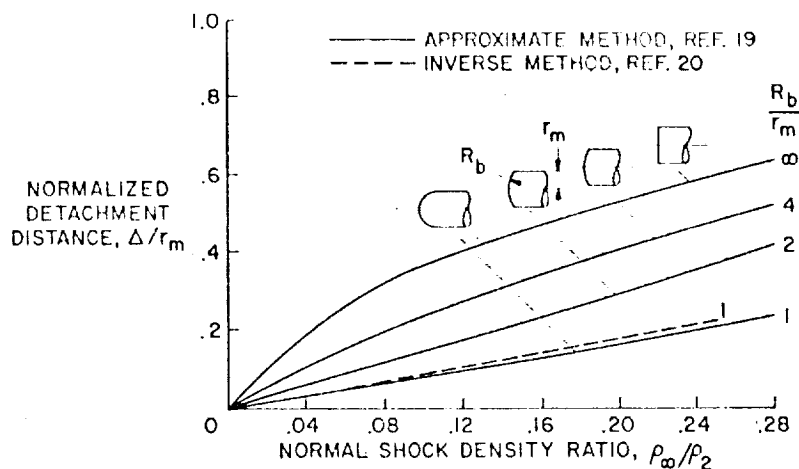
Figure 7.- Stagnation-point shock detachment distance as a function of normal shock density ratio for a family of spherically blunted cylinders.



(a) Shock shape.

(b) Pressure distribution, $\alpha = 20°$.
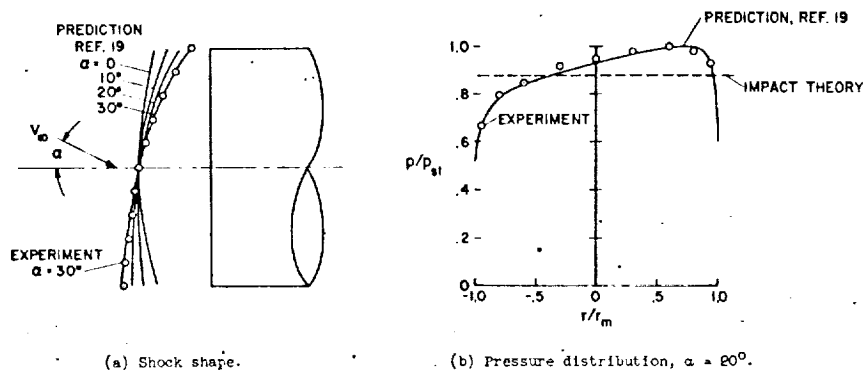
Figure 8.- Shock shape and pressure distribution for flat-faced cylinder at angle of attack.
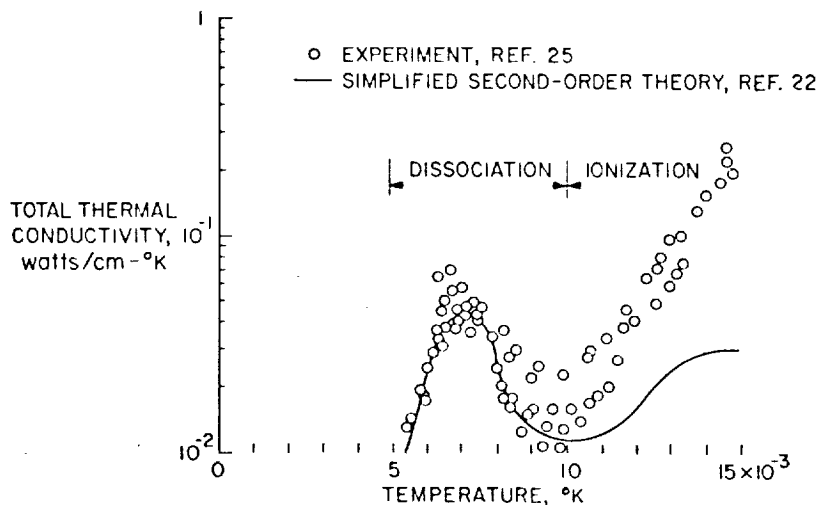


Figure 9.- Total thermal conductivity of nitrogen as a function of temperature at 1 atmosphere pressure - experiment and simplified theory.
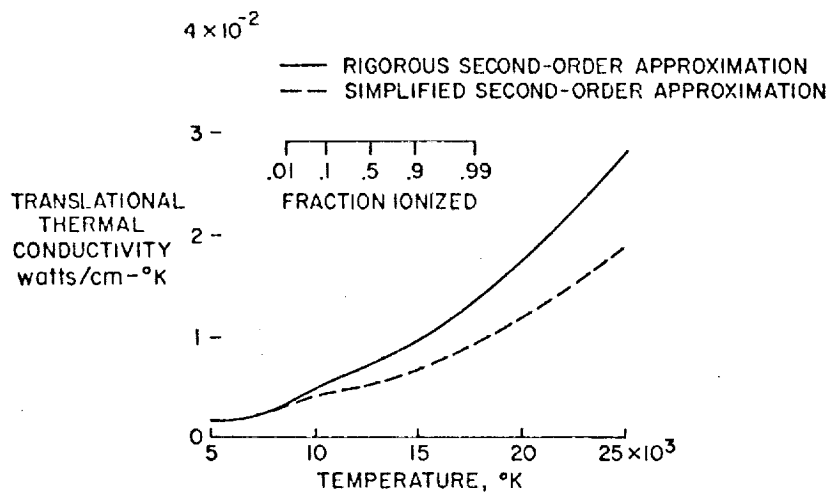
Figure 10.- Comparison of simplified and rigorous second-order approximations for translational thermal conductivity of argon, $10^{-1}$ atmosphere.
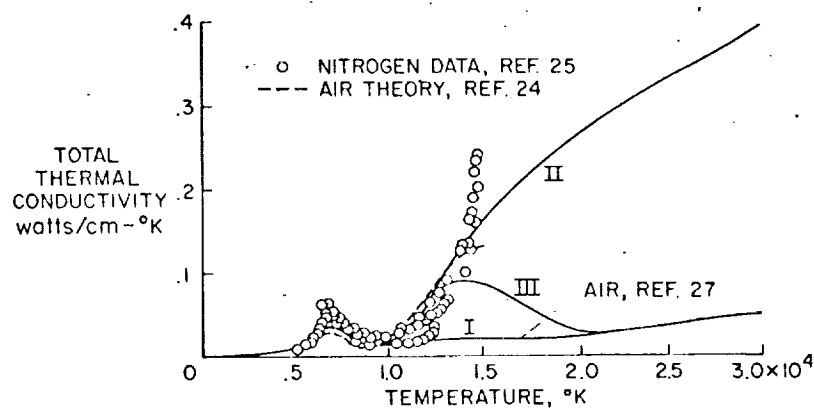


Figure 11.- Total thermal conductivity of air as a function of temperature; arbitrary extrapolations, 1 atmosphere.
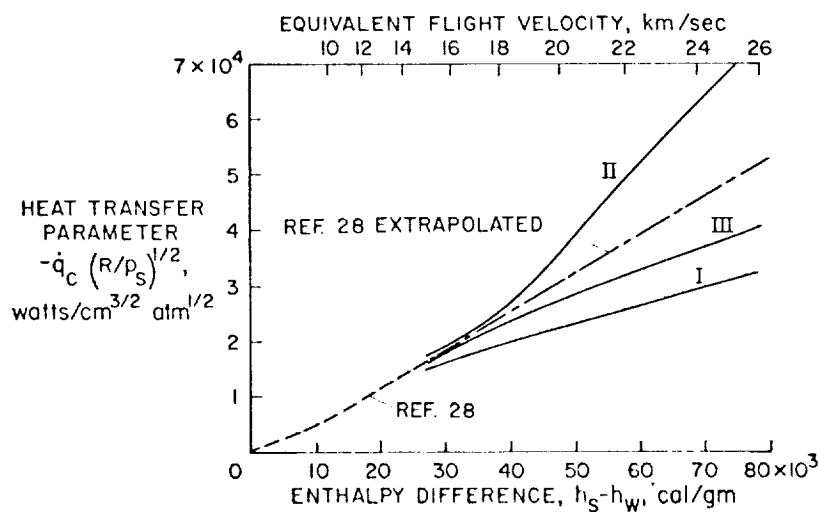


Figure 12.- Stagnation-point convective heat-transfer parameter for three different assumed total thermal conductivities of ionized air.
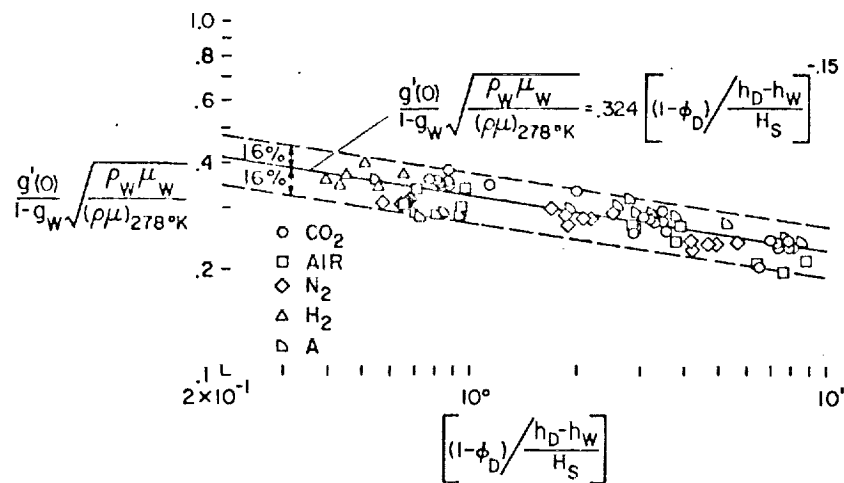
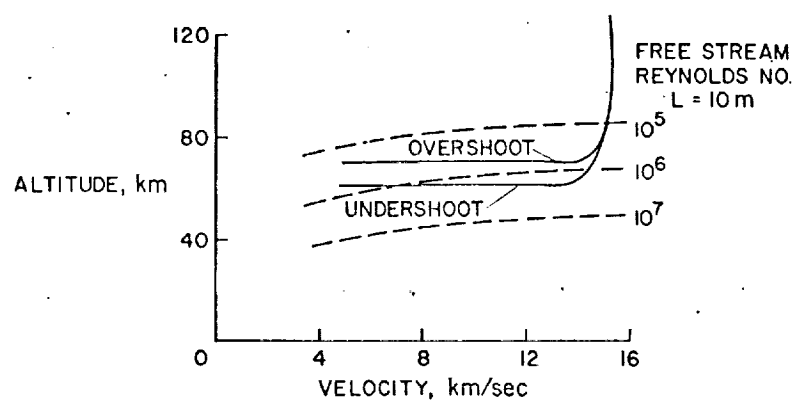Figure 13.- Correlation of stagnation heat transfer for a number of gases.

$$\frac{g'(0)}{1-g_W}\sqrt{\frac{\rho_W \mu_W}{(\rho\mu)_{278°K}}} = .324\left[(1-\phi_D)\!\left/\frac{h_D-h_W}{H_S}\right.\right]^{-.15}$$

$$\frac{g'(0)}{1-g_W}\sqrt{\frac{\rho_W \mu_W}{(\rho\mu)_{278°K}}}$$

$$\left[(1-\phi_D)\!\left/\frac{h_D-h_W}{H_S}\right.\right]$$

o $CO_2$
□ AIR
◇ $N_2$
△ $H_2$
◩ A



Figure 14.- Reynolds number flight regime for typical hyperbolic earth entry; $V_E$ = 15.2 km/sec, L/D = 1.



DATA
o REF. 34, 9% $CO_2$-91% $N_2$, $\rho_\infty/\rho_0$ = .018-.12
◻ REF. 36, 7-1/2% $CO_2$, 92-1/2% $N_2$, $\rho_\infty/\rho_0$ = .08
◇ REF. 37, 9% $CO_2$-91% $N_2$, $\rho_\infty/\rho_0$ = .001-.04
△ REF. 38, 9% $CO_2$-90% $N_2$-1% A, $\rho_\infty/\rho_0$ = .002-.02

EMISSION PARAMETER
$E/(\rho/\rho_0)^{1.55}$, watts/cm$^3$

PREDICTIONS
—— REF. 34, 9% $CO_2$-91% $N_2$, $\rho_\infty/\rho_0$ = .018-.12 (MOLECULAR RADIATORS ONLY)
——— REF. 37, 9% $CO_2$-91% $N_2$, $\rho_\infty/\rho_0$ = .01 (INCLUDES CONTINUUM)
═══ REF. 35, AIR, $\rho_\infty/\rho_0$ = .013-.08
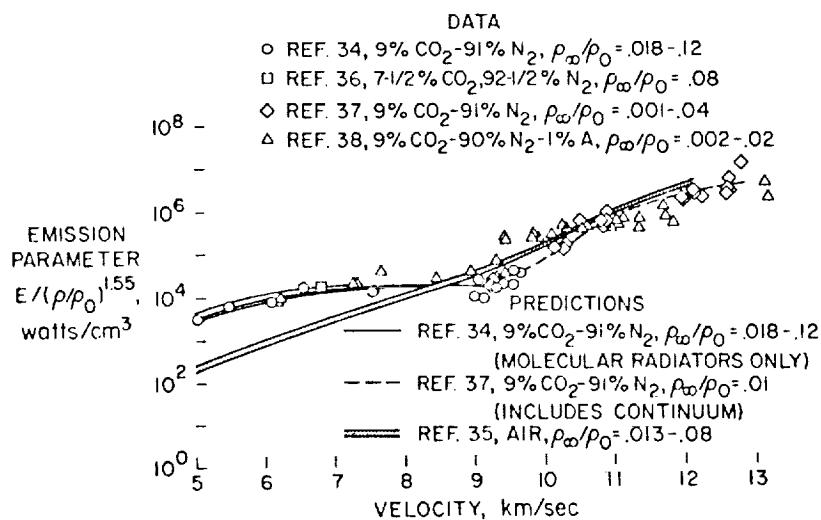
Figure 15.- Equilibrium radiation from a $CO_2$-$N_2$ mixture.
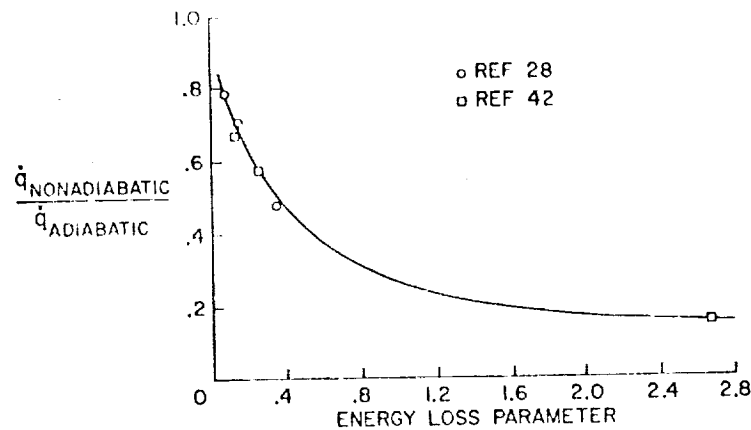
Figure 16.- Reduction in stagnation radiative heat-transfer rate as a
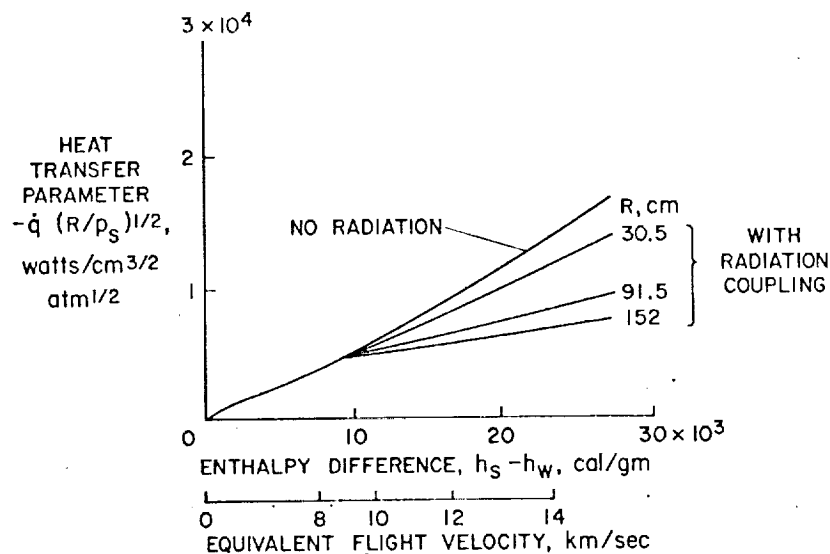function of energy loss parameter.



Figure 17.- Effect of radiation energy loss on convective stagnation-
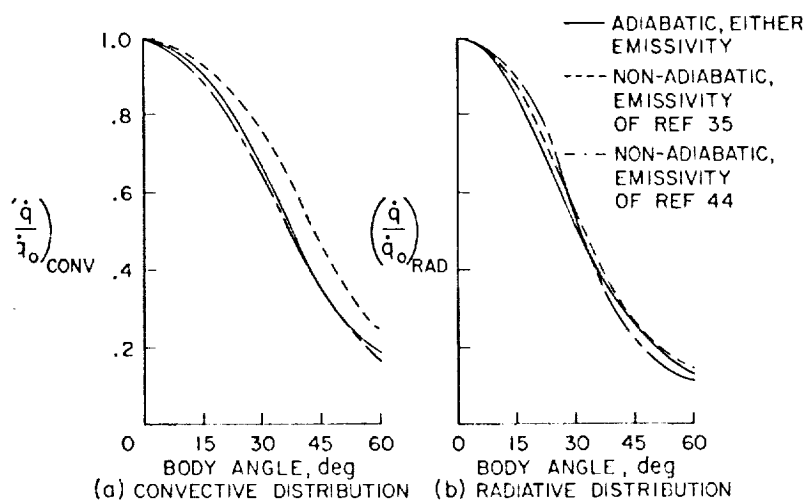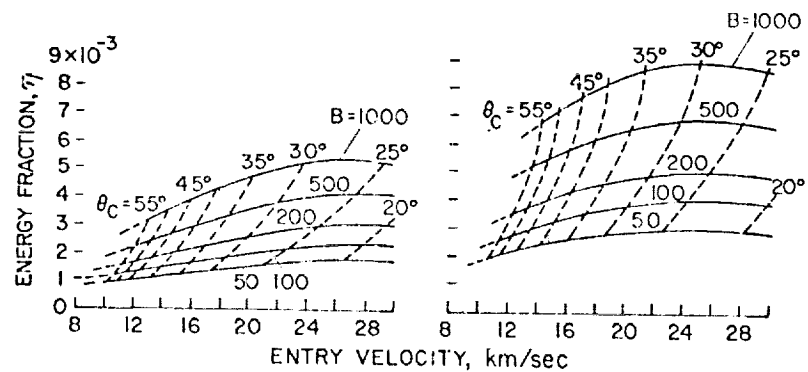point heat-transfer rate, 1 atmosphere pressure.
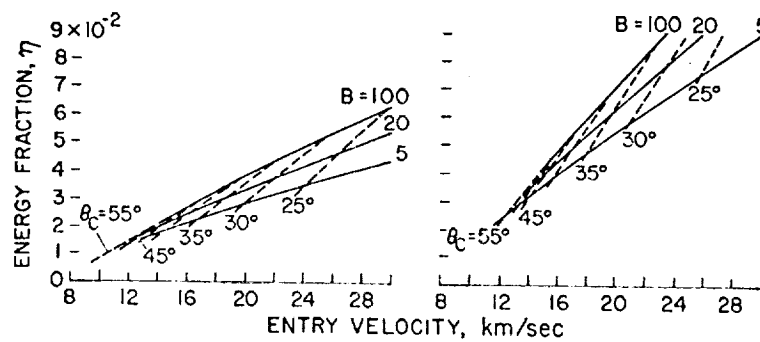


(a) CONVECTIVE DISTRIBUTION   (b) RADIATIVE DISTRIBUTION

Figure 18.- Effect of radiative cooling on convective and radiative
heat-transfer distributions for a hemisphere; V = 15.2 km/sec,
altitude = 58 km, radius = 1.52 m.

126

(a) Teflon ablator. (b) Vaporizing quartz ablator.

Figure 19.- Minimum absorbed energy fractions for optimum cones with all laminar flow.



(a) Teflon ablator.    (b) Vaporizing quartz ablator.

Figure 20.- Minimum absorbed energy fractions for optimum cones with all turbulent flow.
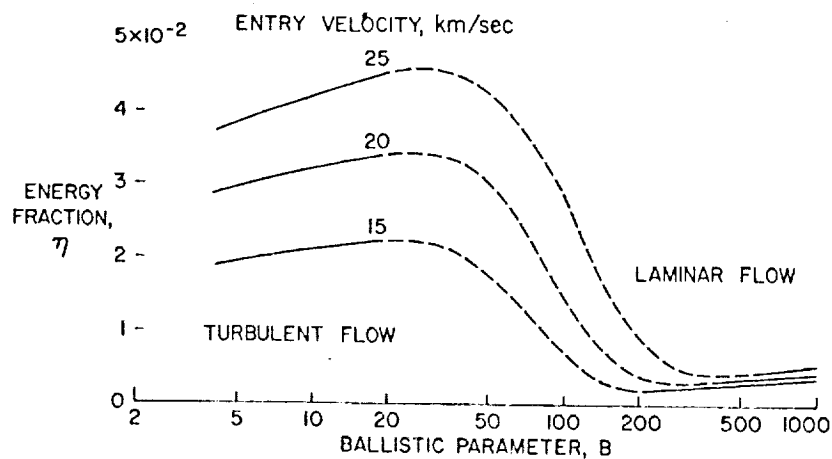


Figure 21.- Variation of minimum absorbed energy fraction with ballistic parameter for several entry velocities, teflon ablator.
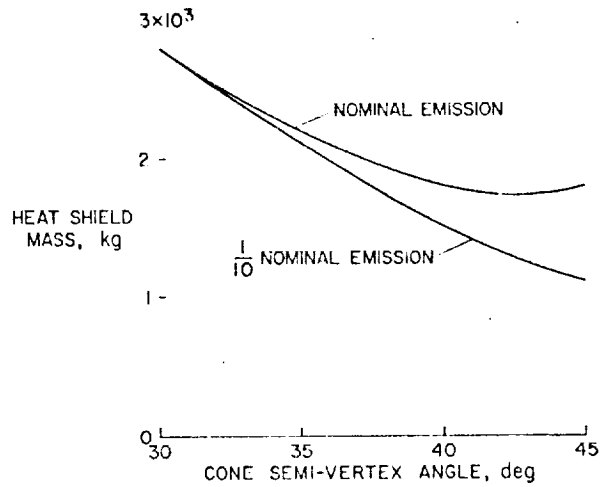
Figure 22.- Heat-shield mass as a function of cone semivertex angle for a lifting entry vehicle; $L/D = 0.6$, $V_E = 19.8$ km/sec. Effect of level of emission.
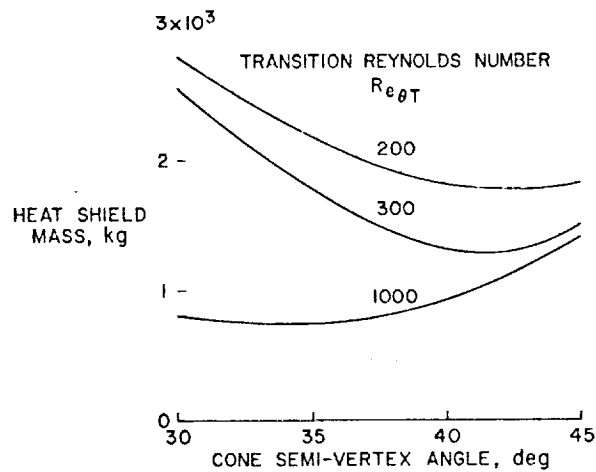


Figure 23.- Heat-shield mass as a function of cone semivertex angle for a lifting entry vehicle; $L/D = 0.6$, $V_E = 19.8$ km/sec. Effect of transition Reynolds number.
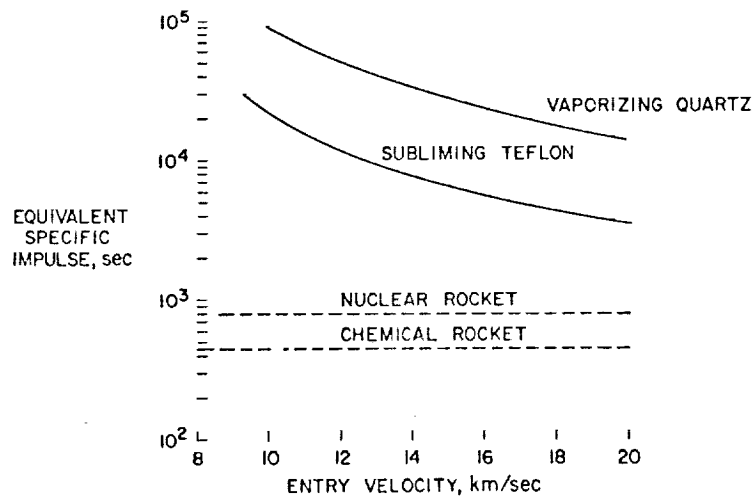


Figure 24.- Equivalent specific impulse of aerodynamically braked vehicle, laminar flow.